

Sensor and Simulation Notes

Note 276

30 September 1982

MEASURED CHARACTERISTICS OF MGL AND ACD SENSORS

V. V. Liepa and T.B.A. Senior
Radiation Laboratory
Department of Electrical and Computer Engineering
The University of Michigan
Ann Arbor, Michigan 48109

Abstract

The frequency responses of the MGL-2D(A), MGL-6A(A) and ACD-4A(R) free-space sensors have been measured and analyzed. The measurements were made over the frequency range 118 to 4400 MHz whose upper limit far exceeds the 3-dB roll-off frequencies for the sensors. All three sensors were evaluated in terms of the linearity of the frequency response, the angular behavior vis-a-vis a dipole pattern, and the rotational symmetry (MGL sensors only). Whereas the linearity persists only slightly beyond the roll-off frequencies, the dipole and symmetry properties extend to frequencies two or three times greater.

In addition, some preliminary data for the MGL-5B(R) and MGL-7A(R) ground plane sensors are presented.

CLEARED
FOR PUBLIC RELEASE

PL/PA 31 DEC 96

PL 96-1145

ACKNOWLEDGEMENT

The authors are indebted to H. Yoon for making the measurements, sometimes two or three times over; to C. Bickley and T. M. Willis, III for developing the data processing techniques and writing the programs; and to W. Rasey for typing the manuscript. We are especially grateful to Dr. C. Baum of AFWL for his suggestions in the area of data analysis and presentation.

TABLE OF CONTENTS

ACKNOWLEDGEMENT	2
ILLUSTRATIONS	4
TABLES	8
1. INTRODUCTION	9
2. GENERAL FORMULAS	11
2.1 Theoretical Considerations	11
2.2 Practical Considerations	
3. EXPERIMENTAL FACILITY	20
4. GROUND PLANE SENSOR EVALUATION	24
4.1 Ground Plane	24
4.2 Measurements and Calibrations	25
4.3 Sensor Responses	35
4.4 Discussion	43
5. FREE-SPACE SENSOR EVALUATION	54
5.1 The Sensors	54
5.2 Experimental Techniques	57
5.3 Angular Response Measurements	62
5.3.1 ACD-4A(R) Sensor	62
5.3.2 MGL-2D(A) and MGL-6D(A)	64
5.4 Angular Response Data Analysis	67
5.5 Frequency Response Data Analysis	89
6. SUMMARY	95
7. REFERENCES	98
APPENDIX A: ACD-4A(R) DIPOLE RESPONSE DATA (RAW)	99
APPENDIX B: MGL-2D(A) AND MGL-6A(A) DIPOLE RESPONSE DATA (RAW)	115
APPENDIX C: MGL-2D(A) AND MGL-6A(A) ROTATIONAL RESPONSE DATA (RAW)	144

ILLUSTRATIONS

<u>Figure</u>		<u>Page</u>
1	Coordinate systems used for theoretical analysis.	14
2	Block diagram of the facility.	21
3	Resistively loaded ground plane used in the measurements.	26
4	Ground plane sensors used in the evaluation.	28
5	Calibration of the 20-dB attenuator, deduced from measurements numbers 5 and 7.	32
6	Calibration of the 6-dB attenuator, deduced from measurements numbers 6 and 7.	33
7	Calibration for the 0.020-inch coax, deduced from measurements numbers 9 and 10.	34
8	Computed calibration for the 0.020-inch coax.	36
9	Calibration for the 0.030-inch coax, deduced from measurements numbers 7 and 8.	37
10	Computed calibration for the 0.030-inch coax.	38
11	Response of the MGL-7 sensor referenced to that of the MGL-8.	39
12	Response of the MGL-7 sensor with MGL-8 used as a standard.	41
13	Response of the MGL-7 sensor referenced to that of the MGL-8.	42
14	Response of the MGL-5 sensor with the MGL-8 used as a standard.	44
15	Amplitude of the MGL-7 response compared with the Sharpe-Roussi simulation. The dots show the frequencies corresponding to the dominant poles in the 10-pole simulation.	46
16	Phase of the MGL-7 response compared with the Sharpe-Roussi simulation. The dots show the frequencies corresponding to the dominant poles in the 10-pole simulation.	47

<u>Figure</u>	<u>Page</u>	
17	Amplitude of the MGL-5 response compared with the Sharpe-Roussi simulation. The dots show the frequencies corresponding to the 18 poles used in the simulation.	50
18	Phase of the MGL-5 response compared with the Sharpe-Roussi simulation. The dots show the frequencies corresponding to the 18 poles used in the simulation.	51
19	Amplitude of a portion of the MGL-5 compared with the Sharpe-Roussi simulation using 14 poles.	52
20	Phase of a portion of the MGL-5 compared with the Sharpe-Roussi simulation using 14 poles.	53
21	Sensors used in the study.	56
22	Modified MGL-9(R). (The coaxial cables were bent 4.75 inches from the loop to adapt for H-vertical polarization. In the original design the coax was straight.)	58
23	Twinaxial to dual-coaxial adapters.	61
24	Measurement geometry for the ACD sensors. (The θ -variation produces the angular (dipole) response.)	63
25	Measurement geometry for MGL-series sensors. (The θ -variation produces angular (dipole) response and ϕ -variation produces azimuthal (constant) response.)	65
26	Styrofoam jig used for support and rotation of MGL-2 and MGL-6 sensors. (The incident field is from the right-hand side.)	66
27	Measured angular response of MGL-2D(A) at 150 MHz.	68
28	$A_n(f)$ for ACD-4A(R).	70
29	$Z_d(f)$ for ACD-4A(R).	71
30	$\mathcal{E}_{\max}(f)$ for ACD-4A(R), $ \theta \leq 60^\circ$.	71
31	$\mathcal{E}_{\max}(f)$ for ACD-4A(R), $ \theta \leq 30^\circ$.	72
32	$\mathcal{E}_{\max}(f)$ for ACD-4A(R), $\theta = 0^\circ$.	72

<u>Figure</u>		<u>Page</u>
33	$A_n(f)$ for MGL-2D(A), gap No. 1 at $\phi = 90^\circ$.	73
34	$\mathcal{E}^2(f)$ for MGL-2D(A), gap No. 1 at $\phi = 90^\circ$.	74
35	$\mathcal{E}_{\max}(f)$ for MGL-2D(A), $ \theta \leq 60^\circ$, gap No. 1 at $\phi = 90^\circ$.	74
36	$\mathcal{E}_{\max}(f)$ for MGL-2D(A), gap No. 1 at $\phi = 90^\circ$, $ \theta \leq 30^\circ$.	75
37	$\mathcal{E}_{\max}(f)$ for MGL-2D(A), gap No. 1 at $\phi = 90^\circ$, $\theta = 0^\circ$.	75
38	$A_n(f)$ for MGL-2D(A), gap No. 1 at $\phi = 45^\circ$.	76
39	$\mathcal{E}^2(f)$ for MGL-2D(A), gap No. 1 at 45° .	77
40	$\mathcal{E}_{\max}(f)$ for MGL-2D(A), gap No. 1 at 45° , $ \theta \leq 60^\circ$.	77
41	$\mathcal{E}_{\max}(f)$, for MGL-2D(A), gap No. 1 at 45° , $ \theta \leq 30^\circ$.	78
42	$\mathcal{E}_{\max}(f)$, for MGL-2D(A), gap No. 1 at 45° , $\theta = 0^\circ$.	78
43	$B_n(f)$ for MGL-2D(A).	79
44	$\mathcal{E}_r^2(f)$ for MGL-2D(A).	80
45	$\mathcal{E}_{r_{\max}}(f)$ for MGL-2D(A).	80
46	$A_n(f)$ for MGL-6A(A), gap No. 1 at $\phi = 90^\circ$.	81
47	$\mathcal{E}^2(f)$ for MGL-6(A), gap No. 1 at $\phi = 90^\circ$.	82
48	$\mathcal{E}_{\max}(f)$ for MGL-6(A), gap No. 1 at $\phi = 90^\circ$, $ \theta \leq 60^\circ$.	82
49	$\mathcal{E}_{\max}(f)$ for MGL-6A(A), gap No. 1 at 90° , $ \theta \leq 30^\circ$.	83
50	$\mathcal{E}_{\max}(f)$ for MGL-6A(A), gap No. 1 at 90° , $\theta = 0^\circ$.	83
51	$A_n(f)$ for MGL-6A(A), gap No. 1 at $\phi = 45^\circ$.	84
52	$\mathcal{E}^2(f)$ for MGL-6A(A), gap No. 1 at $\phi = 45^\circ$.	85
53	$\mathcal{E}_{\max}(f)$ for MGL-6A(A), gap No. 1 at $\phi = 45^\circ$, $ \theta \leq 60^\circ$.	85

<u>Figure</u>		<u>Page</u>
54	$\mathcal{E}_{\max}(f)$ for MGL-6A(A), gaps at $\phi = 45^\circ$, $ \theta \leq 30^\circ$.	86
55	$\mathcal{E}_{\max}(f)$ for MGL-6A(A), gaps at $\phi = 45^\circ$, $\theta = 0^\circ$.	86
56	$B_n(f)$ for MGL-6A(A).	87
57	$\mathcal{E}_r^2(f)$ for MGL-6A(A).	88
58	$\mathcal{E}_{r_{\max}}(f)$ for MGL-6A(A).	88
59	Response ratio of ACD-2/MGL-9.	91
60	Response ratio of ACD-4/ACD-2.	92
61	Response ratio of MGL-2/MGL-9.	93
62	Response ratio of MGL-6/MGL-9.	94

TABLES

<u>Table</u>		<u>Page</u>
1	Components Studied	29
2	Measurement Combinations	30
3	Poles and Residues for MGL-7	48
4	Identification of Free-Space Sensors Used	55
5	Summary of Results	96
A1	List of ACD-4 Dipole Data Plots	99
B1	List of MGL-2 Dipole Data Plots	115
C1	List of MGL-2 and MGL-6 Rotational Data Plots	144

1. INTRODUCTION

An electromagnetic field sensor is a special purpose receiving antenna which converts a given electromagnetic field quantity into a voltage or current according to a prescribed relation. The relation should be as simple as possible, e.g., a constant of proportionality, or a linear form involving frequency or time.

As is true with most instruments, however, there is a maximum frequency (frequency domain) or minimum rise time (time domain) beyond which the simple relation no longer holds. In general, the smaller the sensor, the larger the frequency range over which the performance can be prescribed. Since the output of a time derivative sensor is inversely proportional to its size and directly proportional to the frequency, the output of a particular sensor may not be large enough for accurate measurements at low frequencies. In this case one could choose to use a larger sensor to obtain a bigger output at the expense of reducing the upper frequency limit for the prescribed behavior. If used at frequencies beyond this limit (the roll-off frequency), erroneous data will result; and though two sensors of different sizes might seem to constitute a solution, their use would complicate the data acquisition procedures. In addition, there may not be room on the test object to mount more than one sensor.

For these and other reasons, it is desirable to obtain as much information as possible about the behavior of the sensors

that are used. The purpose of the present study was to investigate and analyze the responses of various EMP sensors over a frequency range extending well beyond the so-called 3-dB roll-off frequencies. The sensors which were studied were the MGL-2D(A), MGL-6A(A) and ACD-4A(R) free-space sensors, and the MGL-5B(R) and MGL-7A(R) ground plane versions. In each instance the responses were measured as a function of frequency and, in addition, for the free-space sensors, the dipole patterns and rotational symmetry were determined.

The mathematical formulas which define the responses and which were used in analyzing the data are presented in Chapter 2, and this is followed (Chapter 3) by a description of the experimental facility used to make the measurements. Chapter 4 is concerned with the ground plane sensors and includes a detailed presentation of the data and the results of the analyses. The majority of the effort was devoted to the free-space sensors, which are treated in Chapter 5. The significant results are summarized in Chapter 6 in a manner such that the performance of the various sensors can be compared.

2. GENERAL FORMULAS

Since the MGL and ACD electromagnetic field sensors were developed to measure electromagnetic fields in the time domain, it is natural to evaluate them in the time domain by measuring their impulse or step responses. In general, however, such tests are not accurate enough to quantify their detailed performance in the frequency domain. This is particularly true at the higher frequencies where the response cannot be deduced from the time domain behavior because of instrument and/or recording limitations, and in the study reported here the frequency response of the MGL and ACD sensors was measured directly in the frequency domain.

2.1 Theoretical Considerations

The sensors that were tested were designed [1] to provide a simple mathematical relation between a designated field quantity and the output voltage over a wide range of frequencies. For the ACD sensors the voltage response is [2]

$$V_o(t) = R_{\epsilon_o} \bar{A}_{eq} \cdot \frac{d}{dt} \bar{E}(t) \quad (\text{time domain})$$

or

$$V_o(f) = j2\pi f \epsilon_o \bar{A}_{eq} \cdot \bar{E}(f) \quad (\text{frequency domain})$$

(1)

where V_o is the sensor output (volts),
 R is the sensor's characteristic load impedance
 (usually 100 ohms),
 A_{eq} is the sensor's equivalent area (in m^2),
 $\epsilon_o \approx (36\pi)^{-1} 10^{-9}$ (Farad/m),
 \bar{E} is the electric field intensity (volt/m),
 f is the frequency (Hz),

and a time dependence $\exp(j2\pi ft)$ has been assumed. For the MGL sensors,

$$V_o(t) = \mu_o \bar{A}_{eq} \cdot \frac{d}{dt} \bar{H}(t) \quad (\text{time domain})$$

or

$$V_o(f) = j2\pi f \mu_o \bar{A}_{eq} \cdot \bar{H}(f) \quad (\text{frequency domain}) \quad ,$$

where $\mu_o = 4\pi \times 10^{-7}$ (Henry/m) and

\bar{H} is the magnetic field intensity (Ampere/m).

Each sensor is a calibrated device, and its equivalent area is specified.

The above formulas can be obtained by retaining only the dipole terms in the low frequency expansions of the responses, and are valid for sufficiently low frequencies. As the frequency is increased, the influence of higher order multipoles becomes significant, leading to a response which is no longer linear in frequency and does not have the aspect dependence characteristic of a dipole, e.g., the dot product (cosine) behavior as a function of angle.

The coordinate systems used in analyzing the measured data for the responses of the ACD (electric dipole) and MGL (magnetic dipole) free space sensors are shown in Fig. 1. In each case the z axis is fixed by the sensor, and the relevant incident field vector (\bar{E} for the ACD sensor and \bar{H} for the MGL sensor) is chosen to be in the θ' direction of a spherical polar coordinate system (r, θ', ϕ) . The frequency domain responses (1) and (2) then become

$$V_o(f) = j2\pi f R \epsilon_o A_{eq} E(f) \sin \theta' \quad (\text{ACD}) \quad (3)$$

$$V_o(f) = j2\pi f \mu_o \bar{A}_{eq} H(f) \sin \theta' \quad (\text{MGL}) \quad (4)$$

and both can be written as

$$V(\theta', \phi; f) = A(f) F \sin \theta' \quad (5)$$

where $A(f)$ is a function of the frequency alone and F denotes the appropriate incident field quantity (E for the ACD sensor and H for the MGL). Outside the frequency range where (1) and (2) are applicable,

$$V(\theta', \phi; f) = \{A(f) \sin \theta' + \epsilon(\theta', \phi; f)\} F \quad (6)$$

where ϵ is an error term embodying, amongst other things, the effect of the higher order multipoles.

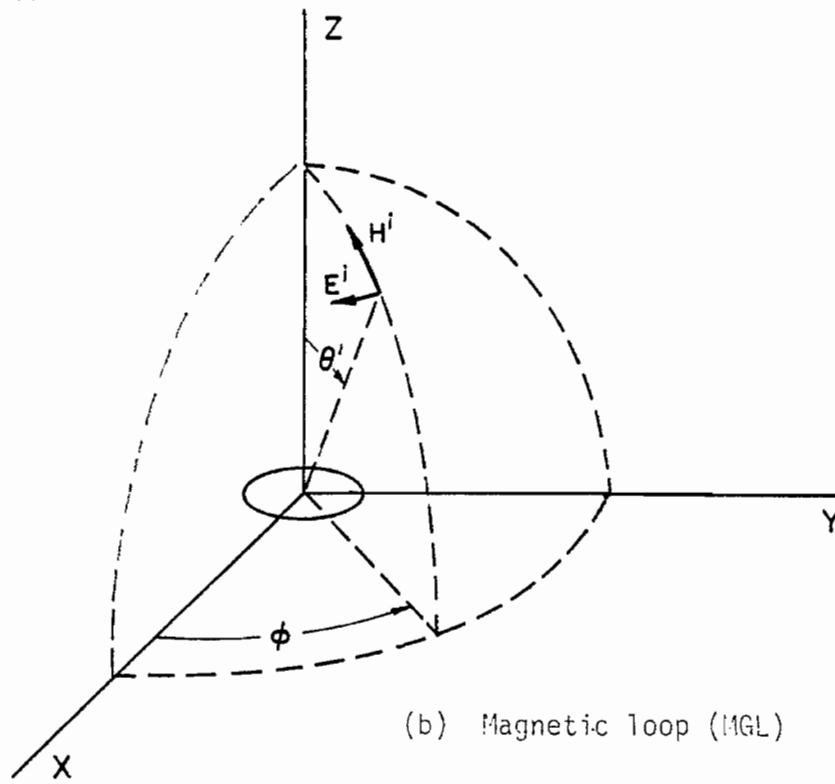
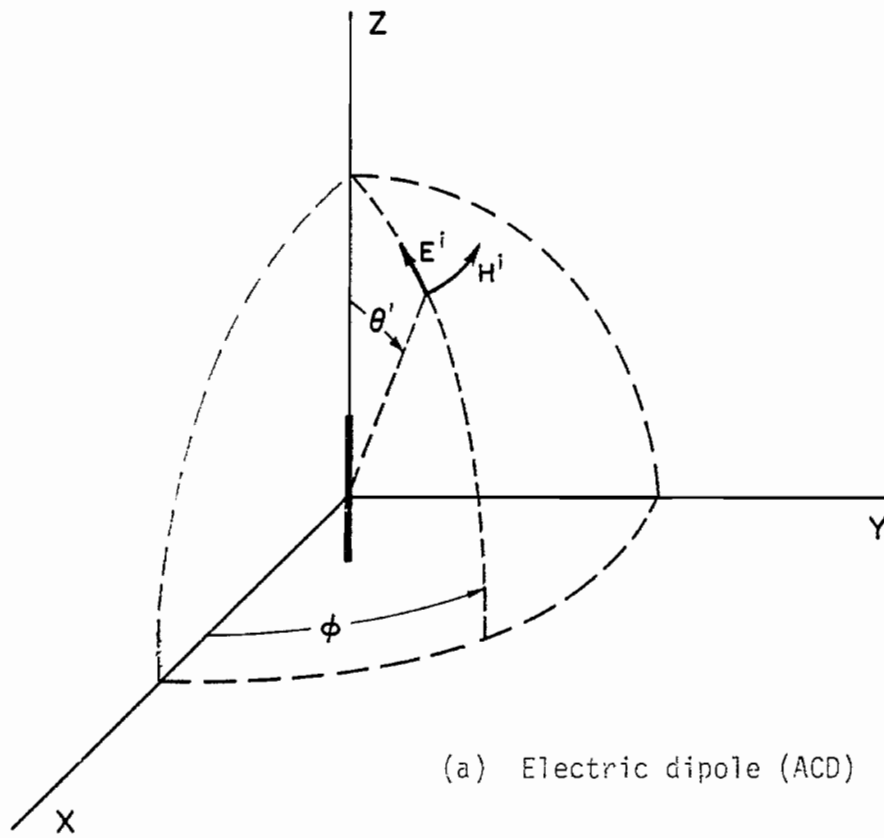


Fig. 1: Coordinate system used for theoretical analysis.

To determine A and ϵ from V, the standard procedure is to expand $V(\theta', \phi; f)$ in zonal harmonics [3], so that

$$\tilde{V}(\theta', \phi; f) = A(f)P_1^1(\cos \theta') + \{\text{terms in } \theta', \phi, f\}$$

where \tilde{V} is the recorded signal normalized relative to the incident field strength, i.e., $\tilde{V} = V/F$. We can now find A(f) by using the orthogonality properties of the zonal harmonics. If \tilde{V} is assumed independent of ϕ , multiplication by $P_1^1(\cos \theta')$ and integration over 4π steradians ($d\Omega = \sin \theta' d\theta' d\phi$) gives

$$A(f) = \frac{3}{4} \int_0^\pi \tilde{V}(\theta', \phi; f) \sin^2 \theta' d\theta' \quad (7)$$

We note in passing that if the entire right-hand side of (6) is assumed to be independent of ϕ rather than just the first term, an alternative approach is to expand \tilde{V} in a Fourier sine series. This leads to an alternative weighting factor in (7) which gives more weight to the angles at which the sensor is end-on, but is less defensible as a general procedure.

From (7) the mean squared angular error is defined as

$$\xi^2(f) = \frac{\int_{\Omega} |\tilde{V}(\theta', \phi; f) - A(f) \sin \theta'|^2 d\Omega}{\int_{\Omega} |A(f) \sin \theta'|^2 d\Omega}$$

i.e.,

$$\mathcal{E}^2(f) = \frac{3}{4} |A(f)|^{-2} \int_0^{\pi} |\tilde{V}(\theta', \phi; f) - A(f) \sin \theta'|^2 \sin \theta' d\theta' \quad (8)$$

and is a measure of the mean squared deviation of the angular response data from the dipole behavior. The maximum error $\mathcal{E}_{\max}(f)$ is likewise defined as

$$\mathcal{E}_{\max}(f) = \max_{\pi - \theta'_{\max} \leq \theta' \leq \theta'_{\max}} \frac{|\tilde{V}(\theta', \phi; f) - A(f) \sin \theta'|}{|A(f) \sin \theta'|} \quad (9)$$

and indicates the maximum deviation from the dipole pattern over a specified angular range.

2.2 Practical Considerations

In antenna work the angle defining the angular response or pattern is generally measured from the direction of the peak response, and this is the convention used in the sensor catalog [2] where, for example, data sheet 1118 cites the response of an ACD sensor as

$$V = R\bar{A}_{\text{eq}} \cdot \frac{d}{dt} \bar{D} \quad \text{or} \quad V = RA_{\text{eq}} \frac{d}{dt} D \cos \theta \quad (10)$$

Here, θ is the angle between the direction of the vector equivalent area \bar{A}_{eq} and that of the appropriate field vector, so that

$$\theta = \theta' - \pi/2 \quad (11)$$

where θ' is the spherical polar angle defined in the previous section. For consistency with the literature, we shall henceforth express all results in terms of θ , where $-\pi/2 \leq \theta \leq \pi/2$.

Consider also the nature of the signal $v(\theta, \phi; f)$ present at the output of a sensor. In practice,

$$v(\theta, \phi; f) = V(\theta, \phi; f) F K \quad (12)$$

where V is the sensor response to a unit incident field, F is an incident field of unknown strength, and K is the response of the chamber, cables, amplifiers, etc. In our measurements it is postulated that F and K are time invariant, and thus, for example, the ratio of measurements made for some value of θ and for $\theta = 0$ (broadside) at two different times yields

$$V_n(\theta, \phi; f) = \frac{V(\theta, \phi; f)}{V(0, \phi; f)} \quad (13)$$

where V_n is independent of F and K . $V_n(\theta, \phi; f)$ is the response relative to that of the same sensor at broadside incidence, and (7) through (9) are readily expressed in terms of this normalized quantity:

$$A_n(f) = \frac{3}{4} \int_{-\pi/2}^{\pi/2} V_n(\theta, \phi; f) \cos^2 \theta \, d\theta \quad (14)$$

$$\xi^2(f) = \frac{3}{4} |A(f)|^{-2} \int_{-\pi/2}^{\pi/2} |V_n(\theta, \phi; f) - A_n(f) \cos \theta|^2 \cos \theta \, d\theta \quad (15)$$

$$\xi_{\max}^2(f) = \max \frac{|V_n(\theta, \phi; f) - A_n(f) \cos \theta|}{|A_n(f) \cos \theta|}, \quad |\theta| < \theta_{\max} \quad (16)$$

In the derivation of (7) through (16) it was assumed that the sensor response is independent of ϕ (see Fig. 1), and ϕ has been shown as one of the variables of V_n only for generality. For the ACD sensors the response is ϕ independent from symmetry, but this is not true for an MGL sensor. The free-space version evaluated in this study has four gaps which, at low frequencies, should be "invisible." As shown later, however, at high frequencies the response is affected by the orientation of the field with respect to the gaps.

To assess the rotational response of the MGL sensors, an average rotational response coefficient is defined as

$$B_n(f) = \frac{1}{2\pi} \int_0^{2\pi} V_n(0, \phi; f) d\phi \quad (17)$$

(cf. (14)). By analogy with (15), the mean squared rotational error is

$$\xi_r^2(f) = \frac{1}{2\pi} |B_n(f)|^{-2} \int_0^{2\pi} |V_n(0, \phi; f) - B_n(f)|^2 d\phi \quad (18)$$

and the maximum rotational error is

$$\xi_{r \max}(f) = \max \frac{|V_n(0, \phi; f) - B_n(f)|}{|B_n(f)|} \quad (19)$$

The formulas in (14) through (19) were programmed in BASIC for the HP9845 calculator, and results are presented in Chapter 5.

3. EXPERIMENTAL FACILITY

The measurements were made in the University of Michigan's surface (and near) field facility, a block diagram of which is shown in Fig. 2. The system is a CW one in which the frequency is swept (stepped) over a wide range, and a key part of the facility is a tapered anechoic chamber approximately 50 feet in length. The rectangular test region is 18 feet wide and 12 feet high. The rear wall is covered with 72-inch-high performance pyramidal absorber, with 18-inch material used on the side walls, floor and ceiling. The material in the tapered section (or throat) is 2-inch hairflex absorber. The chamber can be thought of as a lossy wall horn antenna terminated by the rear wall. The signal is launched from a single exponentially tapered broadband antenna located at the apex of the chamber. The antenna is fixed and since the radiated signal is horizontally polarized, the pseudo plane wave in the center ('quiet zone') portion of the test region is also horizontally polarized.

The instrumentation is centered around a Hewlett-Packard 8410B network analyzer, and is computer controlled. An HP9830A calculator controls the frequency to be generated, switches in the appropriate power amplifiers and low-pass filters, and reads and stores the amplitude and phase of the signal picked up by the sensor. During a run, the frequencies are typically stepped from 118 to 4400 MHz. Because of the limited memory size of the calculator, this frequency range is recorded in four bands: 118 to 550 MHz (in 4.8 MHz steps), 550 to 1100 MHz (in 4.8 MHz steps),

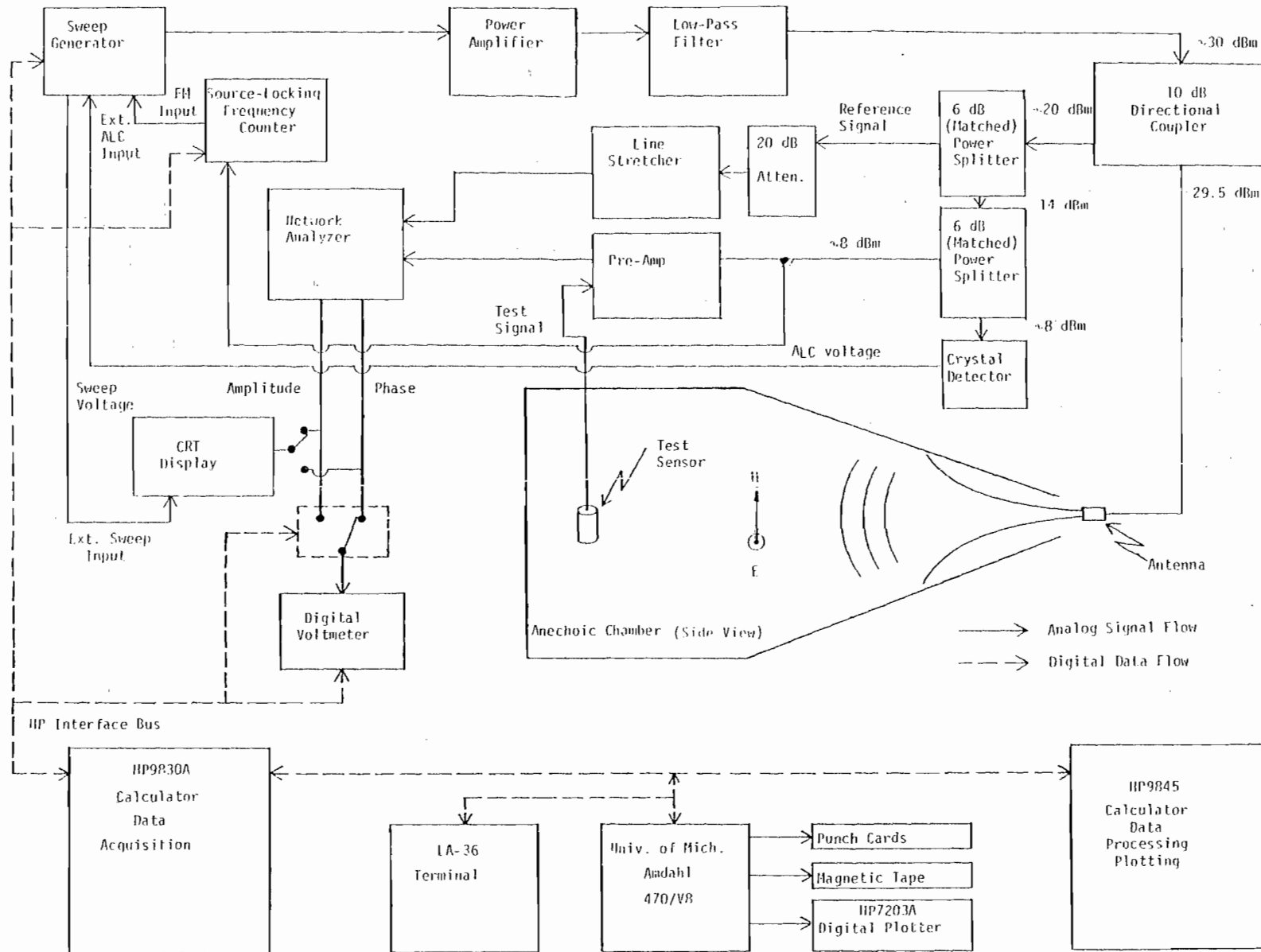


Fig. 2: Block diagram of the facility.

1100 to 2000 MHz (in 9.6 MHz steps), and 2000 to 4400 MHz (in 16 MHz steps). The data from each band are stored by the HP9830A calculator on a cassette for later transfer to an HP9845B calculator which processes and plots the data. If substantial processing or computation is involved, or if a need exists to write the data on standard computer tape, the data are transmitted to the central University of Michigan AMDAHL/V8 (IBM compatible) computer.

The signal picked up by the sensor is a function of the response not only of the sensor but also of the entire facility, including chamber, antenna, amplifiers and cabling, and it would be a virtually impossible task to separate out the contributions of each. An alternative approach is to apply some form of calibration or normalization whereby the facility response is, in principle, eliminated. When measuring the surface fields on, say, a scale model aircraft, two distinct measurements are made using the same probe or sensor: one on the aircraft, and the other on a metallic sphere or other object whose surface field is known. In conjunction with the known sphere solution, the ratio of the two measurements gives the aircraft response relative to the incident field.

In the present study, two different calibration procedures were used. To determine the angular response characteristics of a sensor, the data were normalized to the measured values of the maximum response (broadside incidence) for the same sensor. This eliminated the effects of any cable mismatch. To obtain the frequency response, each set of measurements was followed immediately by the analogous measurements

for a small sensor such as the ACD-2(R) or MGL-9(R), whose response is believed uniform and predictable out to frequencies beyond those of interest for the original sensor. The procedure worked well for the ground plane sensors (Chapter 4), but the results were less satisfactory for the free-space sensors (Chapter 5). One reason for this was the presence of currents induced on the sensor leads by "stray" fields in the chamber that ultimately affect (especially the ACD-type) sensor response, but a more severe problem was caused by the mismatches in the twin-axial leads, particularly at the twin-coax to twin-axial junctions.

The details of the measurement procedures for each type of sensor are described in the section devoted to that sensor.

4. GROUND PLANE SENSOR EVALUATION

Although the study was primarily directed at the MGL and ACD lines of free space sensors, it was felt prudent to start with MGL ground plane sensors to gain experience in the simpler situation that results. Because of the ground plane, the possibility of any lead interaction is greatly reduced, and, in addition, the probes do not have the aspect sensitivity that the free-space ones do.

In the following sections we describe the ground plane that was used, the measurements that were carried out on three different MGL sensors, the calibration of the various components involved, the deduced frequency responses of two of the sensors referenced to the response of the third, and the implications of the results obtained.

4.1 Ground Plane

Ideally the ground plane should be infinite in extent, and one consequence of using a finite size is that the surface field departs from its infinite plane value due mainly to the effect of the edge currents. For normal incidence on a plane several wavelengths in dimension, the departures are primarily due to the edges perpendicular to the incident electric vector that set up a standing wave pattern across the plate. The influence of the other edges is confined to a distance of a wavelength (or less) from them.

For use on another project it was necessary to design and fabricate a ground plane which was small enough to fit comfortably

inside the anechoic chamber but which still simulated an infinite plane over at least a central portion of the surface. To reduce the surface field perturbation created by the vertical edges, resistive sheets were added as shown in Fig. 3. Each sheet was shaped like a quarter cylinder of radius 25.5 in. and had a resistivity which increased quadratically as a function of the surface distance from the metallic plane. The effect of different resistivity variations was determined by numerical experiments carried out using codes based on resistive strip formulations, and the resistivity that was finally selected started with zero at the edge, increasing quadratically to about 1000 ohms/square at the rear.

The sheets were fabricated by spraying thin layers of resistive material on art paper. After each treatment the resistivity was measured with an ohm meter, and the process repeated until the appropriate resistivity profile was achieved. The final products had a resistivity which started at about 10 ohms/square and increased to the required value of 1000 ohms/square at the outer edges. Although the surface fields on the metallic part of the resulting ground plane have not been measured, it is inferred from the numerical experiments that over a central portion of the plane at least, the fields are virtually identical to those on an infinite plane.

4.2 Measurements and Calibrations

The MGL line are B-dot sensors with specified equivalent area A_{eq} . Three different size versions were available for this study: MGL-5B(R), serial no. 14, having $A_{eq} = 10^{-3} \text{ m}^2$; MGL-7A(R), serial no. 5, having $A_{eq} = 10^{-4} \text{ m}^2$; and MGL-8A(R), serial no. 1, having $A_{eq} = 10^{-5} \text{ m}^2$.

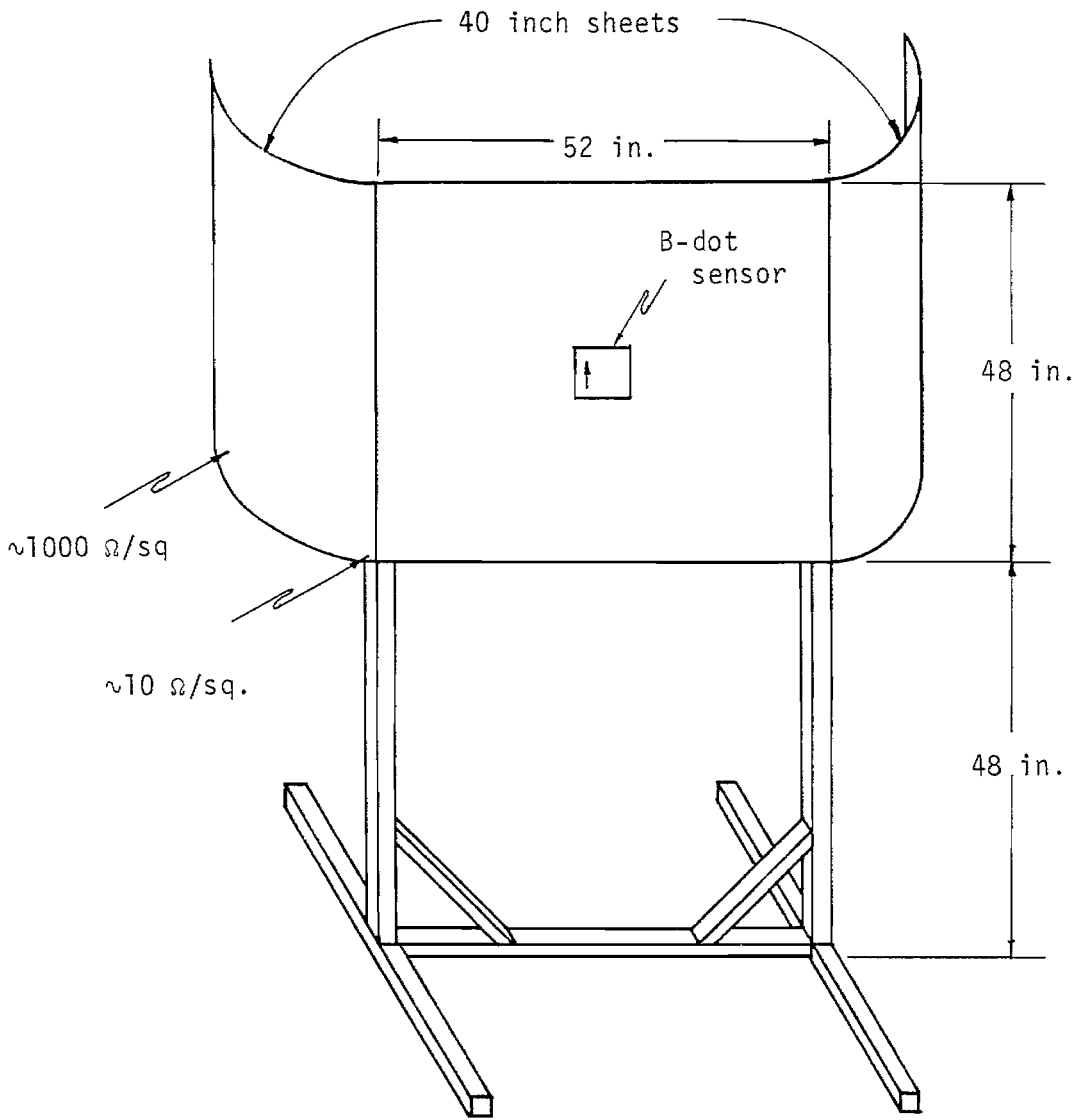


Fig. 3: Resistively loaded ground plane used in the measurements.

All were manufactured by EG&G Inc. and are described in their catalog [2]. Figure 4 is a photograph of the three sensors.

Each sensor was mounted in turn at the center of the ground plane in our surface field facility, and its output was measured as the frequency was scanned (or digitally stepped) from 118 to 4400 MHz. To connect a sensor to the system it was necessary to use adaptors as indicated in the first three lines of Table 1. These adaptors are henceforth regarded as part of the sensors, and no attempt has been made to compensate for their presence.

Any quantitative measurement is, by its nature, a comparison process in which the reference is either the response of the same system to a known field, or of a calibrated system to the existing (unknown) field. For the sensor measurements the incident field was unknown, but reproducible over a sufficient length of time to enable each sensor to be mounted in turn at the same location on the ground plane and have its response to the same field recorded. Any one sensor can therefore serve as the reference for the other two.

In practice, however, there is a difficulty. To connect a sensor to the measurement lead requires a length of coaxial cable, and because of the larger outputs from the larger sensors, attenuators must also be inserted. To eliminate their effect, it is necessary to calibrate both the cable and the attenuator. To do so, two cables and two attenuators were used as indicated in Table 1, and measurements were made on various combinations of these sensors, and the four components. The measurements performed are listed in Table 2.

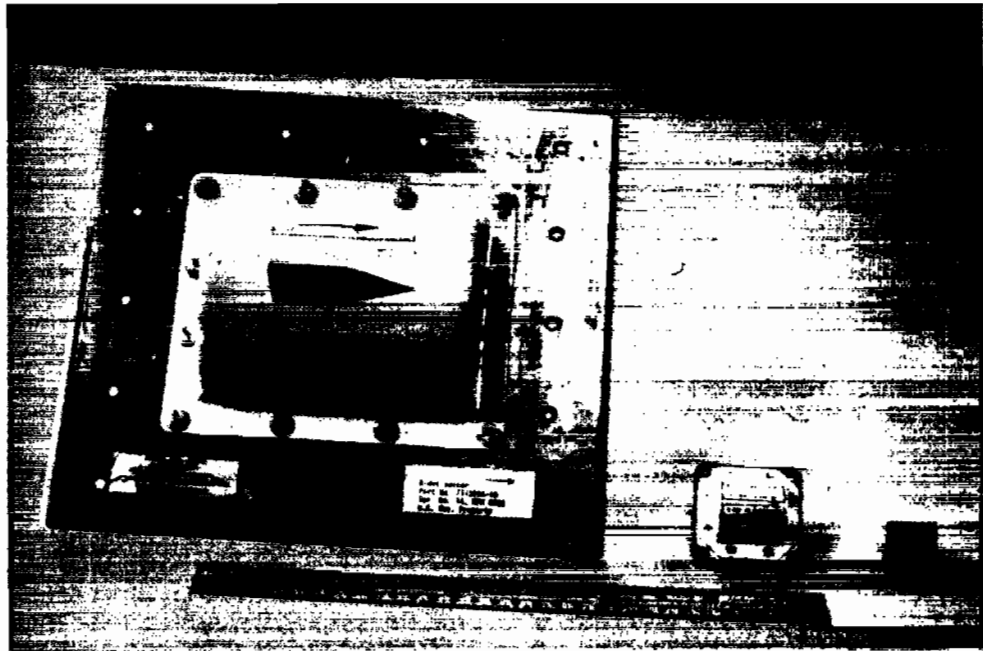


Fig. 4: Photograph of the ground plane sensors used in the evaluation.

Table 1: Components Studied

Component	Description
MGL-8A(R)	B-dot sensor, $A_{eq.} = 10^{-5} \text{ m}^2$, Ser. No. 1; with BRRM(F) → OSSM(F), OSSM(M) → OSM(F) adaptors
MGL-7A(R)	B-dot sensor, $A_{eq.} = 10^{-4} \text{ m}^2$, Ser. No. 5; no adaptors
MGL-5B(R)	B-dot sensor, $A_{eq.} = 10^{-3} \text{ m}^2$, Ser. No. 14; GR → SMA(F) adaptors
20-dB attenuator	Attenuator, Midwest Microwave, Model 444-20
6-dB attenuator	Attenuator, Midwest Microwave, Model 444-6
0.020-inch coax	35.5 cm long coax with OSSM connectors at each end; Uniform Tubes, UT20
0.030-inch coax	61.6 cm long coax with OSSM connectors at each end; Uniform Tubes, UT34

Table 2: Measurement Combinations

Meas. No.	Data File	Sensor	Atten. (dB)	Cable dia. (inches)	Calibration	Result; Figure
1	P4557	MGL-5	20	0.020	P4673	(MGL-5)/(MGL-7); Fig. 13
2	P4565	MGL-7	20	0.020	P4673	
3	P4573	MGL-7	6	0.020	P4673	(MGL-7)/(MGL-8); Fig. 11
4	P4673	MGL-8	6	0.020		
5	C4701	MGL-7	20 3	0.020	C4717	20-dB att; Fig. 5
6	C4709	MGL-7	6 3	0.020	C4717	6-dB att; Fig. 6
7	C4717	MGL-7	3	0.020		
8	C4725	MGL-7	3	0.030, 0.020	C4717	0.030-inch coax; Fig. 9
9	C4733	MGL-7	3	0.030		
10	C4741	MGL-7	3	0.020, 0.030	C4733	0.020-inch coax; Fig. 7

Note: The measurements 1 through 4 and 5 through 10 were done on different days and the two sets of data should not be intermixed.

From measurements numbers 5 and 7 using the MGL-7 sensor with and without the 20-dB attenuator, the effect of the attenuator can be found. The ratio of the measured outputs is the response of the attenuator, and its amplitude and phase are plotted in Fig. 5. Although the amplitude is slightly noisy, the noise is almost certainly due to mismatches in the system rather than to the attenuator itself. Indeed the attenuator is a physically small device with a specified operating range of 0 to 18 GHz, and should have a constant response up to and beyond the highest frequency used in the measurements. This would seem to justify taking an average value for both the amplitude and phases. From Fig. 3 the average amplitude is 0.1019 (= -19.48 dB), and the average phase is -0.0326667 degrees/MHz. The latter is equivalent to an effective free space length of 2.722 cm.

Similarly, from measurements numbers 6 and 7 the response of the 6-dB attenuator can be found. The amplitude and phase are shown in Fig. 6, and average 0.5183 (= -5.71 dB) and 2.387 cm of electrical length, respectively.

The same procedure was also used to calibrate the coaxial cables (see Table 2 for the data sets involved), and the results for the 0.020-inch coax are shown in Fig. 7. The noise is again attributed to the entire system rather than to this single component, and since the skin effect is the main source of cable loss in this frequency range, the amplitude of the response should be $\exp(-\alpha\sqrt{f})$ where α depends on the length and characteristics of the cable, but is independent of the frequency f . By eyeball fit, the (average) amplitude at 3000 MHz is estimated to be 0.8, implying $\alpha = 7.438 \times 10^{-5}$ per MHz. The resulting

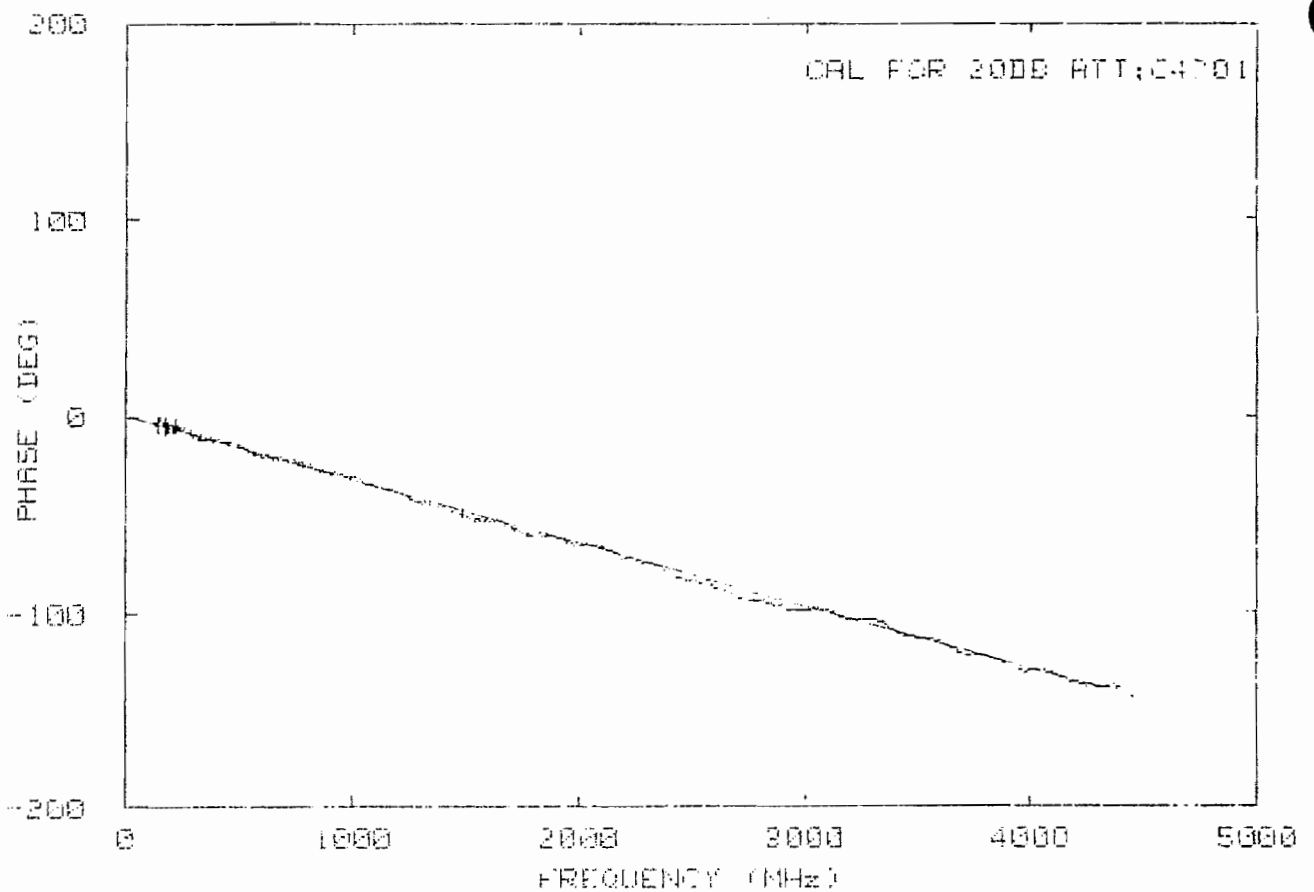
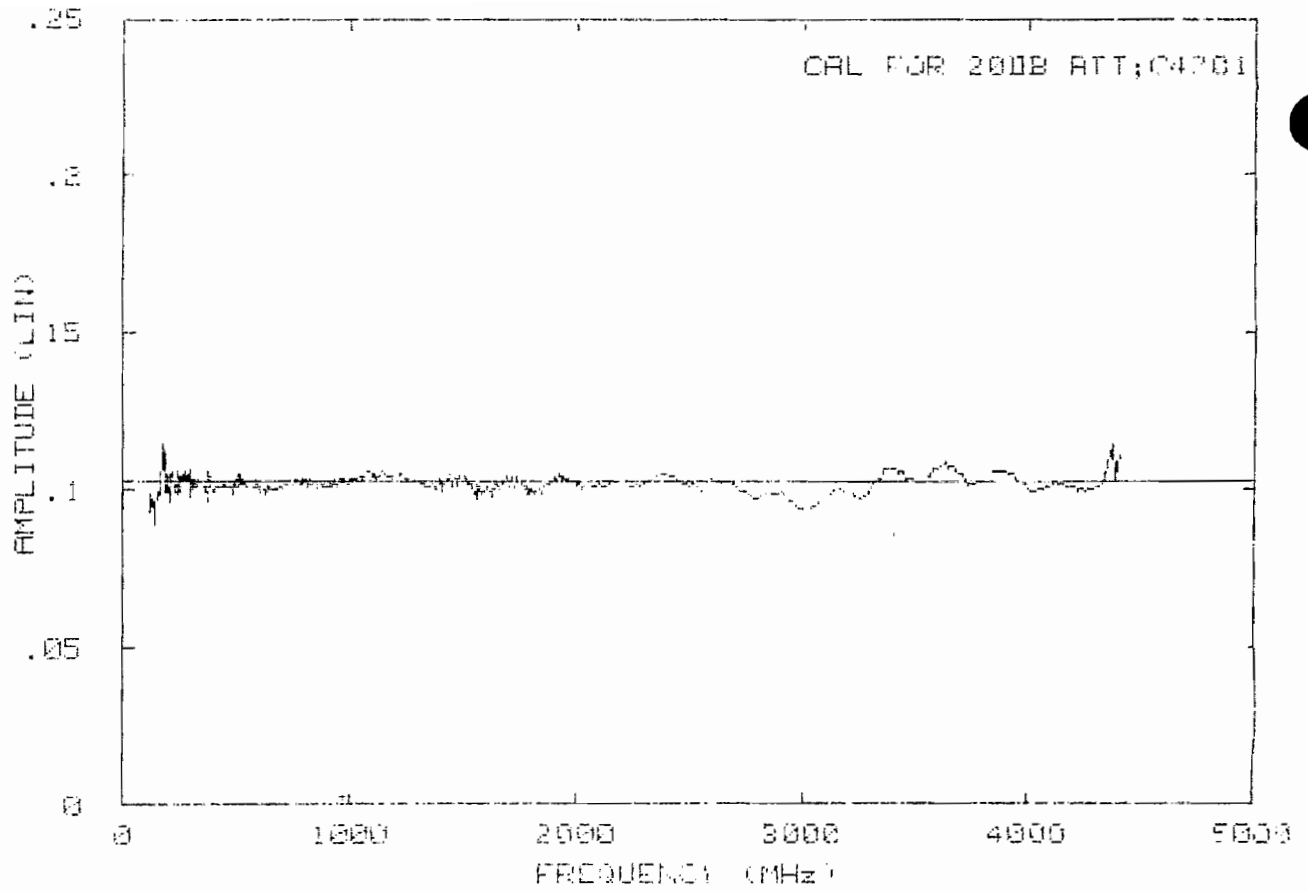


Fig. 5: Calibration of the 20-dB attenuator, deduced from measurements numbers 5 and 7.

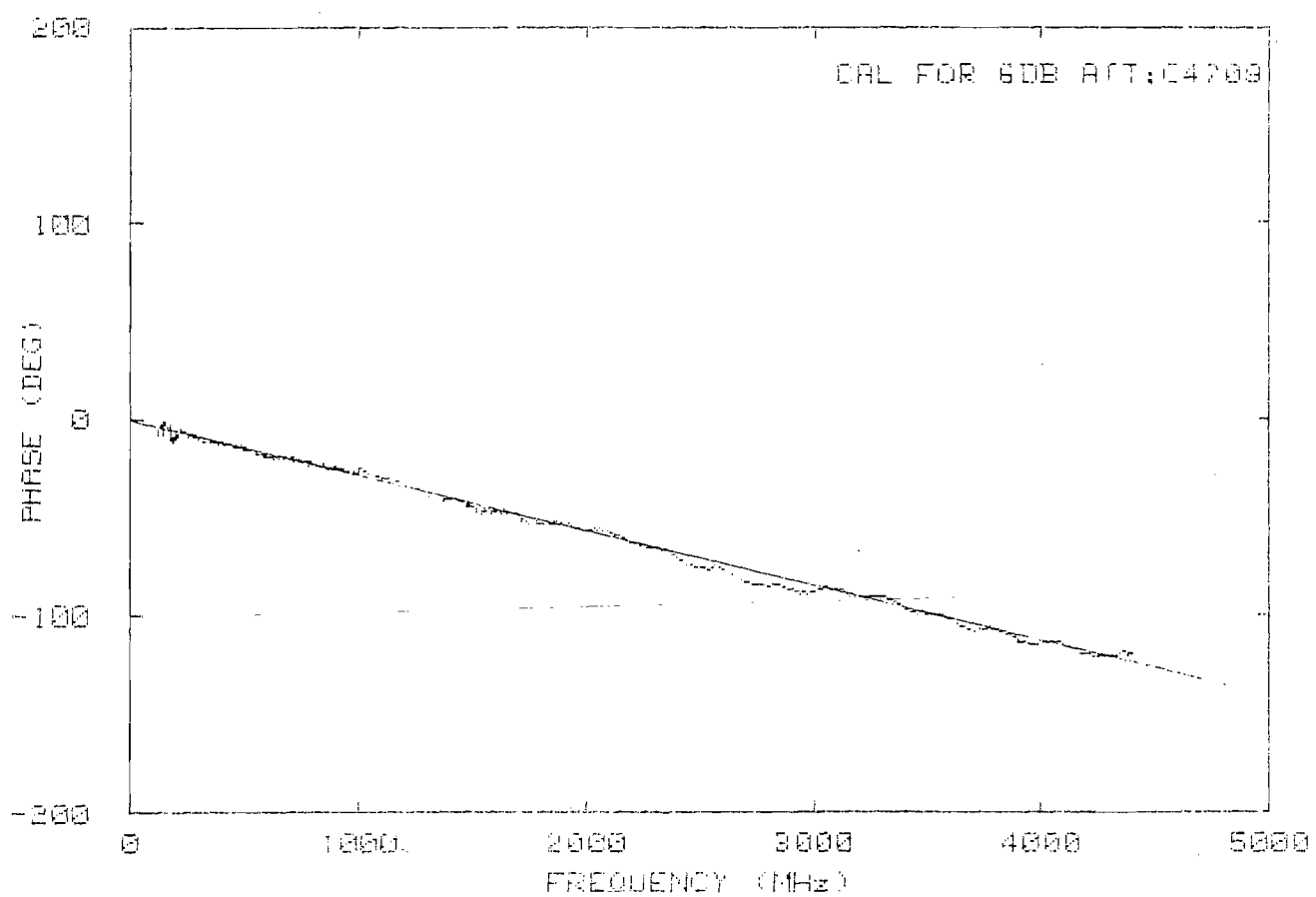
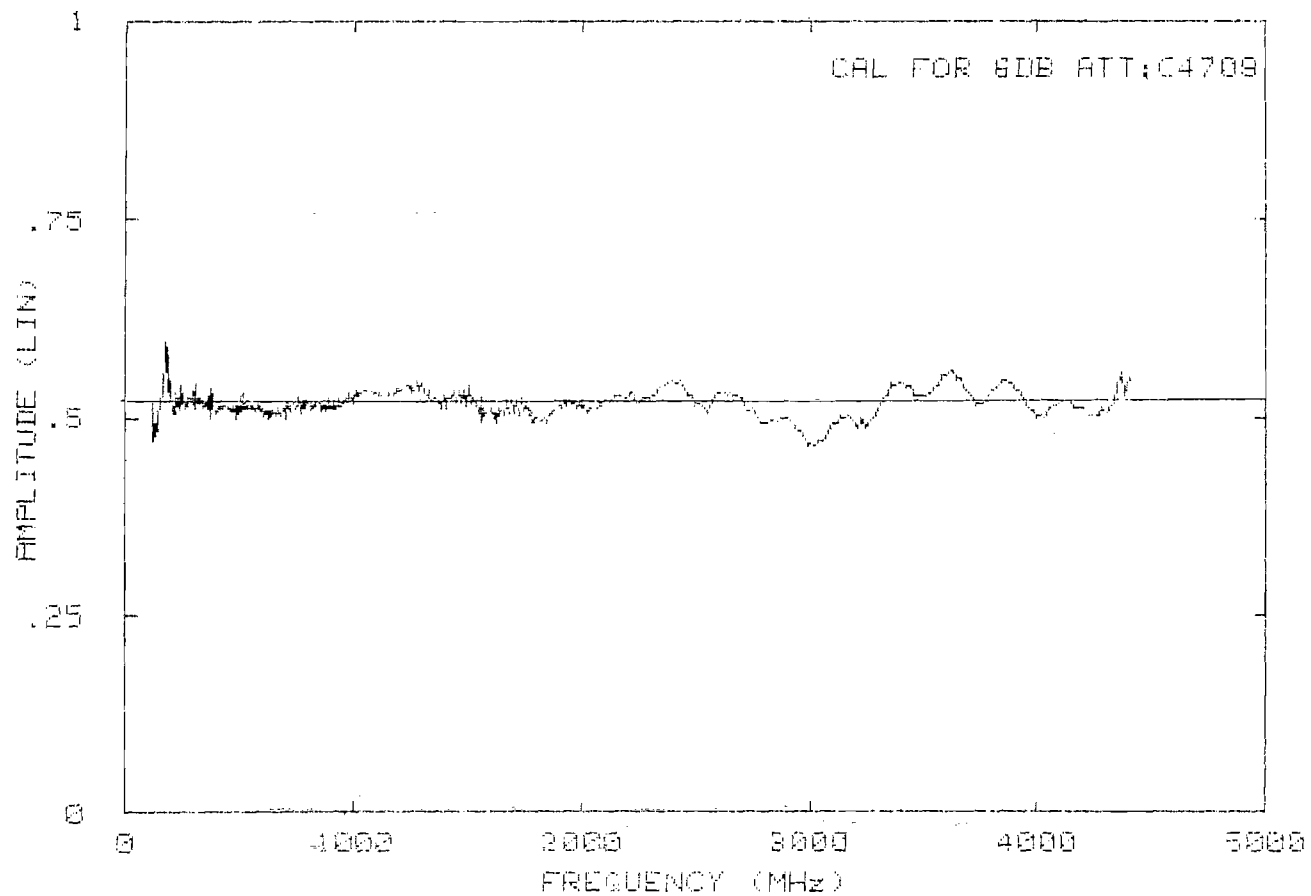


Fig. 6: Calibration of the 6-dB attenuator, deduced from measurements numbers 6 and 7.

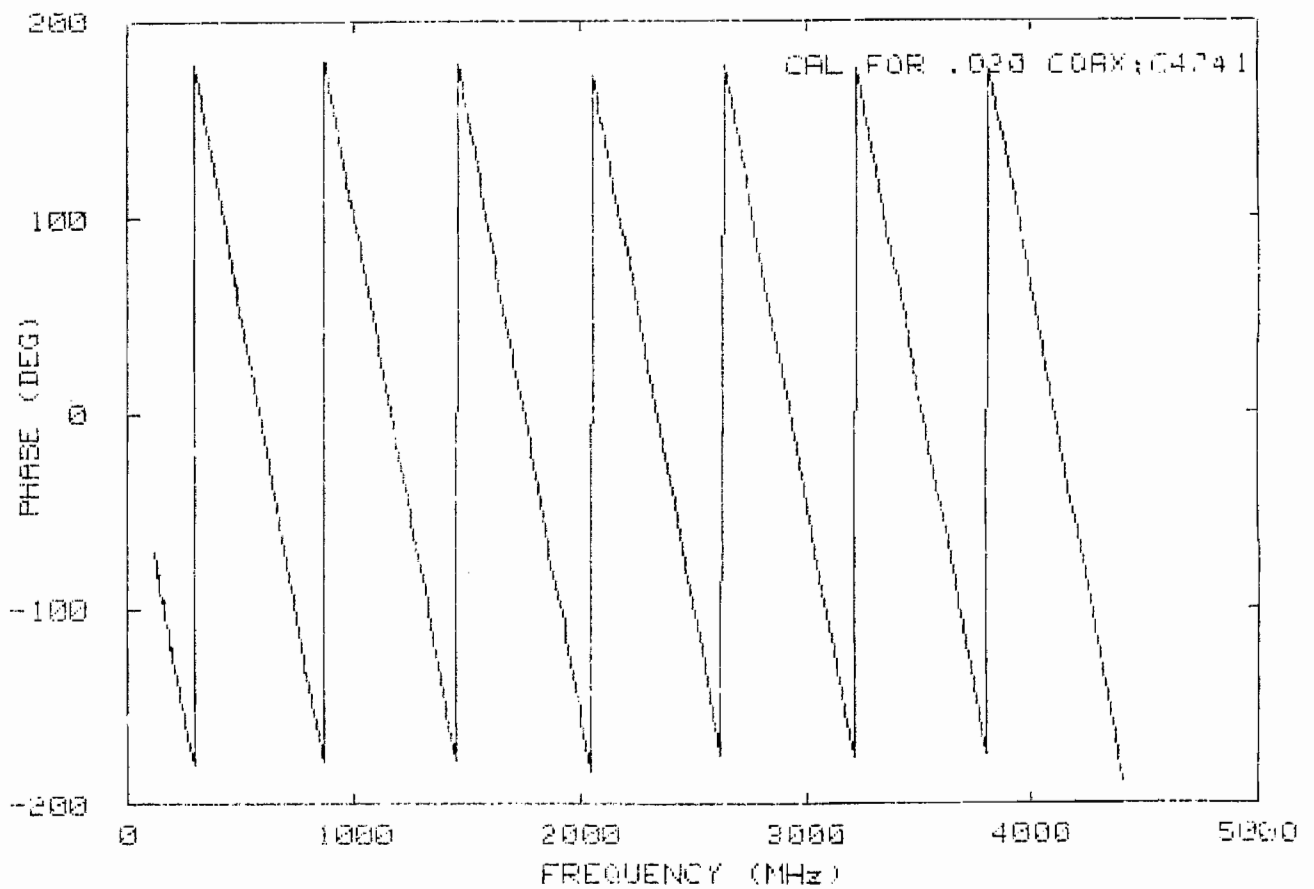
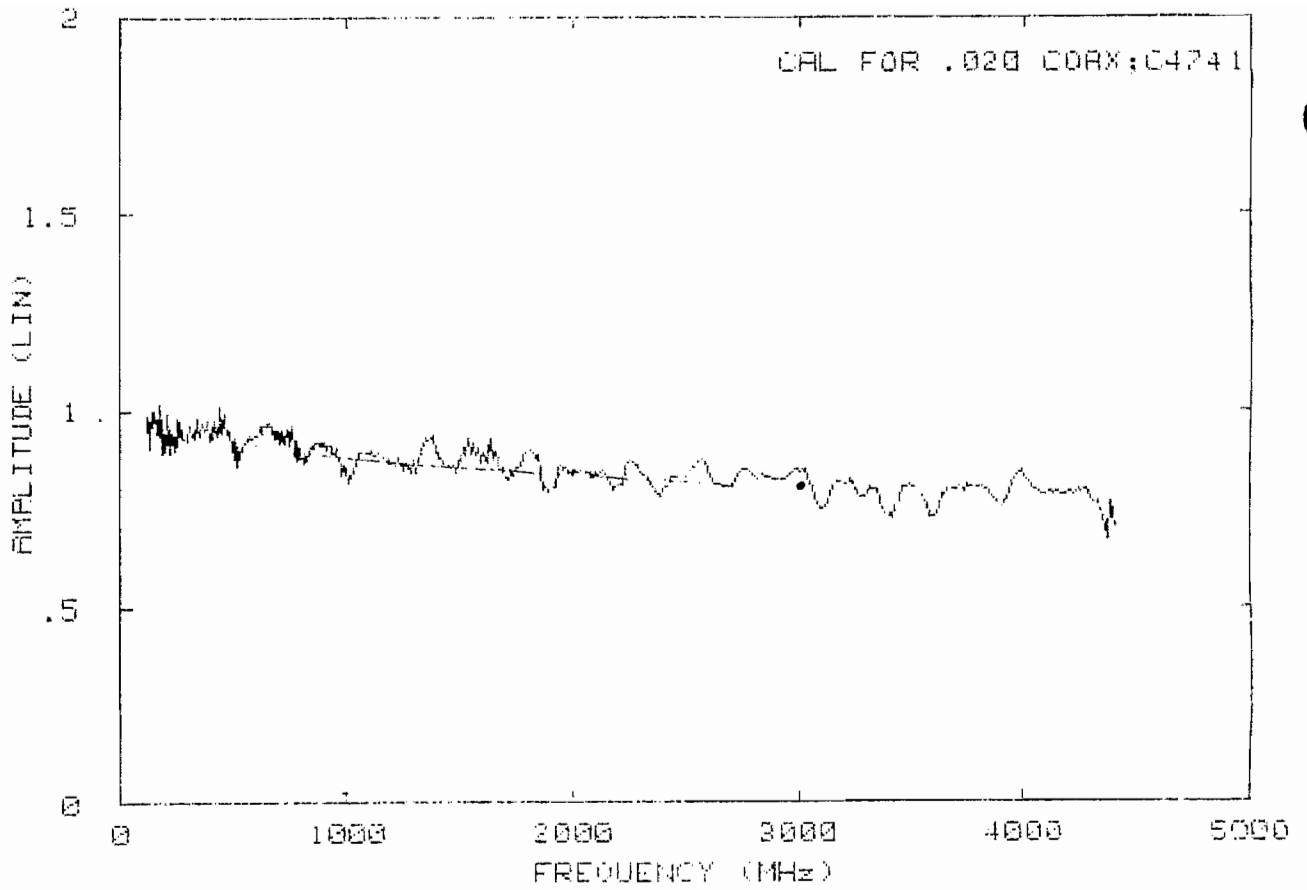


Fig. 7: Calibration for the 0.020-inch coax, deduced from measurements numbers 9 and 10.

amplitude curve is shown in Fig. 8 and is seen to provide a good fit to the measured data. The slope of the phase curve is likewise -0.61463 degrees/MHz, corresponding to an effective free space length of 51.216 cm, and the computed phase curve is given in Fig. 8.

The analogous results for the 0.030 -in. coax are shown in Figs. 9 and 10. With the amplitude chosen to be 0.808 at 3000 MHz, the deduced α is 7.106×10^{-5} per MHz, and the slope of the phase curve is -1.0556 degrees/MHz, corresponding to an effective free-space length of 87.970 cm.

4.3 Sensor Responses

Measurements numbered 3 and 4 (see Table 2) were done with the MGL-7 and MGL-8 sensors respectively, using the same cable and attenuator, and the ratios of the measured data are shown in Fig. 11. At low frequencies the ratio is 9.33 , compared with the value 10 obtained from the equivalent areas. The discrepancy is believed due to the small size of the MGL-8 sensor whose construction is inevitably difficult. The phase is zero at low frequencies, but deviates at higher frequencies, due not only to the effect of the sensors individually, but also to the inclusion of the adaptors whose presence has not been compensated for.

The MGL-8 is the smallest sensor of the three, and its response should be linear out to (and beyond) the highest frequency used. According to the quasi-static approximation, its output voltage should therefore be

$$V = j\omega\mu H A_{eq}$$

where ω is the radian frequency, μ is the permeability of free space ($= 1.2566 \times 10^{-6}$), H is the amplitude of the magnetic field, and

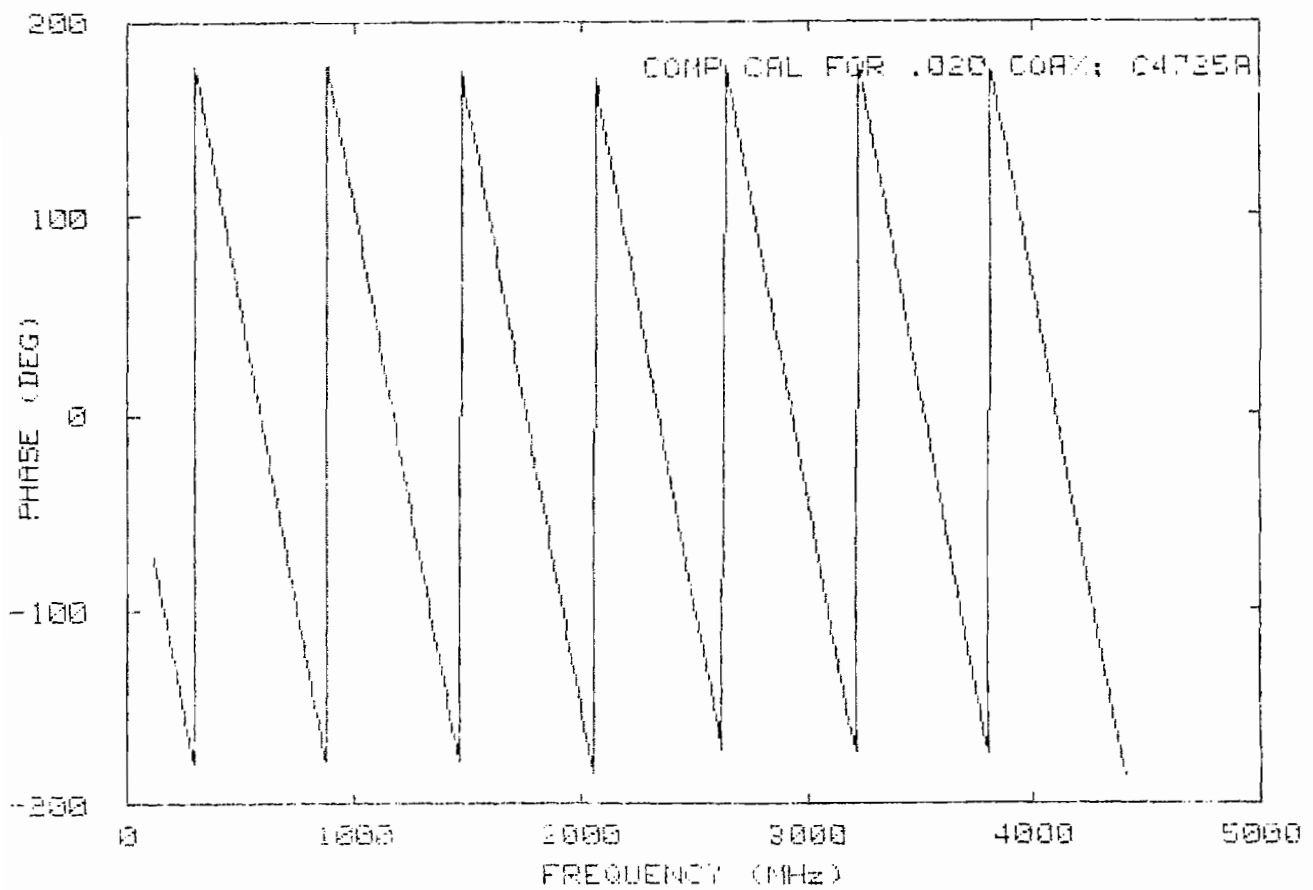
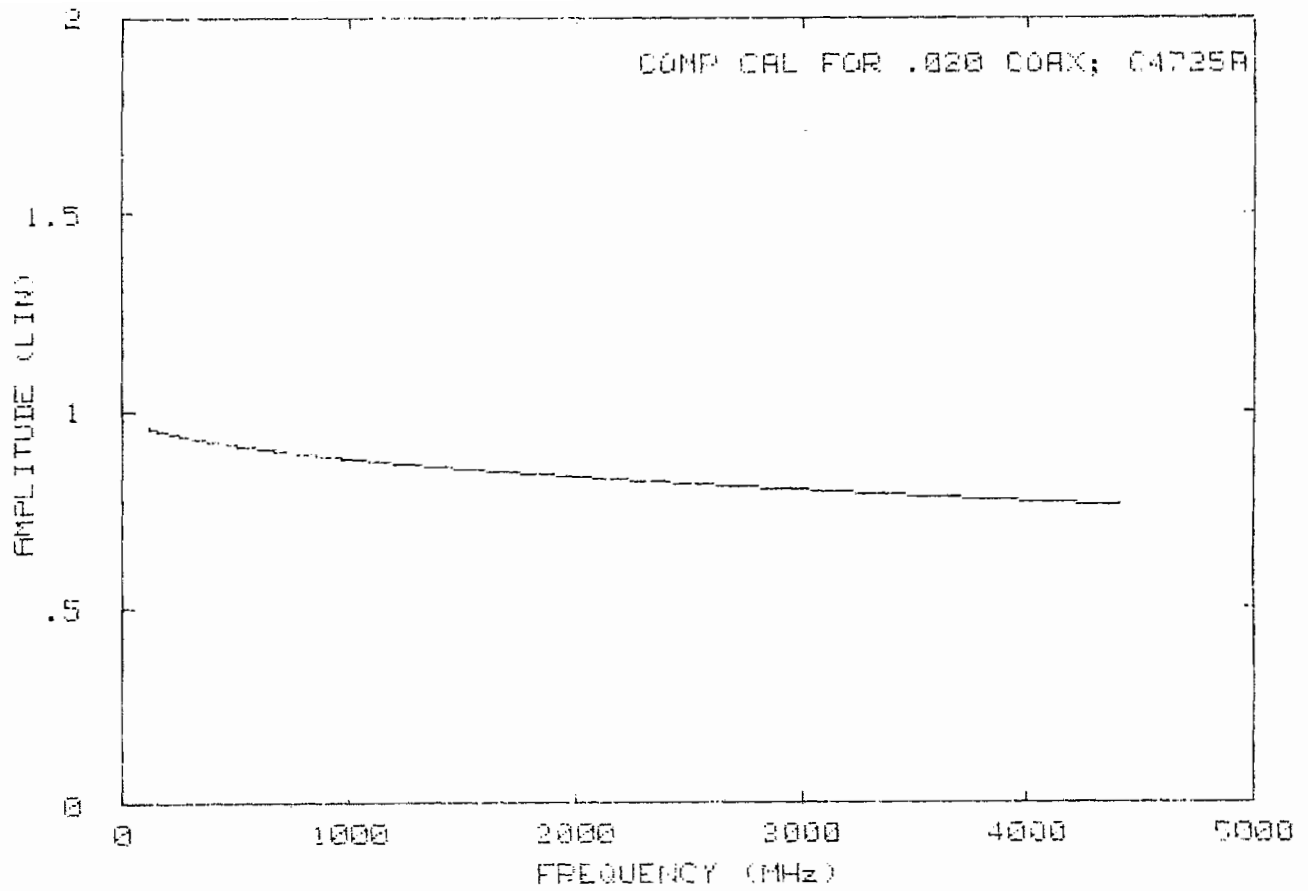


Fig. 8: Computed calibration for the 0.020-inch coax.

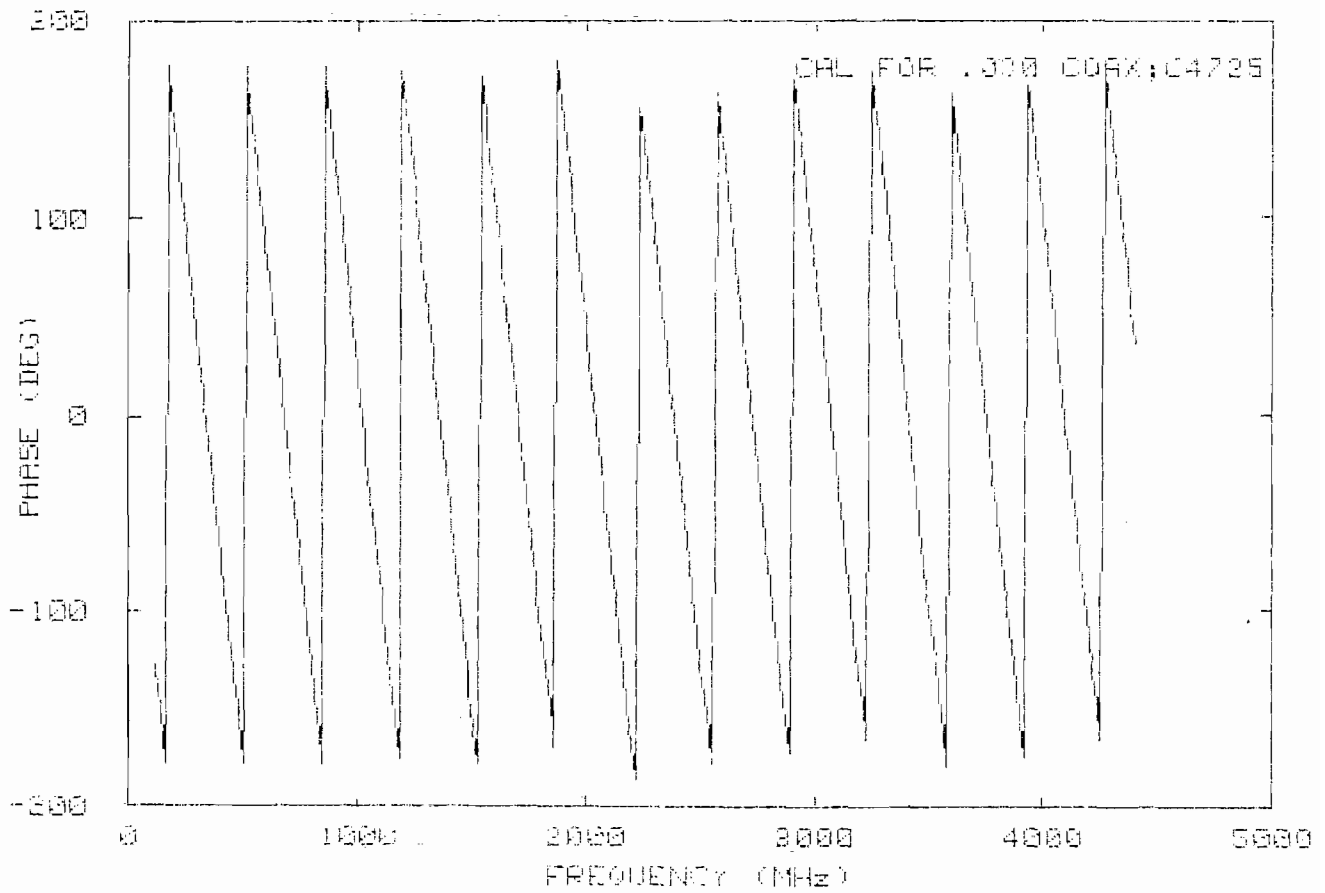
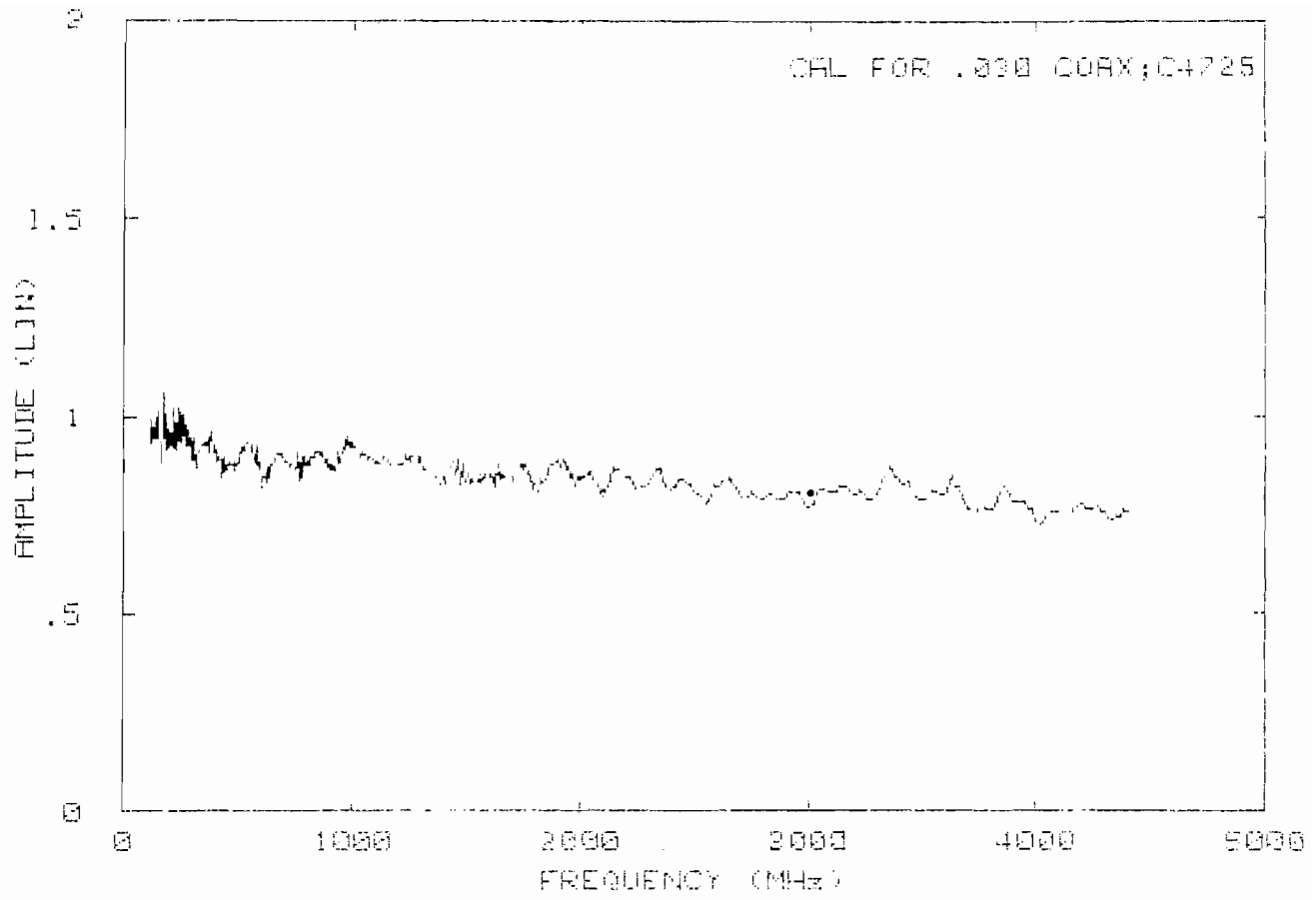


Fig. 9: Calibration for the 0.030-inch coax, deduced from measurements numbers 7 and 8.

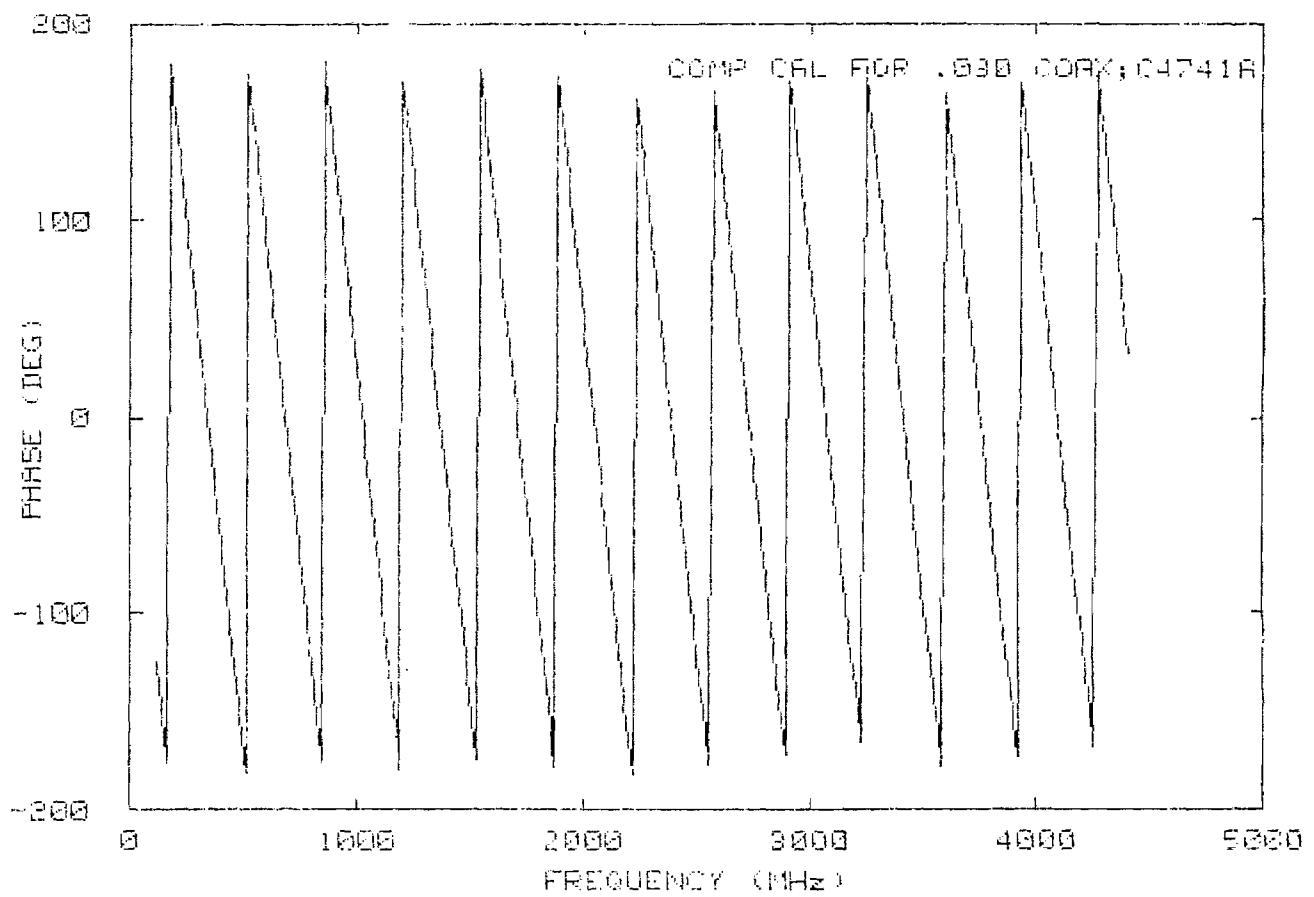
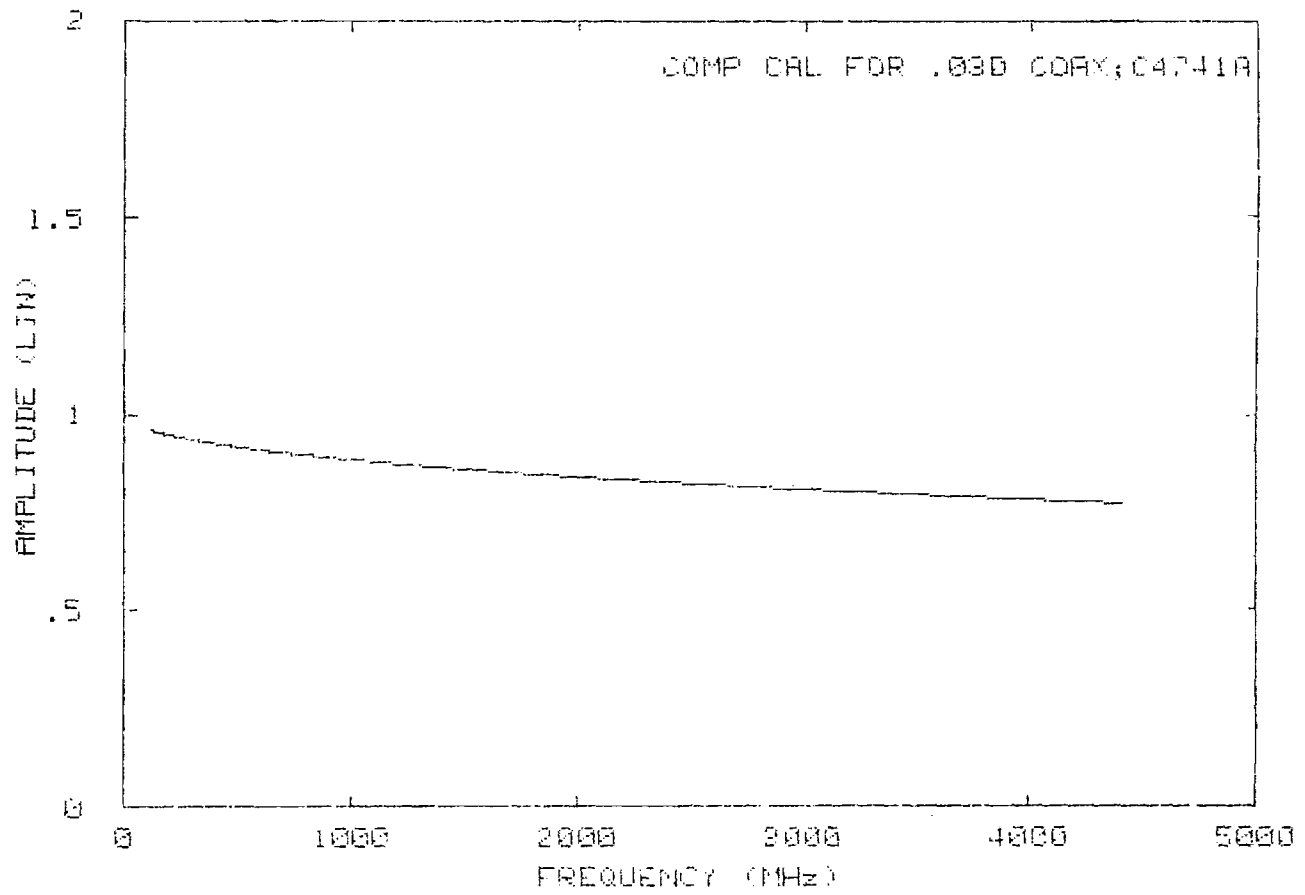


Fig. 10: Computed calibration for the 0.030-inch coax.

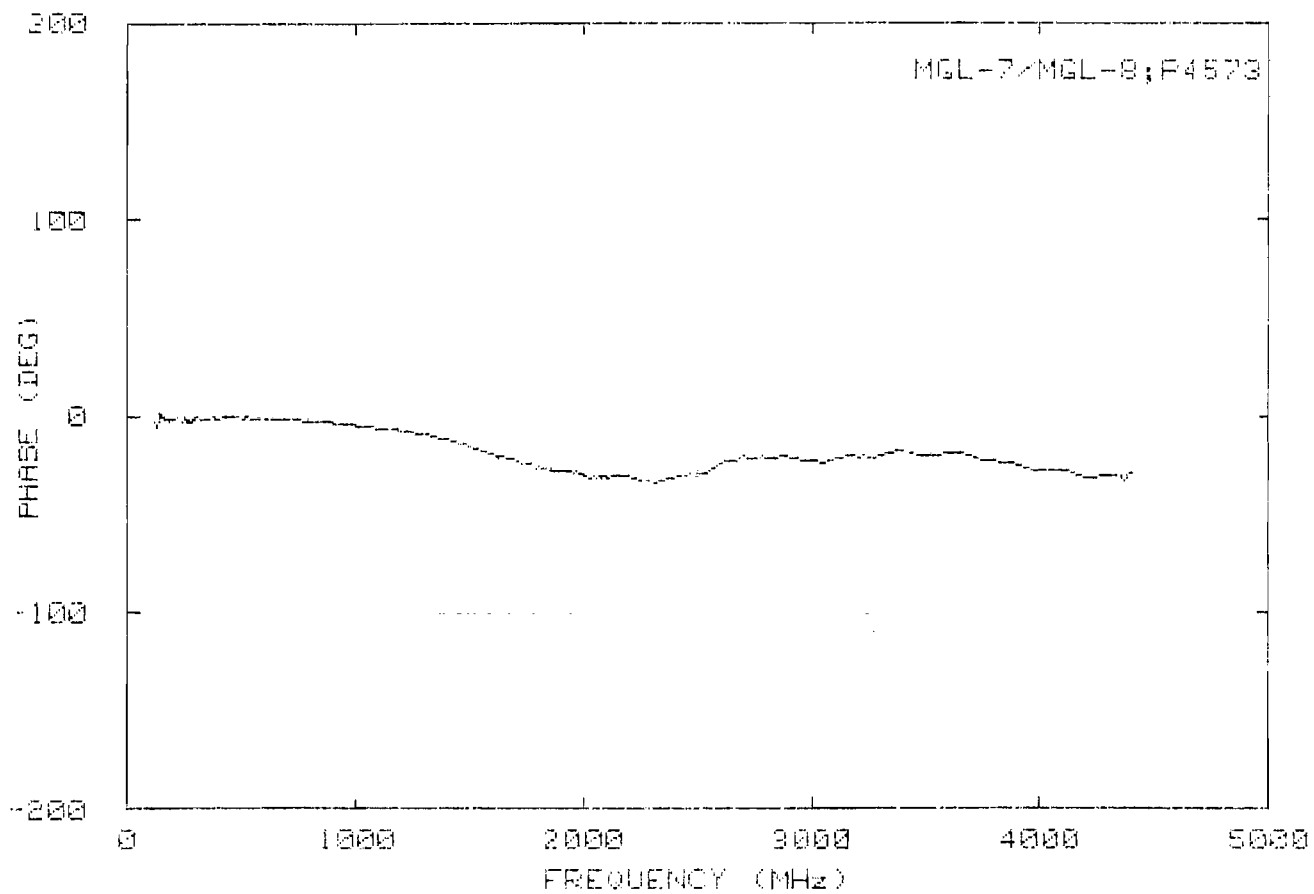
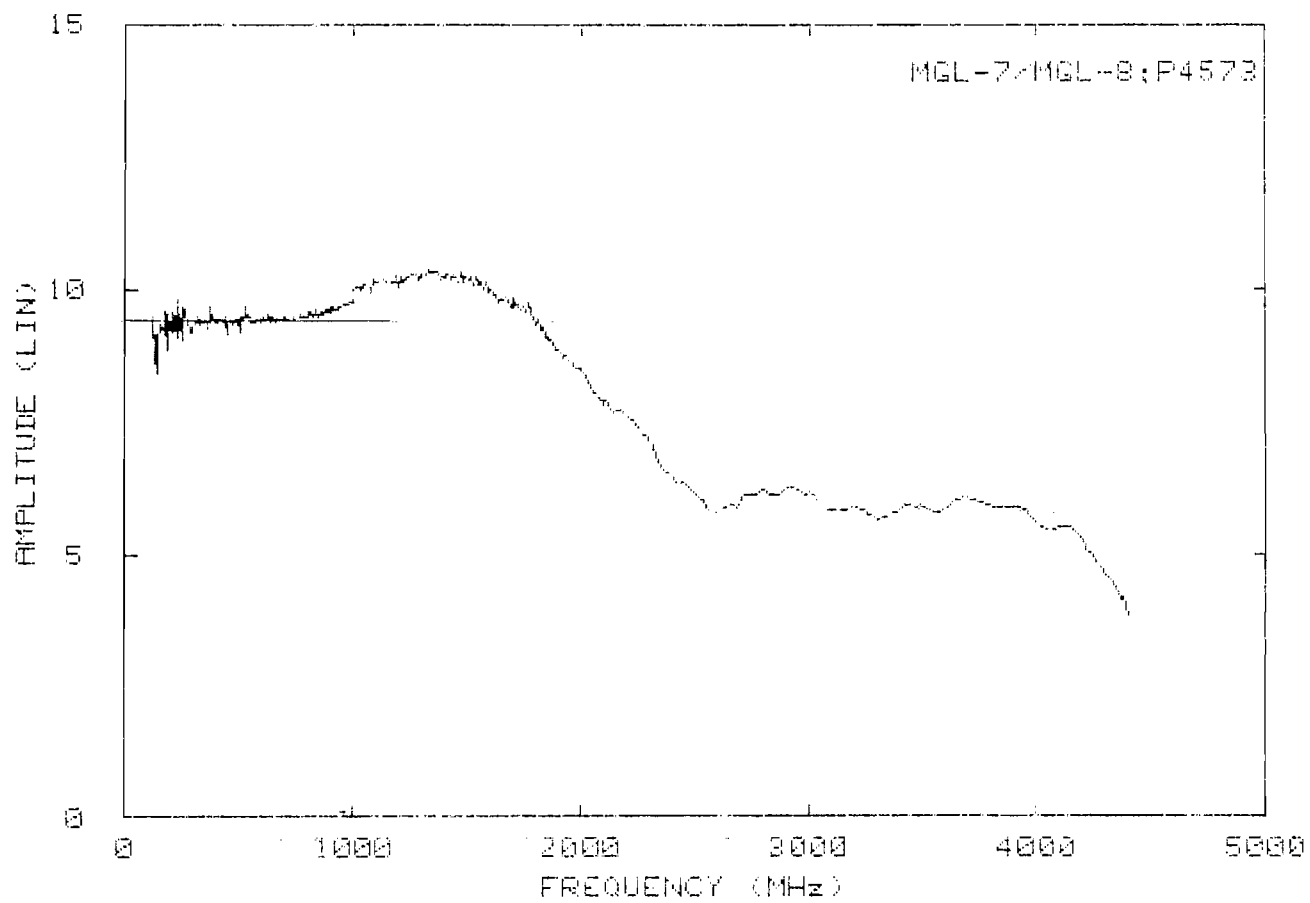


Fig. 11: Response of the MGL-7 sensor referenced to that of the MGL-8.

$A_{eq} = 10^{-5} \text{ m}^2$. On multiplying the data in Fig. 11, by $j\omega\mu A_{eq}$, we obtain the response of the MGL-7. The behavior is not unexpected, but the droop in the amplitude curve at frequencies above 4000 MHz was not present in some of the earlier data, and may be due to an equipment malfunction.

The ratio of the measured responses of the MGL-5 and MGL-8 sensors is shown in Fig. 13. At low frequencies the ratio is 90.0, compared with the value 100 predicted by the equivalent areas of the two sensors. At a frequency of about 500 MHz, there is a sharp notch in the curves, the origin of which is not clear at this time. It occurs in all data that have been obtained with the MGL-5 sensor, and is therefore associated with this sensor rather than the MGL-8.

In an attempt to locate its source, the measurements were repeated with the front of the sensor retaped to the ground plane. We also taped the back of the sensor assembly where it protrudes through the ground plane to eliminate any possibility of resonances in a cavity formed by the plane and the plate on which the sensor is mounted. There was no change in the data, and it would therefore appear that the notch is a feature of this particular MGL-5 sensor.

To test this, it was suggested [4] that the sensor be examined electrically using a time domain reflectometer, and visually as well. It was found that the two 100-ohm lines from the gaps have an electrical length of about 15 cm, but one is about 1 cm shorter than the other. Because of the design of the sensor, the two lines and the

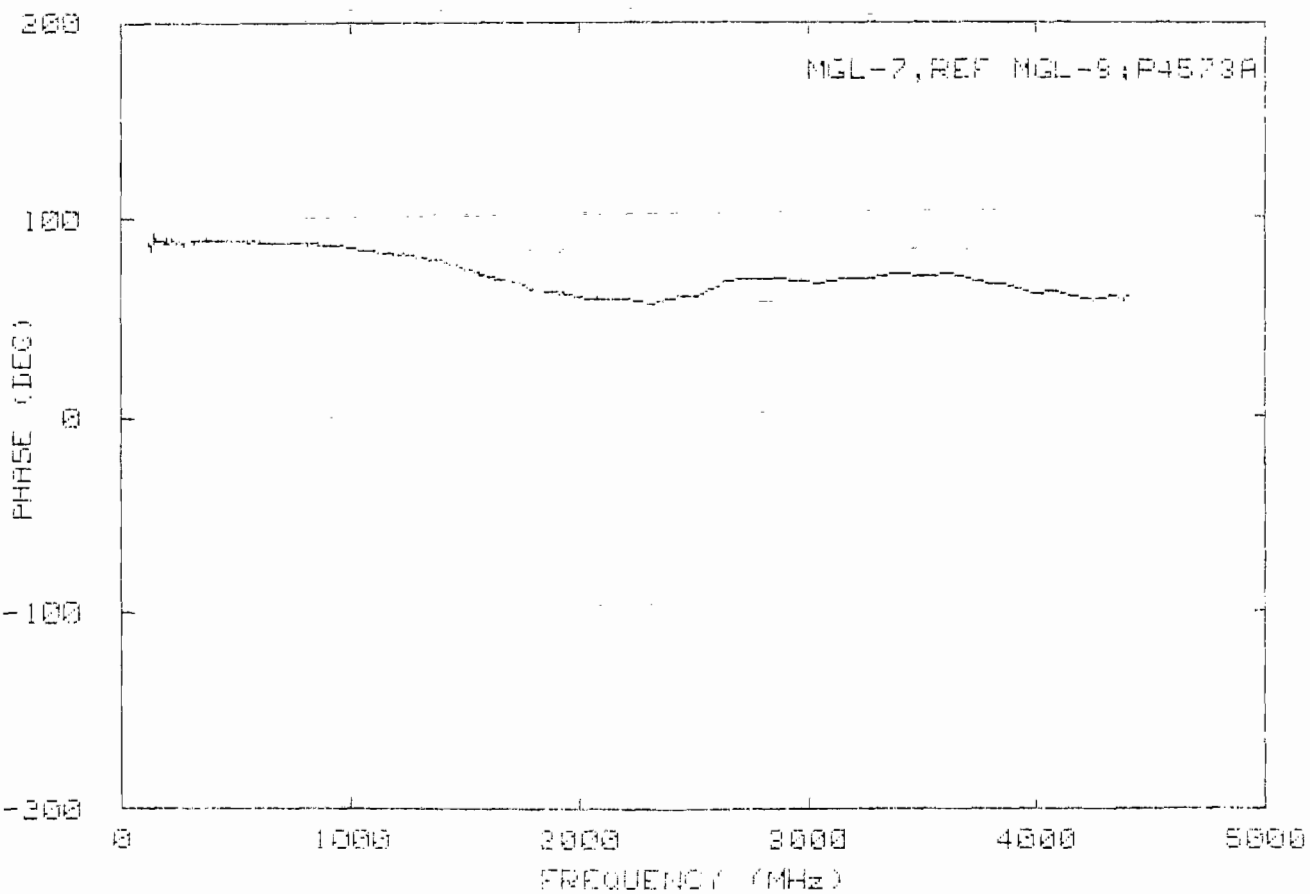
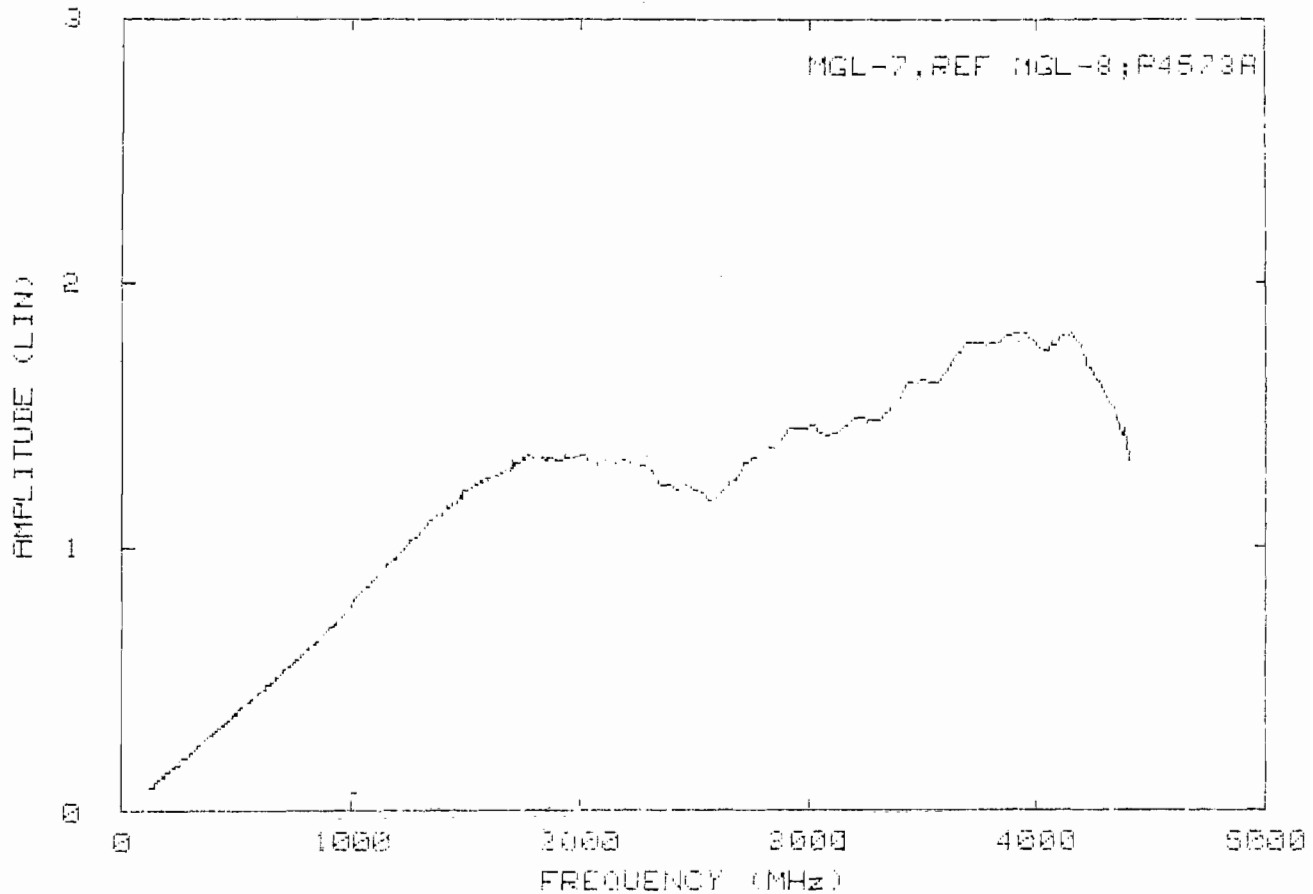


Fig. 12: Response of the MGL-7 sensor with the MGL-8 used as a standard.

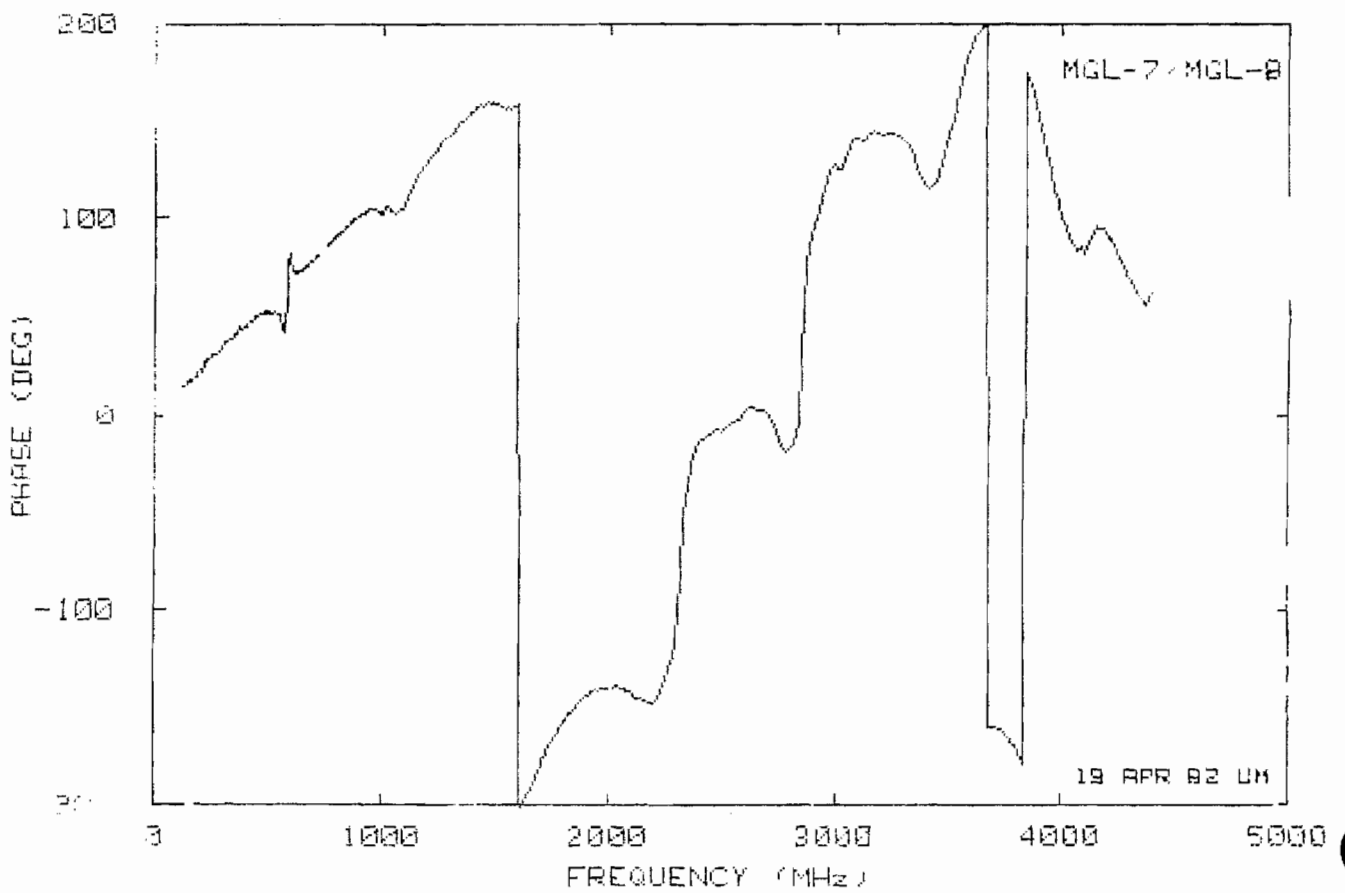
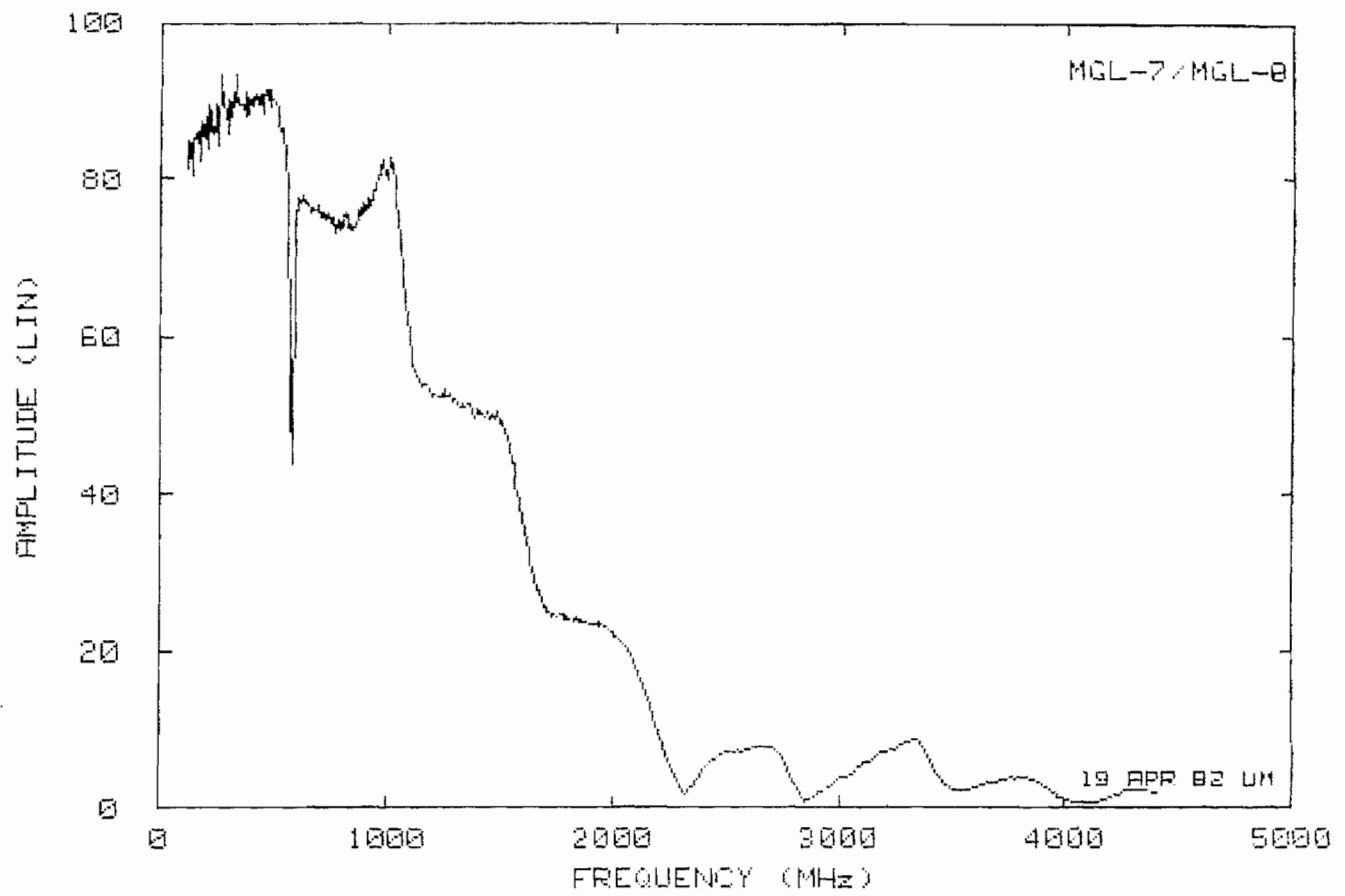


Fig. 13: Response of the MGL-7 sensor referenced to that of the MGL-8.

loop can form a high Q resonant circuit for excitation in the anti-symmetrical mode, and if the 100-ohm lines are not of equal length, the resulting signal could create the notch at 500 MHz.

In presenting the responses of the MGL-5 and MGL-7 sensors, the MGL-8 has been used as a reference because of the expected linearity of its output over a frequency range exceeding the highest frequency used in the measurements. On the other hand, its small size increases the probability that its specified equivalent area is less accurate than those of the larger sensors. To judge from the low frequency limits in Figs. 11 and 13 it would appear that the actual value of A_{eq} for the MGL-8 exceeds 10^{-5} m^2 , and a more probable value is (say) $1/2\{(0.033)^{-1} + (0.966)^{-1}\}10^{-5} \text{ m}^2$, i.e., $A_{eq} = 1.054 \times 10^{-5} \text{ m}^2$. The resulting recalibration of the MGL-5 and MGL-7 responses would uniformly increase the amplitudes in Figs. 12 and 14 by 1.054.

4.4 Discussion

The amplitude and phase of the frequency response of the MGL-7 sensor are shown in Fig. 12. At low frequencies, the response increases linearly with f according to the formula

$$V = j\omega\mu A'_{eq} \quad (20)$$

with $A'_{eq} = 0.933 \times 10^{-4} \text{ m}^2$. It rises above the value predicted by (20) starting at $f = 800 \text{ MHz}$, indicative of the growing influence of the multiple contributions, and then recrosses the linear curve at about 1800 MHz, where the response has its (initial) peak value. Thereafter, the amplitude falls increasingly below the linear curve, and is more than 3 dB below for all $f > 2300 \text{ MHz}$.

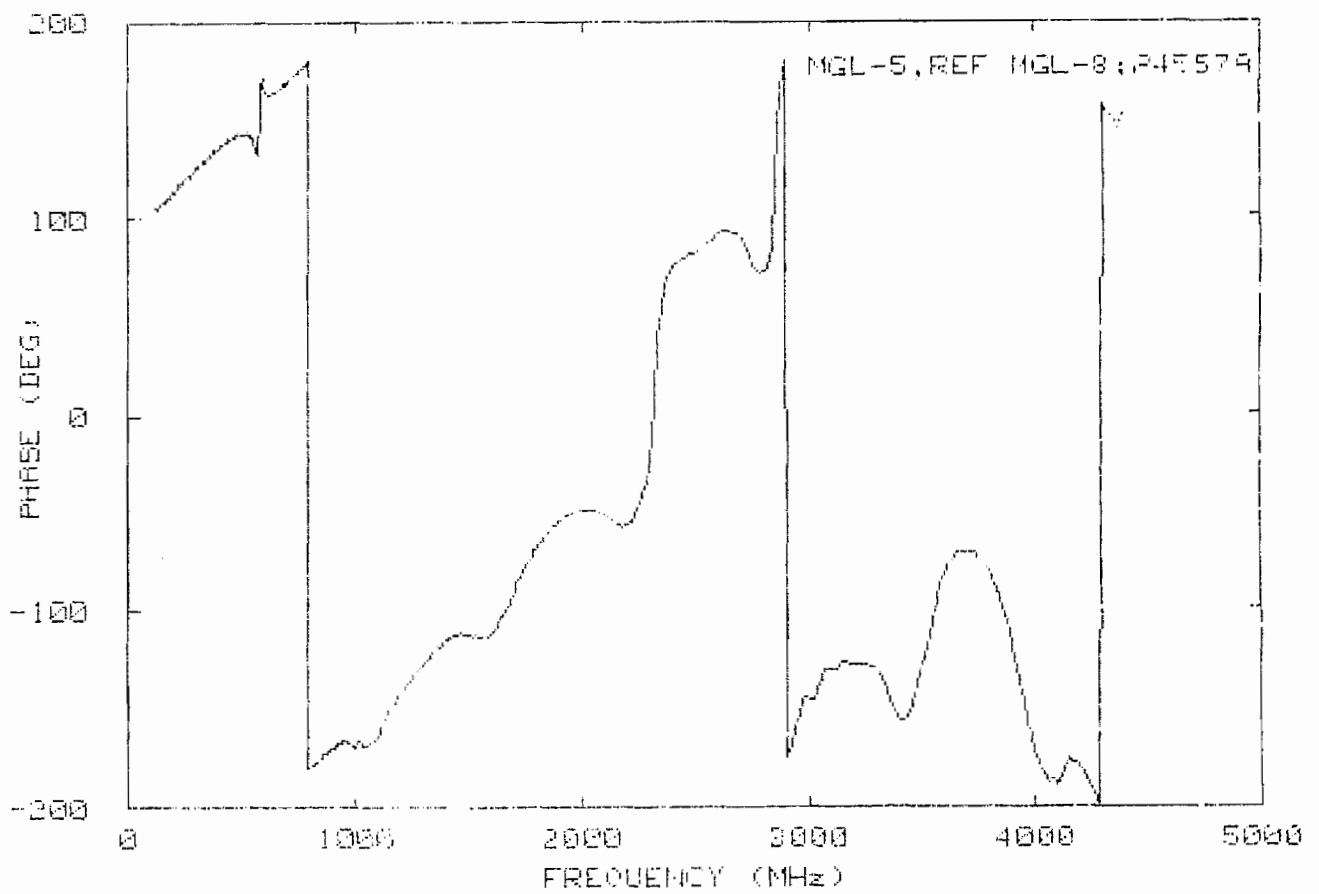
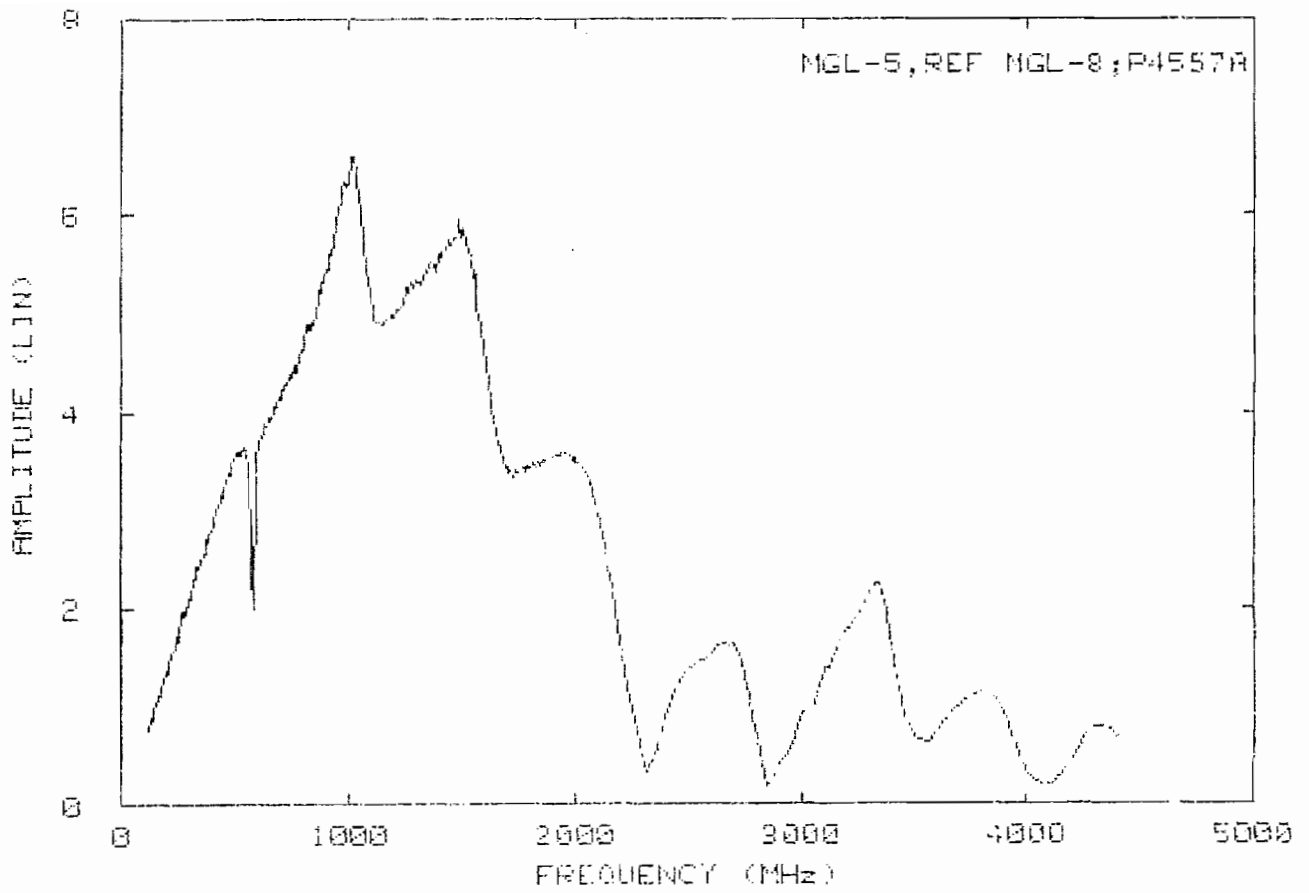


Fig. 14: Response of the MGL-5 sensor with the MGL-8 used as a standard.

Some additional information can be obtained by applying the Sharpe-Roussi program [5] to give a partial fraction representation of a real (as a function of $s = j\omega$) rational function approximation to the response. For this purpose it is convenient to write the response as a function of ω in units of 10^9 radians/sec. Using ten poles, the fit to the measured amplitude and phase is shown in Figs. 15 and 16, and we note that even the small amplitude dip near 4000 MHz ($\omega \approx 25$) was faithfully reproduced. The poles and residues are given in Table 3. The resonant frequencies are therefore 12.19, 18.10, 25.58 and 26.23 G rad/sec, but because of its small residue, the one at 25.58 can be ignored. The other three are indicated in Fig. 15. The fundamental corresponds to that of a loop of radius 2.496 cm, and the next two values are then consistent with the first anti-resonance and the second resonance, respectively. It is not known whether the loop radius can be identified as the dimension of a specific structural element of the sensor.

For $\omega \ll 12$, the partial fraction representation of V can be expanded as a power series in ω , giving

$$V = -0.0216 + j\omega 0.1174 + \omega^2 0.001678 + j\omega^3 0.0001399 + O(\omega^4) \quad . \quad (21)$$

The non-zero constant is physically unrealistic, and is due to noise in the measured data and/or the approximations inherent in the numerical simulation. The dipole contribution (proportional to $j\omega$) implies (see eq. 1) $A'_{eq} = 0.934 \times 10^{-4} \text{ m}^2$, in excellent agreement with

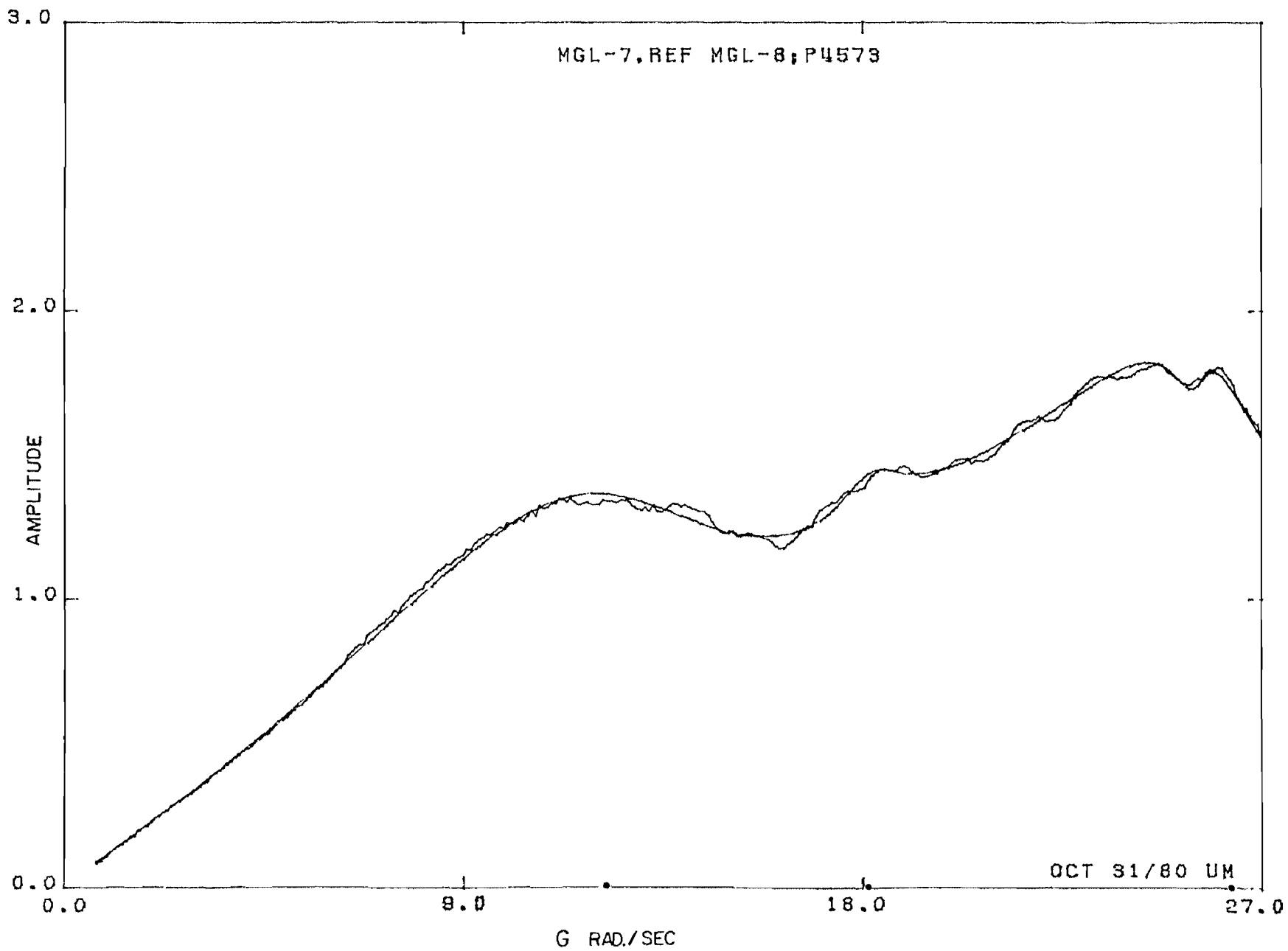


Fig. 15: Amplitude of the MGL-7 response compared with the Sharpe-Roussi simulation. The dots show the frequencies corresponding to the dominant poles in the 10-pole simulation.

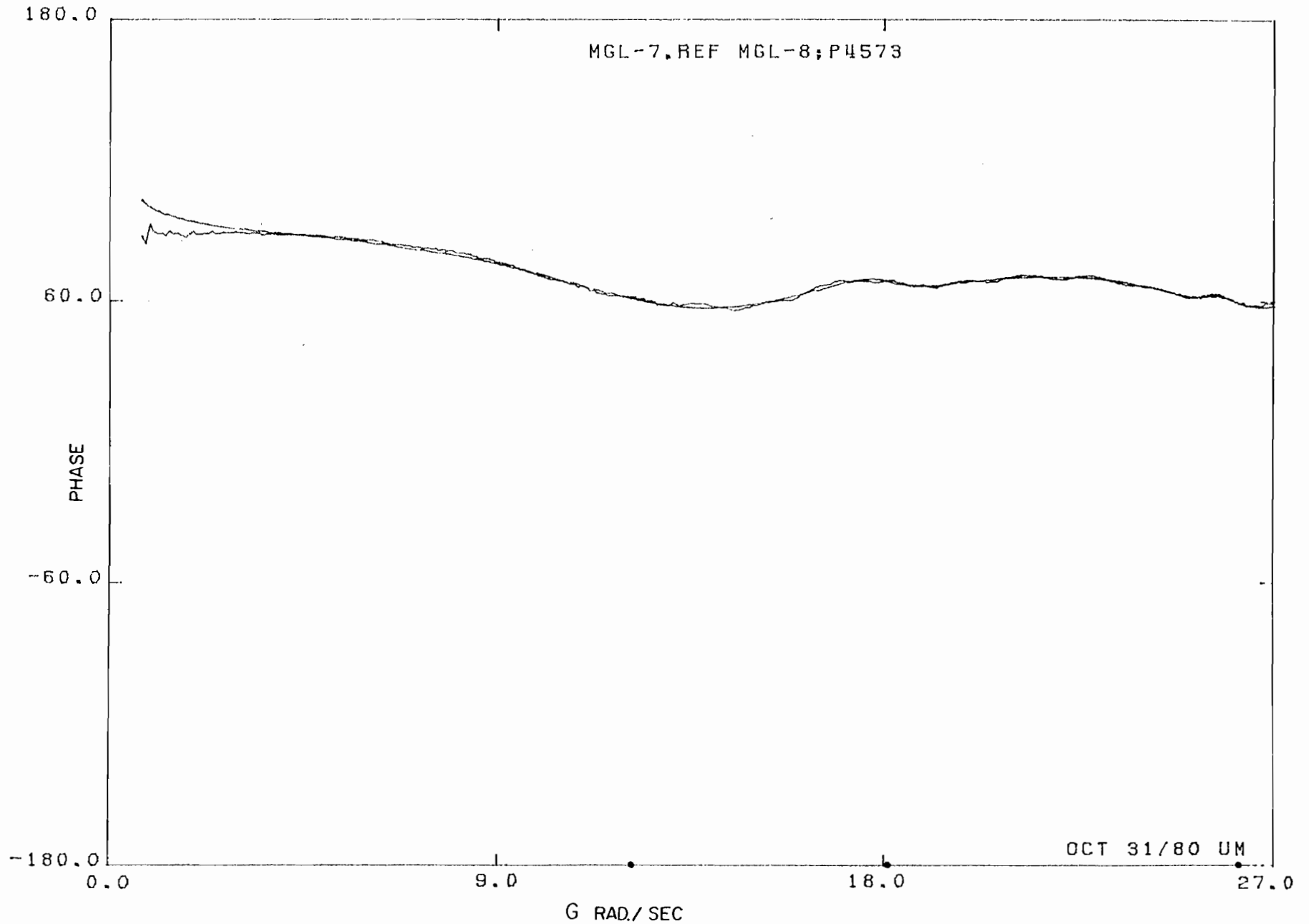


Fig. 16: Phase of the MGL-7 response compared with the Sharpe-Roussi simulation. The dots show the frequencies corresponding to the dominant poles in the 10-pole simulation.

Table 3: Poles and Residues for MGL-7

Poles ω_i	Residues R_i
$12.19 + j4.452$ $-12.19 + j4.452$	$1.521 - j2.839$ $-1.521 - j2.839$
$18.10 + j0.9277$ $-18.10 + j0.9277$	$0.1528 - j0.008782$ $-0.1528 - j0.008782$
$25.58 + j0.4500$ $-25.58 + j0.4500$	$-0.01499 + j0.07588$ $0.01499 + j0.07588$
$26.23 + j2.384$ $-26.23 + j2.384$	$-2.703 - j1.759$ $2.703 - j1.759$
$j83.96$ $j93.29$	$j277.7$ $j311.5$

the value deduced from Fig. 11. The other terms in (21) are then the next higher order multipole contributions, and bearing in mind that (21) requires $\omega \ll 12$, their coefficients are remarkably small. Although these terms are responsible for the initial departure from the linear behavior with frequency, it is evident that a study of the quadrupole contributions to the sensor response would provide little in the way of an improved representation of the output.

For the MGL-5 sensor the amplitude and phase of the response (see Fig. 14), replotted as a function of ω in G rad/sec, are shown in Figs. 17 and 18, along with the simulation provided by the Sharpe-Roussi program using 18 poles. The frequencies appropriate to the pole locations are indicated, and we observe that these do not always correspond to the peaks and nulls in the response. Nevertheless, the overall fit is excellent except at frequencies in the vicinity of $\omega = 3.7$ where the notch occurs, and where the simulation averages through the increased response at the lower frequencies and the subsequent deep null. Because of this, the low frequency behavior of the simulated voltage differs from the known behavior of the sensor. Indeed, by expansion of the partial fractions we obtain

$$V = 0.0607 + j\omega 1.068 + O(\omega^2)$$

implying $A'_{eq} = 0.903 \times 10^{-3} \text{ m}^2$, which is still 7 percent less than the value obtained from Fig. 13.

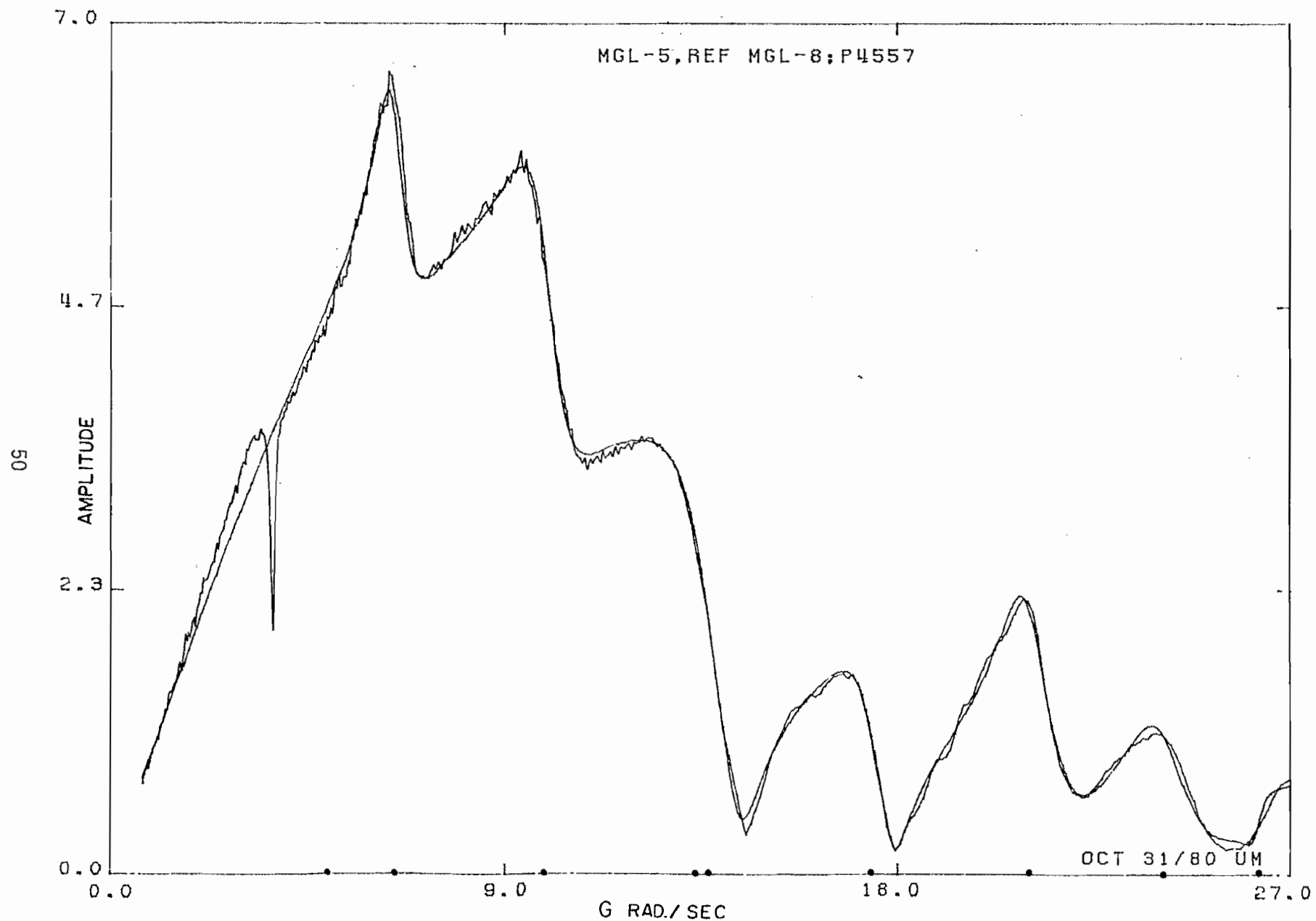


Fig. 17: Amplitude of the MGL-5 response compared with the Sharpe-Roussi simulation. The dots show the frequencies corresponding to the 18 poles used in the simulation.

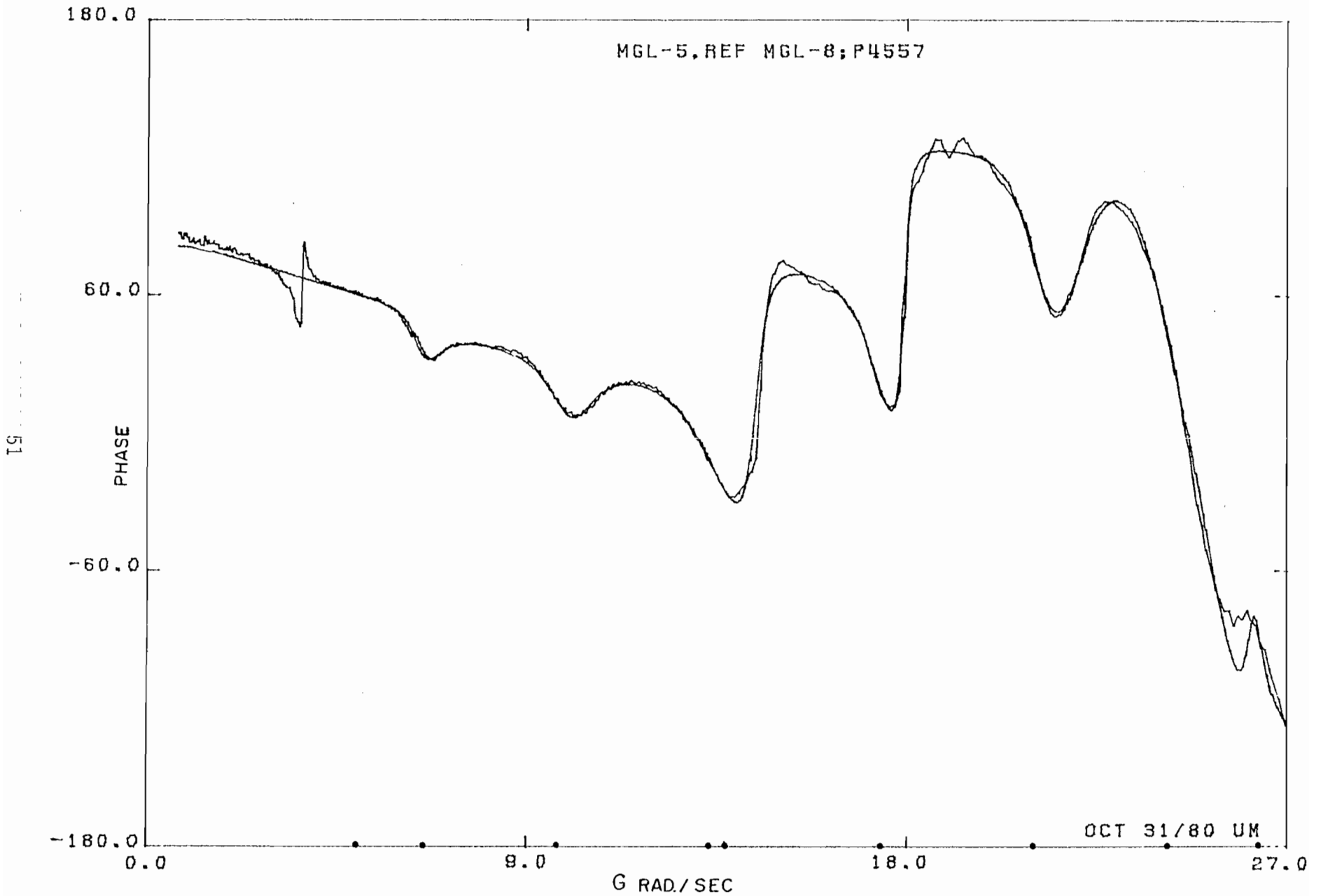


Fig. 18: Phase of the MGL-5 response compared with the Sharpe-Roussi simulation. The dots show the frequencies corresponding to the 18 poles used in the simulation.

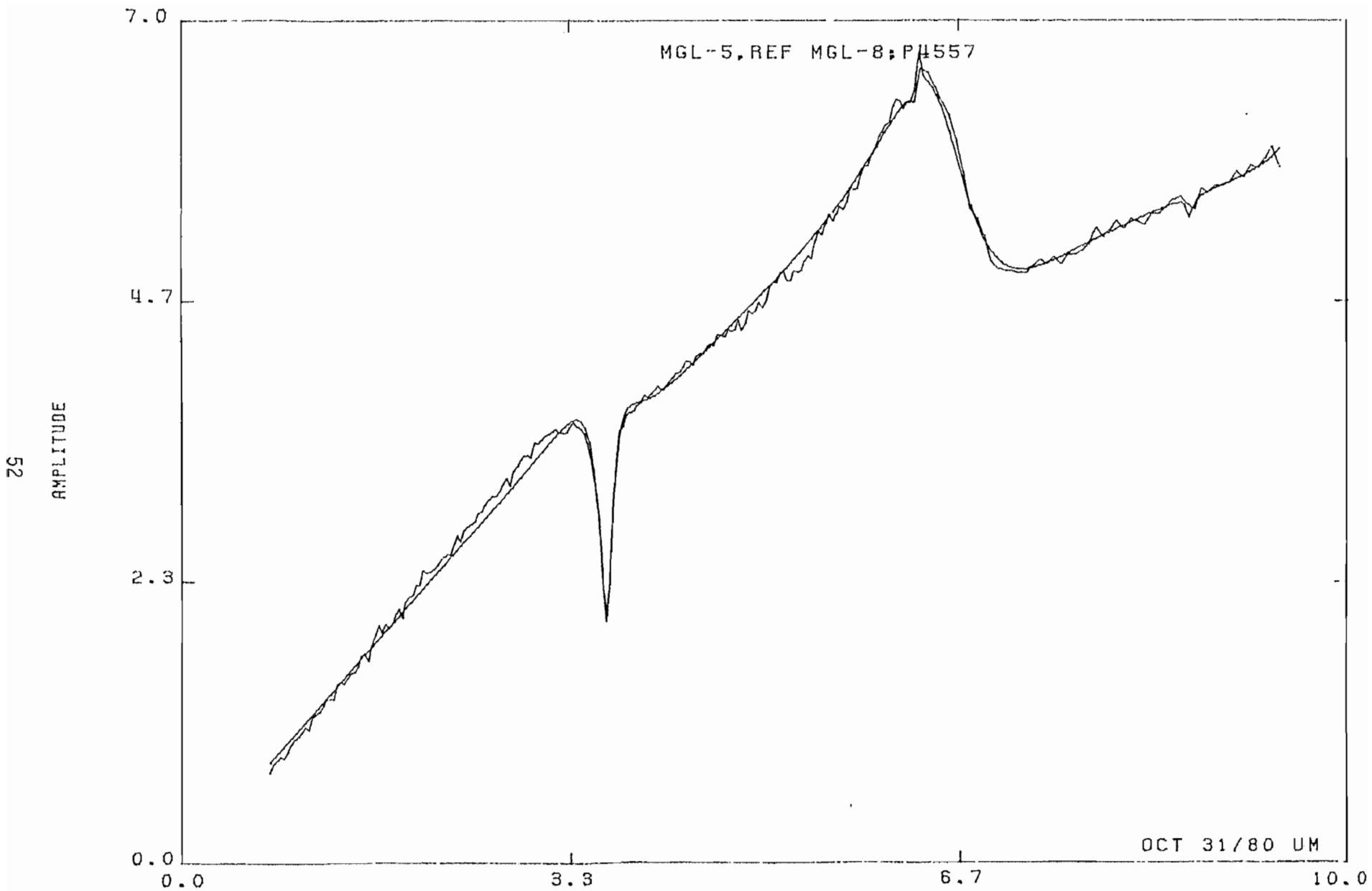


Fig. 19: Amplitude of a portion of the MGL-5 compared with the Sharpe-Roussi simulation using 14 poles.

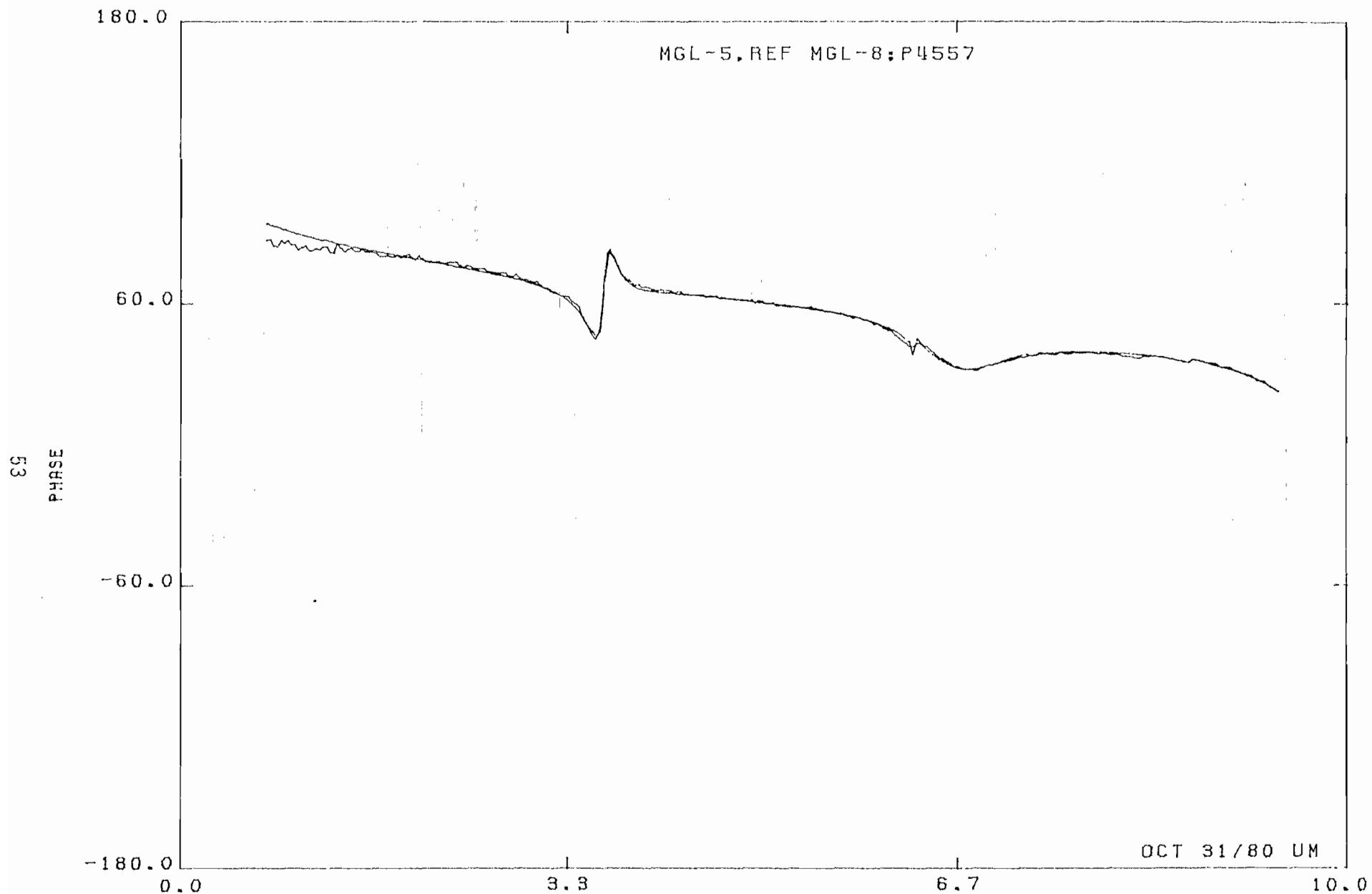


Fig. 20: Phase of a portion of the MGL-5 compared with the Sharpe-Roussi simulation using 14 poles.

5. FREE SPACE SENSOR EVALUATION

Apart from its intrinsic value, the preceding study of ground plane sensors was helpful in enabling us to develop the experimental techniques necessary to tackle the more difficult problem of evaluating the free space sensors.

5.1 The Sensors

The free space sensors studied were the MGL-2D(A), MGL-6A(A) and ACD-4A(R), but in addition the smaller size MGL-9(R) and ACD-2(R) were used as references for the frequency variation study since their regions of linearity extend well beyond the largest frequency used in the measurements.

Table 4 identifies the particular sensors, and we note that two MGL-6's are listed. Because of the poor performance of the first model (serial No. 2), it was felt that the sensor was defective, and a second model (serial No. 1) was requested from the Air Force. It turned out that this was no better, and we eventually decided to employ the second one only. Figure 21 is a photograph of the five sensors used in the study, with the ACD-4 and ACD-2 on top and the MGL-2, MGL-6 and MGL-9 below. The dual coax leads on the MGL-9 have been bent through 90 degrees to make the sensor compatible with the other two. Since the incident electric field in the chamber is horizontal, it was necessary for us to bend the original straight leads to enable the sensor to receive the (vertical) magnetic field

Table 4. Identification of Free Space Sensors Used

Model	Type Connector	Equiv Area (m) Max Frequency	Part No. Mfg.	Serial No.	Notes
ACD-2(R)	D-Dot Pair of SMAs	0.0001 7.5 GHz	-- EG&G	--	--
ACD-4(R)	D-Dot Twinaxial	0.01 750 MHz	7713650 EG&G	4	--
MGL-2D(A)	B-Dot Twinaxial	0.01 300 MHz	7114070-10 EG&G	24	--
MGL-6A(A)	B-Dot Twinaxial	0.001 1.8 GHz	7413327-10 EG&G	2	The unit appeared to have a bad mismatch in twinaxial connector. Unit was not used in the analysis.
MGL-6A(A)	B-Dot Twinaxial	0.001 1.8 GHz	7413327-10 EG&G	1	This unit was used in tests as a replacement for Ser. No. 2
MGL-9(R)	B-Dot Pair of SMAs	0.00002 10 GHz	-- EG&G	--	The double coaxial cable was bent to 90 degrees at 4.75 inches from the loop. See Fig. 22.



ACD-4A(R)

ACD-2(R)



MGL-2D(A)

MGL-6D(A)

MGL-9(R)

Fig. 21: Sensors used in the study.

with the leads vertical. Figure 22 is a close-up of the region near the bend. The coaxial cables were unsoldered and separated up to about 4 inches from the loop, bent with a radius of about 3/4 inches, and then resoldered to avoid the possibility of any loop resonances on the leads.

5.2 Experimental Techniques

The chamber and its instrumentation were described in Chapter 3 and, in principle at least, measuring the frequency response of the free space sensors is straightforward. Each sensor is positioned and supported inside the chamber and its output recorded over the frequency range from 118 to 4400 MHz. The sensor is then replaced by the smaller sized calibration sensor (MGL-9 or ACD-2) and the measurement repeated. From a knowledge of the latter's response, the ratio of the two outputs gives the normalized response of the original sensor.

This procedure worked well for the ground plane sensors. The same signal lead could be connected directly to the base of each sensor and, in addition, all the cabling was beneath the ground plane where it was invisible to the incident field. The situation is very different with the free space sensors. For example, each of the MGL-2, MGL-6 and ACD-4 sensors has a pair of coaxial cables extending out about 18 inches from the sensor and terminating in a connector. The connector is a so-called twinaxial where the transition is made from the pair of coaxial cables to a twinaxial cable. At the far end of the twinax, a transition is again necessary to go to the 50-ohm

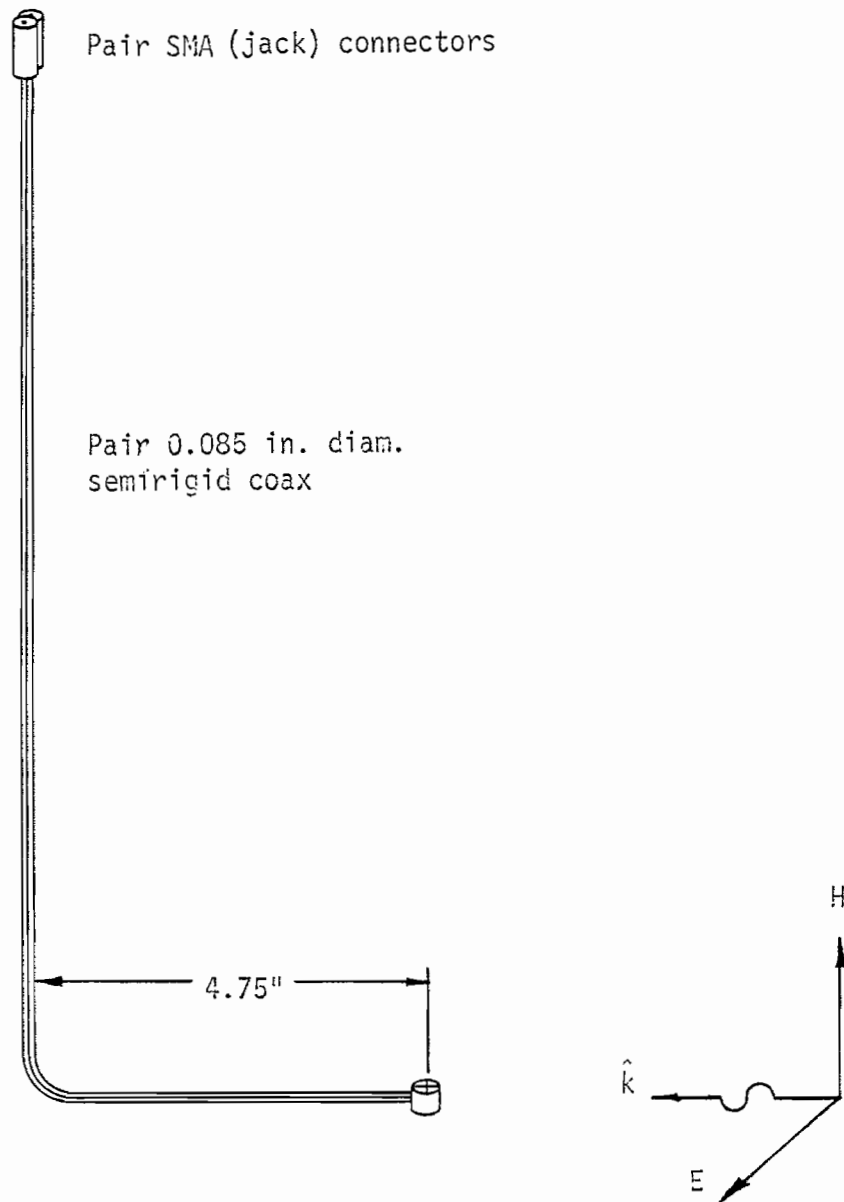


Fig. 22: Modified MGL-9(R). The coaxial cables were bent 4.75 inches from the loop to adapt for H-vertical polarization. In the original design the coax was straight.

coaxial geometry required by the network analyzer. Although balanced to unbalanced transformers are available to fit the connector (EG&G, DLT-96 series), they are usable up to 130 MHz only, and therefore inappropriate to the frequency range of concern to us.

An alternative is to change from the twinaxial transmission line geometry to a twin coaxial one, and to record each of the two outputs individually, combining them digitally using the calculator. A device called a twinaxial connector (EG&G, TCT) is available, but unfortunately it is quite bulky. To avoid interference with the field inside the chamber, it is necessary to place it outside, which then requires a long length of twinaxial cable from the sensor. Because of the discontinuities produced by the two connectors, standing waves are set up on the twinaxial cable which show up as oscillations in the measured data. Though we tried to reduce the oscillations using a 6 dB twin-line attenuator which we designed and built for insertion in the twinax, the resulting data were still unacceptable.

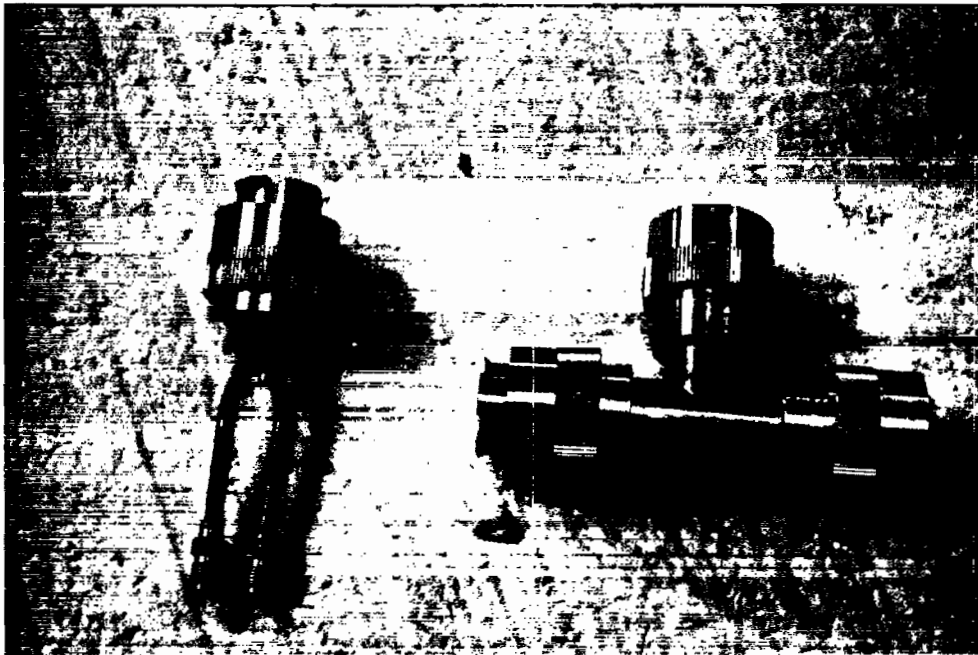
We remark in passing that the removal of the twinaxial connector at the sensor would give direct access to each of the coaxial leads from the sensor, and eliminate most of our problems. However, this would modify the sensor, and since our results would not then be appropriate to the sensors as built, this simple solution was unacceptable.

By this time we had concluded that the most practical approach was to separate the twinax into two coaxes as close to the sensor as possible, thereby minimizing oscillations due to cable mismatches.

A miniature twinaxial to coaxial adaptor was constructed using twinaxial and General Radio coaxial connector parts, and this is shown in Fig. 23 along with the TCT-1A connector. The adaptor is no larger than the twinaxial connector and has two 0.141 inch diam. semi-rigid coaxial cables with SMA connectors coming out. Because of its small size, the adaptor can be attached directly to the sensor and the signal can then be taken out of the chamber with a pair of semi-rigid cables; and since these cables and the connectors have low VSWR, they produce no appreciable mismatches to affect the data. The mismatches that remain are at the sensor, twinaxial connector and the adaptor. These are all close together, and the oscillations that they produce in the frequency data are relatively slow. Such oscillations are of no concern if a sensor response is calibrated against the response of the same sensor at a different aspect, provided the associated cabling is in no way disturbed.

The above problems do not occur with the small calibration sensor. The MGL-9 and ACD-2 do not have twinaxial lines. A pair of semi-rigid coaxial cables lead directly from the sensor to a connector of SMA type, and since there are no discontinuities, there should be no oscillations in the frequency response data. An unfortunate consequence is that the oscillations in the data for the larger sensors are not removed when the data are calibrated against data for these smaller sensors.

Compared to the ground plane sensor study, the measurement of the free space sensor responses was difficult and frustrating. In spite of our best endeavors, all of the procedures tried led to noisy



(a) Miniature

(b) TCT-1A

Fig. 23: Twinaxial to dual-coaxial adapters.

data. Whenever a cable was changed or even moved in the chamber, the oscillations were affected to such a degree that they were no longer eliminated by the calibration. To obtain data which are, as much as possible, independent of cable mismatches, and require minimal disturbance of the sensor in the chamber, it was therefore decided to separate the measurements into two parts:

- (i) angular response measurements,
- (ii) frequency response measurements.

In (i) the procedure is to record the data for a variety of θ and/or ϕ , and to normalize these data against the maximum response for that sensor, e.g., the data for broadside incidence for the ACD sensor.

In (ii) the response is measured only under the maximum signal condition and normalized with respect to the corresponding response of the appropriate calibration sensor to determine the frequency response of the test sensor.

5.3 Angular Response Measurements

The difficulties described above ate up considerable time, and many measurements were made before usable data were obtained.

5.3.1 ACD-4A(R) Sensor

This was the easiest to measure and was the one studied first. The sensor rested on a styrofoam pedestal on which a piece of polar paper was placed to show the sensor orientation, and the two semi-rigid coaxial leads went up vertically through the roof of the chamber. Figure 24 shows how the angle θ was defined relative to the

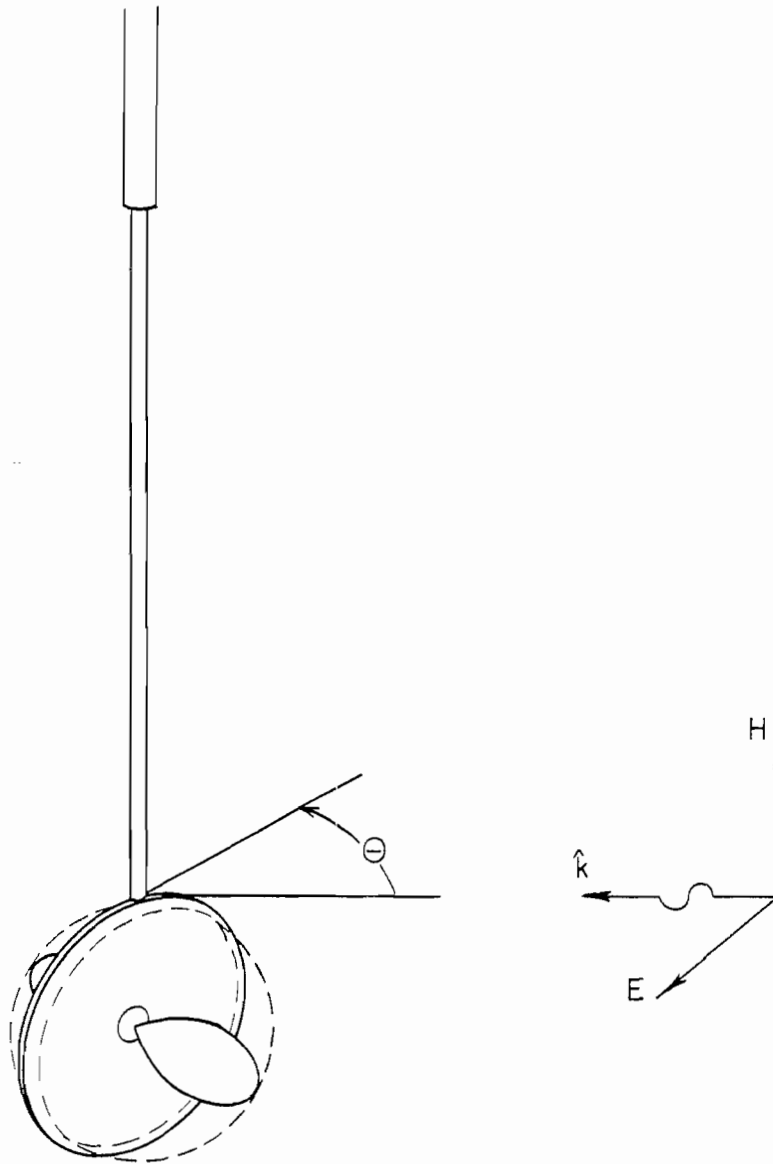


Fig. 24: Measurement geometry for the ACD sensors. (The θ -variation produces the angular (dipole) response.)

direction of the incident electric field, and measurements were made for $\theta = -90(15)90$ degrees. The data were normalized relative to those for $\theta = 0$ and are presented in Appendix A. Thus, for $\theta = 0$, the normalized amplitude is unity and the phase zero.

5.3.2 MGL-2D(A) and MGL-6D(A)

The geometry is shown in Fig. 25. In contrast to the ACD sensor, the MGL are not azimuthally independent, and it was therefore necessary to measure the azimuthal (ϕ) dependence as well as the θ dependence appropriate to the angular or dipole response.

To measure the ϕ variation, the sensor was placed on a styrofoam pedestal to which a piece of polar paper was attached. The output leads were taken vertically up through the roof. With gap No. 1 used as the zero reference for the azimuthal angle ϕ , data were recorded for $\phi = -90(15)90$ degrees with $\theta = 0$, and normalized with respect to the measured data for $\phi = 0$. The normalized data are presented in Appendix C.

To measure the angular response, the sensor was rotated forward through an angle θ (see Fig. 25), and a special jig was constructed to accurately control the tilt angle θ . Figure 26 is a photograph of the jig with a sensor in place. To permit the bending, a matched pair of coaxial cables was inserted above the sensor handle (see Fig. 26), and a braided shield was added to avoid leakage and resonances. For each sensor, measurements were made for $\theta = 0(15)90$ degrees with $\phi = 45$ degrees, corresponding to incidence midway between gaps 1 and 2, and $\phi = 90$ degrees, corresponding to incidence on gap 2. The data were

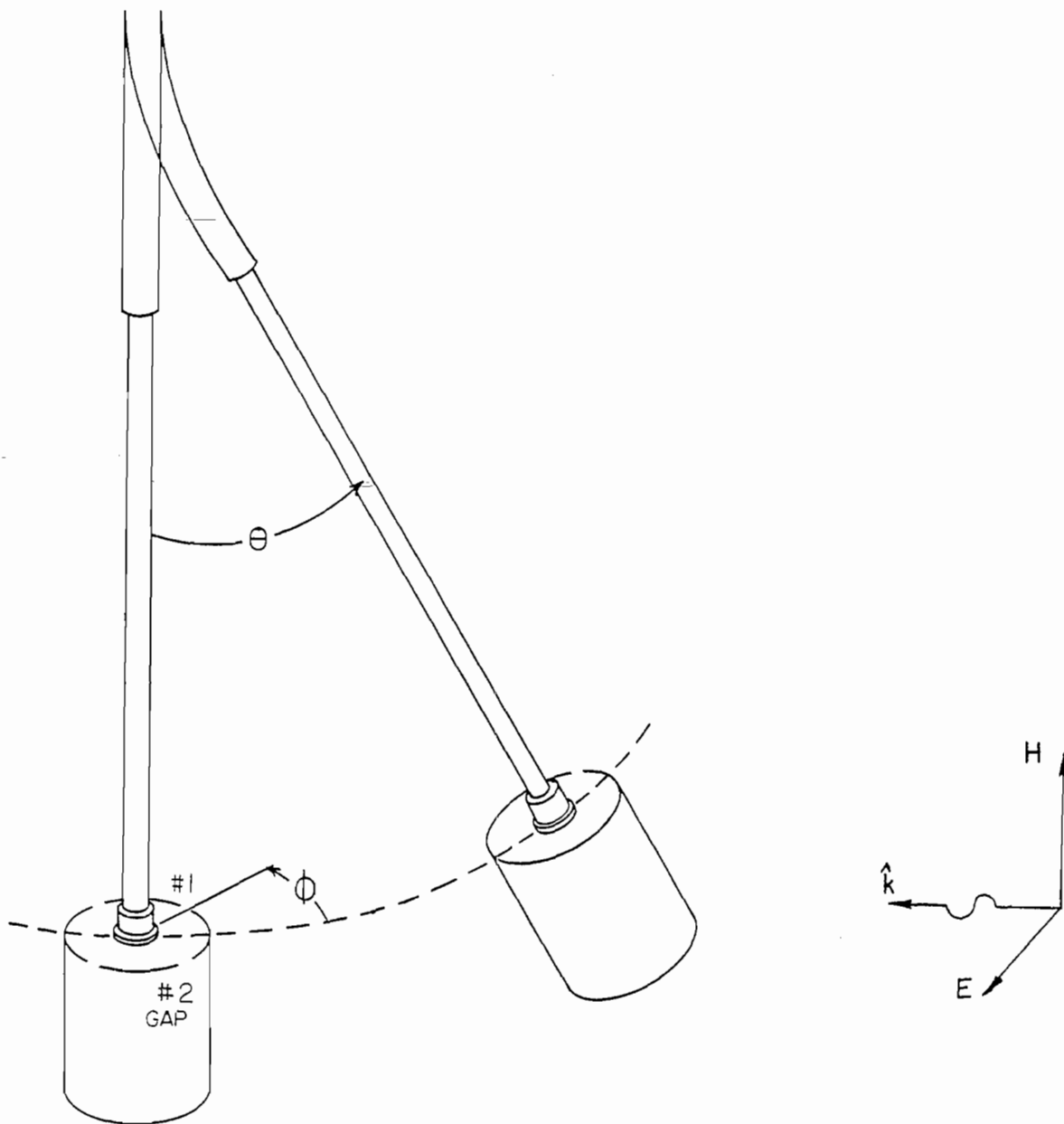


Fig. 25: Measurement geometry for MGL-series sensors. (The θ -variation produces angular (dipole) response and ϕ -variation produces azimuthal (constant) response.)

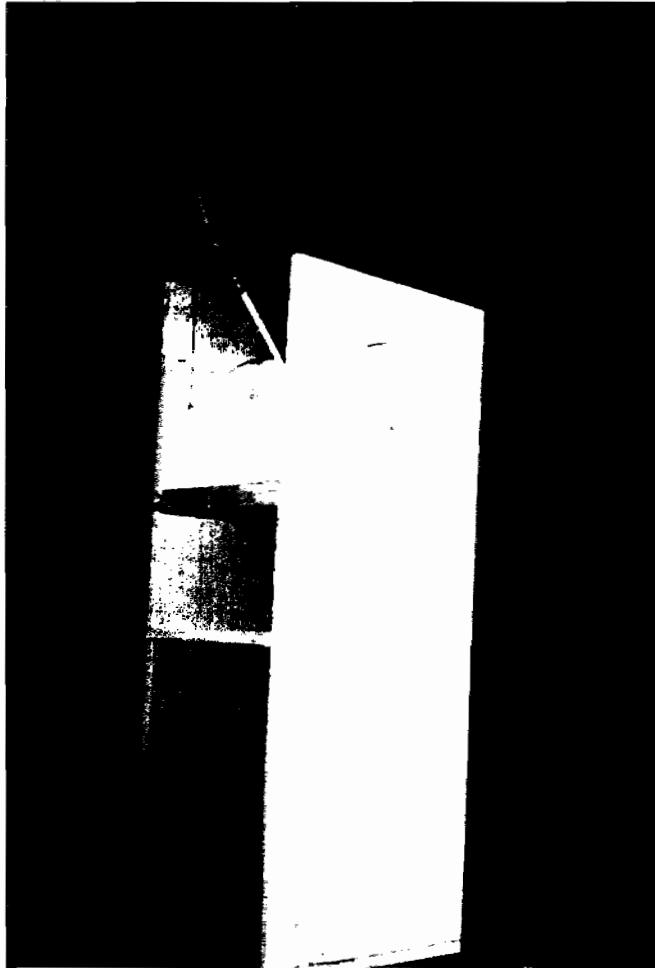


Fig. 26: Styrofoam jig used for support and rotation of MGL-2 and MGL-6 sensors. The incident field is from the right-hand side.

normalized with respect to the measured data for the sensor in question when $\theta = 0$, and are presented in Appendix B.

5.4 Angular Response Data Analysis

The measured data were processed according to the formulas in Chapter 2. For the angular (dipole) response, the quantities computed are

- (i) the dipole response coefficients $A_n(f)$, from (14);
- (ii) the mean squared angular error $\xi^2(f)$, from (15);
- (iii) the maximum error $\xi_{\max}(f)$, from (16).

For the MGL sensors, the following additional quantities were computed to determine the azimuthal variation of the response:

- (iv) the average rotational response coefficient $B_n(f)$, from (17);
- (v) the mean squared rotational error $\xi_r^2(f)$, from (18);
- (vi) the maximum rotational error $\xi_{r \max}(f)$, from (19).

Two programs were written, one for each type of calculation, and the processing and graphics were done on the HP9845 calculator.

Figure 27 shows the angular (dipole) dependence of the response of the MGL-2D(A) sensor as a function of θ with $\phi = 45$ degrees and $f = 150$ MHz. These data were recorded at this one frequency during the "pre-measurement" stage of the study, and are presented here to help in understanding the meaning of $A_n(f)$, $\xi^2(f)$ and $\xi_{\max}(f)$. Thus, $A_n(f)$ is the coefficient of the best fit cosine curve, $\xi^2(f)$ measures how closely the curve fits the data, and $\xi_{\max}(f)$ is a measure of the maximum deviation of the data from the curve. The fit in Fig. 27 is very good but as the frequency increases, so do the deviations. This

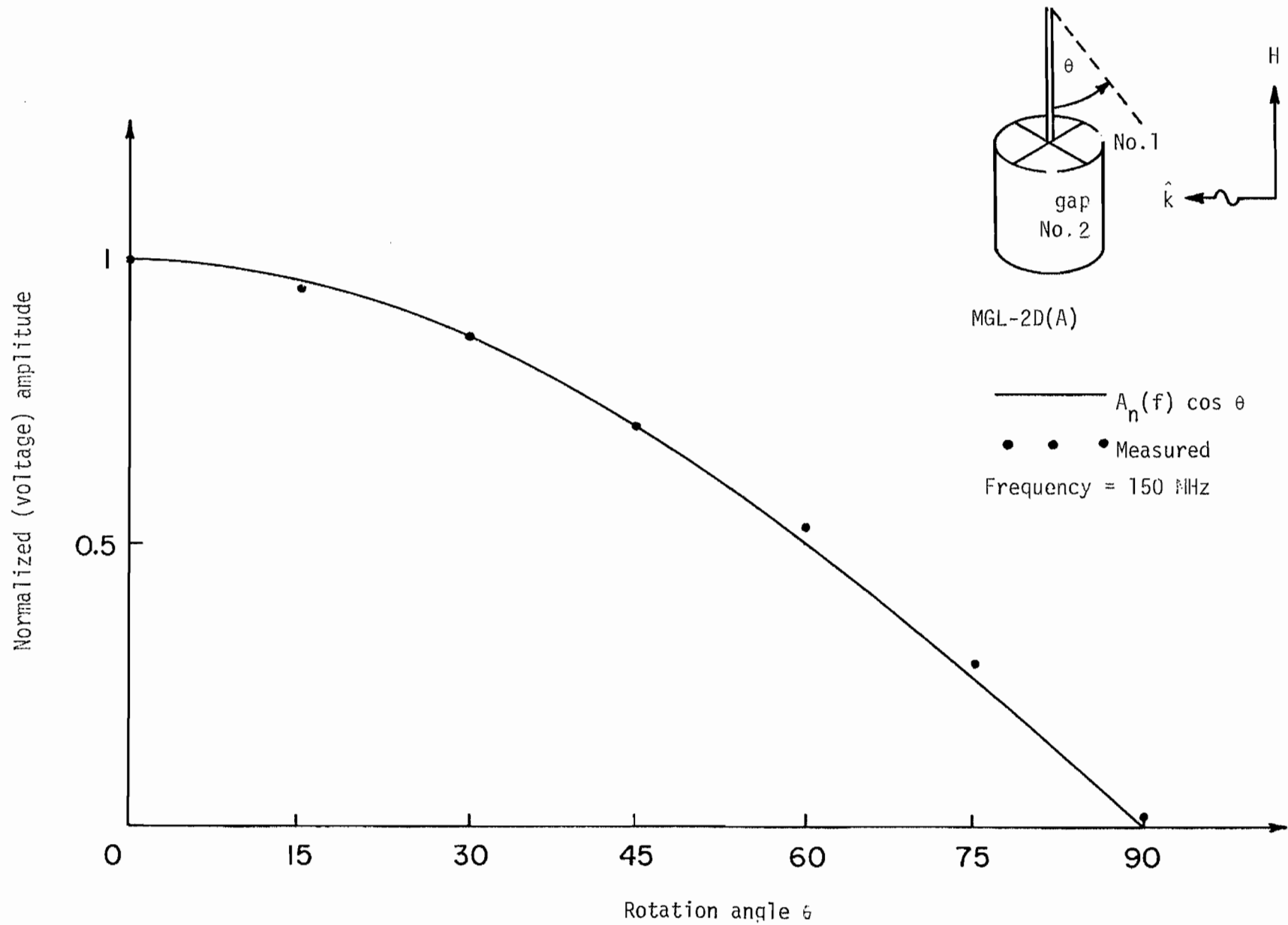


Fig. 27: Measured angular response of MGL-2D(A) at 150 MHz.

is evident from the subsequent figures where the various quantities are presented as functions of frequency;

Figures 28 through 32: dipole response for ACD-4A(R);

Figures 33 through 37: dipole response for MGL-2D(A) with gap No. 1 at $\phi = 90^\circ$;

Figures 38 through 42: dipole response for MGL-2D(A) with gap No. 1 at $\phi = 45^\circ$;

Figures 43 through 45: rotational response for MGL-2D(A);

Figures 46 through 50: dipole response for MGL-6A(A) with gap No. 1 at $\phi = 90^\circ$;

Figures 51 through 55: dipole response for MGL-6A(A) with gap No. 1 at $\phi = 45^\circ$;

Figures 56 through 58: rotational response for MGL-6A(A).

The implications of the 3-dB frequencies shown in these plots are discussed in Chapter 6.

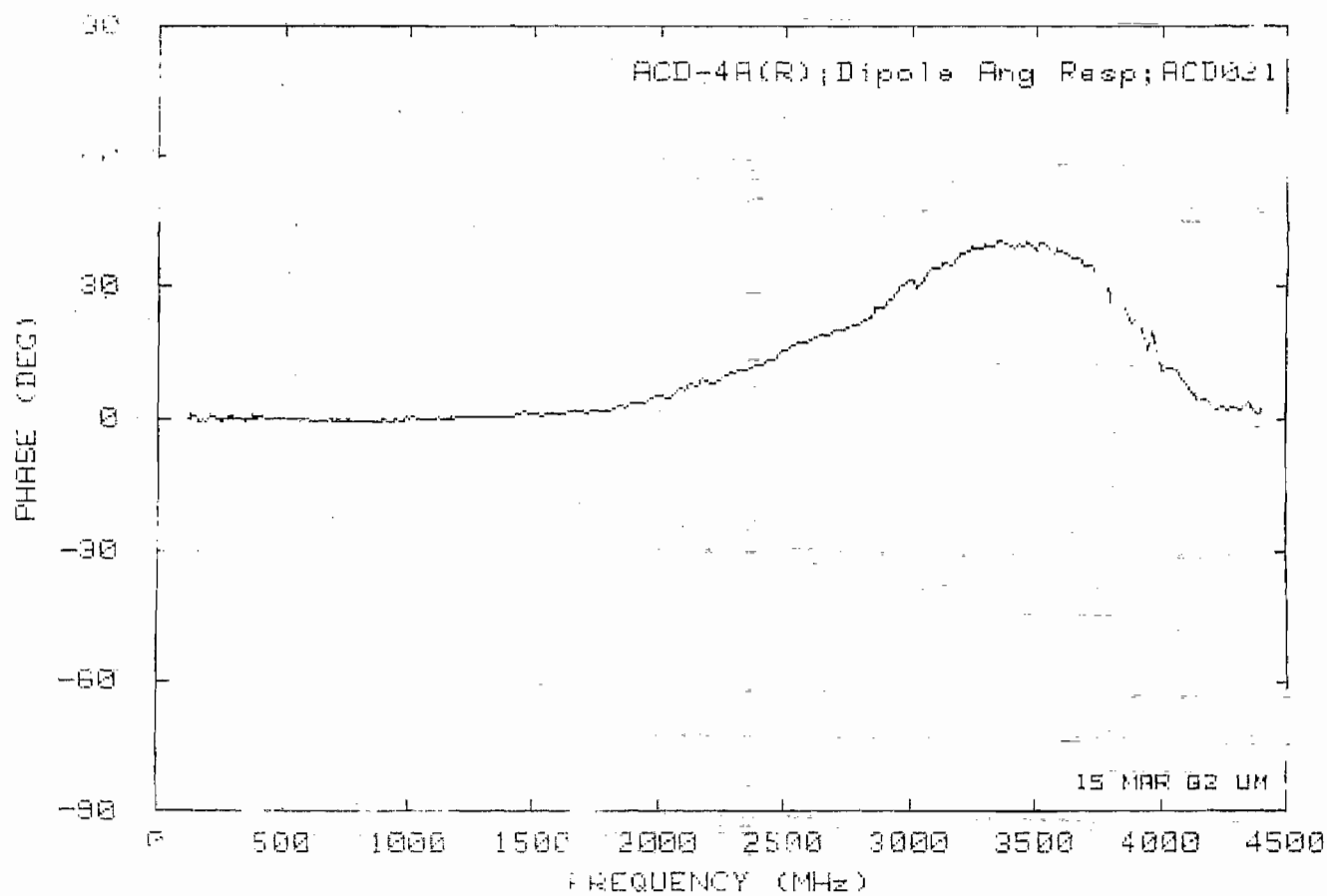
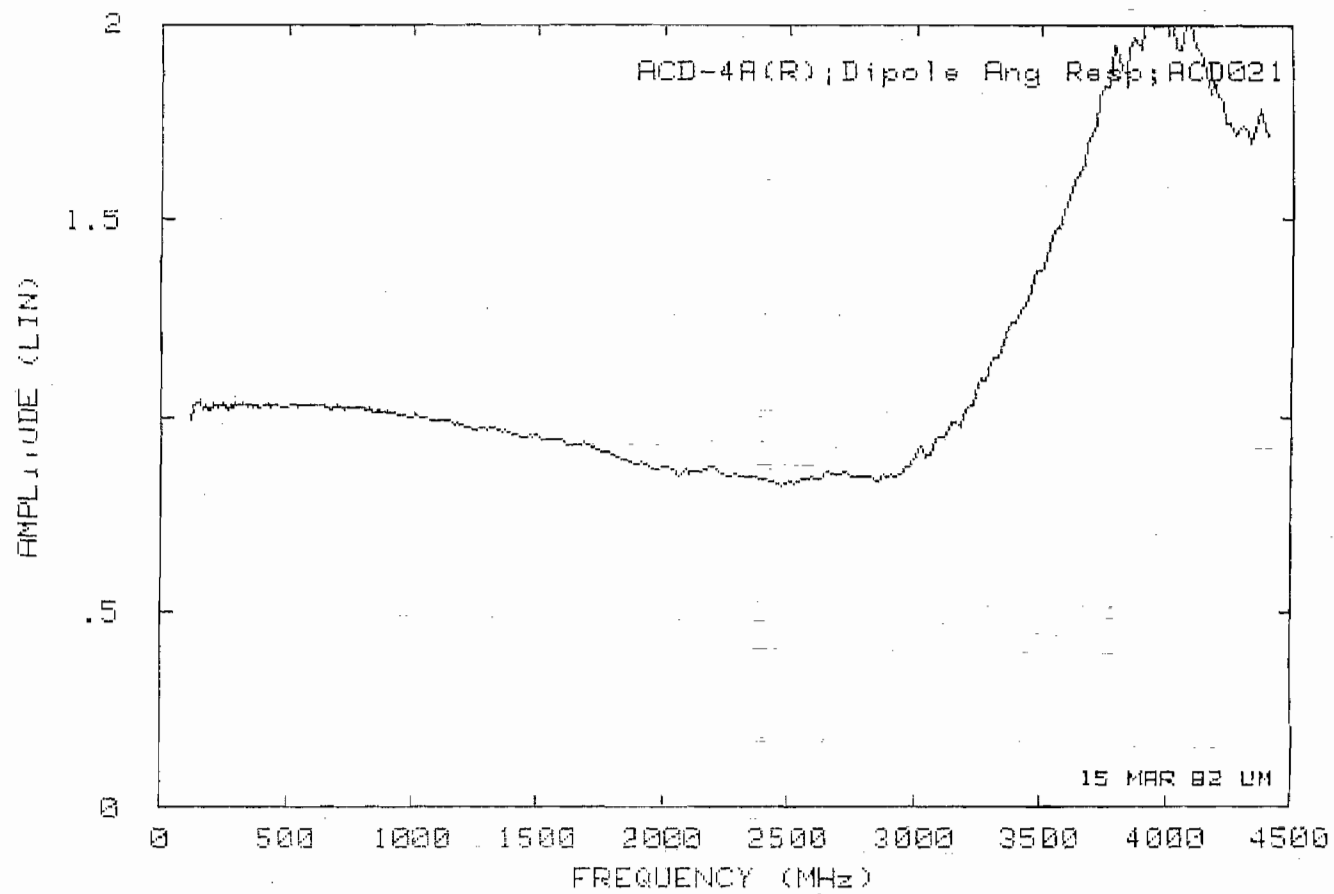


Fig. 28: $A_n(f)$ for ACD-4A(R).

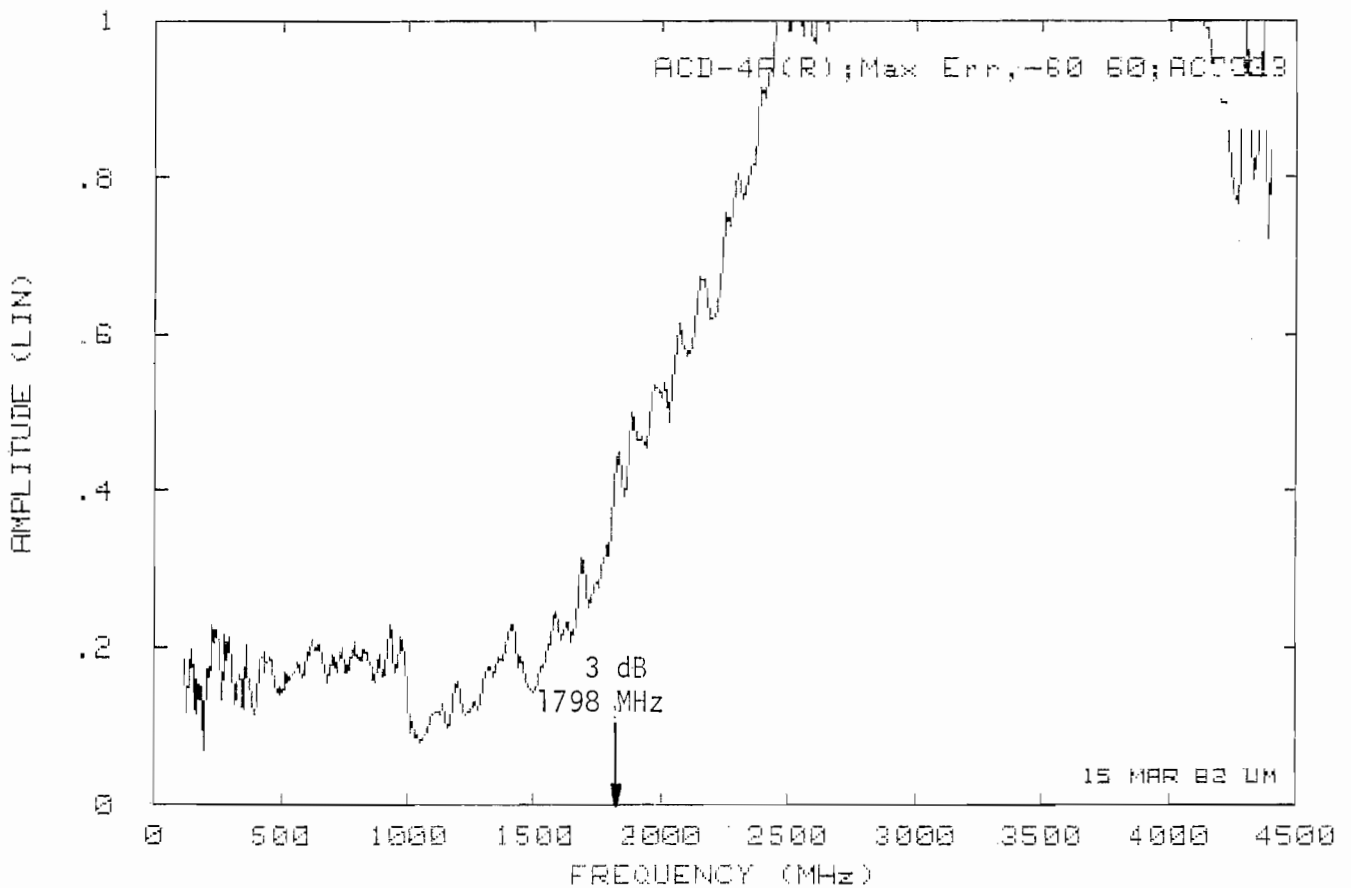
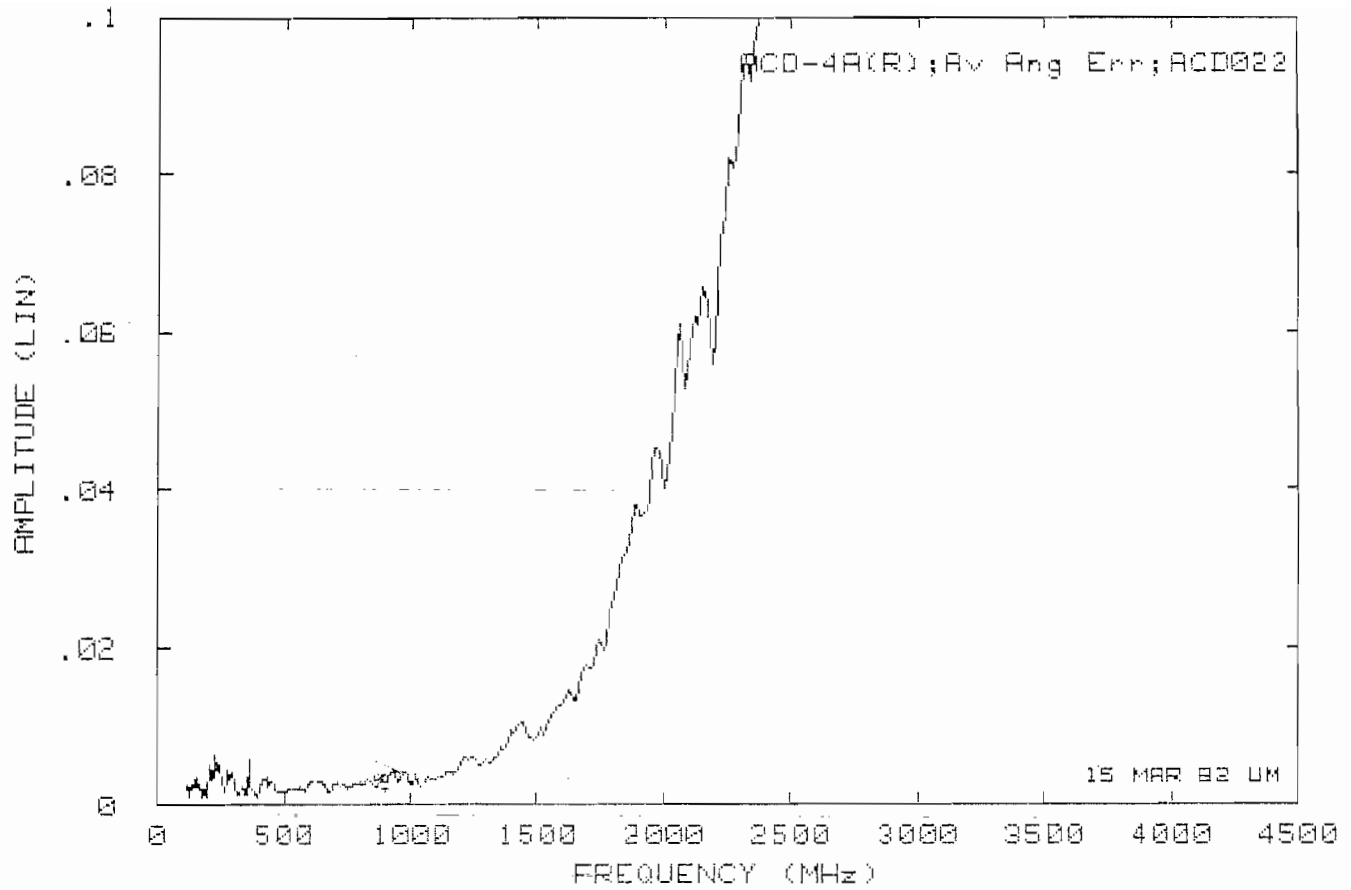


Fig. 29: (top): $\mathcal{E}_d^2(f)$ for ACD-4A(R).

Fig. 30: (bottom): $\mathcal{E}_{\max}(f)$ for ACD-4A(R), $|\theta| \leq 60^\circ$.

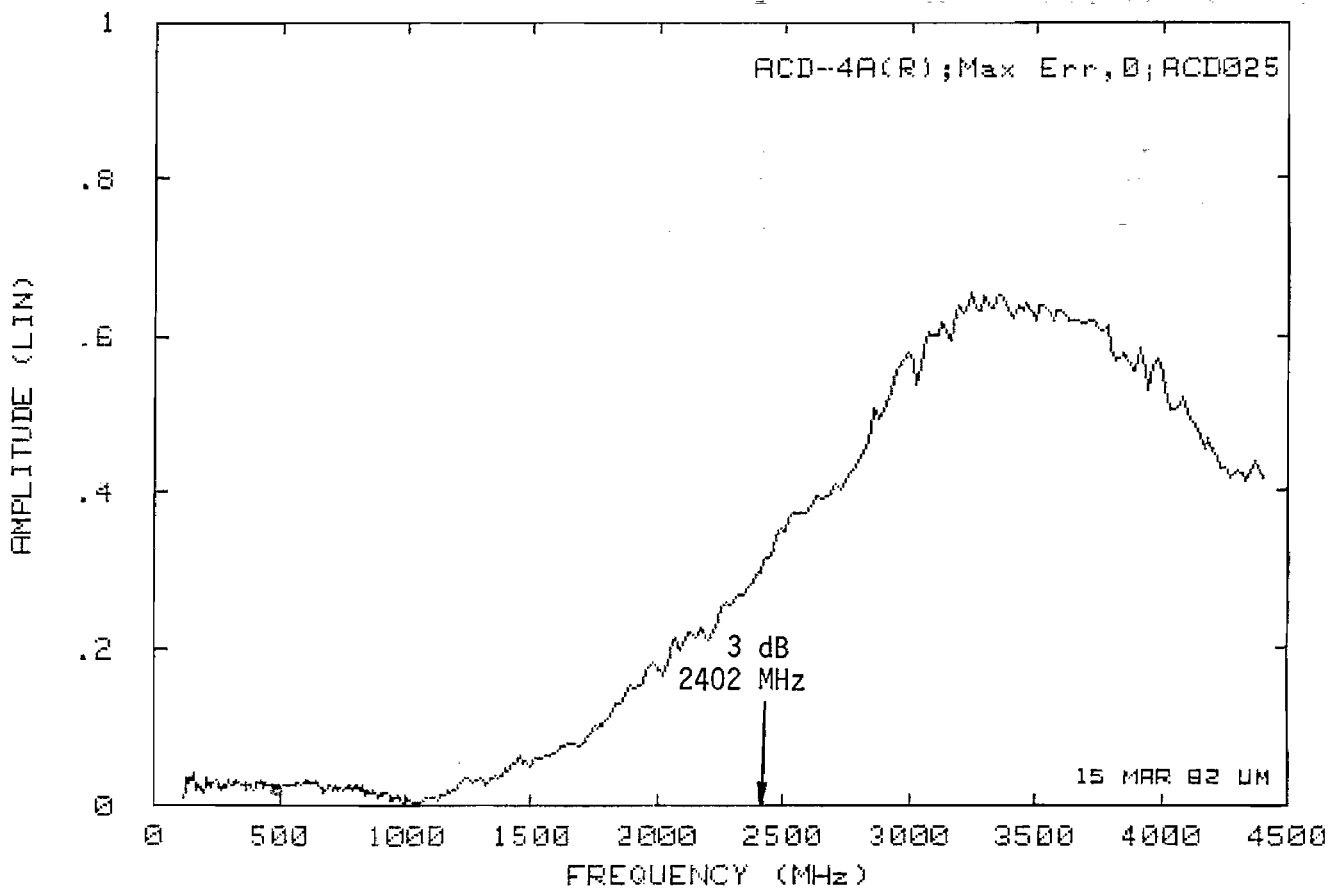
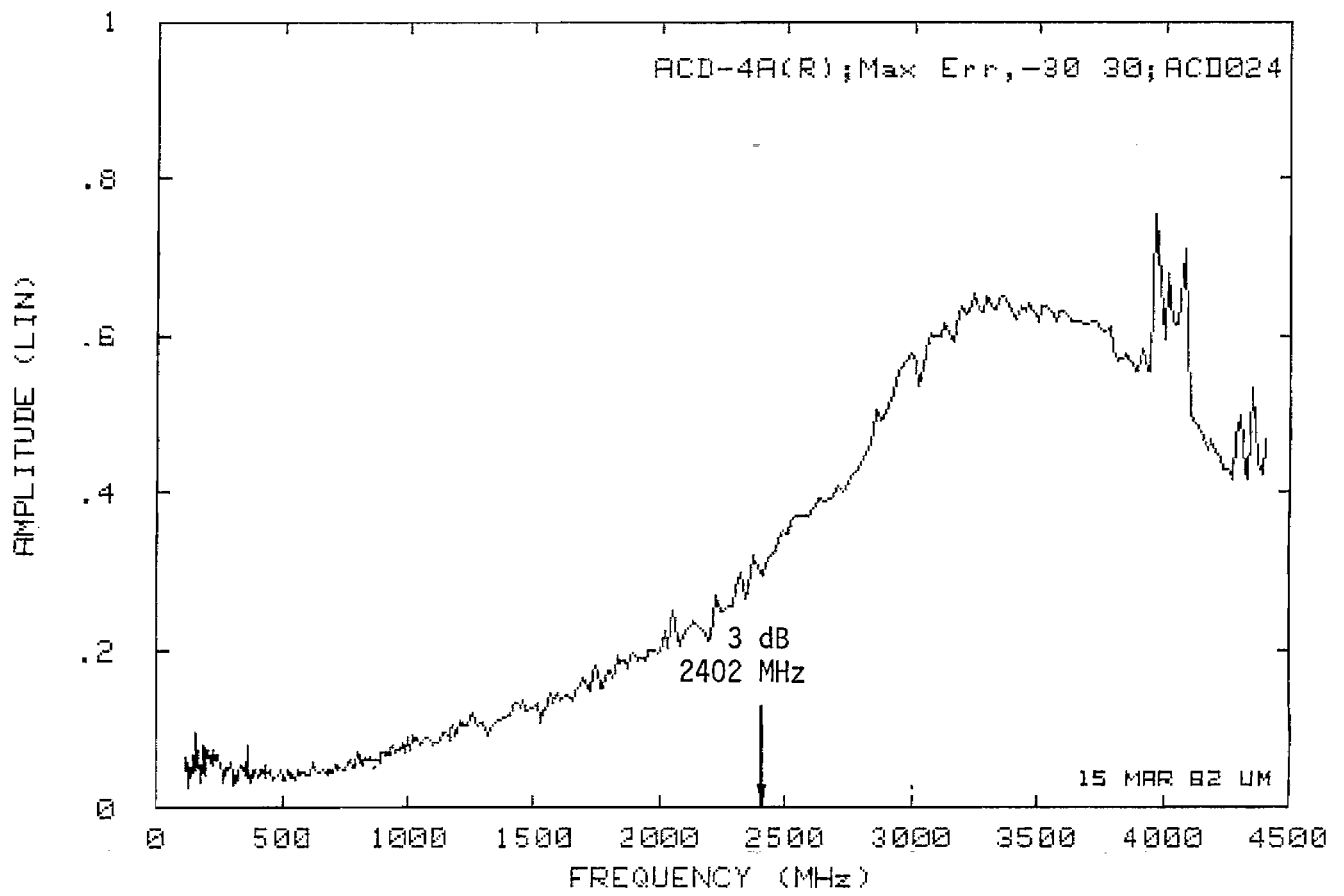


Fig. 31: (top): $\mathcal{E}_{\max}(f)$ for ACD-4A(R), $|\theta| \leq 30^\circ$.

Fig. 32: (bottom): $\mathcal{E}_{\max}(f)$ for ACD-4A(R), $\theta = 0^\circ$.

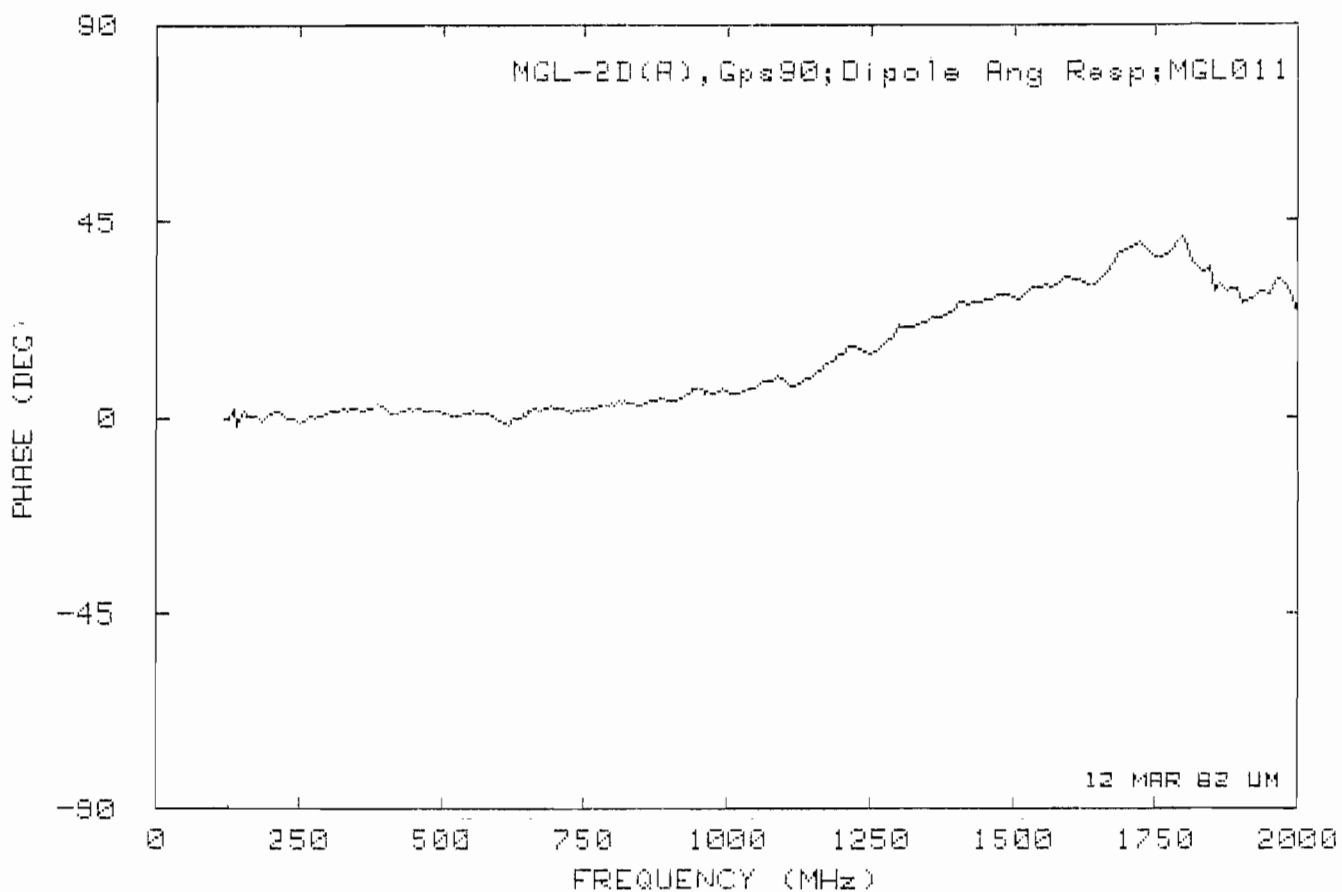
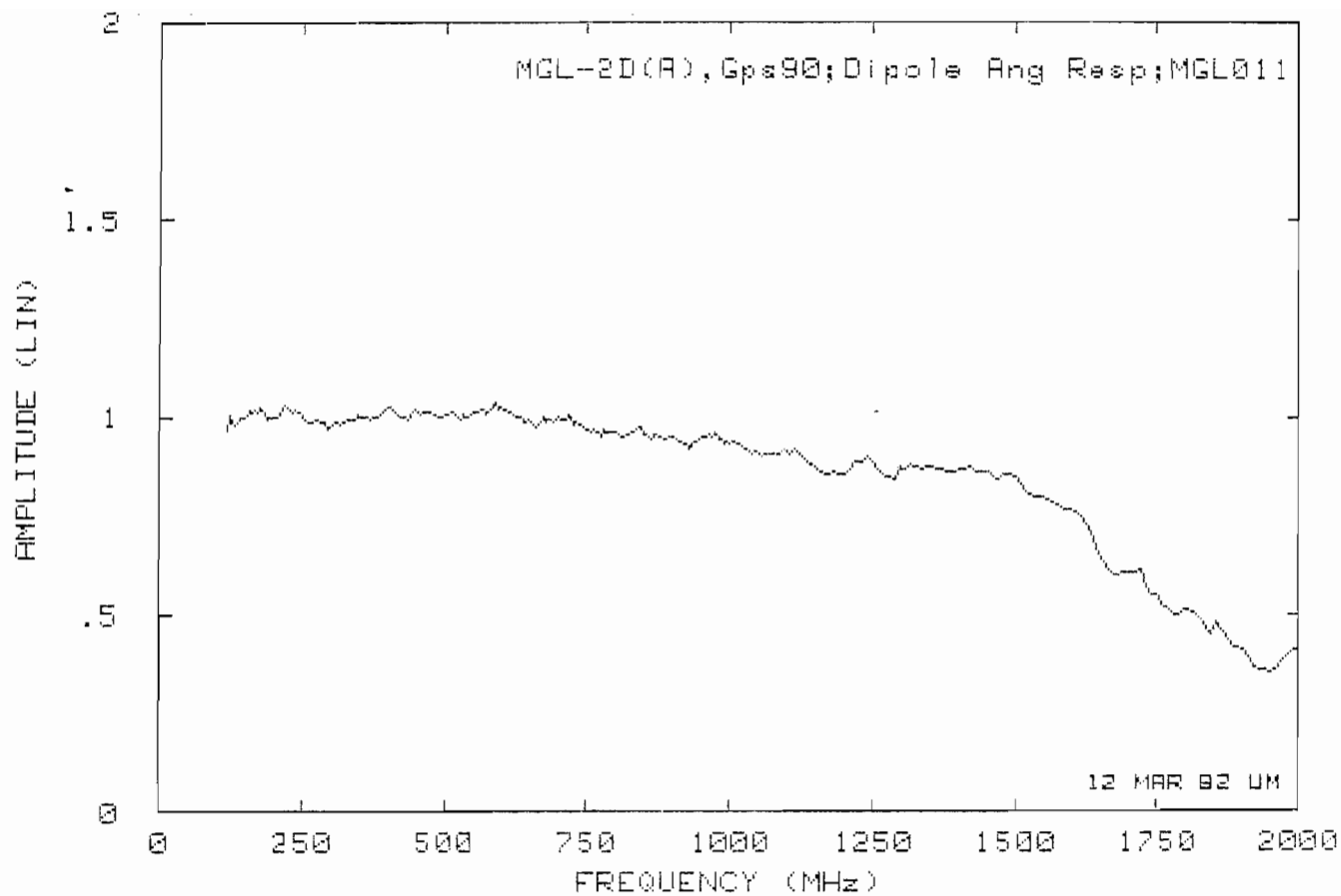


Fig. 33: $A_n(f)$ for MGL-2D(A), gap No. 1 at $\phi = 90^\circ$.

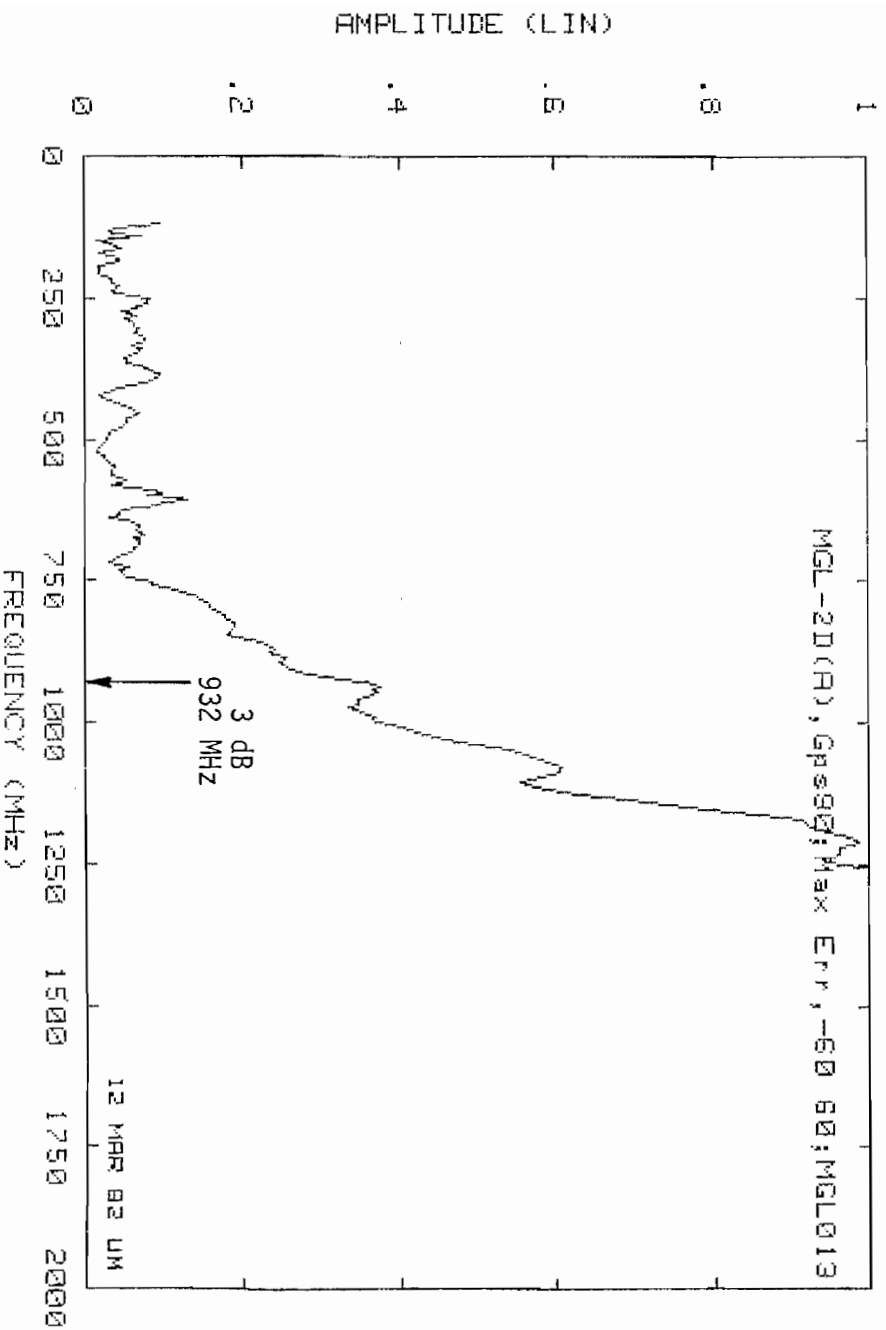
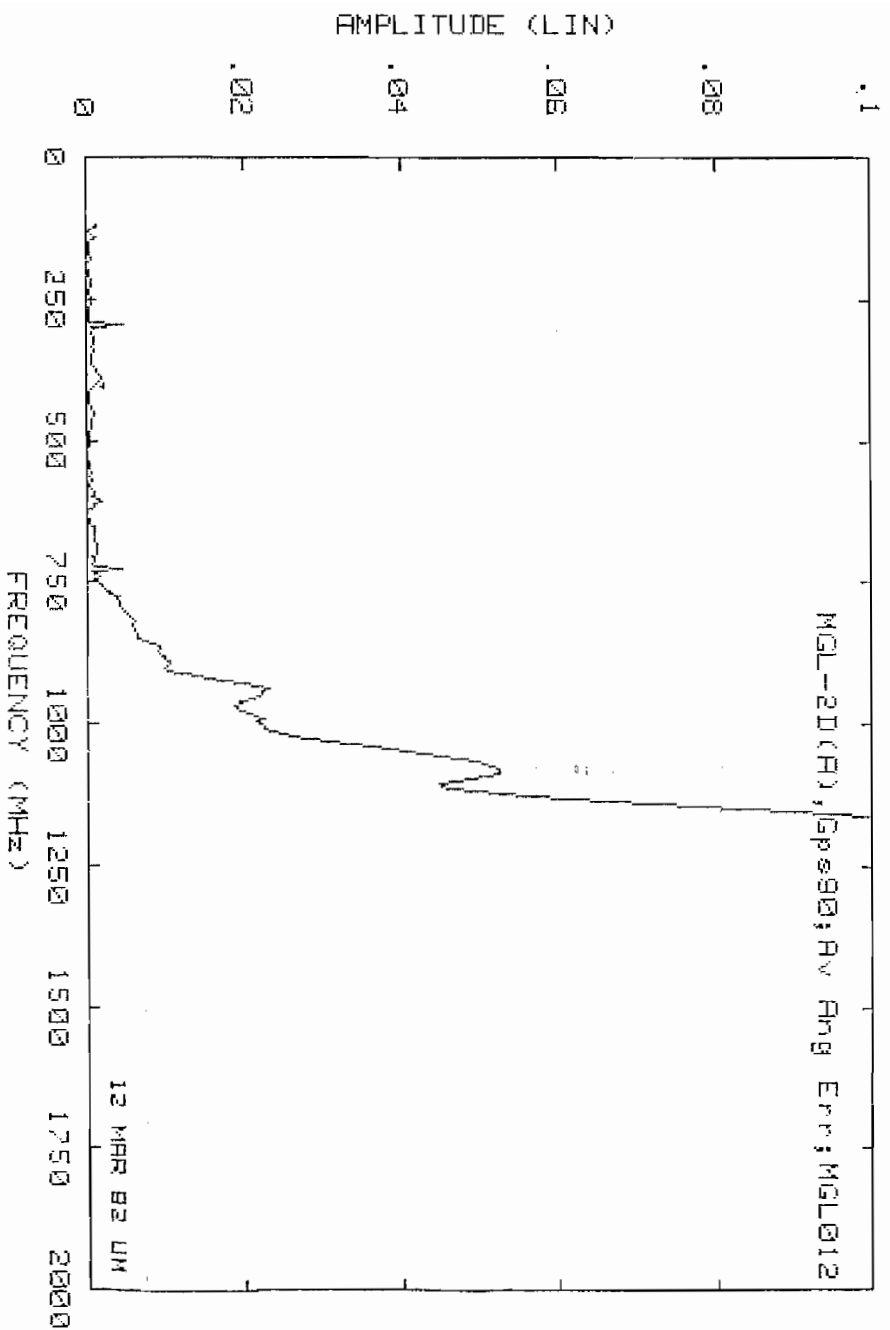


Fig. 34: (top): $\mathcal{E}_2(f)$ for MGL-2D(A), gap No. 1 at $\phi = 90^\circ$.

Fig. 35: (bottom): $\mathcal{E}_{\max}(f)$ for MGL-2D(A), $|\theta| \leq 60^\circ$, gap No. 1 at $\phi = 90^\circ$.

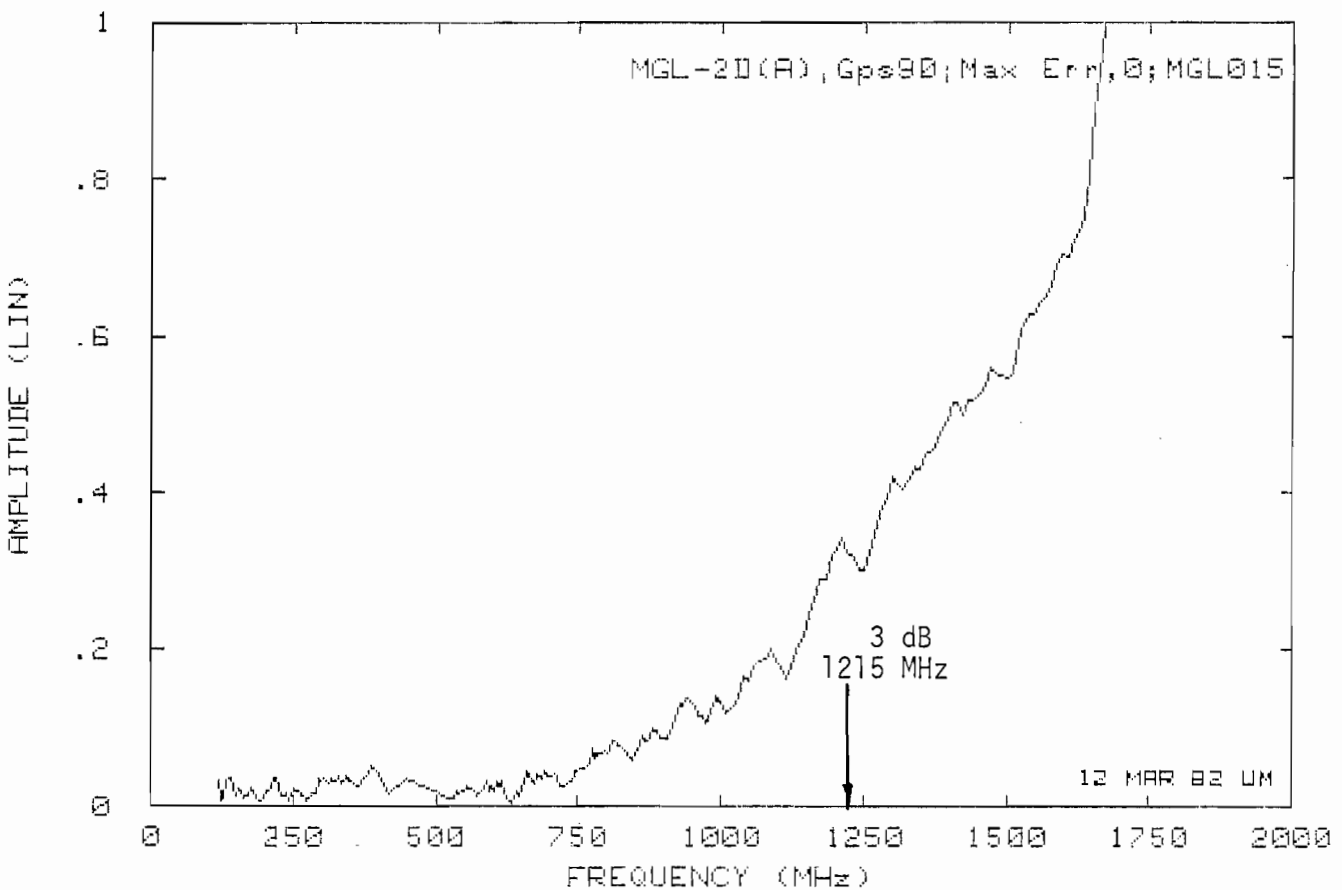
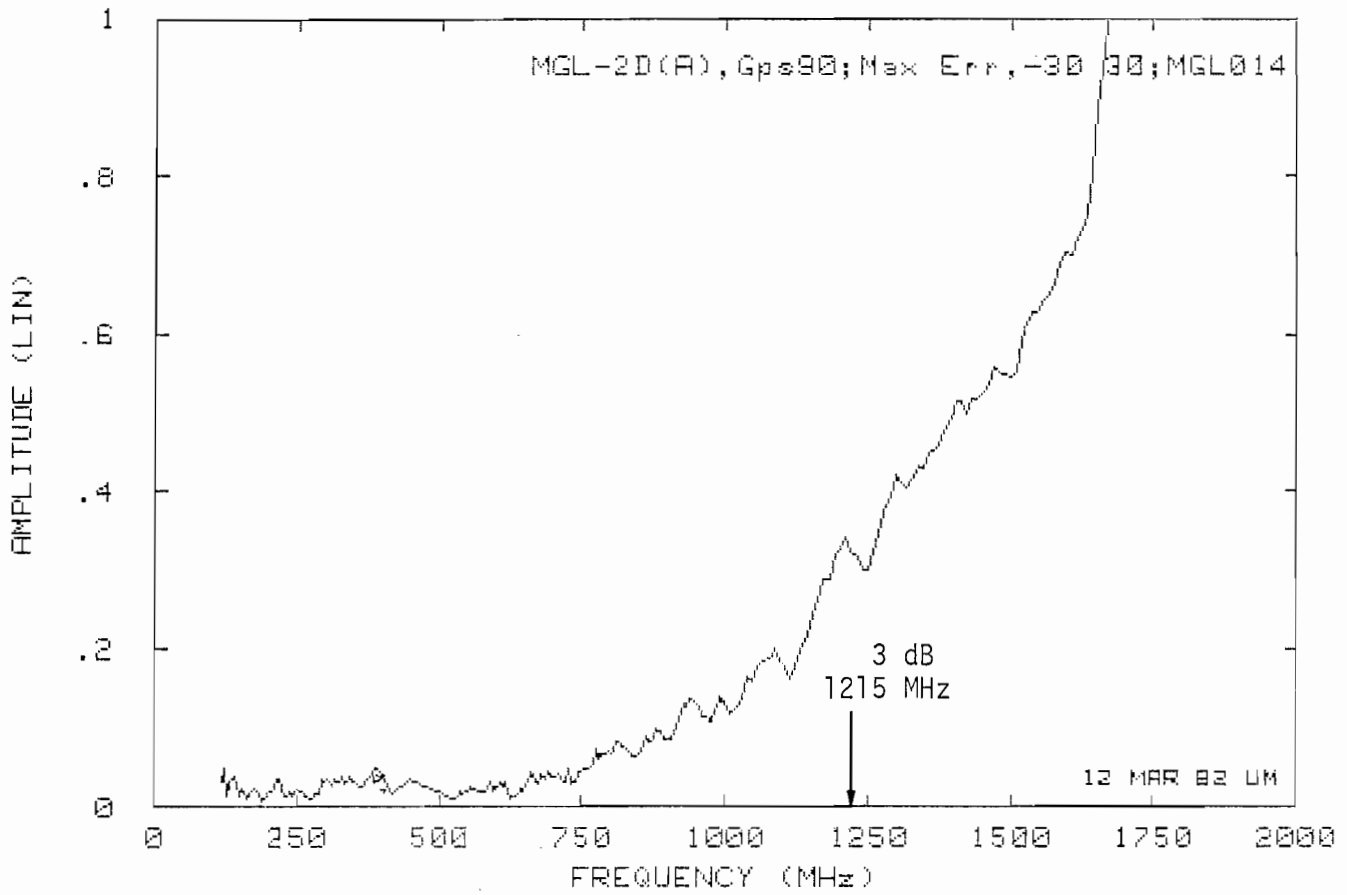


Fig. 36: (top): $\mathcal{E}_{\max}(f)$ for MGL-2D(A), gap No. 1 at $\phi = 90^\circ$, $|\theta| \leq 30^\circ$

Fig. 37: (bottom): $\mathcal{E}_{\max}(f)$ for MGL-2D(A), gap No. 1 at $\phi = 90^\circ$, $\theta = 0^\circ$.

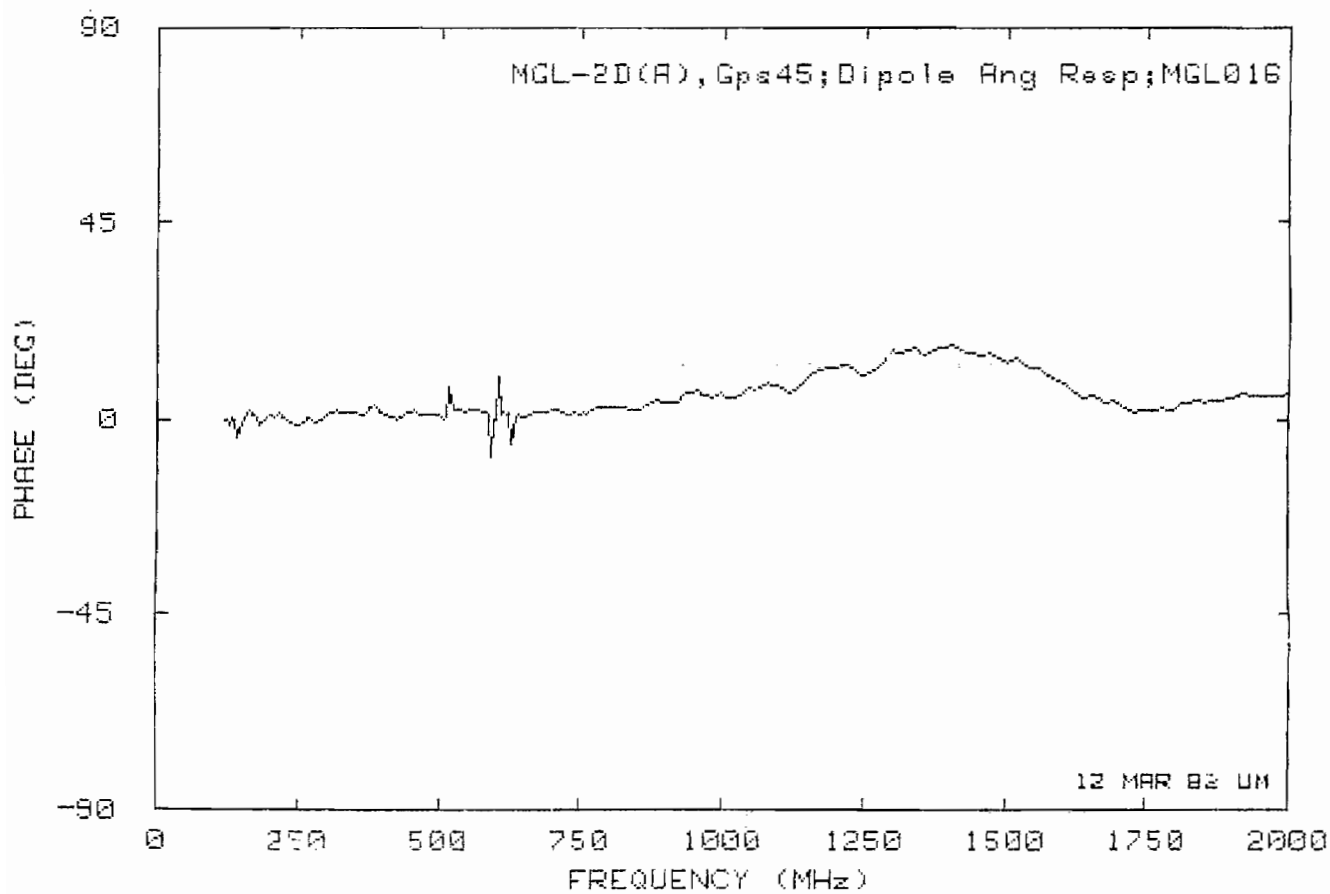
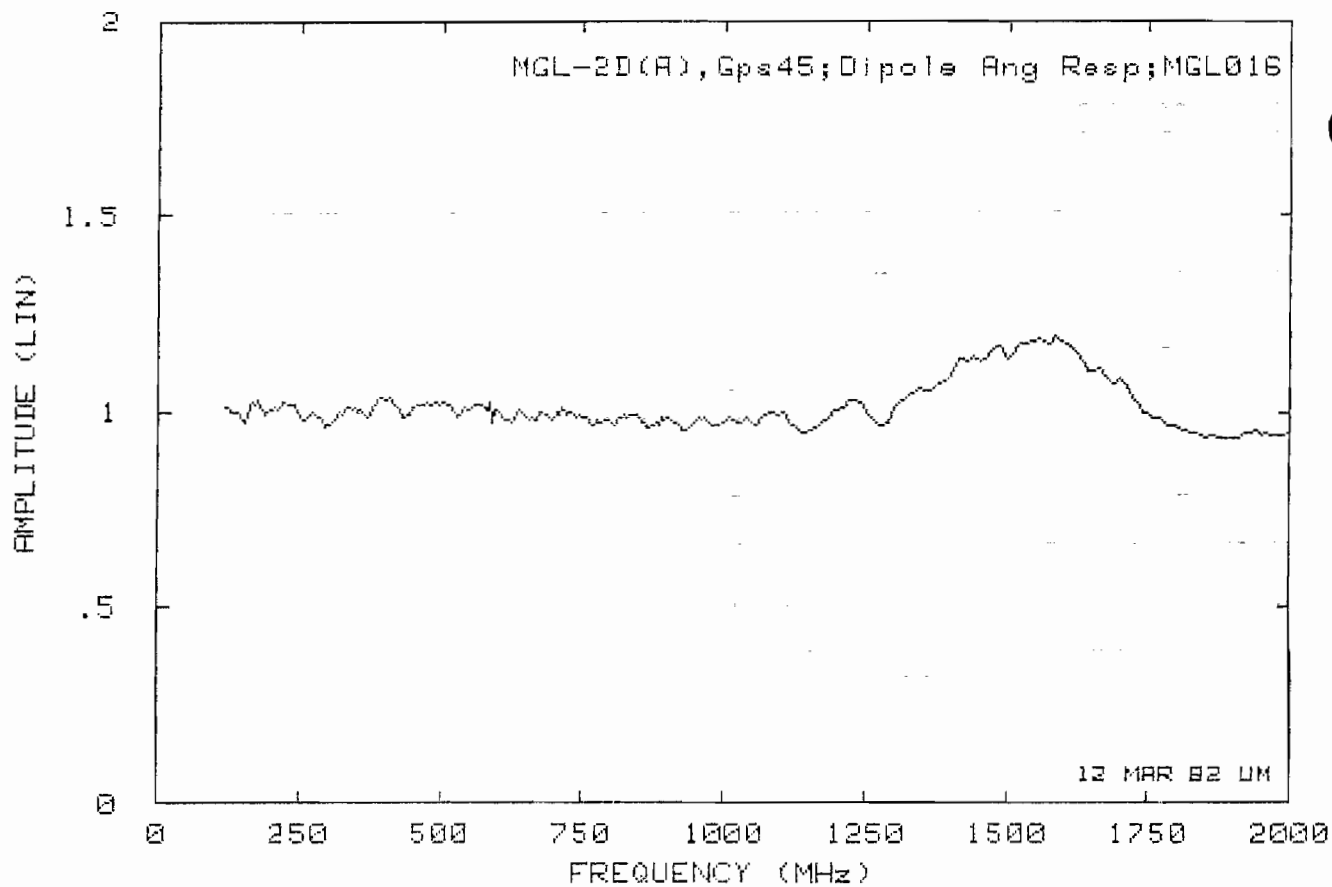


Fig. 38: $A_n(f)$ for MGL-2D(A), gap No. 1 at $\phi = 45^\circ$.

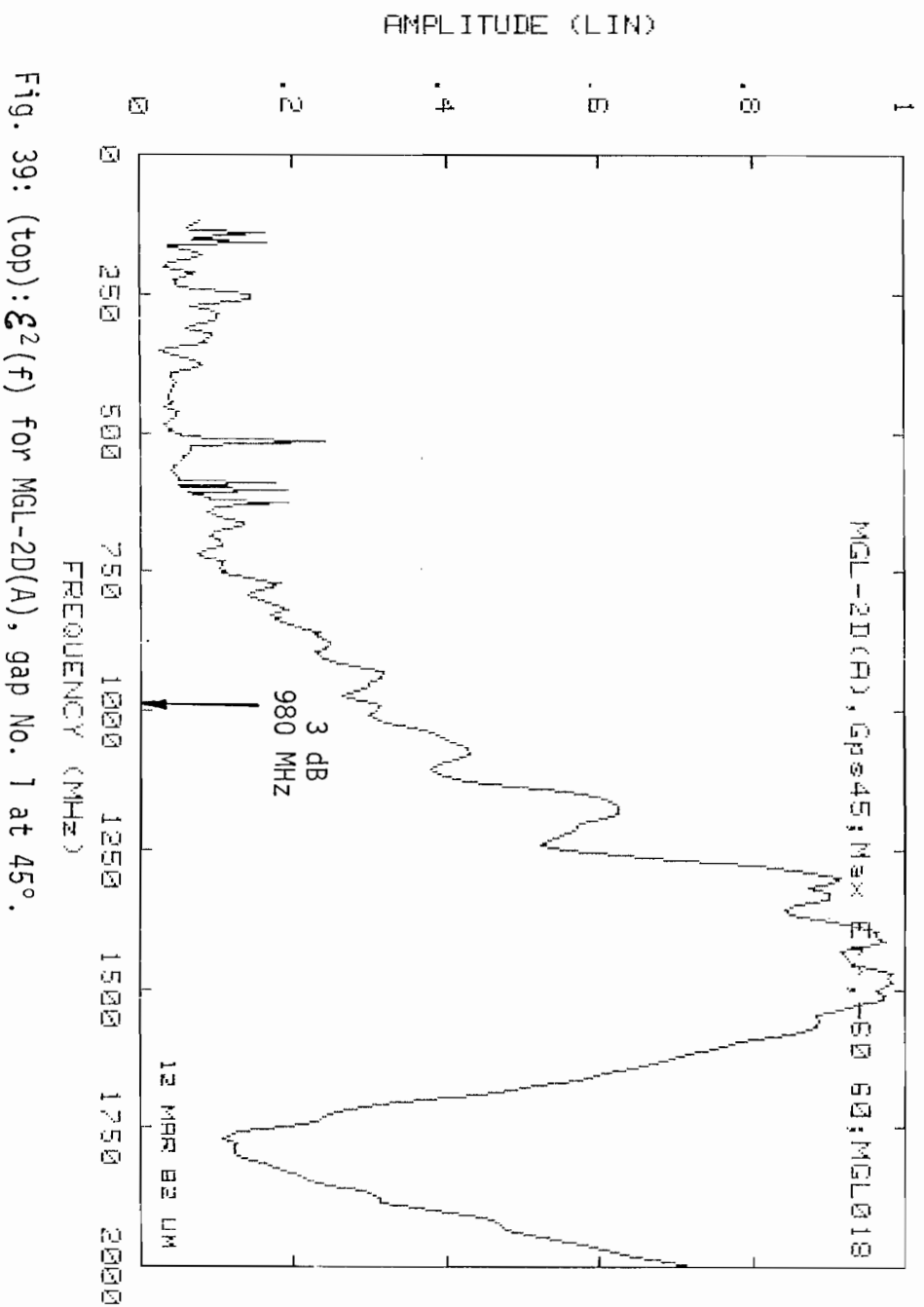
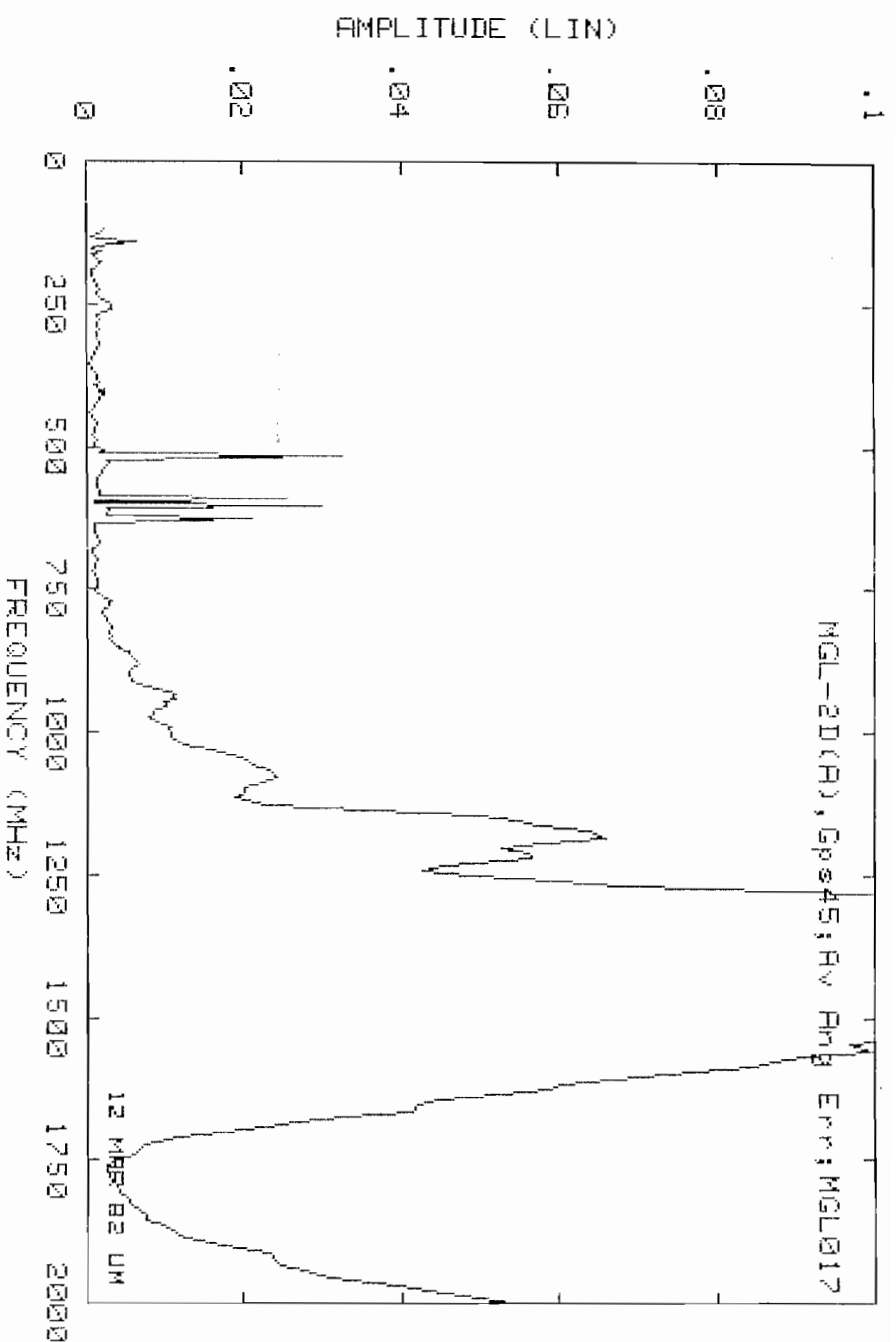


Fig. 39: (top): $\mathcal{E}^2(f)$ for MGL-2D(A), gap No. 1 at 45° .

Fig. 40: (bottom): $\mathcal{E}_{\max}(f)$ for MGL-2D(A), gap No. 1 at 45° , $|\theta| \leq 60^\circ$.

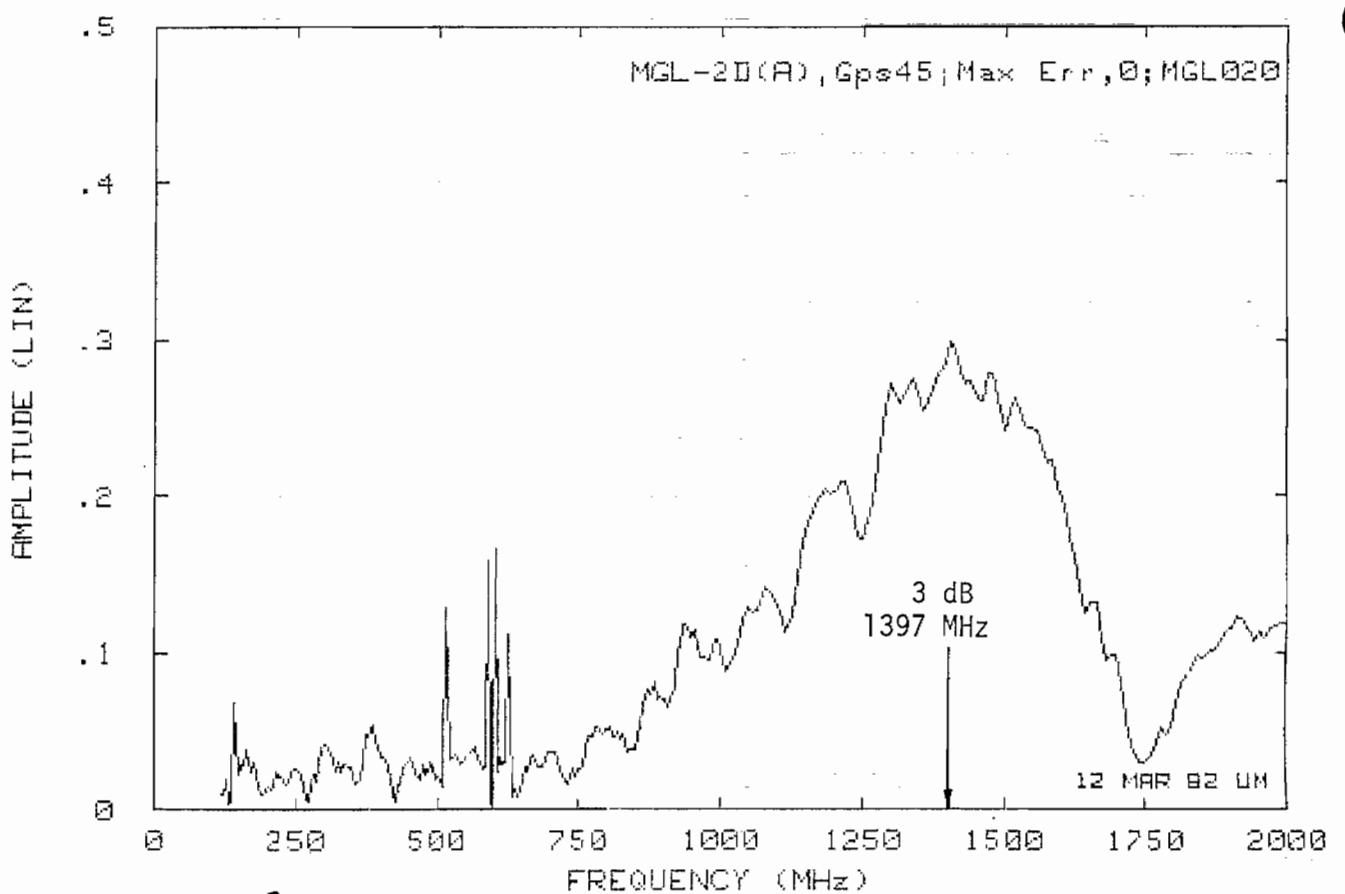
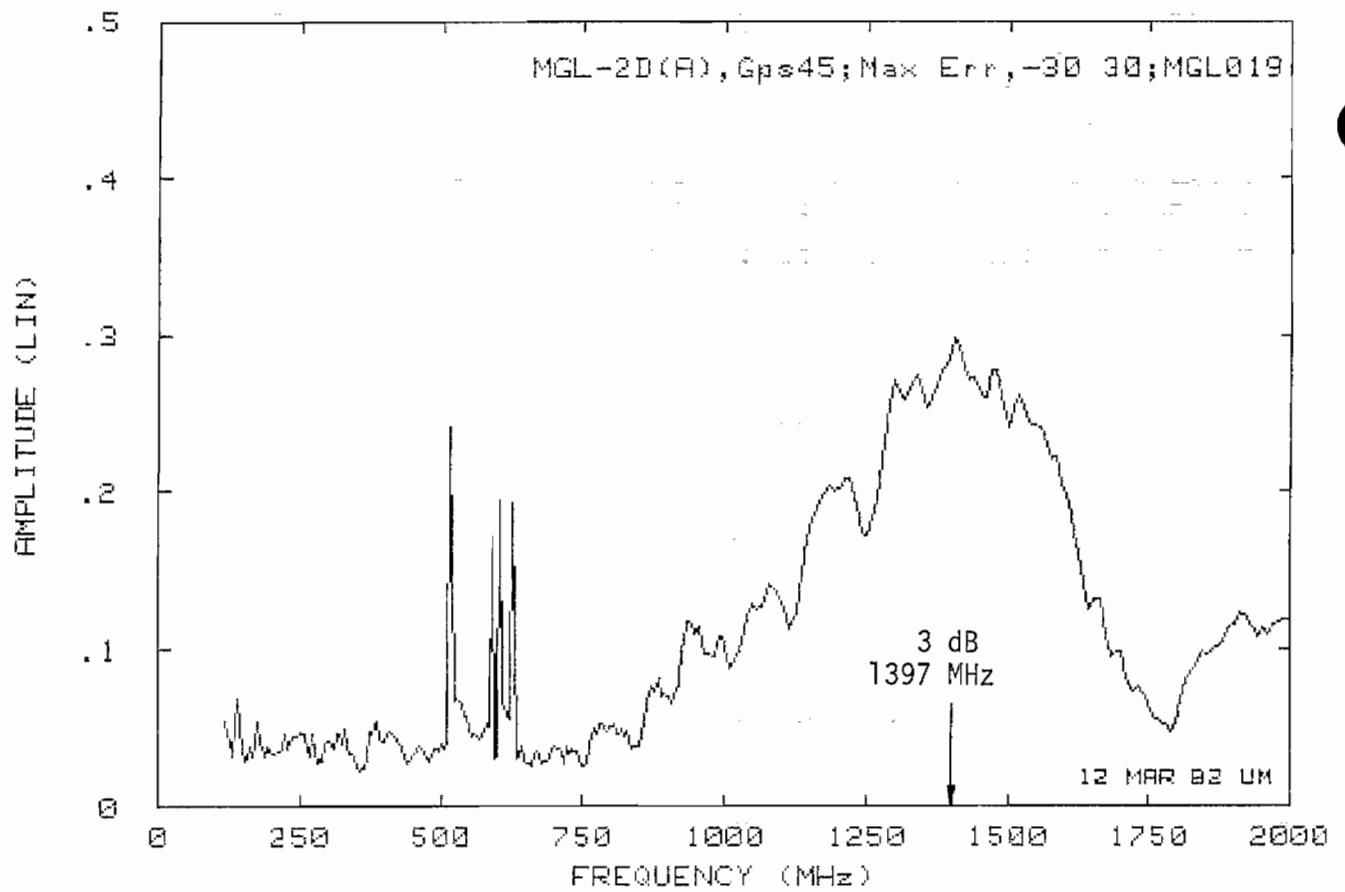


Fig. 41: (top): $\mathcal{E}_{\max}(f)$, for MGL-2D(A), gap No. 1 at 45° , $|\theta| \leq 30^\circ$

Fig. 42: (bottom): $\mathcal{E}_{\max}(f)$, for MGL-2D(A), gap No. 1 at 45° , $\theta = 0^\circ$.

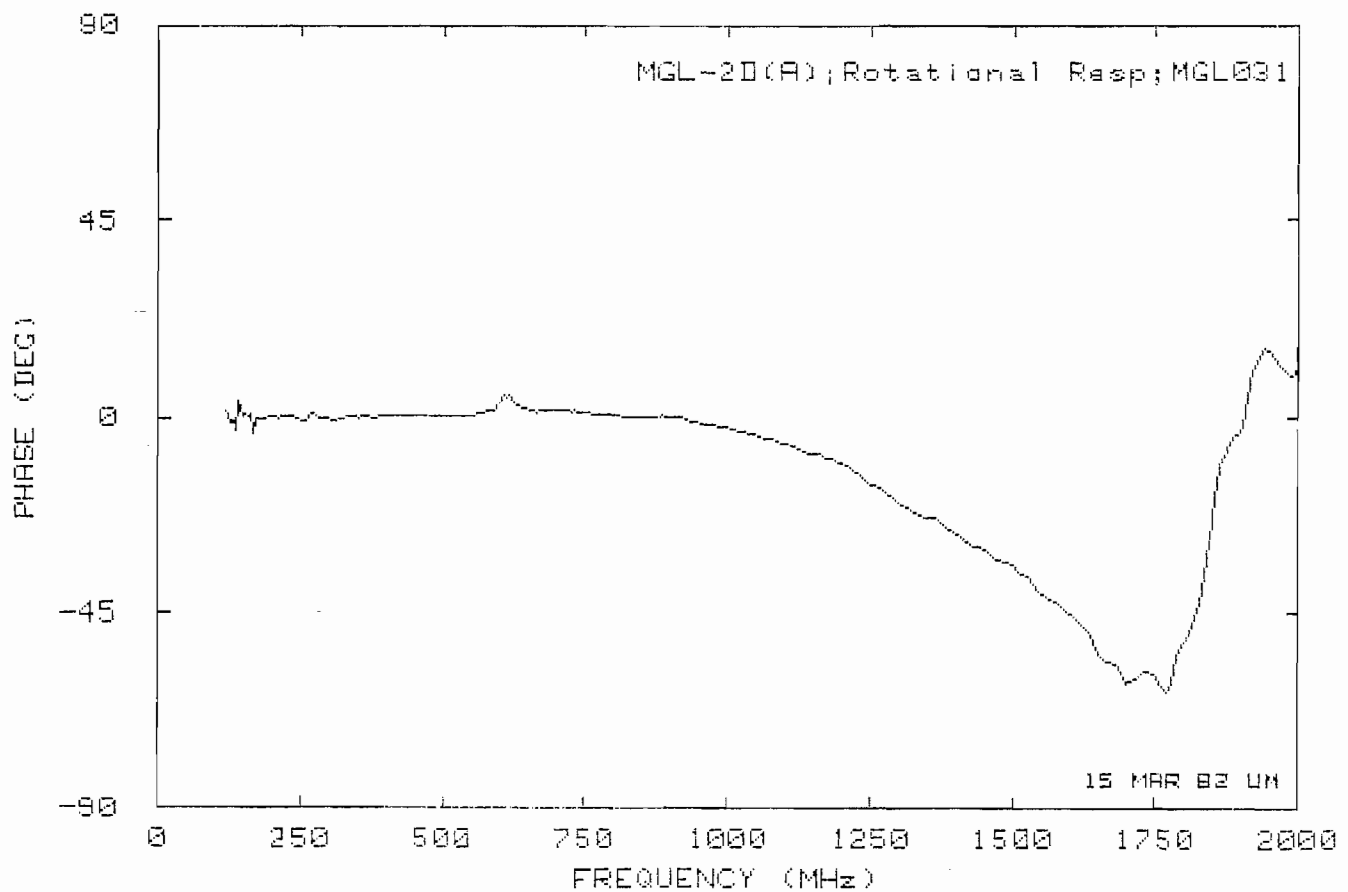
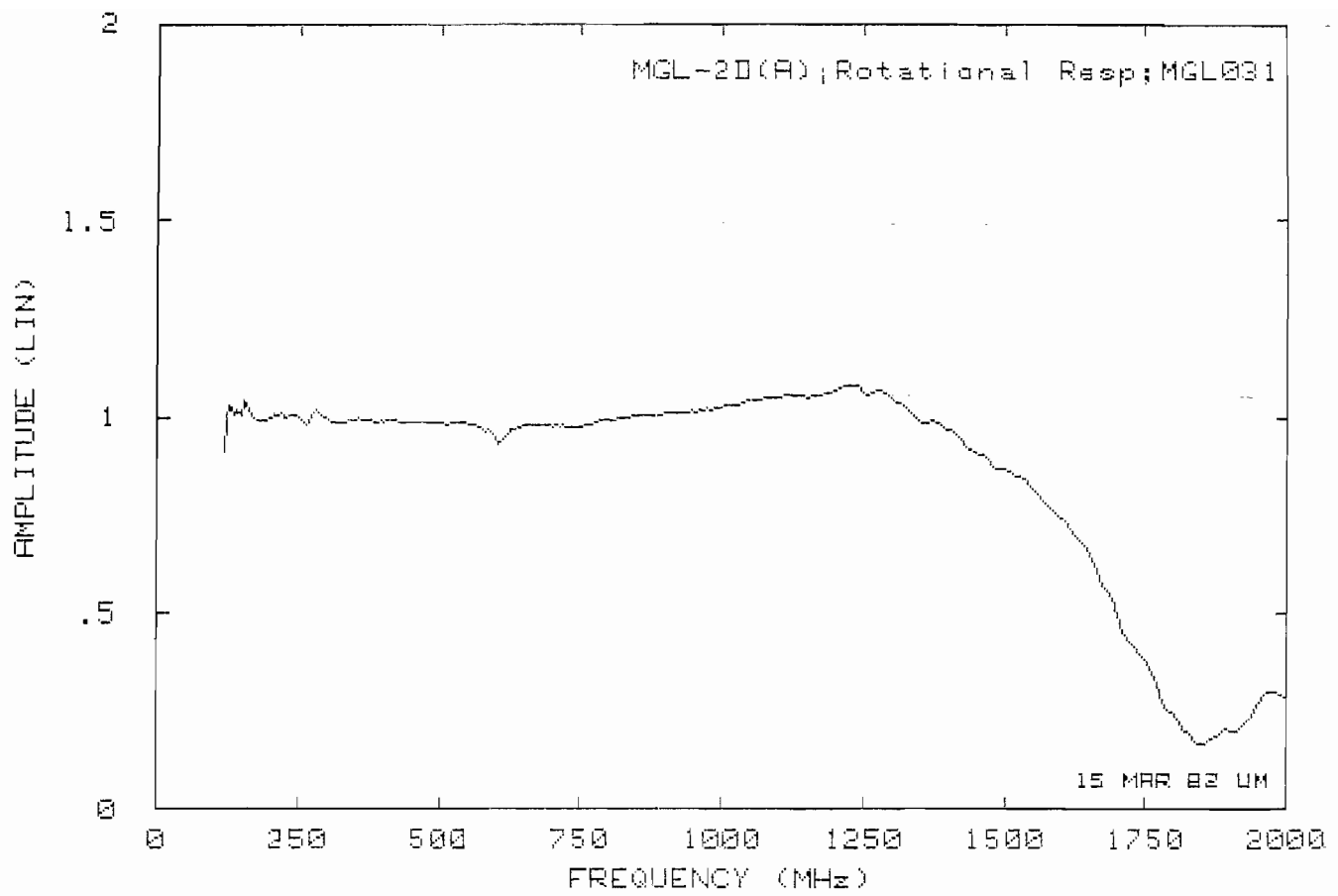


Fig. 43: $B_n(f)$ for MGL-2D(A).

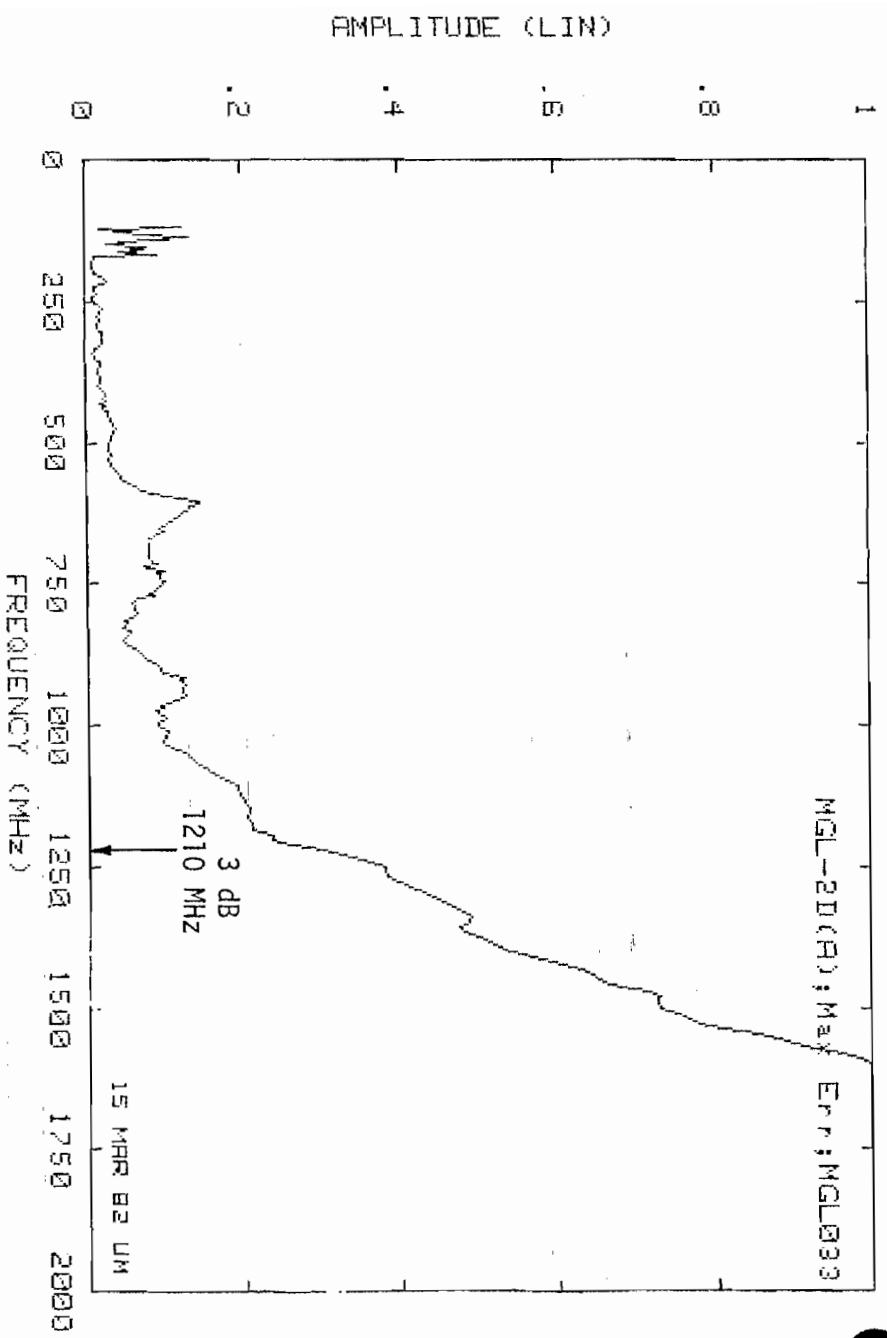
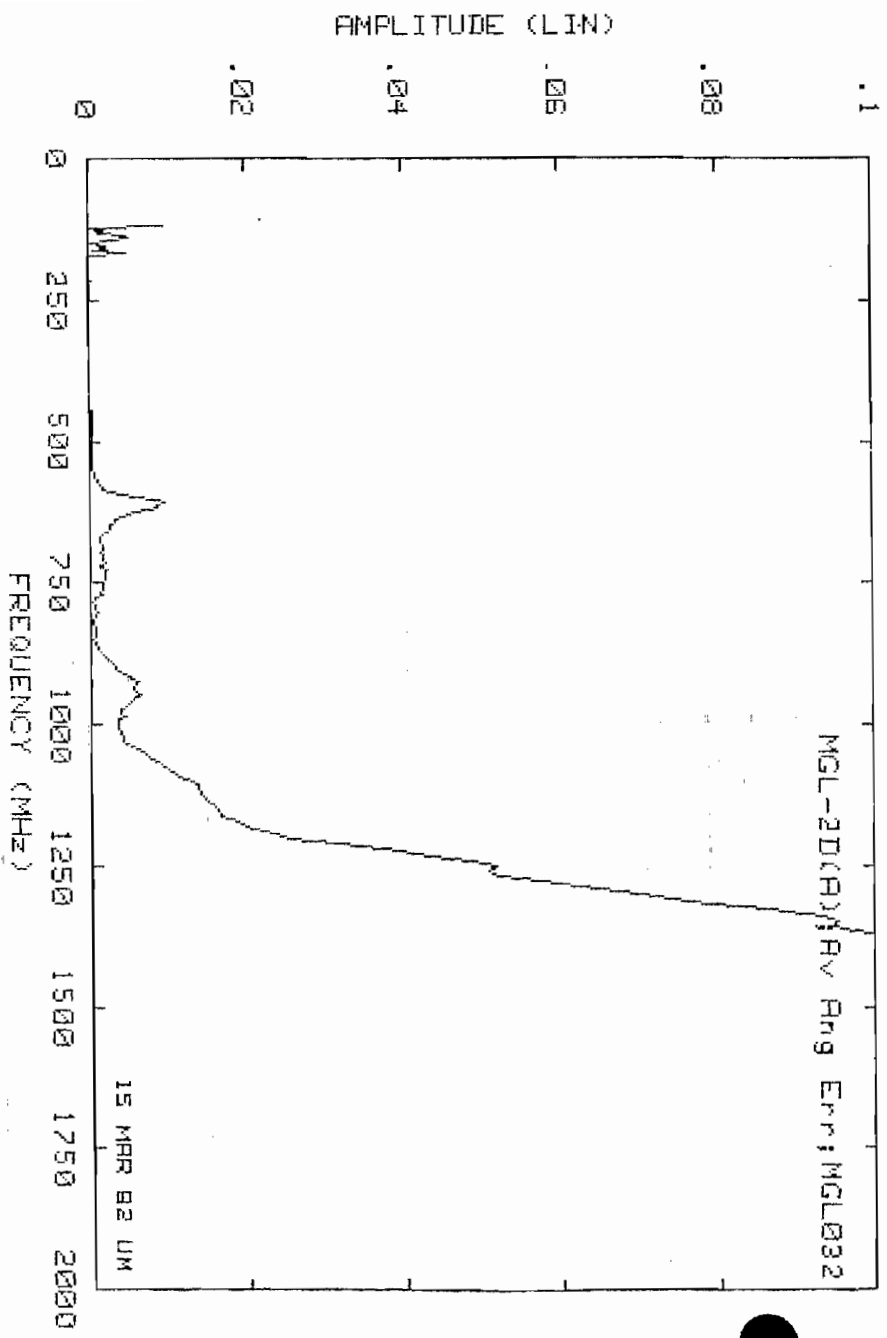


Fig. 44: (top): $\mathcal{E}_r^2(f)$ for MGL-2D(A).

Fig. 45: (bottom): $\mathcal{E}_{r_{max}}(f)$ for MGL-2D(A).

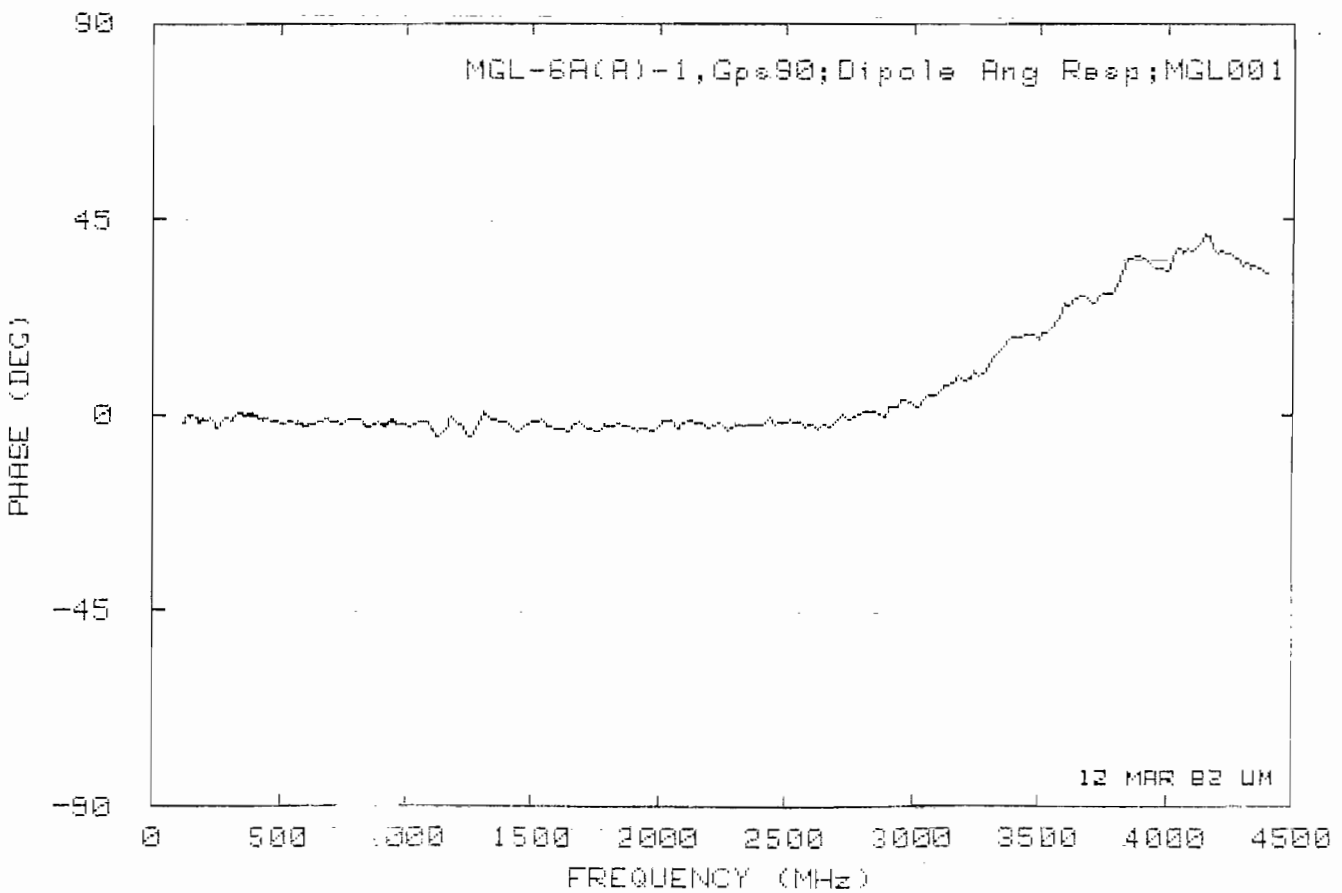
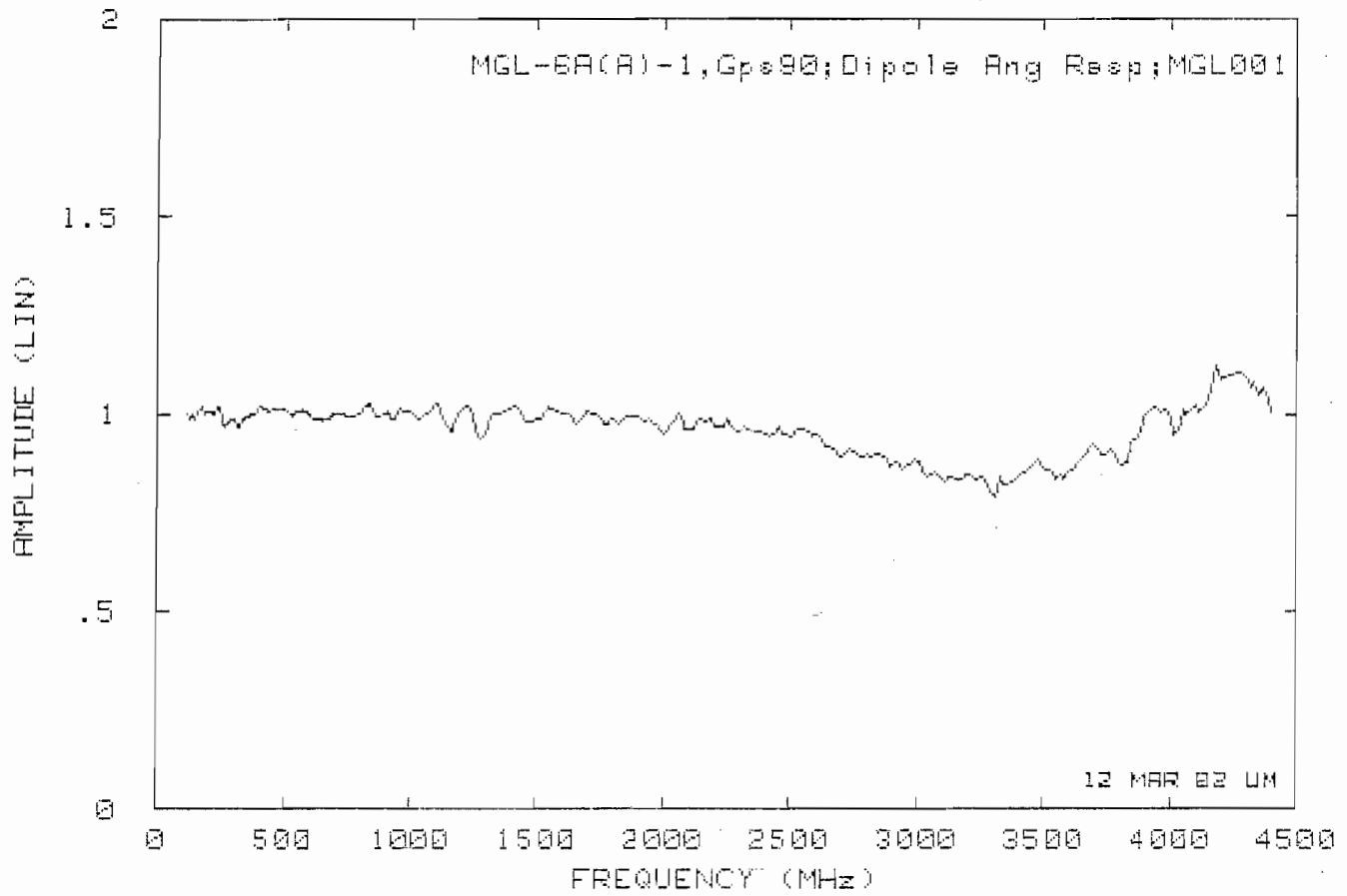


Fig. 46: $A_n(f)$ for MGL-6A(A), gap No. 1 at $\phi = 90^\circ$.

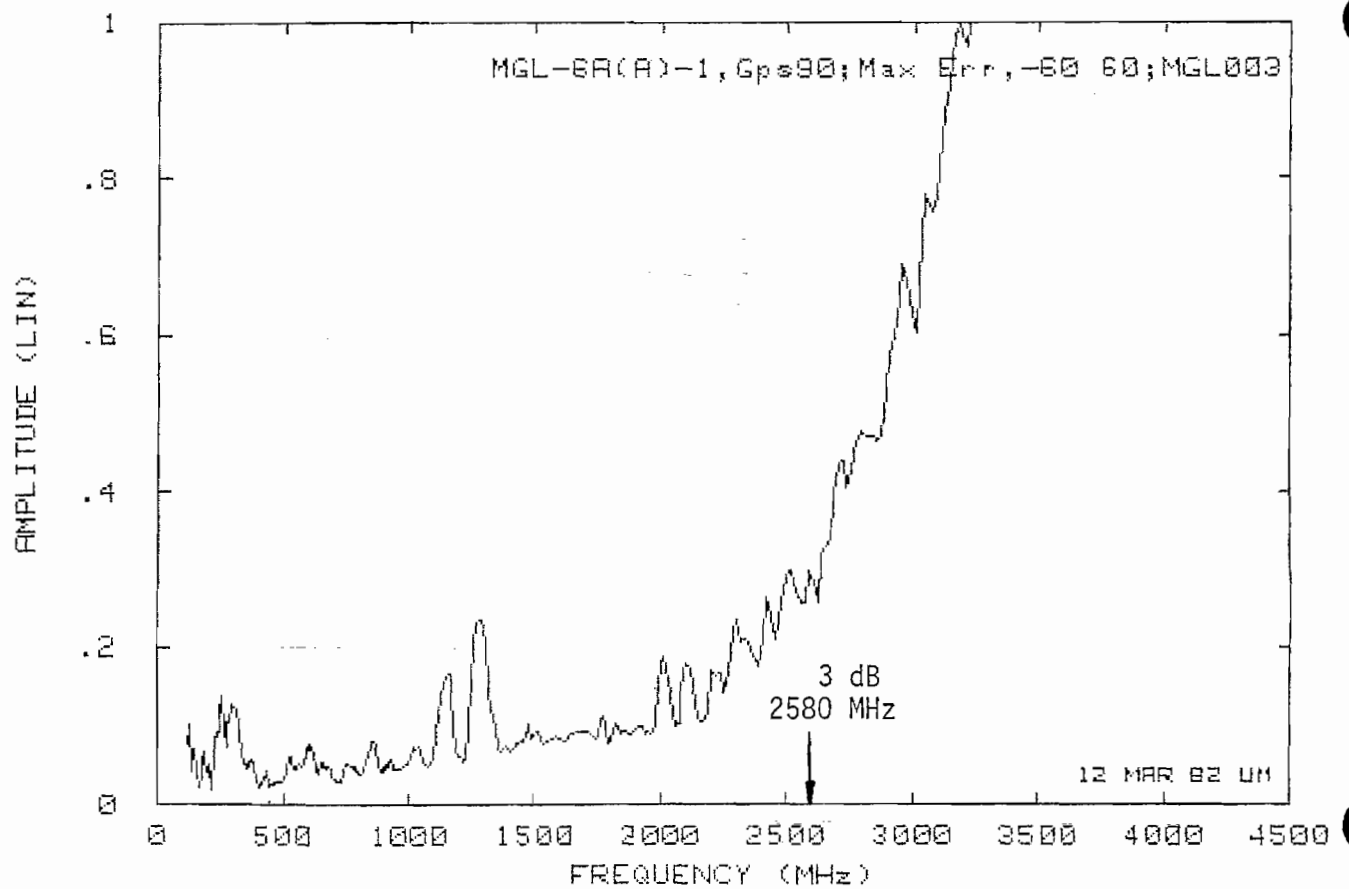
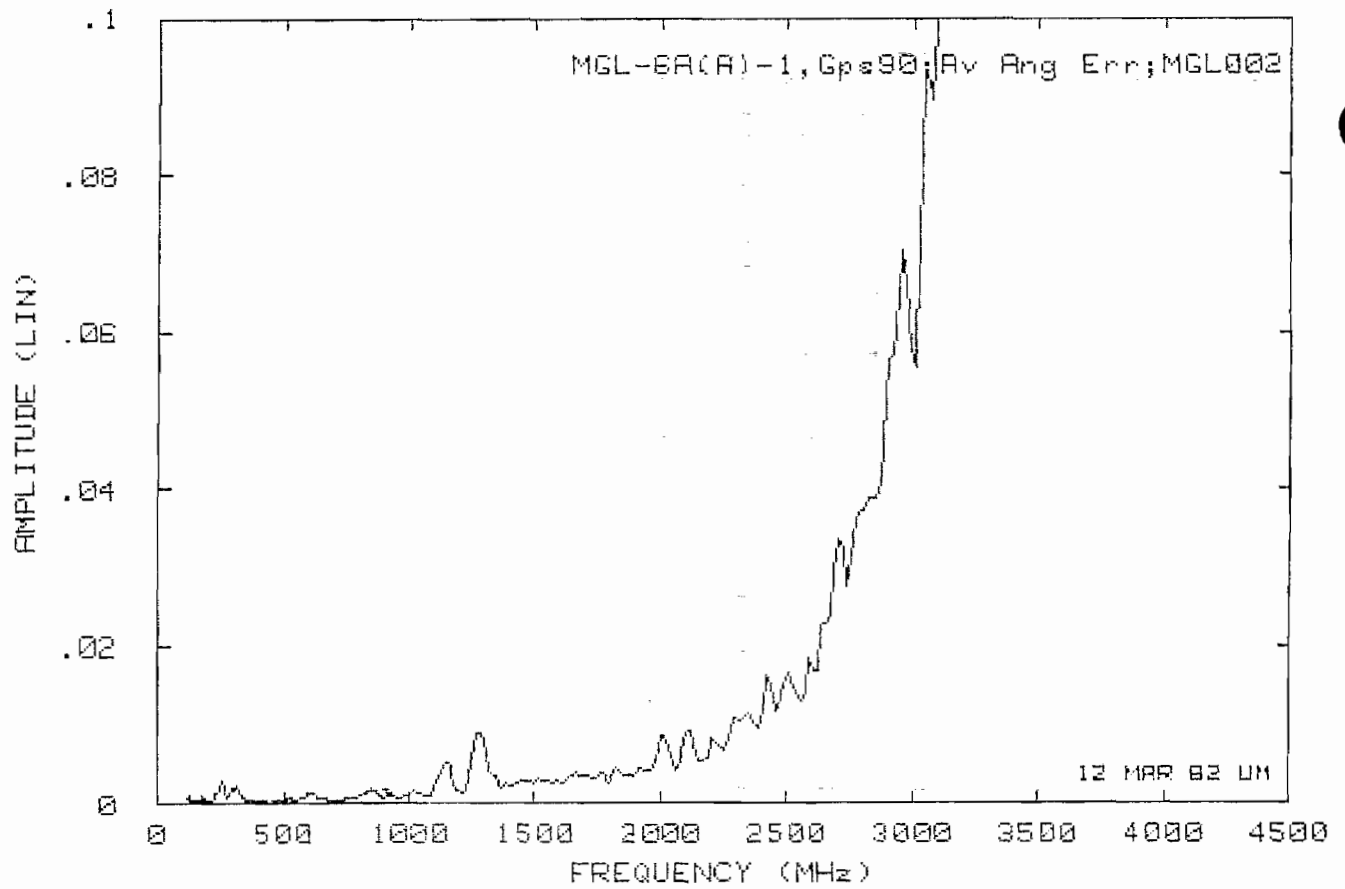


Fig. 47: (top): $\mathcal{E}^2(f)$ for MGL-6(A), gap No. 1 at $\phi = 90^\circ$.

Fig. 48: (bottom): $\mathcal{E}_{\max}(f)$ for MGL-6(A), gap No. 1 at $\phi = 90^\circ, |\theta| \leq 60^\circ$.

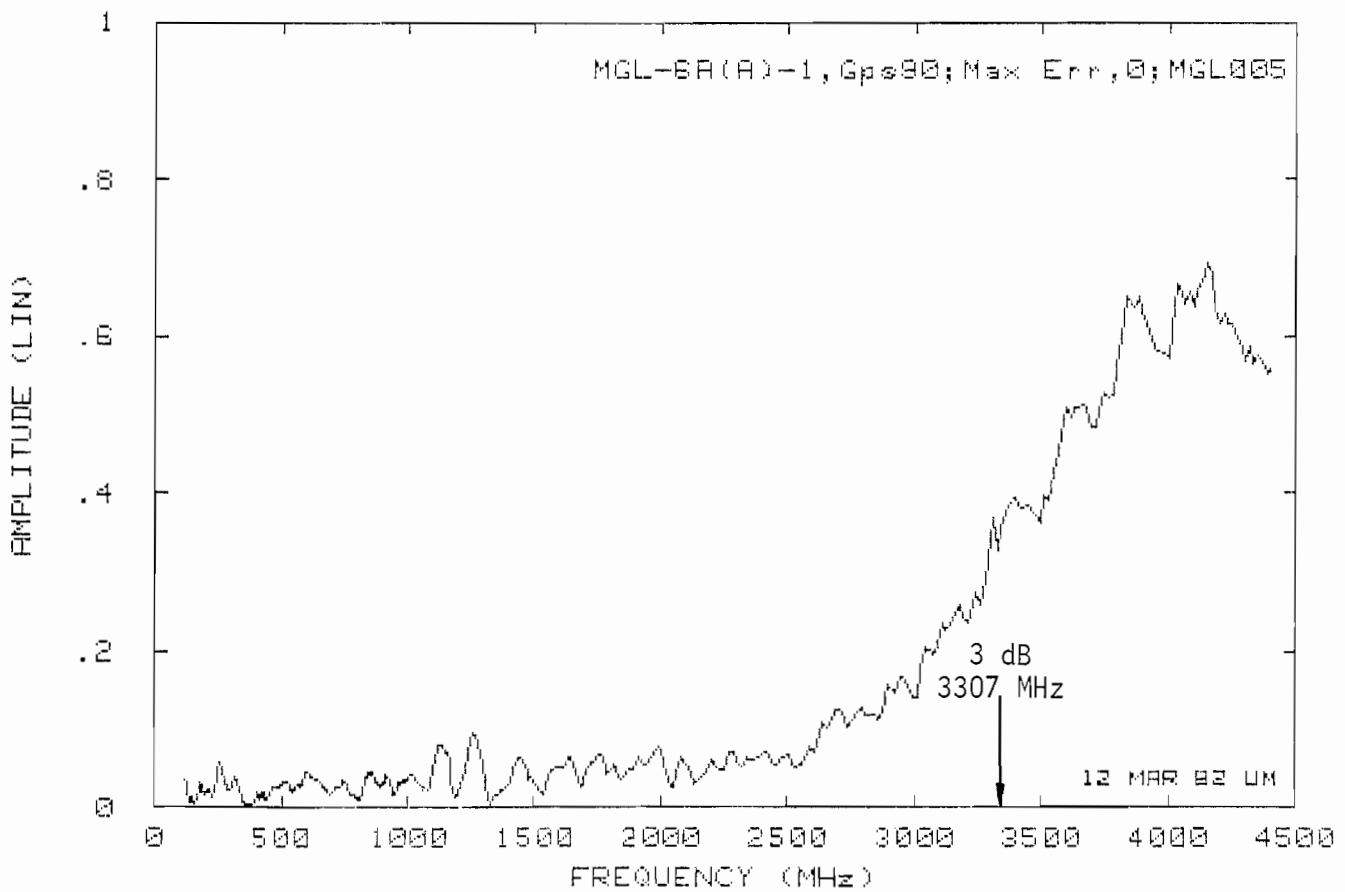
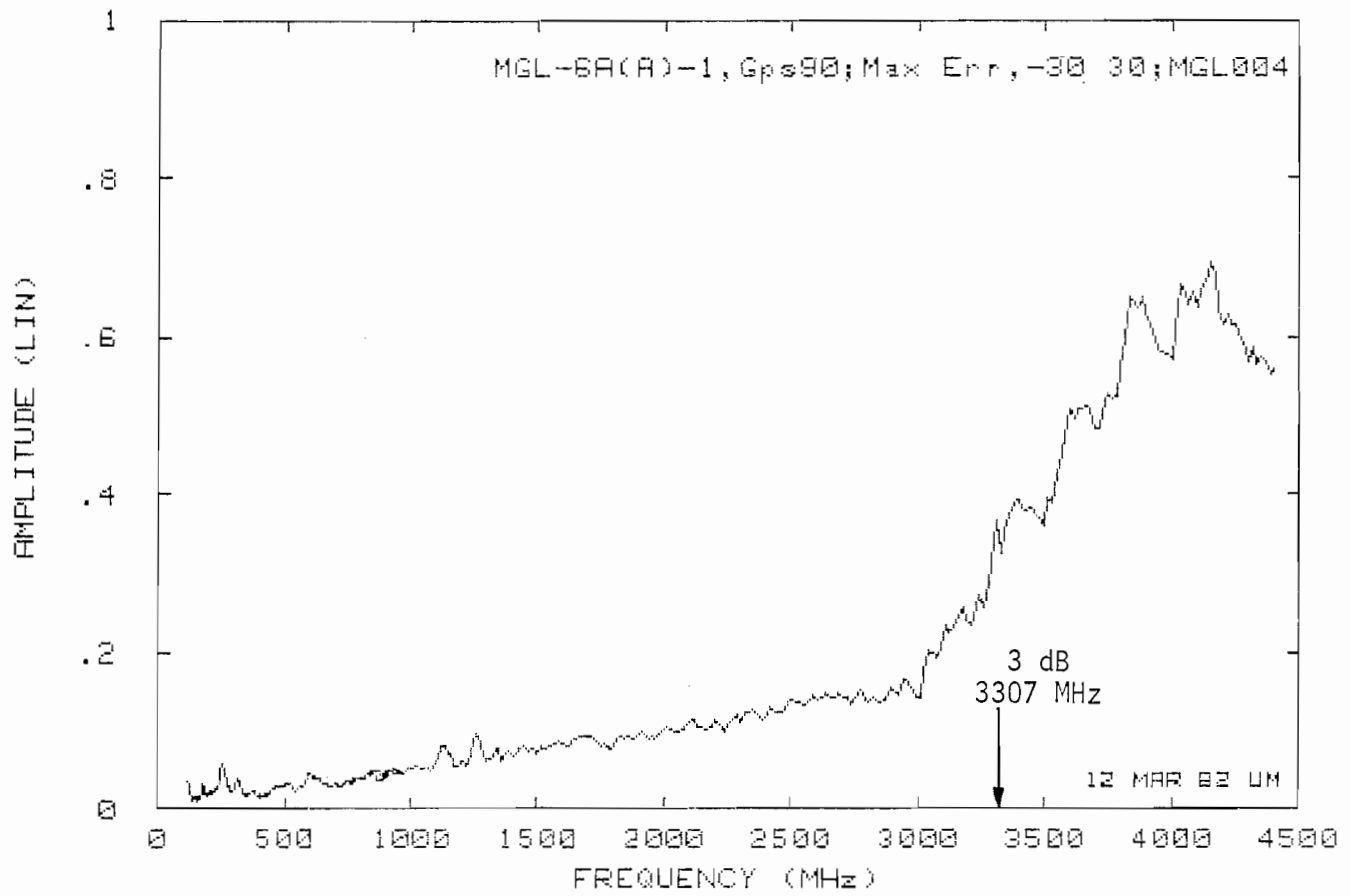


Fig. 49: (top): $\mathcal{E}_{\max}(f)$ for MGL-6A(A), gap No. 1 at 90° , $|\theta| \leq 30^\circ$.

Fig. 50: (bottom): $\mathcal{E}_{\max}(f)$ for MGL-6A(A), gap No. 1 at 90° , $\theta = 0^\circ$

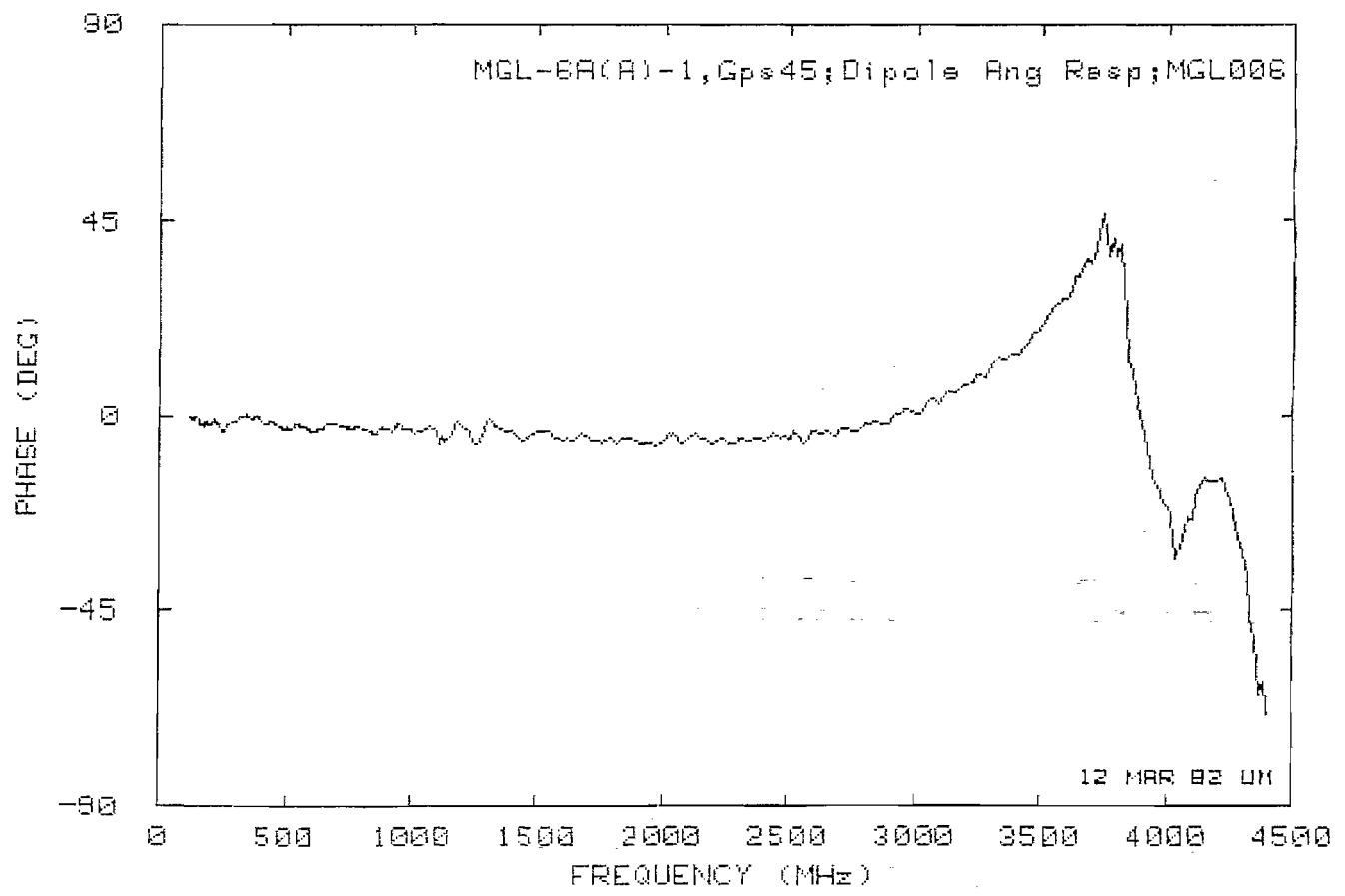
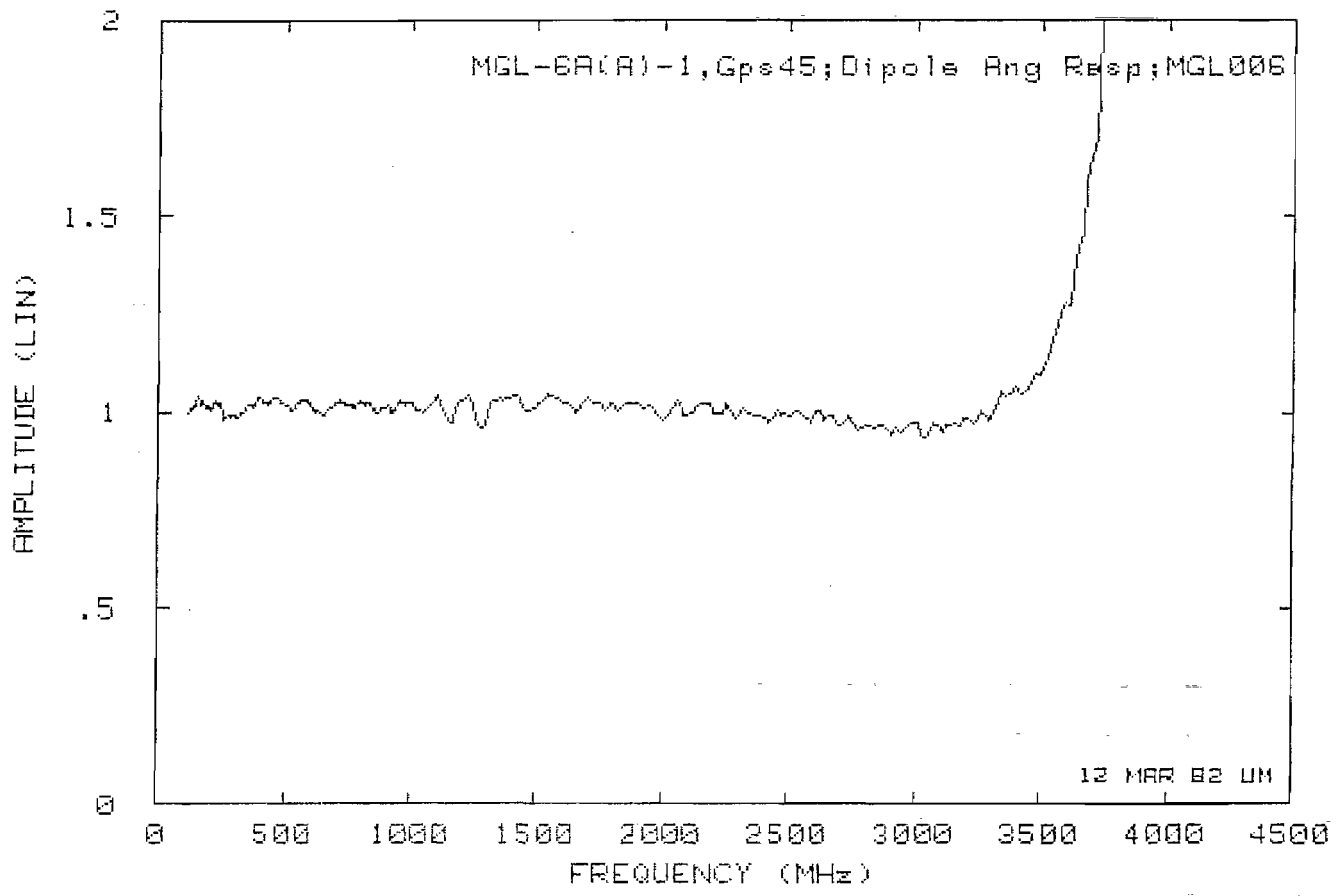


Fig. 51: $A_n(f)$ for MGL-6A(A), gap No. 1 at $\phi = 45^\circ$.

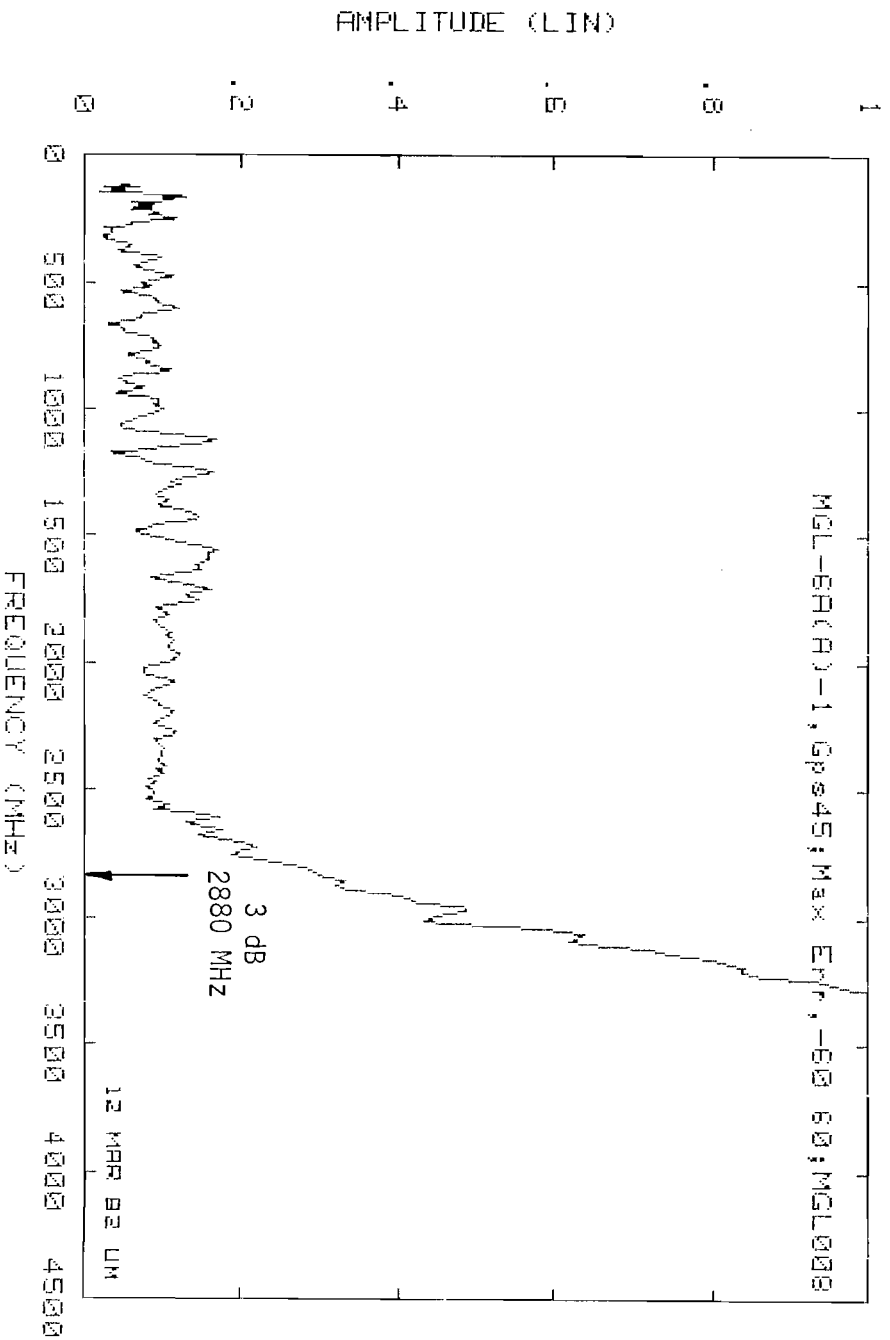
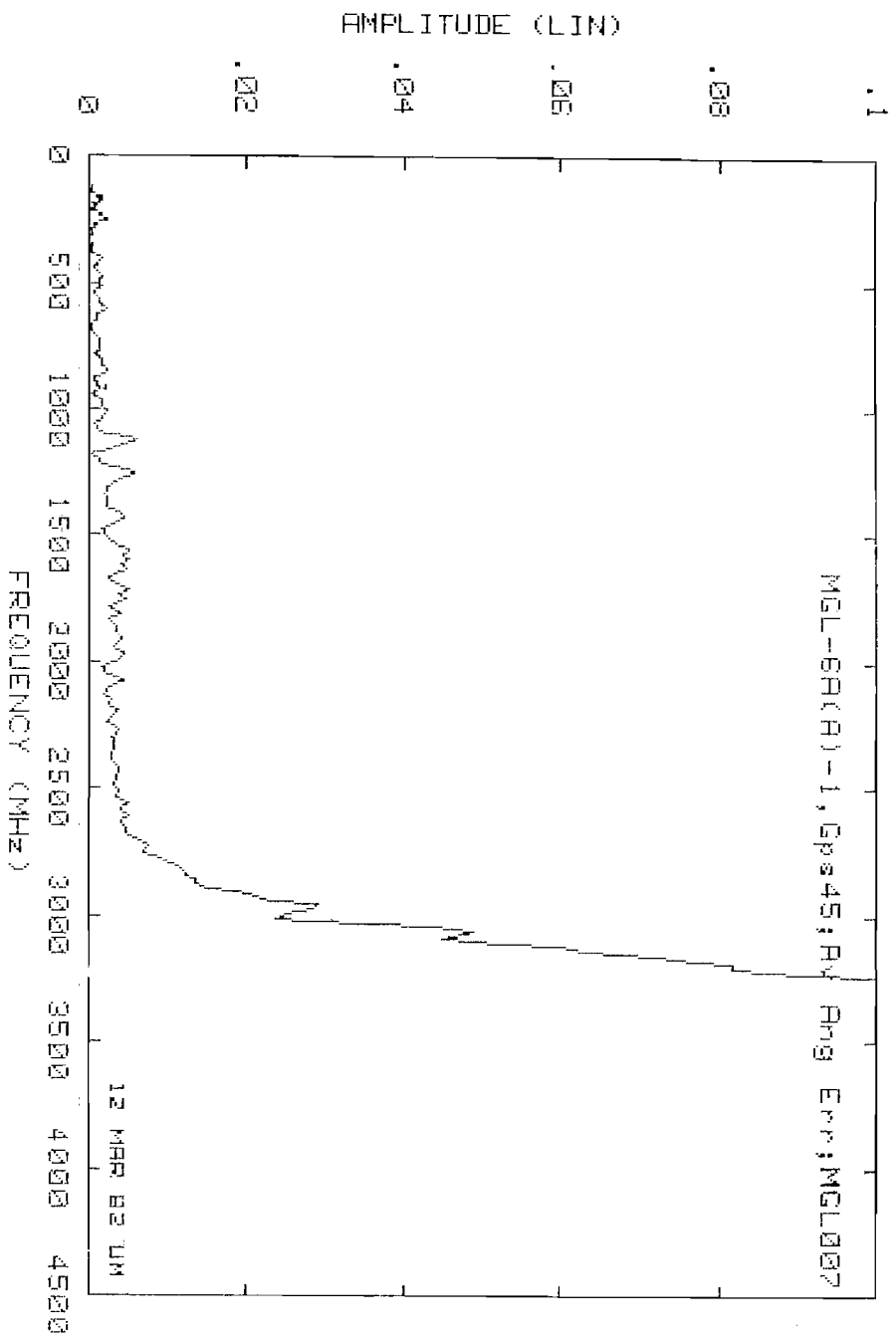


Fig. 52: (top): $\mathcal{E}^2(f)$ for MGL-6A(A), gap No. 1 at $\phi = 45^\circ$

Fig. 53: (bottom) $\mathcal{E}_{\max}(f)$ for MGL-6A(A), gap No. 1 at $\phi = 45^\circ$, $|\theta| \leq 60^\circ$.

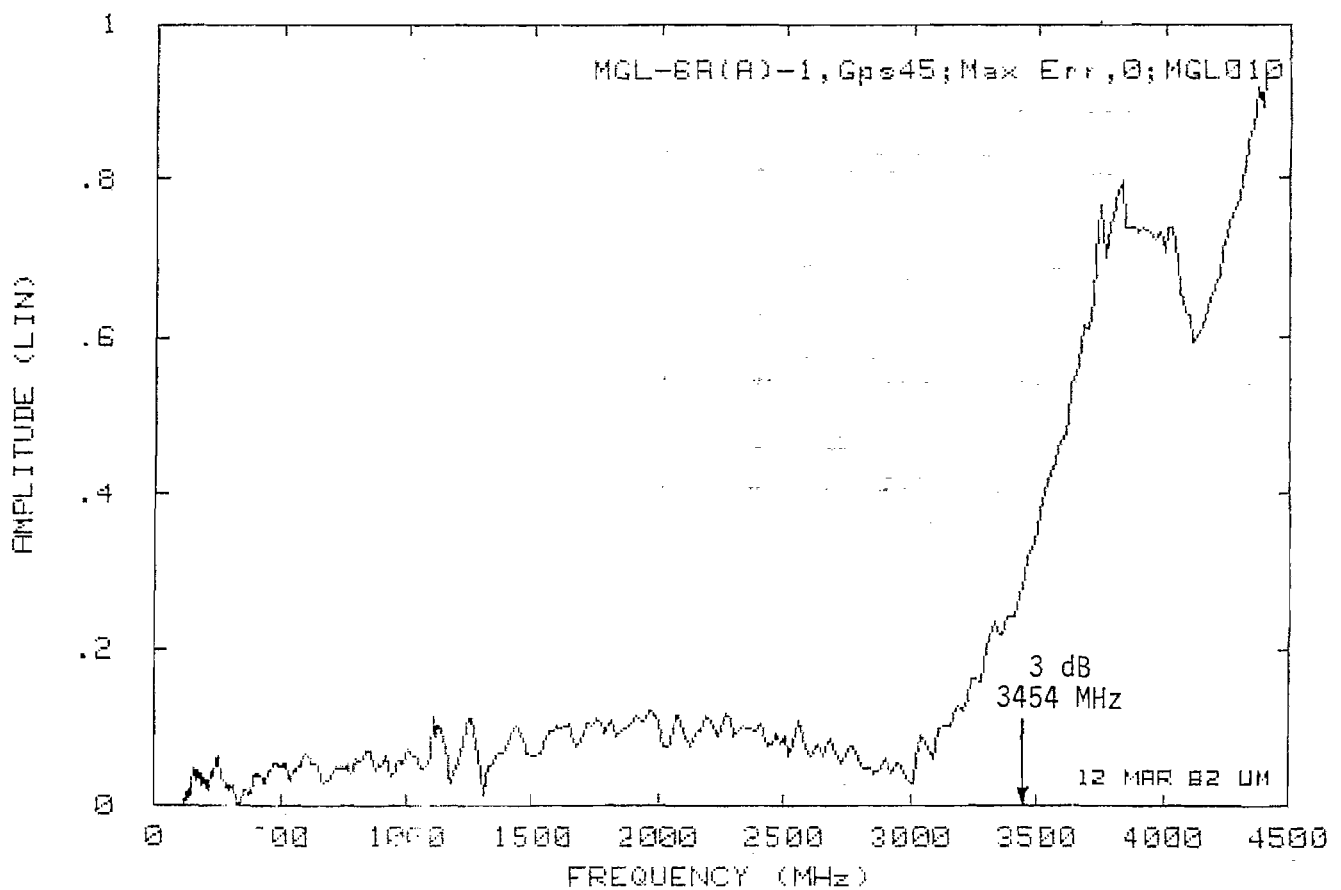
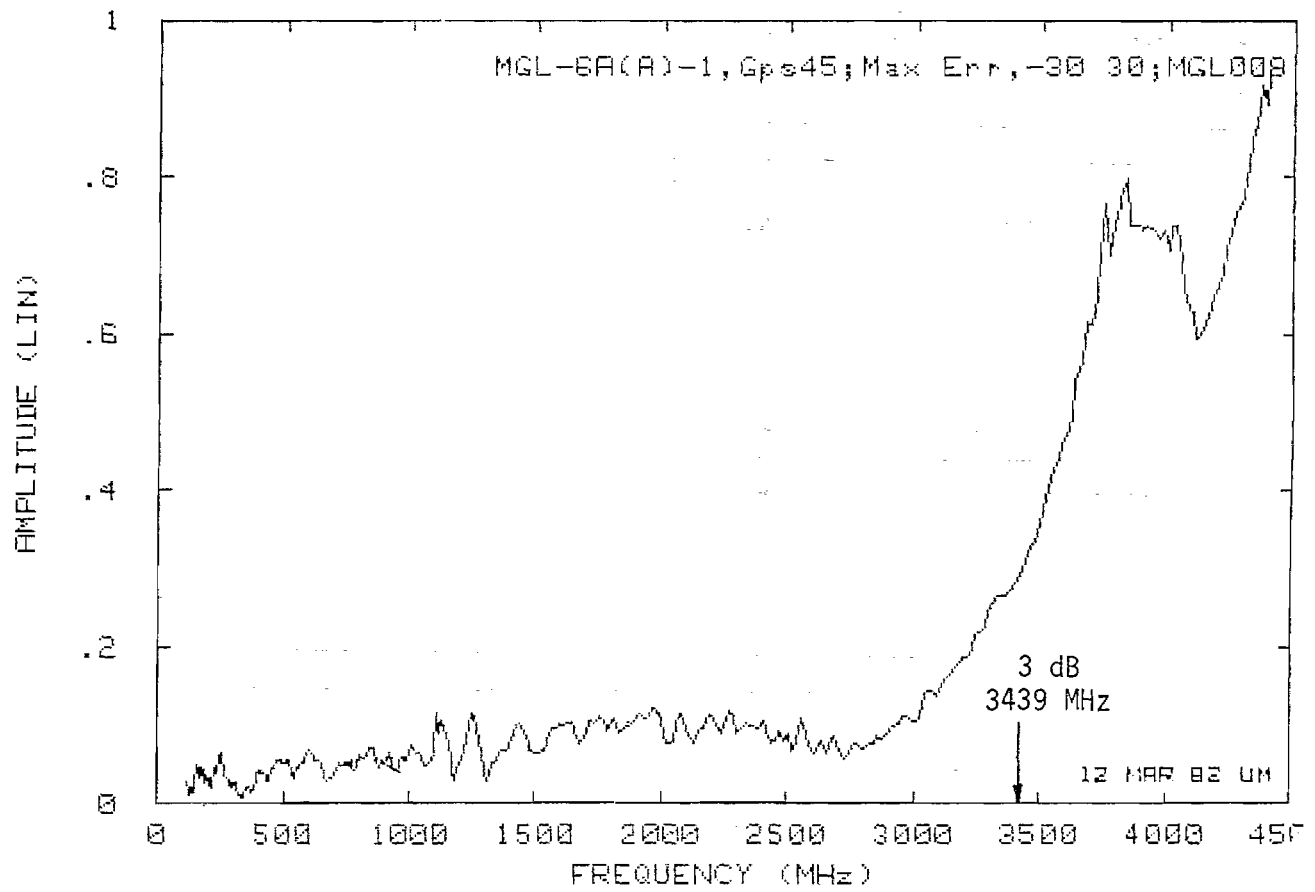


Fig. 54: (top): $\mathcal{E}_{\max}(f)$ for MGL-6A(A), gaps at $\phi = 45^\circ$, $|\theta| \leq 30^\circ$.

Fig. 55: (bottom): $\mathcal{E}_{\max}(f)$ for MGL-6A(A), gaps at $\phi = 45^\circ$, $\theta = 0^\circ$.

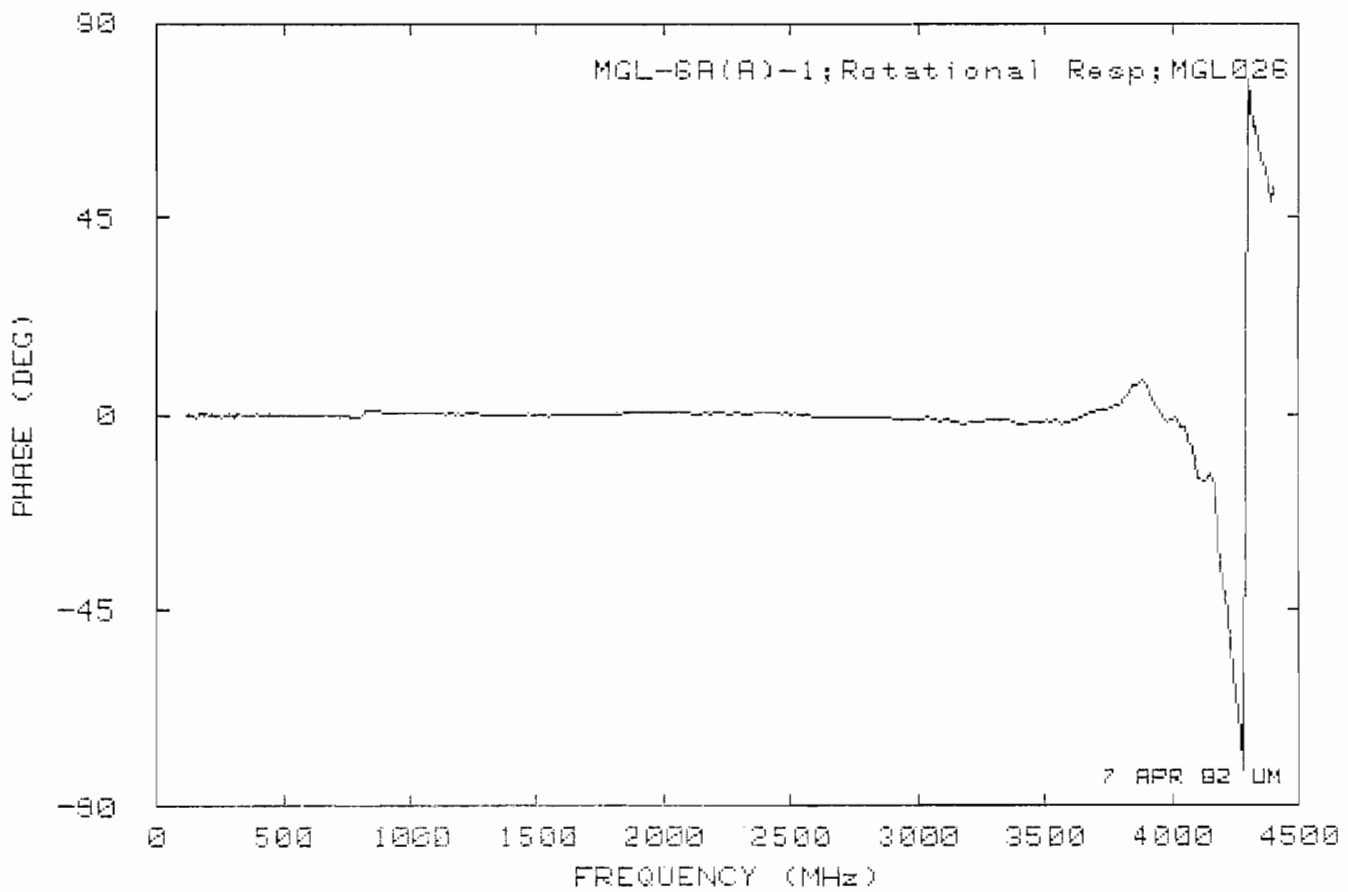
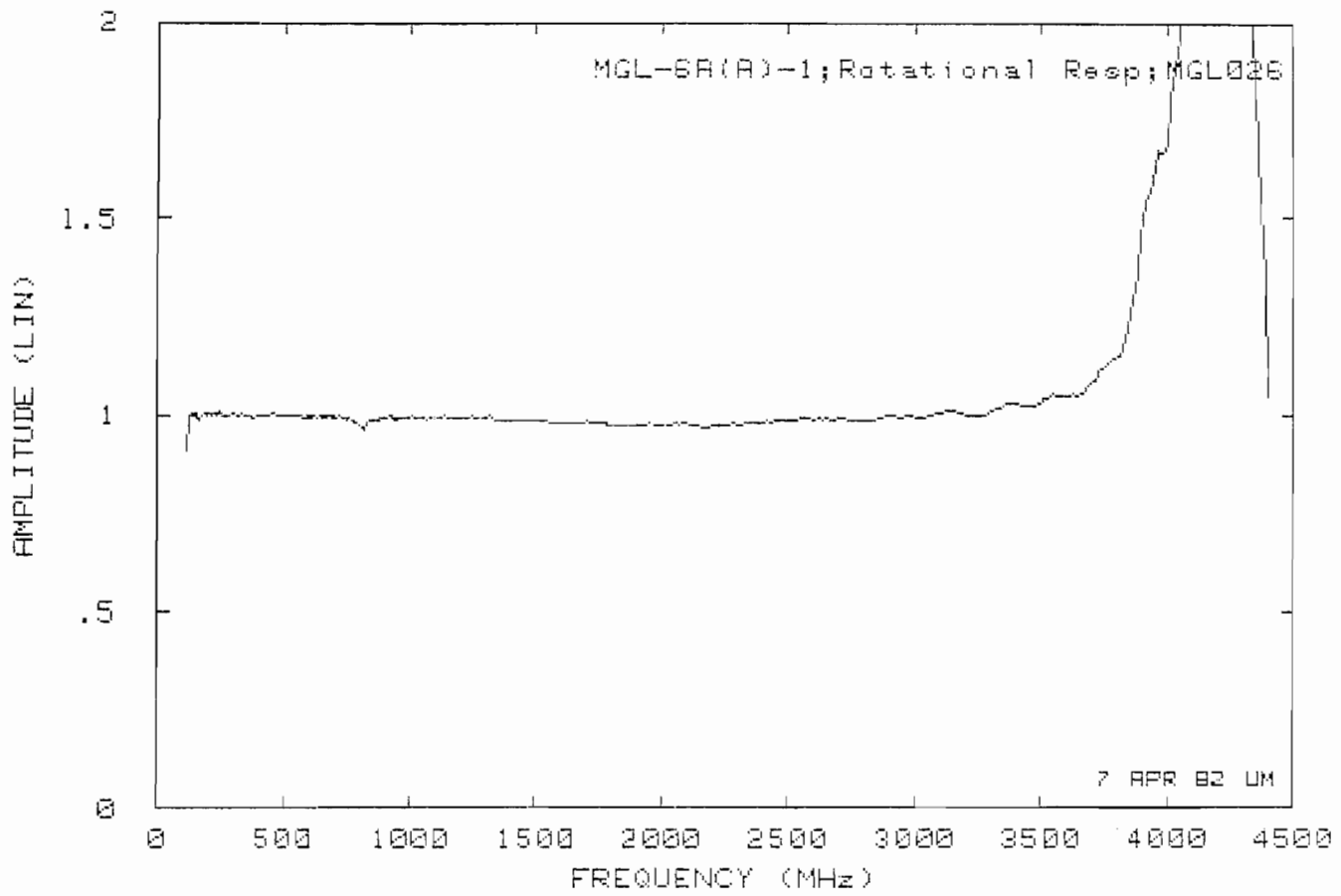


Fig. 56: $B_n(f)$ for MGL-6A(A).

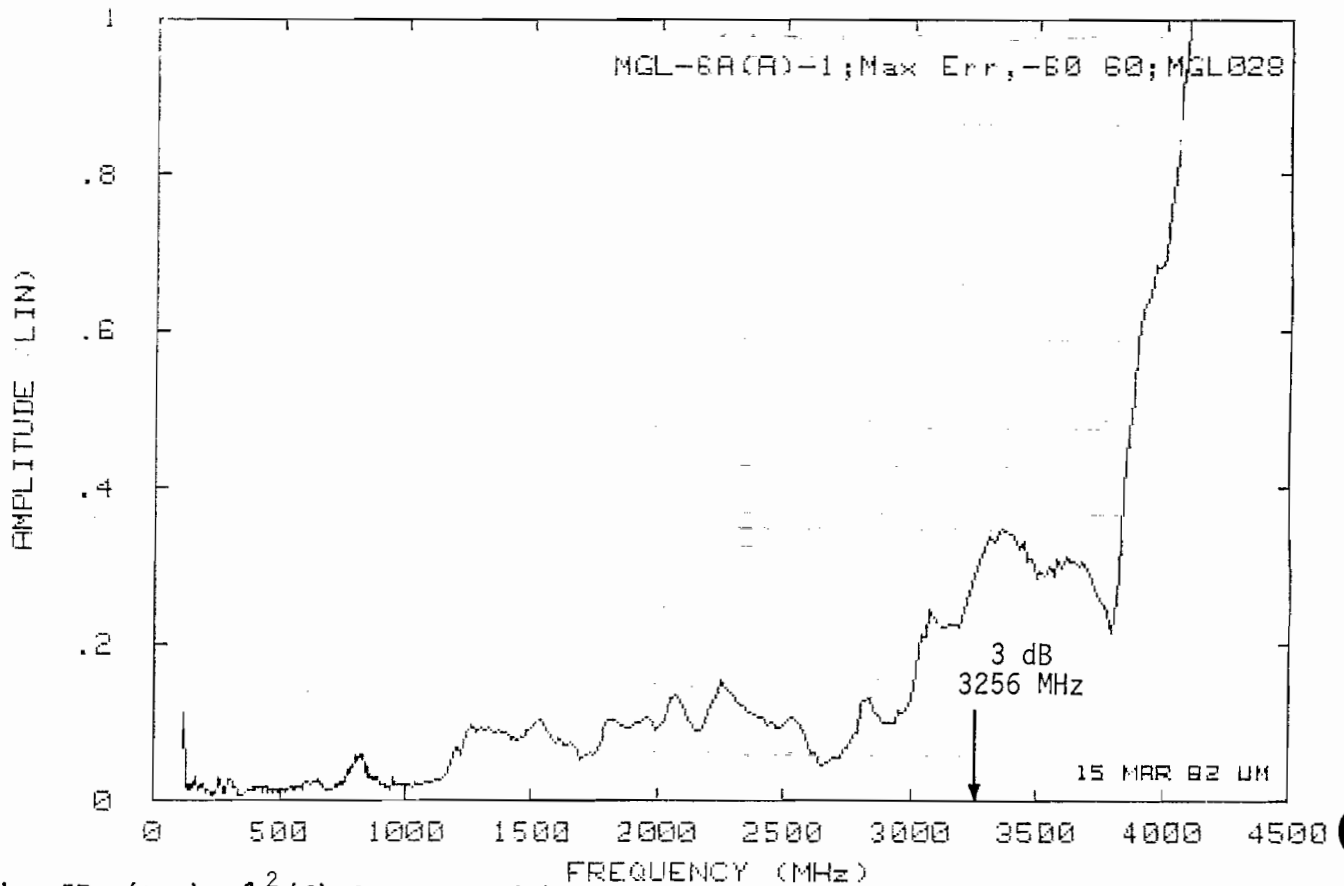
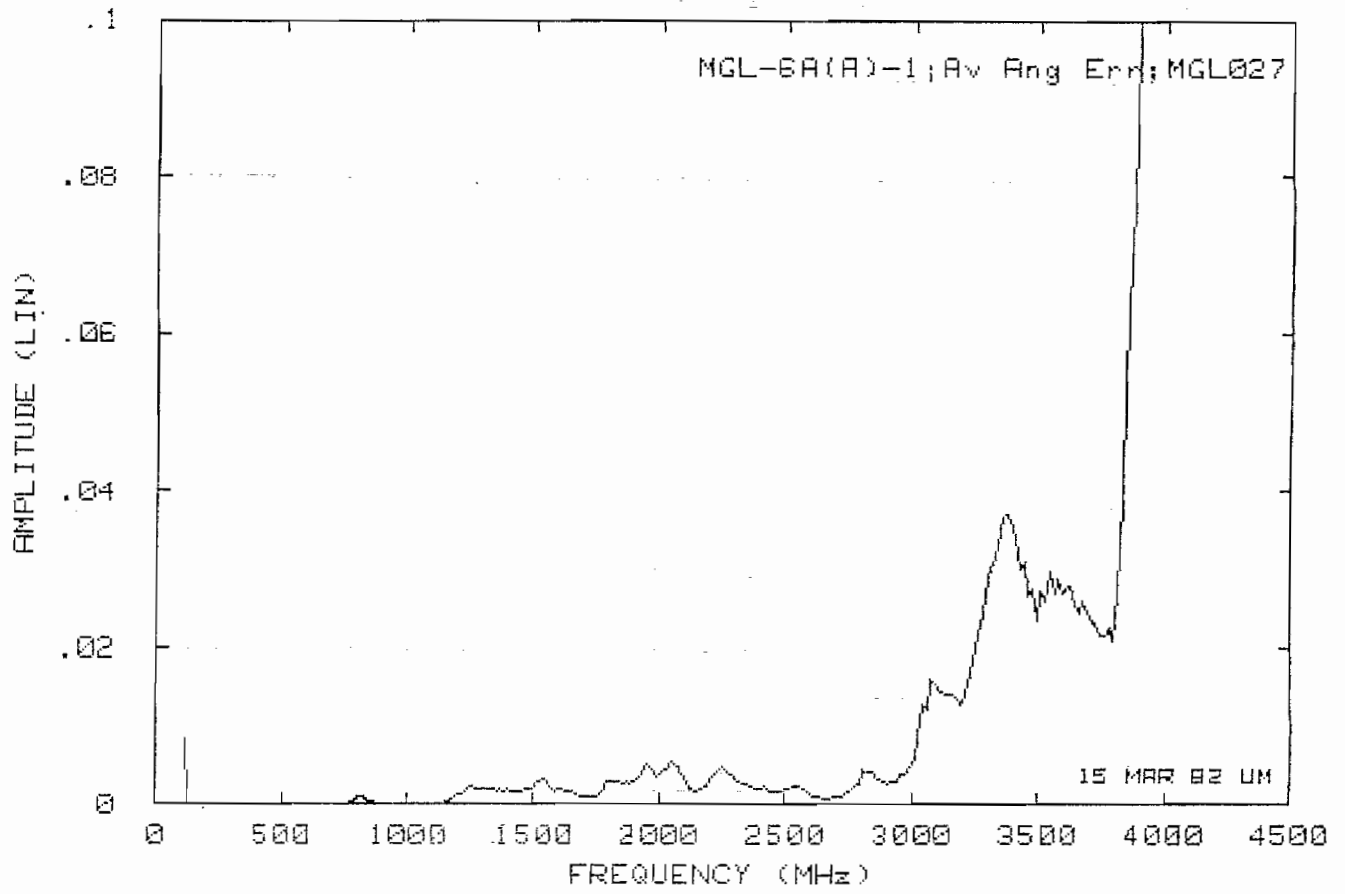


Fig. 57: (top): $\mathcal{E}_r^2(f)$ for MGL-6A(A).

Fig. 58: (bottom): $\mathcal{E}_{r \max}(f)$ for MGL-6A(A).

5.5 Frequency Response Data Analysis

The normalization of the data in Section 5.4 eliminated the effects of many of the cable mismatches, but also removed the true variation with frequency. We now seek this information for the MGL-2, MGL-4 and ACD-4 sensors.

With the sensor oriented for maximum signal the response was recorded for each of the above three sensors as well as for the two calibration sensors. To minimize any errors resulting from changes in the equipment and/or chamber, the measurements were carried out in as short an interval of time as possible. We include here four curves representative of the more than 60 measurements that were performed. In some instances the data were clearly of unacceptable accuracy and were discarded, and where appropriate we have averaged (or combined) two sets of data to produce the curves presented.

Figure 59 shows the response of the ACD-2 sensor normalized with respect to the MGL-9 response. Both are miniature sensors with 3-dB roll-off frequencies of 7.5 and 10 GHz, respectively, and the ratio of their responses should therefore be constant over the measured range of frequencies. It is not. At low frequencies the ratio oscillates around the constant value of approximately 1.25 (compared with the theoretical value 1.33), but for frequencies exceeding about 1600 MHz the oscillation is about a linearly increasing function of frequency. We have no explanation for this increase, and since the effect of cable losses was eliminated by referencing the responses to the output terminals at the sensors, the increase cannot be attributed to this.

For the other (ACD-4, MGL-2 and MGL-4) sensors, the voltages were referenced to the twinaxial connectors and the phase data adjusted by adding a constant multiple of the frequency (equivalent to a delay) to produce the required constant phase at low frequencies.

Figure 60 shows the ratio of the ACD-4 response to that of the ACD-2. If the latter is presumed linear out to 2000 MHz, the curves serve to define the frequency response of the ACD-4. At low frequencies the measured ratio averages 120 compared with the theoretical value 100, but decreases starting at about 800 MHz. The 3-dB roll-off frequency is 1096 MHz, which is consistent with the manufacturer's specification of >750 MHz. The response of the MGL-2 sensor normalized to that of the MGL-9 is shown in Fig. 61. The low frequency ratio is estimated to be 400 and the 3-dB roll-off frequency is 482 MHz. The corresponding values listed by the manufacturer are 500 and >300 MHz.

Finally, Fig. 62 shows the ratio of the MGL-6 and MGL-9 responses, and illustrates the type of difficulty encountered throughout this study. The fact is that a twinaxial system (cables, connectors, baluns, etc.) is not adequate above 100 MHz. The oscillations that are seen are attributable [6] to the MGL-6 geometry, including the handle, and the other model (serial No. 2) of this sensor showed the same behavior. The low frequency ratio is estimated to be 40 compared with the theoretical value 50, and the measured 3-dB roll-off frequency is 1940 (c.f. >1800 MHz).

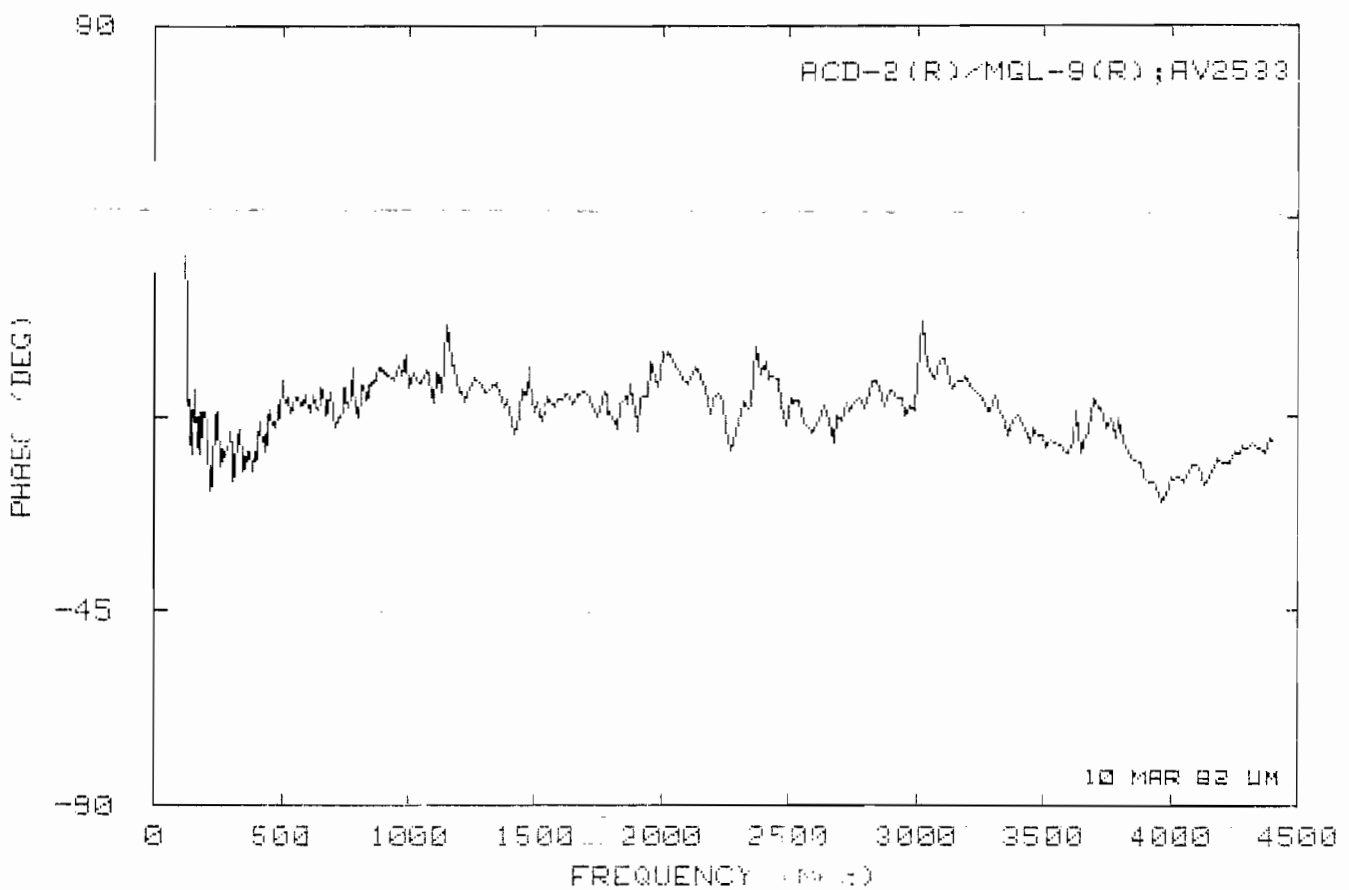
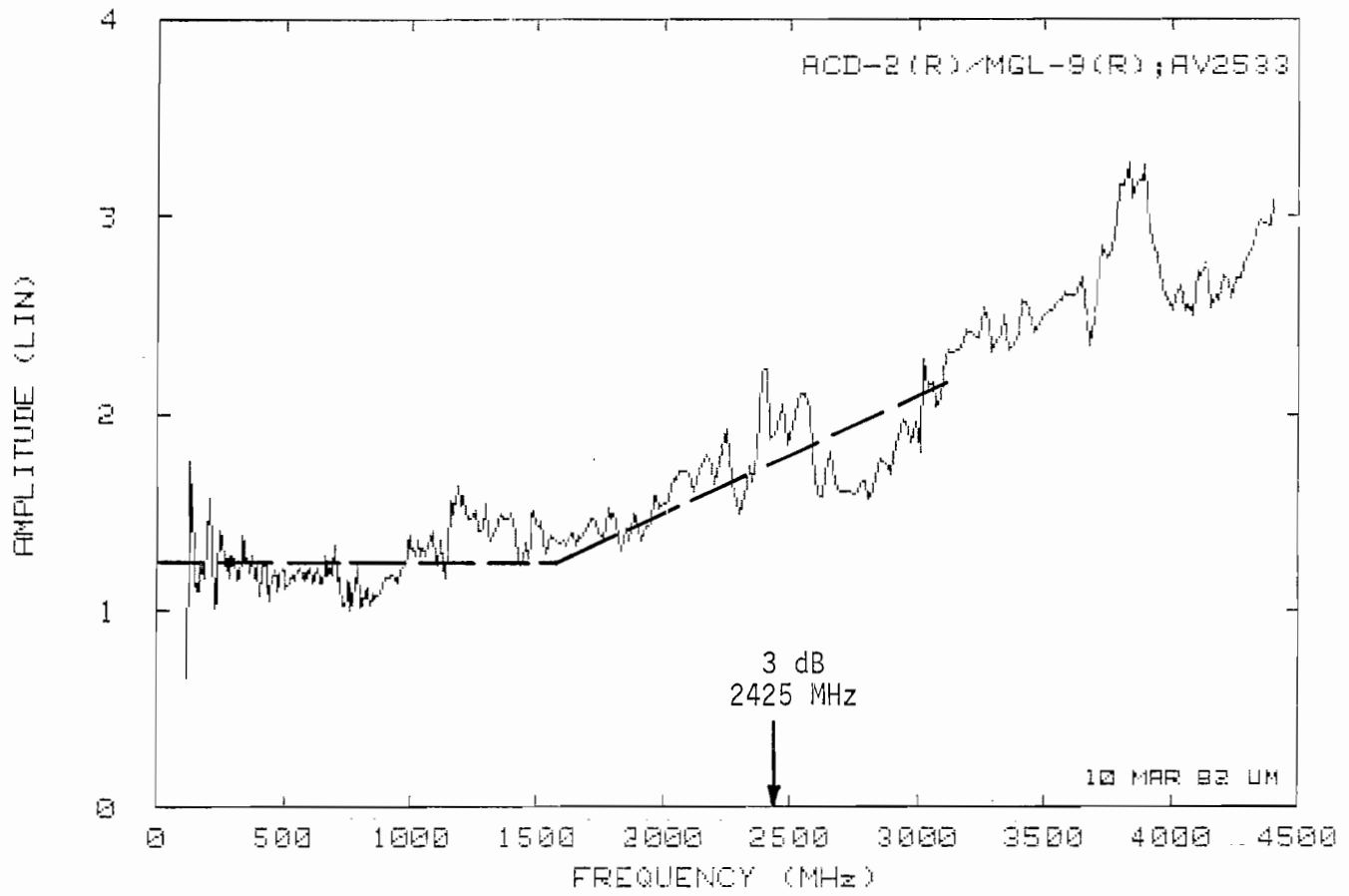


Fig. 59: Response ratio of ACD-2/MGL-9.

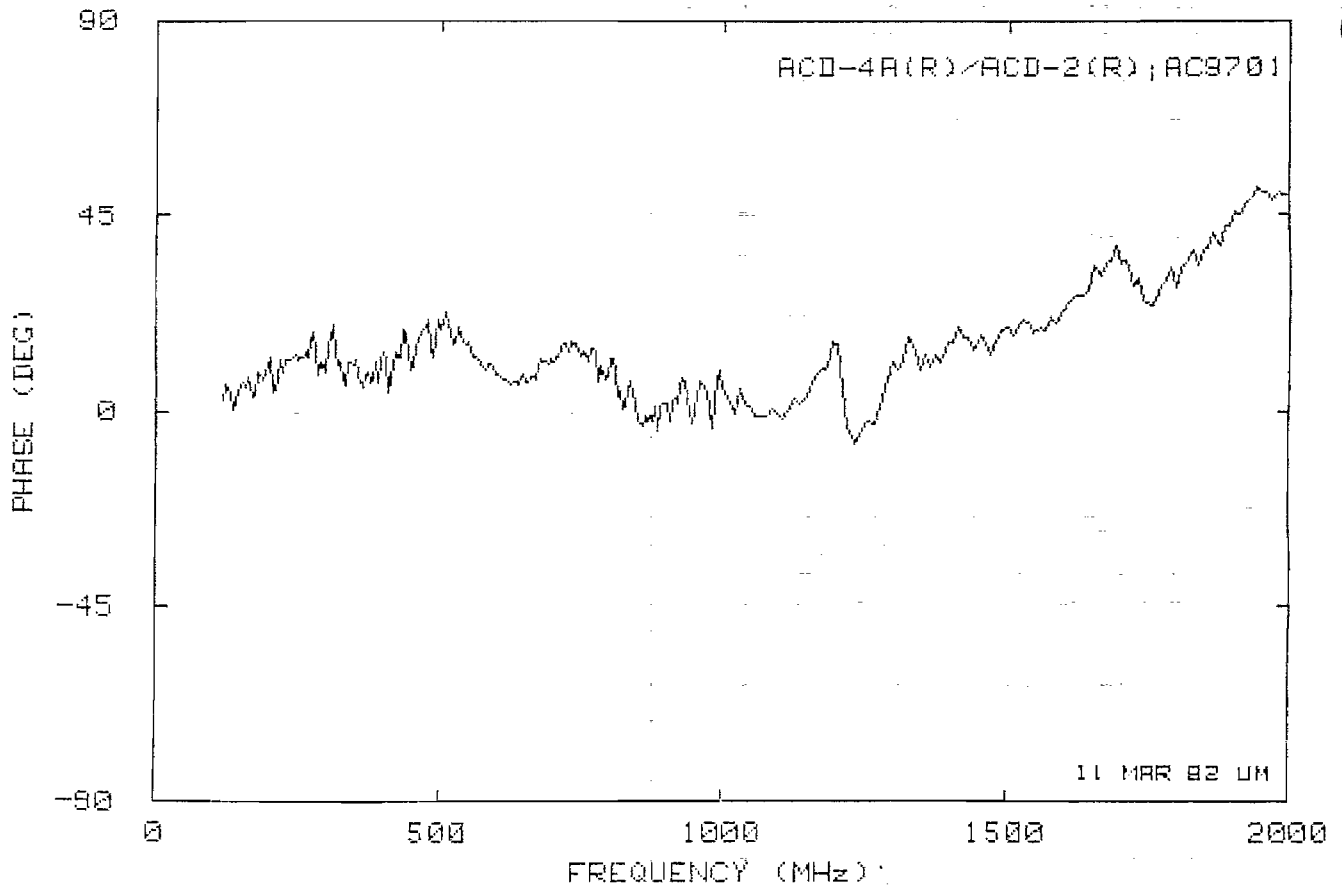
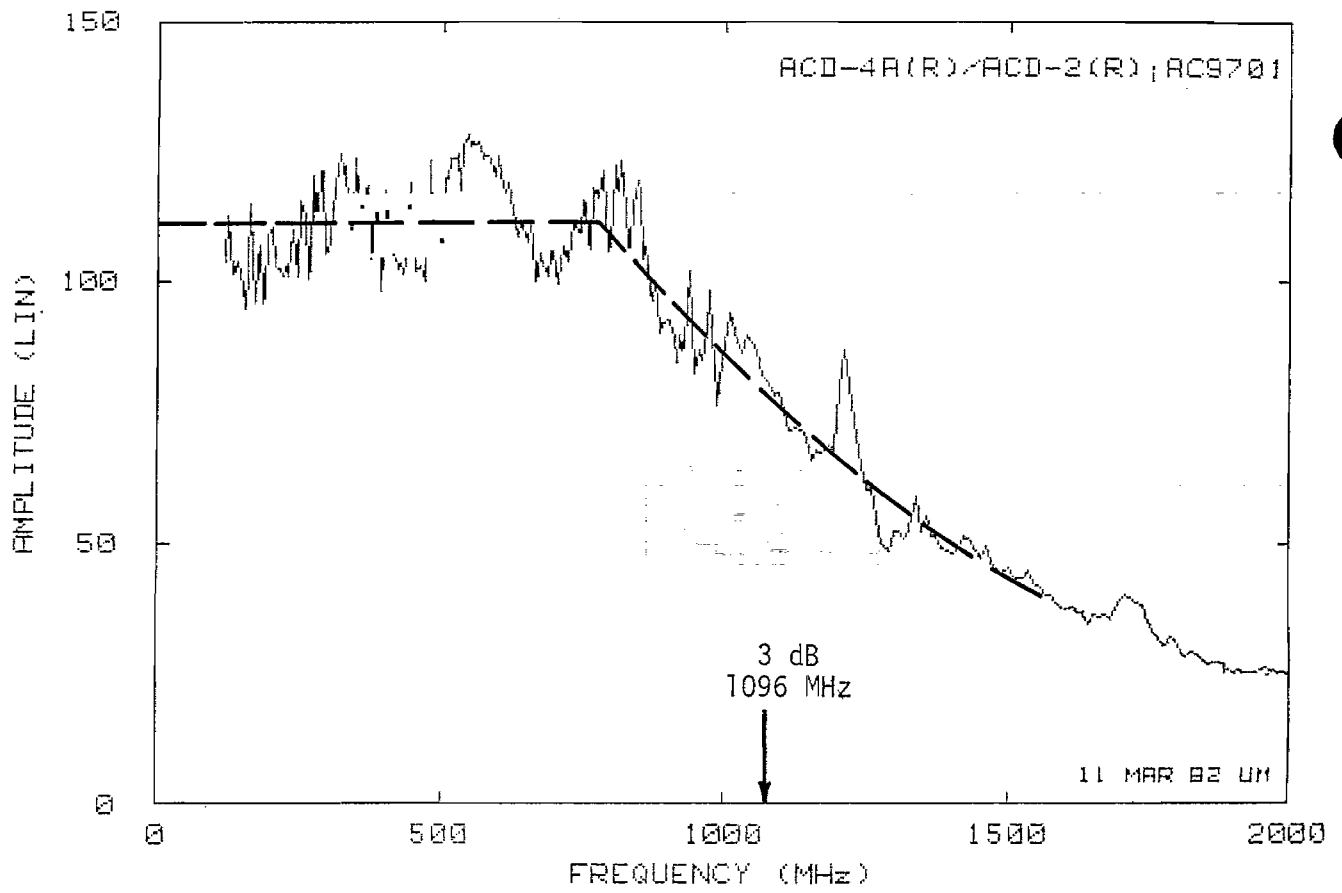


Fig. 60: Response ratio of ACD-4/ACD-2.

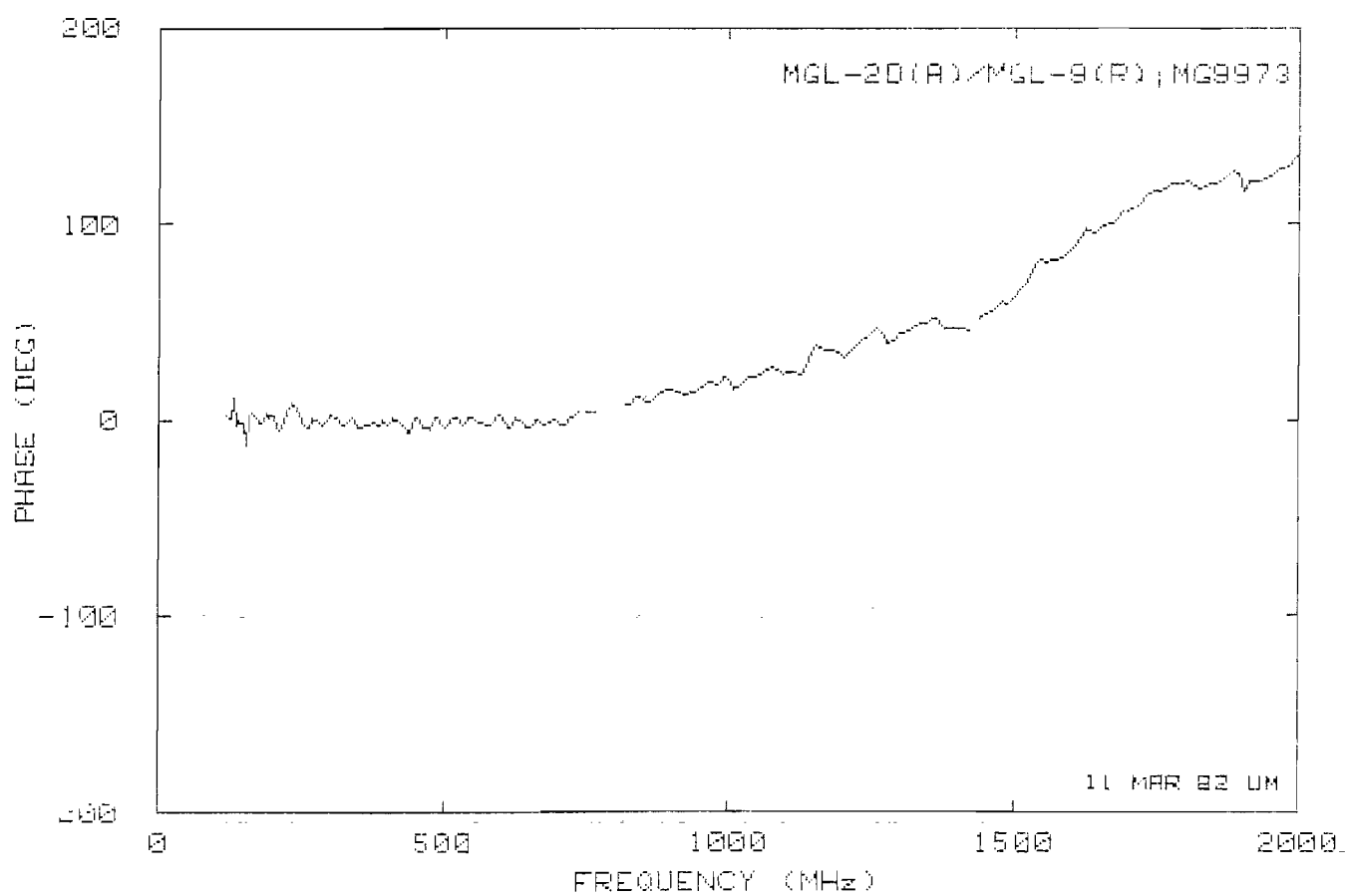
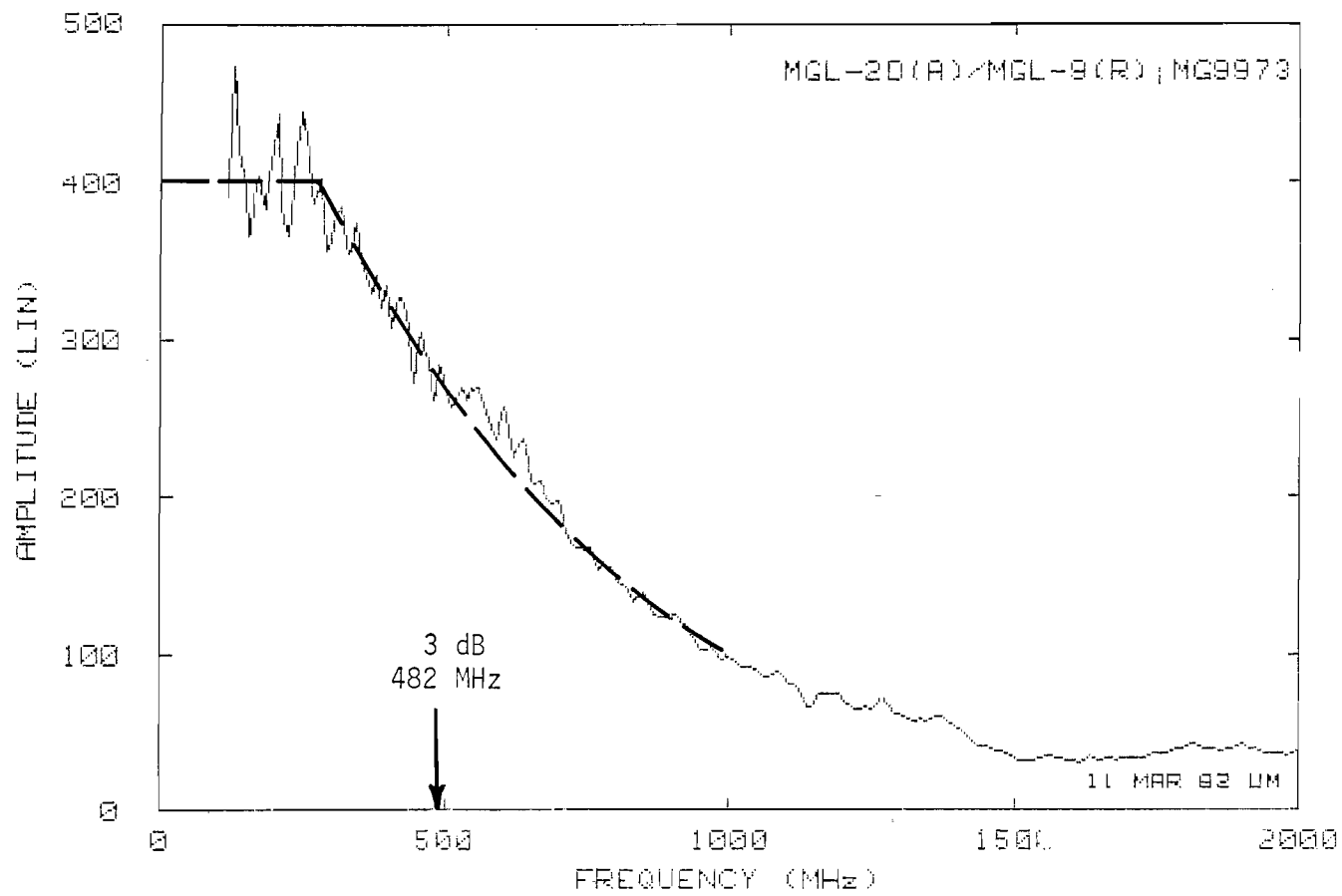


Fig. 61: Response ratio of MGL-2/MGL-9.

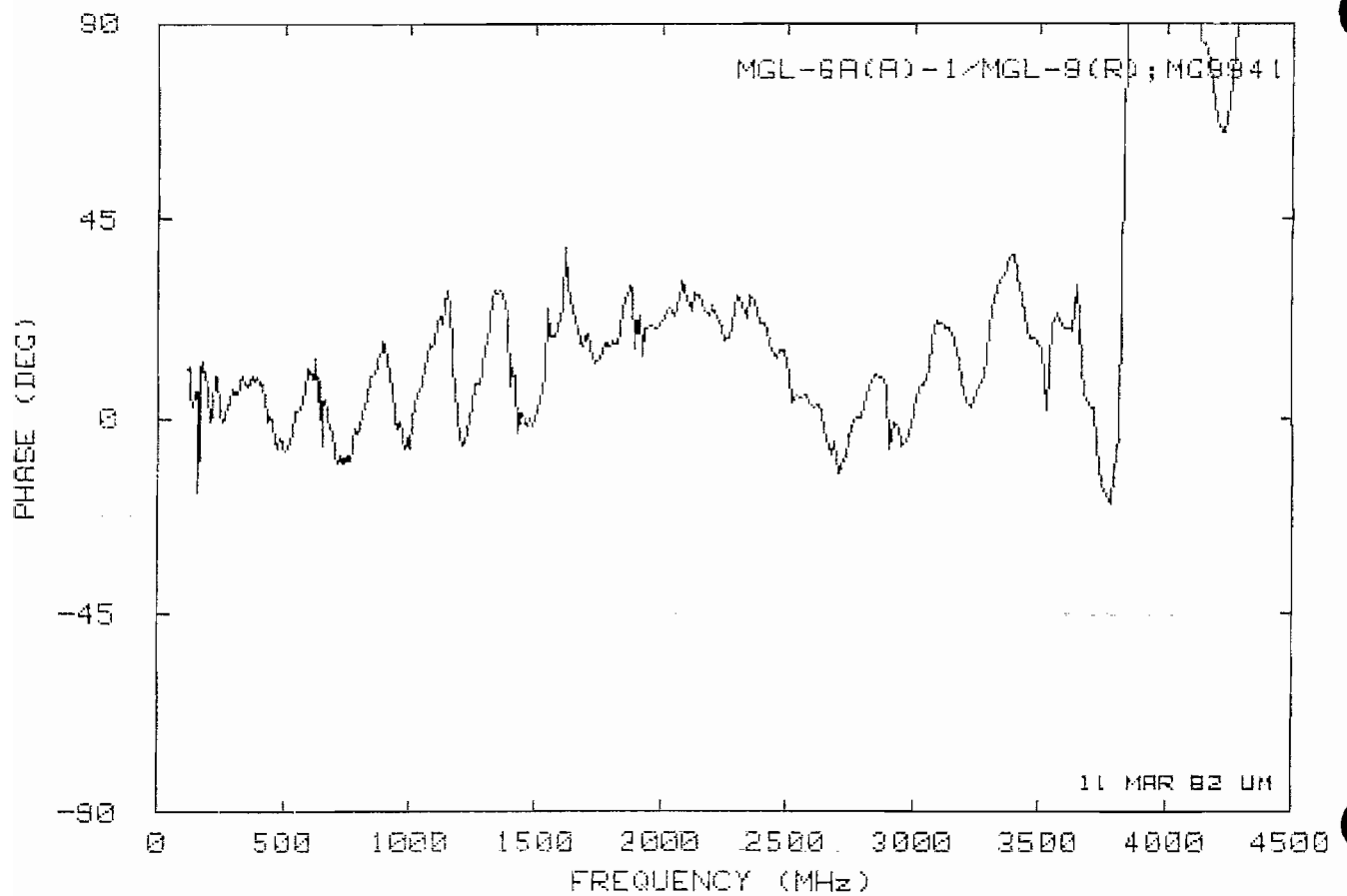
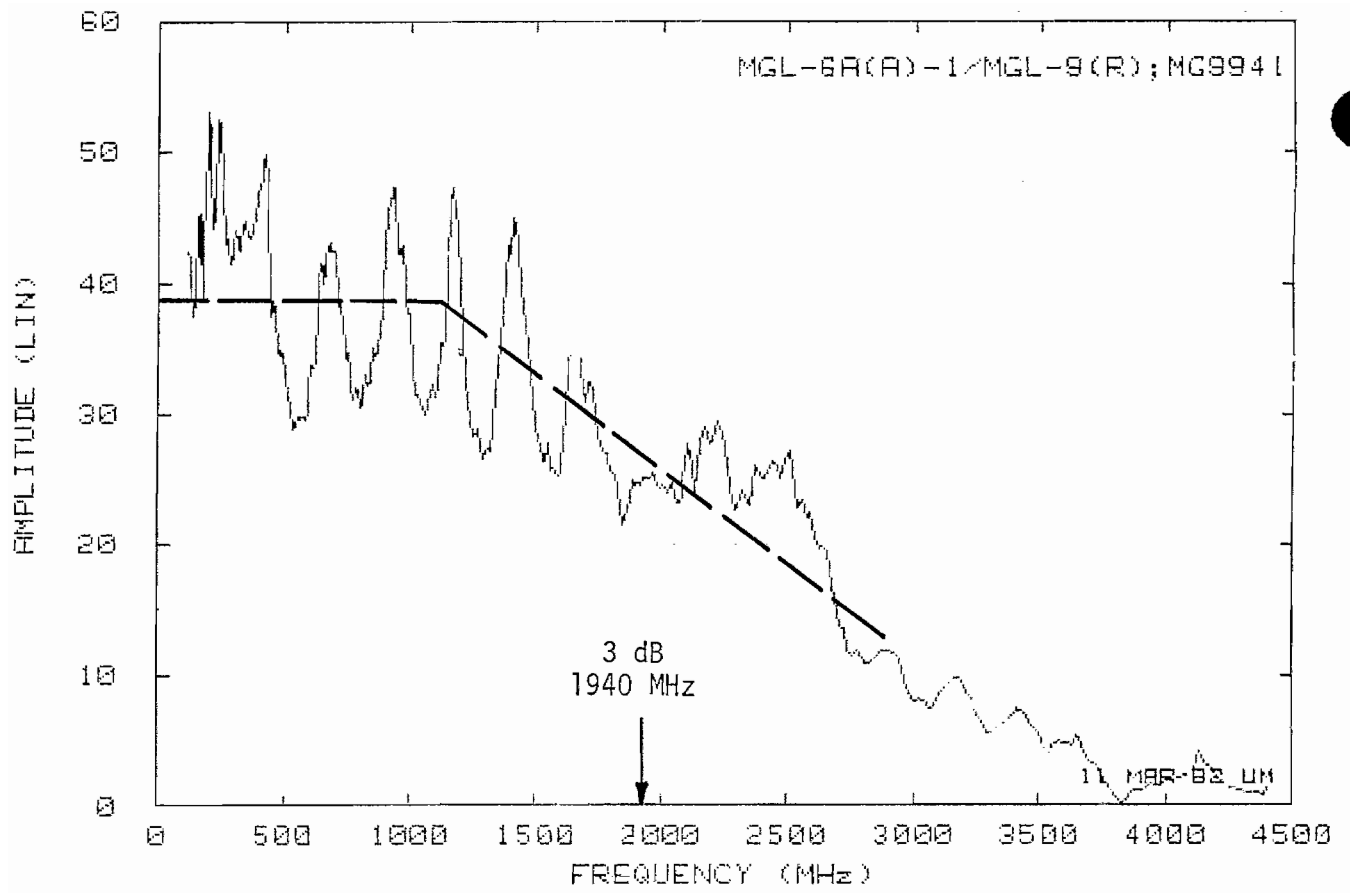


Fig. 62: Response ratio of MGL-6/MGL-9.

6. SUMMARY

Table 5 summarizes the main conclusions of the study. The first two columns identify the sensors, and the third lists the minimum 3-dB roll-off frequencies as specified by the manufacturer. The remaining columns contain the information obtained from our measurements. The fourth column shows the measured 3-dB roll-off frequencies, and in each instance the value exceeds that given by EG&G [2]. The next three columns (Columns 5,6 and 7) relate to the angular behavior of the sensors and list the frequencies at which the patterns deviate from the ideal $(\cos \theta)$ dipole pattern fitted to angular data in the least squares sense. The eighth column gives the frequencies at which the azimuthal (rotational) symmetry breaks down and is applicable only for the MGL free space sensors. The last column gives the deduced figures of merit as defined by Baum et al,

$$A_{0.707}^e = \left[\frac{Z_c}{Z_0} \right]^{1/2} \cdot A_{eq} \left[\frac{2\pi f_c}{c} \right]^2 \quad \text{and} \quad A_{0.707}^h = \left[\frac{Z_0}{Z_c} \right]^{1/2} \cdot A_{eq} \left[\frac{2\pi f_c}{c} \right]^2$$

for electric and magnetic sensors respectively. The 0.707 subscript indicates that the value is based on the cut-off frequency f_c of the sensor (Column 4). In the formulae Z_c is the sensor load impedance (100 ohms) for both the free space and ground plane sensors, Z_0 is the free space characteristic impedance, A_{eq} is the equivalent area as given in the EG&G catalog but doubled for the ground plane sensors, and c is the velocity of light.

In essence Table 5 shows the frequencies up to which each sensor could be used. As already noted, the measured 3-dB roll-off frequency exceeds the manufacturer's (minimum) specification in each case, but

Table 5. Summary of Results

1	2	3	4	5	6	7	8	9
Sensor Model	Part No. Ser. No.	Spec. 3-dB Freq. Resp.	Meas. 3-dB Freq. Resp.	Meas. 3-dB $\pm 0^\circ$ beam	Maximum Angular Response Error		Meas. 3-dB Rot. Error	Figure of Merit
					$\pm 30^\circ$ beam	$\pm 60^\circ$ beam		
ACD-4A(R) free space	7713650 4	750 MHz	1096 MHz Fig. 60	2402 MHz Fig. 32	2402 MHz Fig. 31	1798 MHz Fig. 30		2.713
MGL-2D(A) free space	7114070 -10 24	300 MHz	482 MHz Fig. 61	1215 MHz (45)* 1397 MHz (90) Figs. 42,37	1215 MHz (45) 1397 MHz (90) Figs. 41,36	932 MHz (45) 980 MHz (90) Fig. 40,35	1210 MHz Fig. 45	1.979
MGL-6A(A) free space	7413327 -10 2	1800 MHz	1940 MHz Fig. 62	3455 MHz (45) 3307 MHz (95) Figs. 55,50	3412 MHz (45) 2307 MHz (90) Figs. 54,49	2850 MHz (45) 2580 MHz (90) Figs. 53,48	3356 MHz Fig. 58	3.205
MGL-5A(R) gd plane	7113295 -10 --	700 MHz	1100 MHz					2.062
MGL-7A(R) gd plane	7613070 -10 --	2000 MHz	2367 MHz					0.954

*Position of gaps relative to the incident field.

it is also substantially less than the frequencies derived from the measured angular responses. This suggests that a sensor could, in fact, be used with confidence at frequencies up to two or three times the manufacturer's specification, provided the responses were corrected for the frequency roll-off. In practice, the maximum frequency will depend on the particular sensor used, and to see this, consider the data for the MGL-2D(A). The measured 3-dB roll-off frequency is 482 MHz, but the angular response frequencies are considerably larger. Suppose one wishes to receive a signal over ± 60 degrees range of angle. The maximum frequency is then 932 MHz, and since this is less than the value in the last column, the rotational symmetry would still exist. Nevertheless, to use the sensor at frequencies up to 932 MHz it would be necessary to correct for the frequency roll-off either with a specially designed (analog) compensating network or by correcting the measured values when processing the data.

The study was a classic example of one which is theoretically and conceptually straightforward, but difficult to accomplish in practice. The most severe difficulties were encountered with the free-space sensors that use twinaxial cable systems. Such systems are not effective above about 100 MHz, and generated oscillation that degraded the accuracy of our measured data. The high (> 100 MHz) frequency performance of the free-space sensors merits further study, and we remark that the performance could be improved if the sensors were designed with twin coaxial rather than twinaxial output lines.

7. REFERENCES

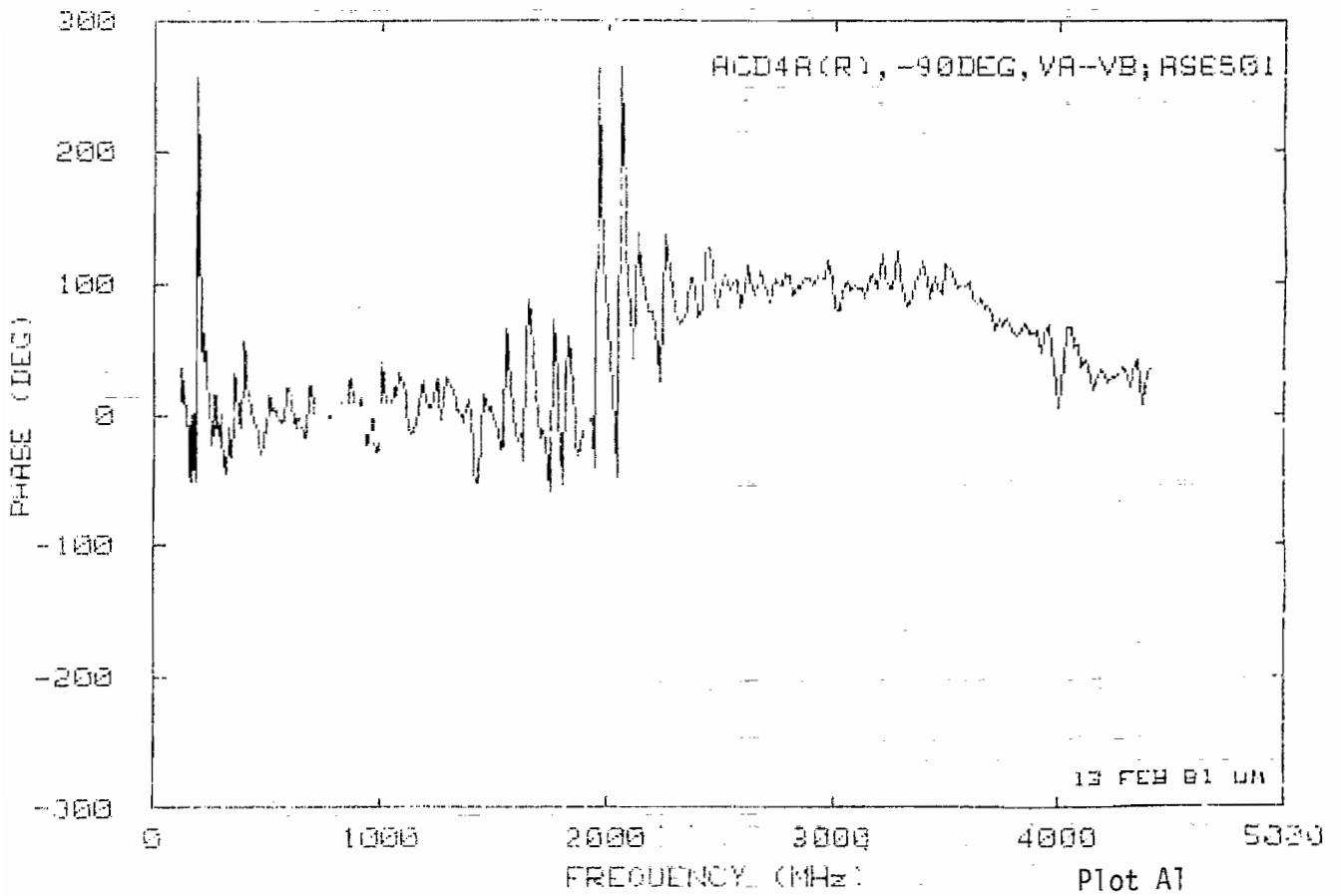
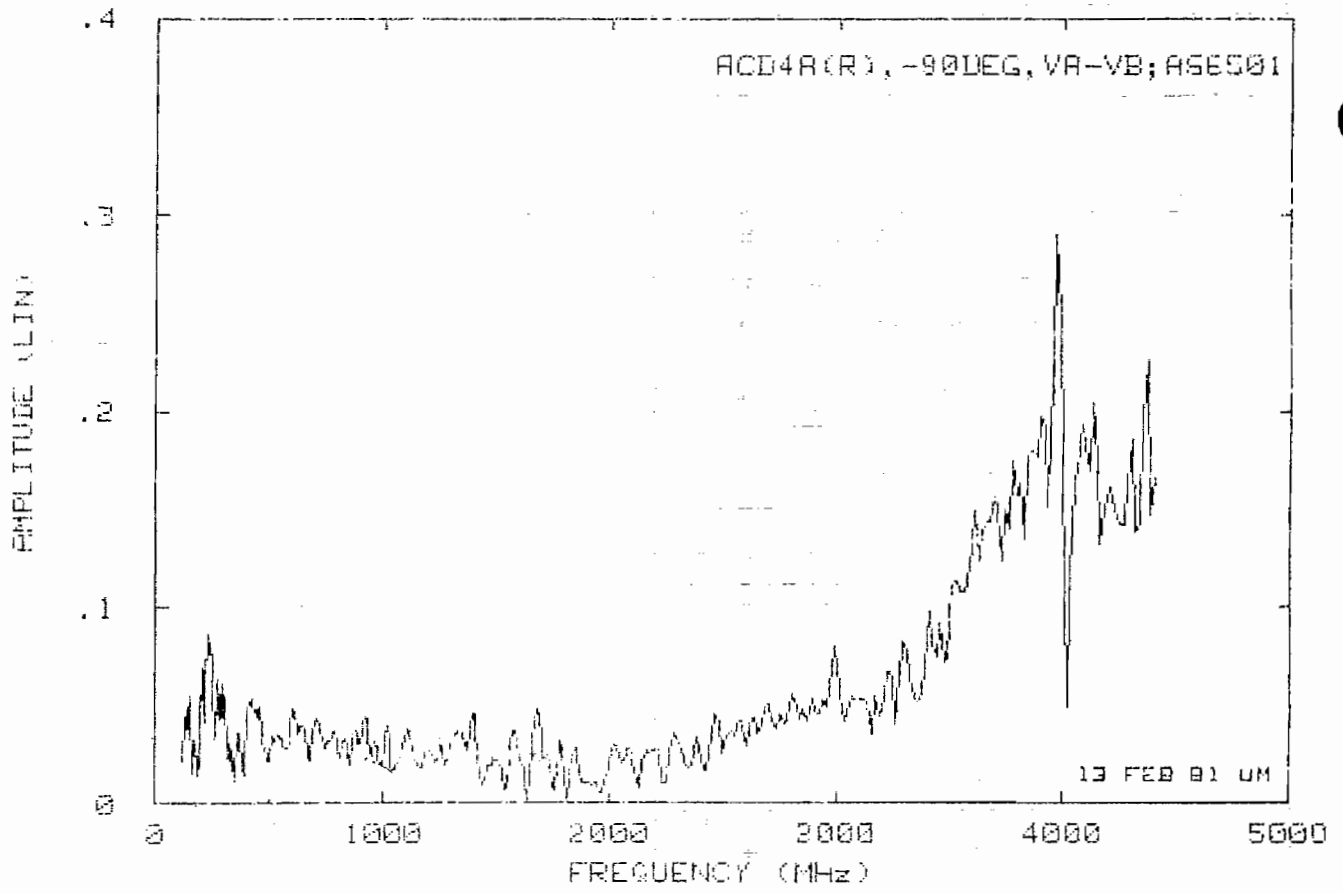
- [1] Baum, C. E., E. L. Breen, J. G. Giles, J. O'Neill, and G. Sower, "Sensors for electromagnetic pulse measurement both inside and away from nuclear source regions," IEEE Trans. Antennas Propagat., AP-26, 22-35, 1978.
- [2] EG&G, Inc. Catalog, "Standard EMP instrumentation," Albuquerque, NM, 87117, 1979.
- [3] Stratton, J. A., "Electromagnetic theory," McGraw-Hill Book Co., Inc., New York, 1941.
- [4] Baum, C. E. and E. Breen, personal communication, AFWL, Albuquerque, NM, 87117, 1980.
- [5] Senior, T.B.A. and J. Pond, "Pole extraction in the frequency domain," Radiation Laboratory Final Report No. 017815-1-F, AFWL Interaction Note 408, December 1981.
- [6] Edgel, W. R., "MGL-6 B-dot sensor development," EG&G Report No. AL-1101, Albuquerque, NM, 87117, 1974.

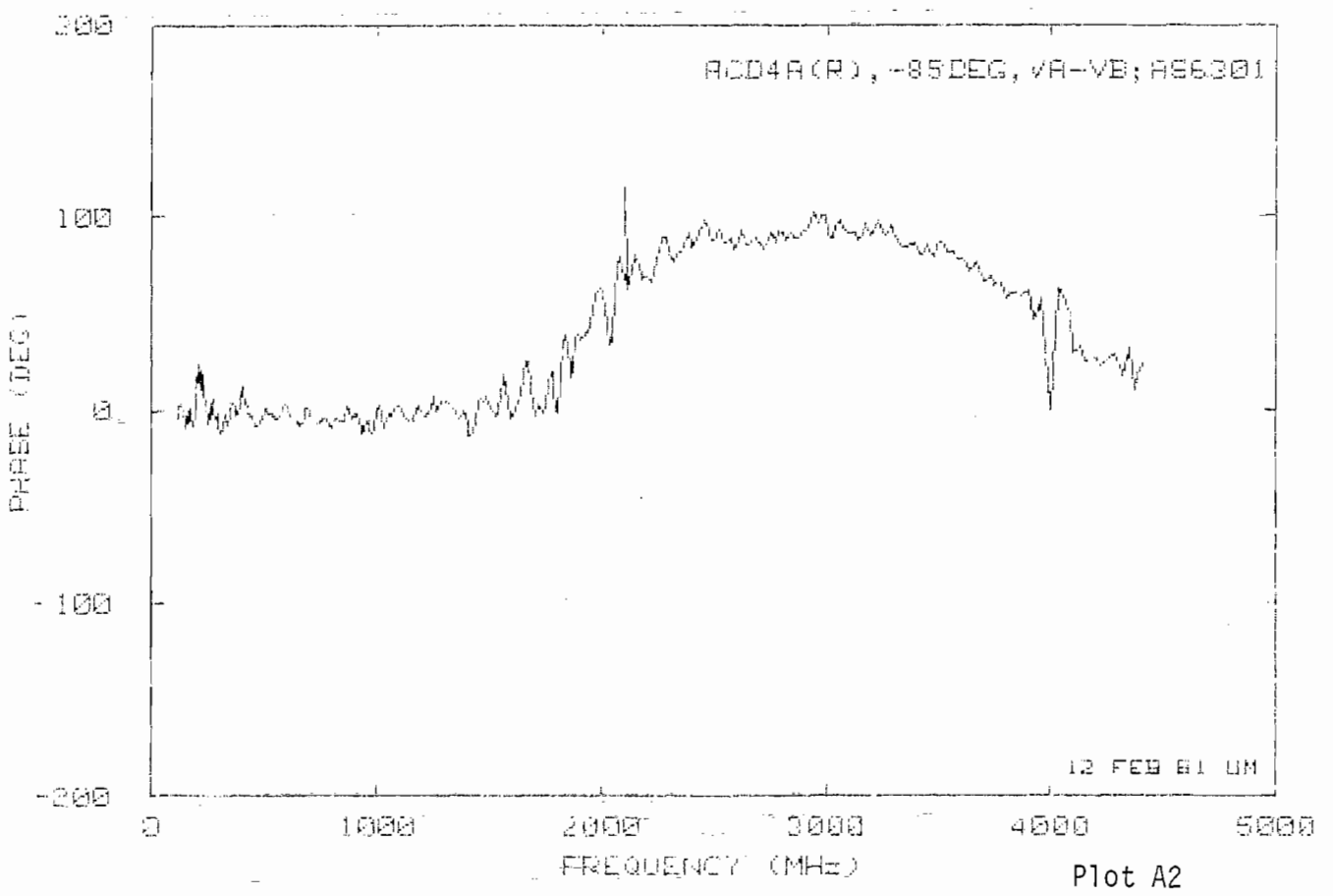
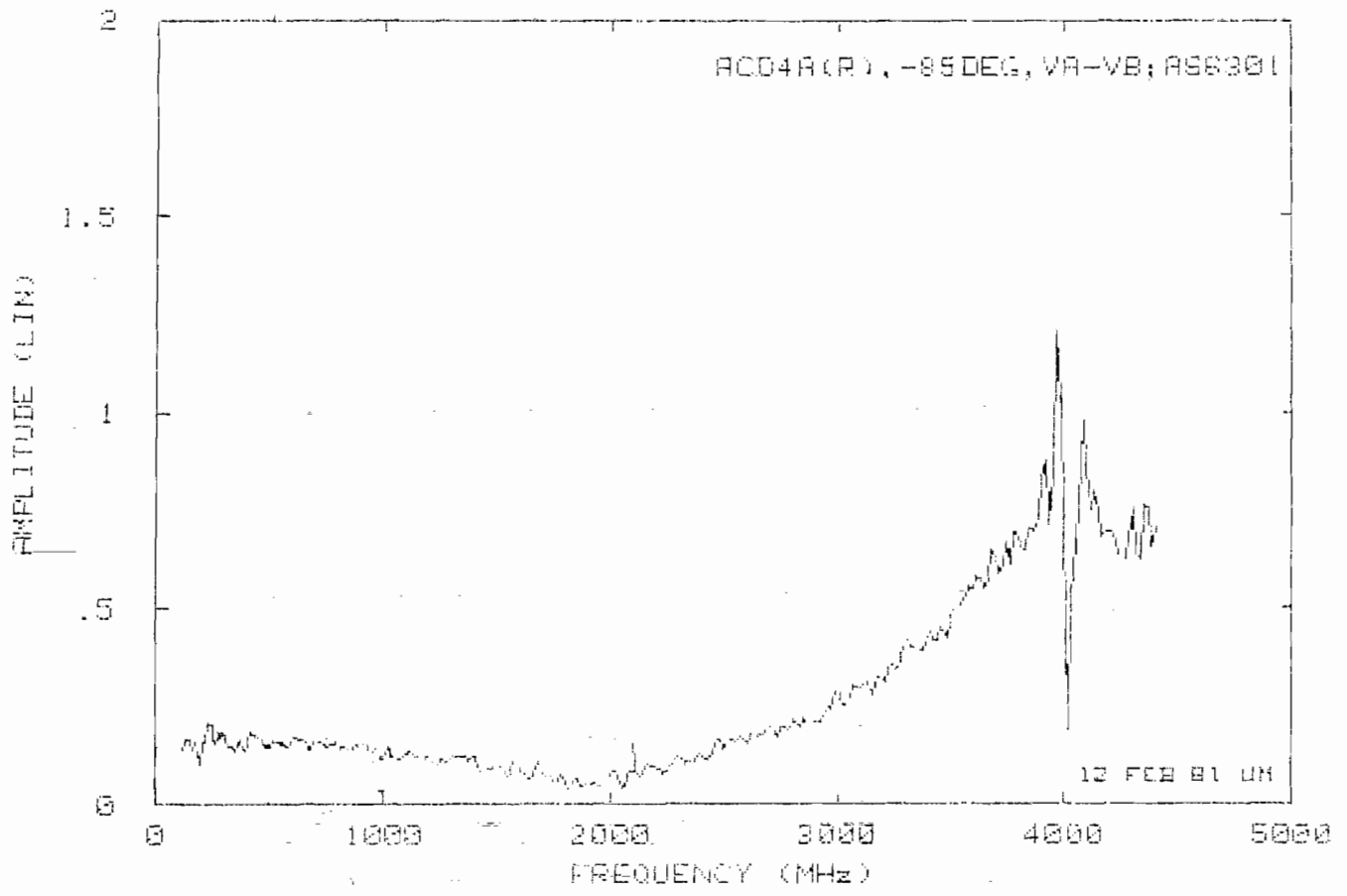
APPENDIX A: ACD-4A(R) DIPOLE RESPONSE DATA (RAW)

Measured data are presented for the ACD-4 sensor as functions of the frequency for the rotation angles $\theta = -90(15)90$ degrees (see Fig. 1). The data are normalized to the measured values for $\theta = 0$, producing unity plots for $\theta = 0$ (see Plot A8). Data for $\theta = \pm 85$ degrees are also included, but were not used in the analyses described in Section 5.4.

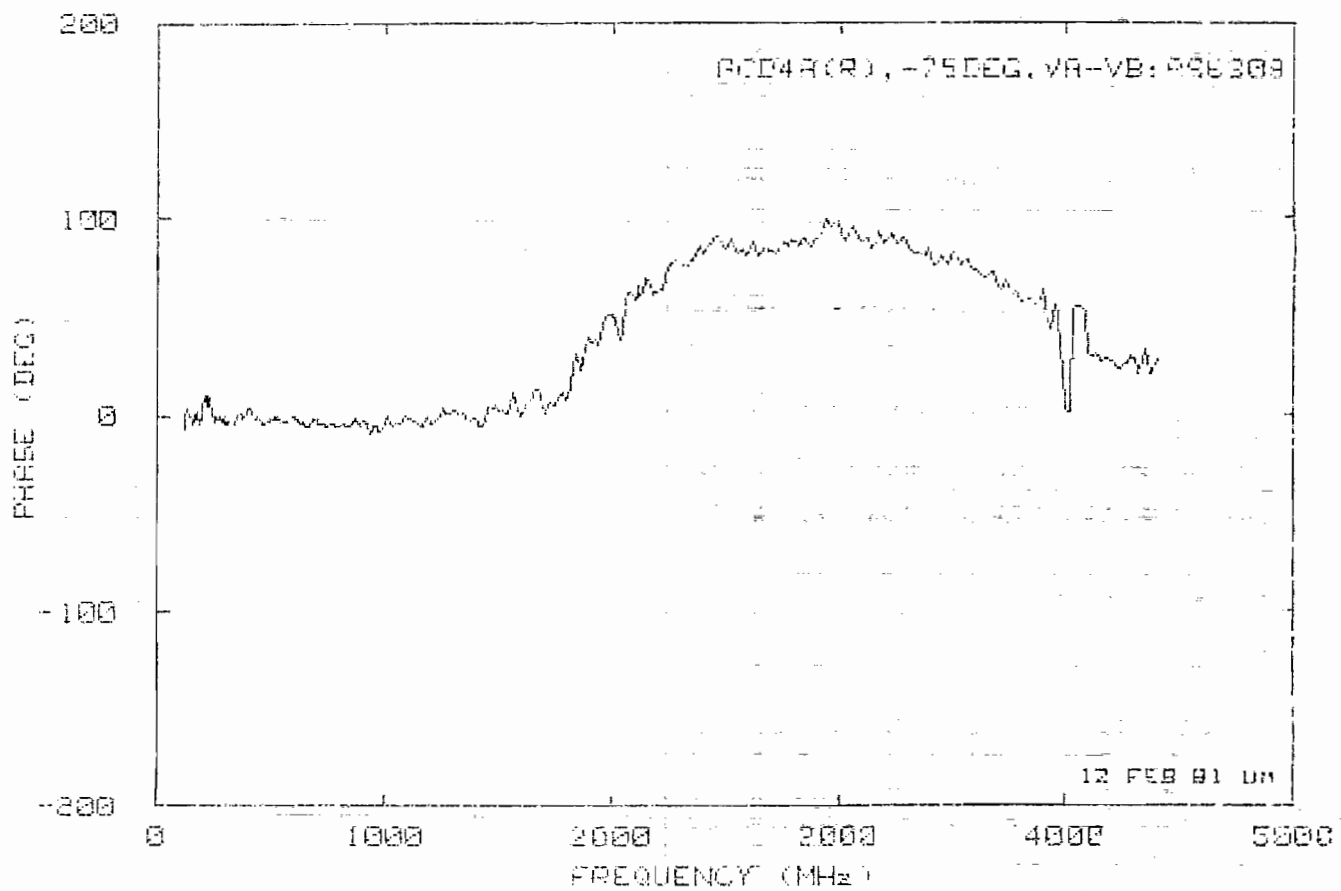
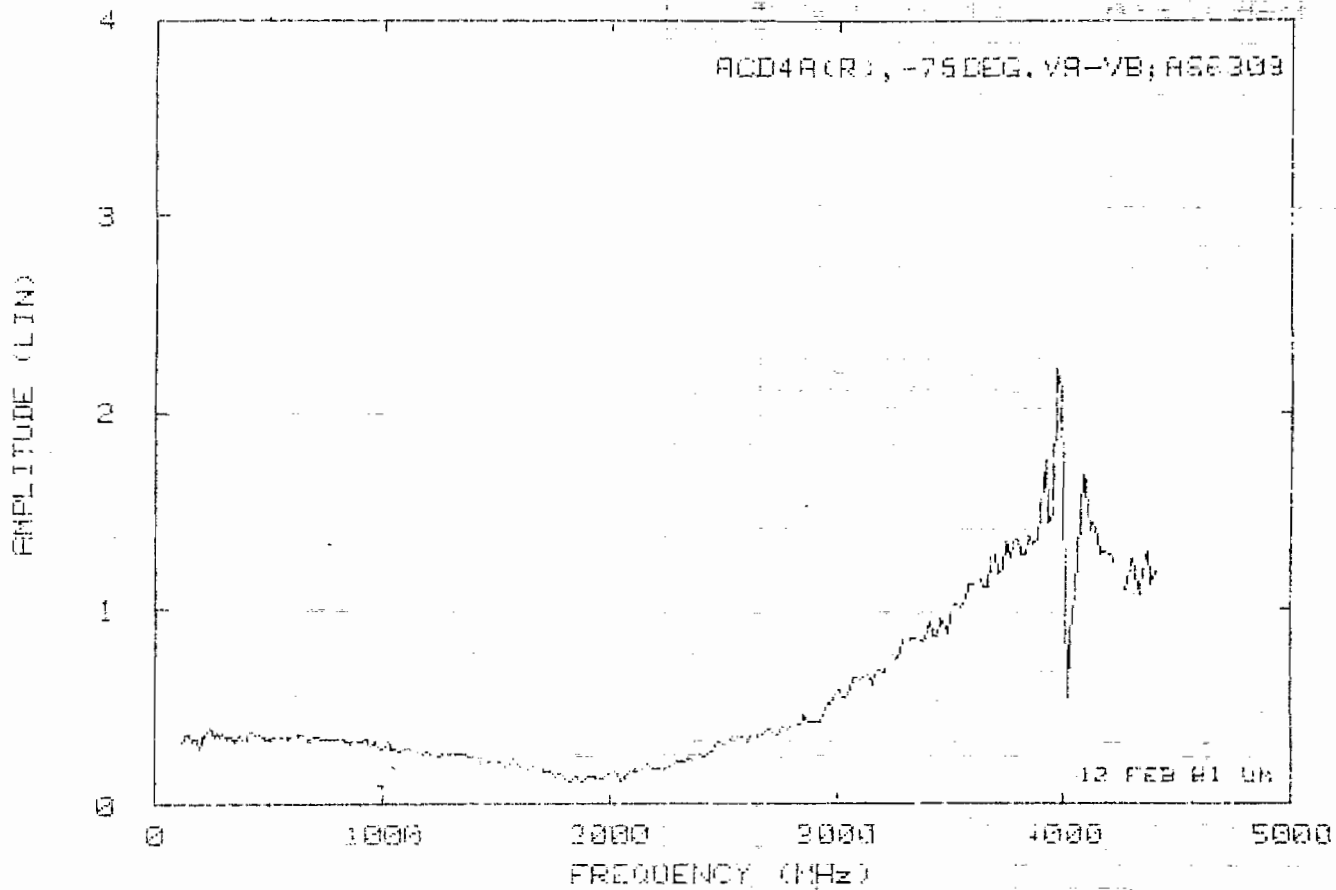
Table A1: List of ACD-4 Dipole Data Plots

θ (degrees)	Plot No.	File No.
-90	A1	AS 6501
-85	A2	AS 6301
-75	A3	AS 6309
-60	A4	AS 6317
-45	A5	AS 6325
-30	A6	AS 6333
-15	A7	AS 6341
0	A8	AS 6349
15	A9	AS 6357
30	A10	AS 6365
45	A11	AS 6373
60	A12	AS 6441
75	A13	AS 6449
85	A14	AS 6457
90	A15	AS 6473

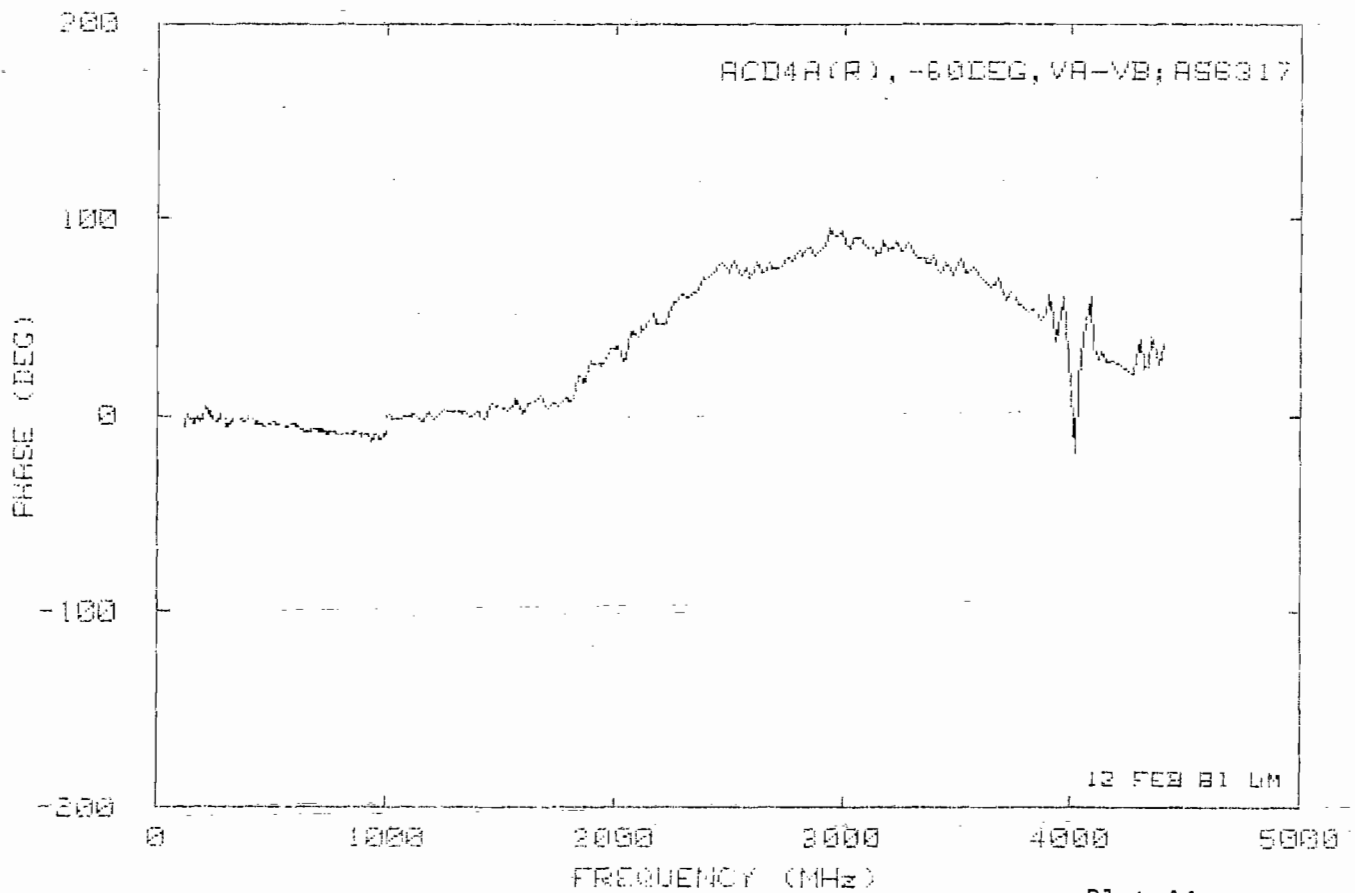
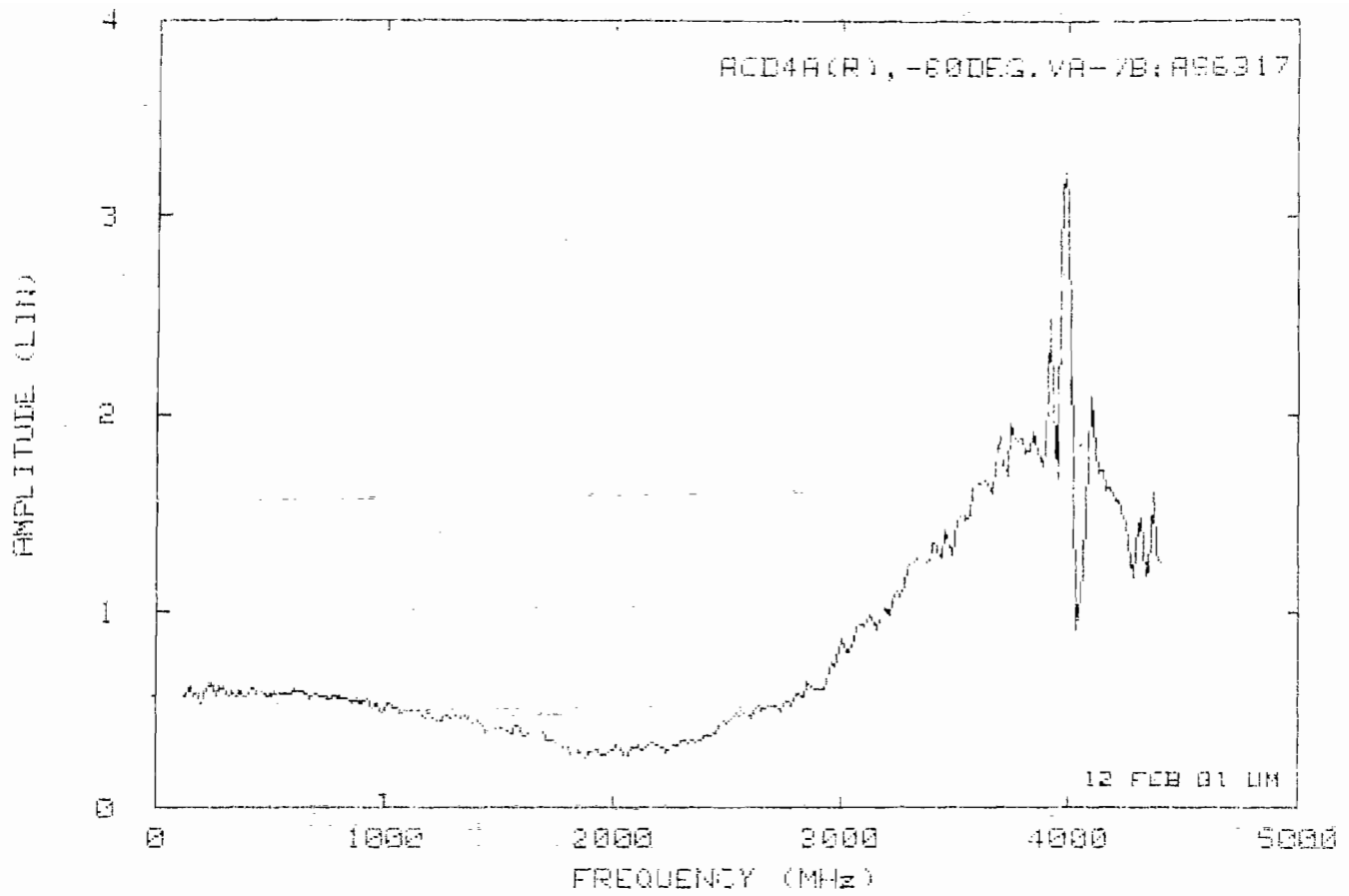




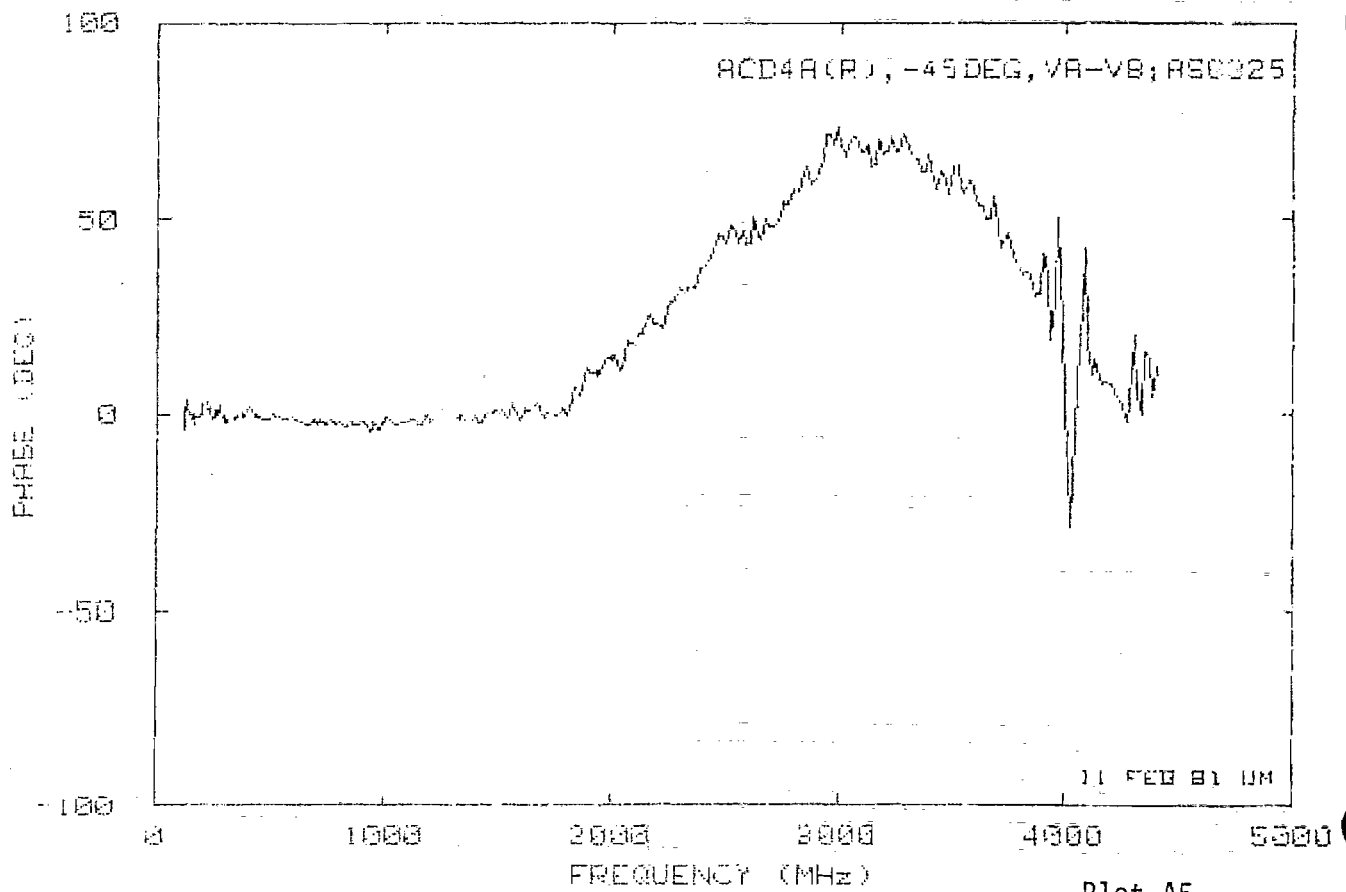
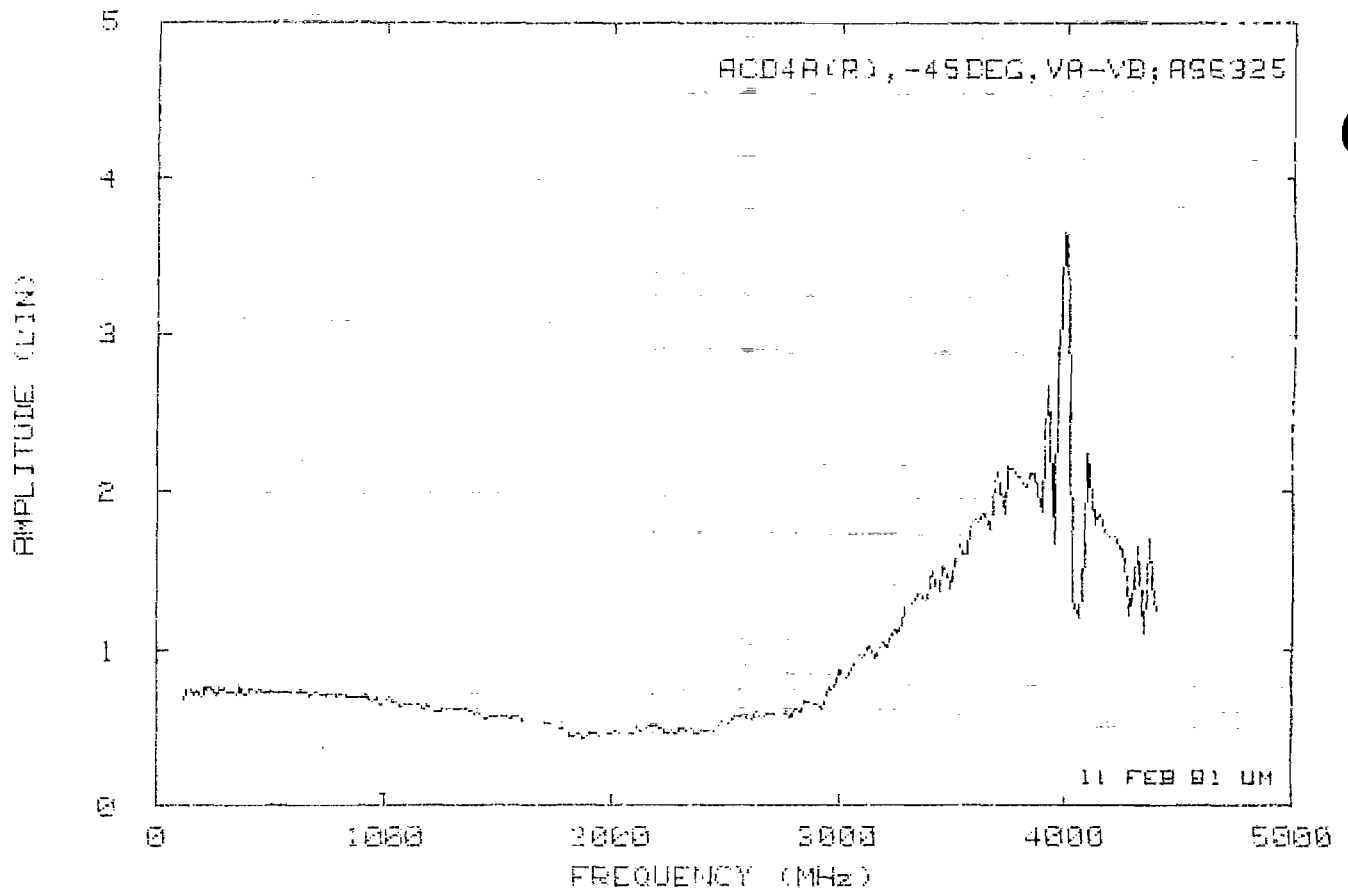
Plot A2



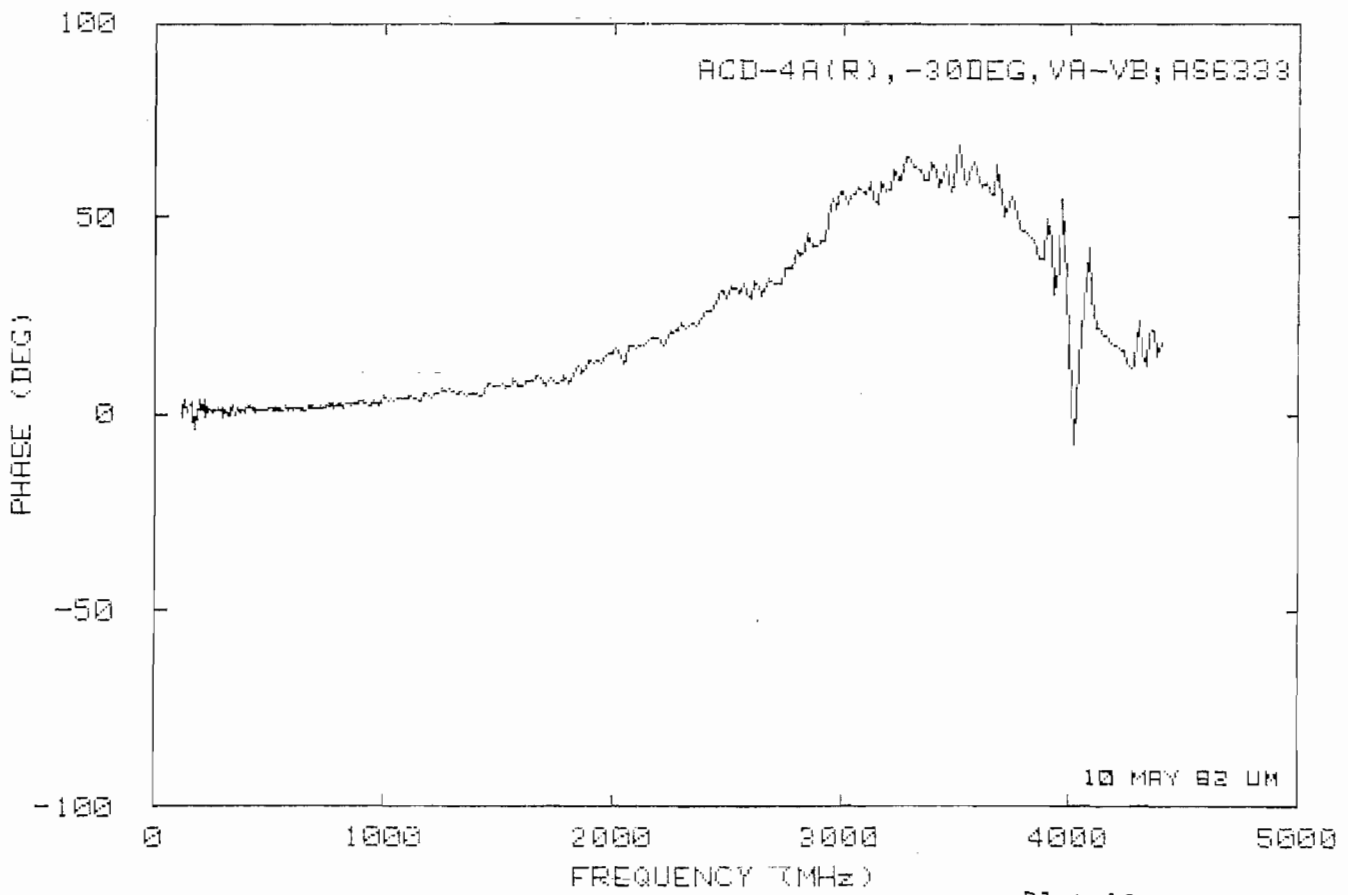
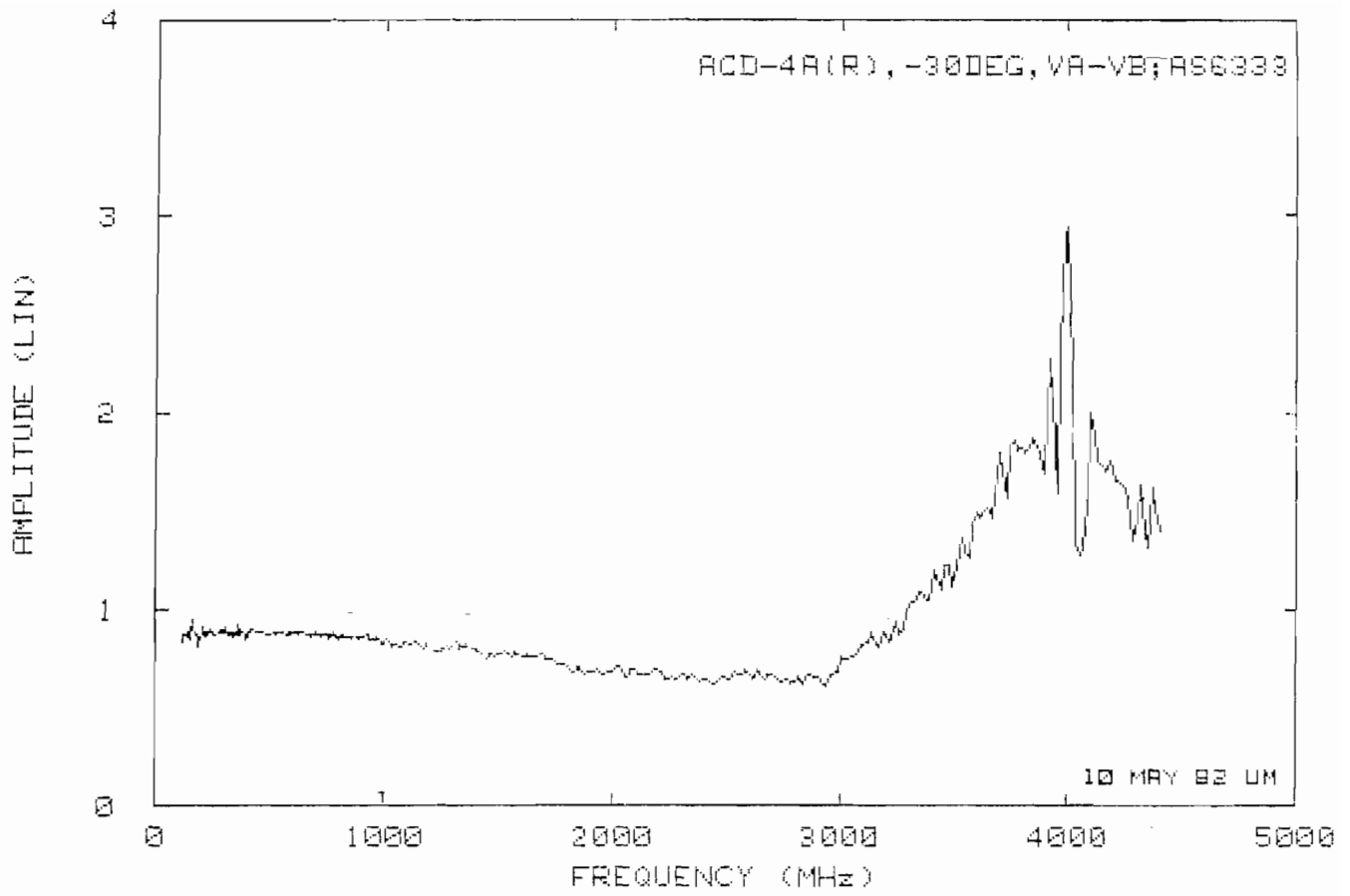
Plot A3



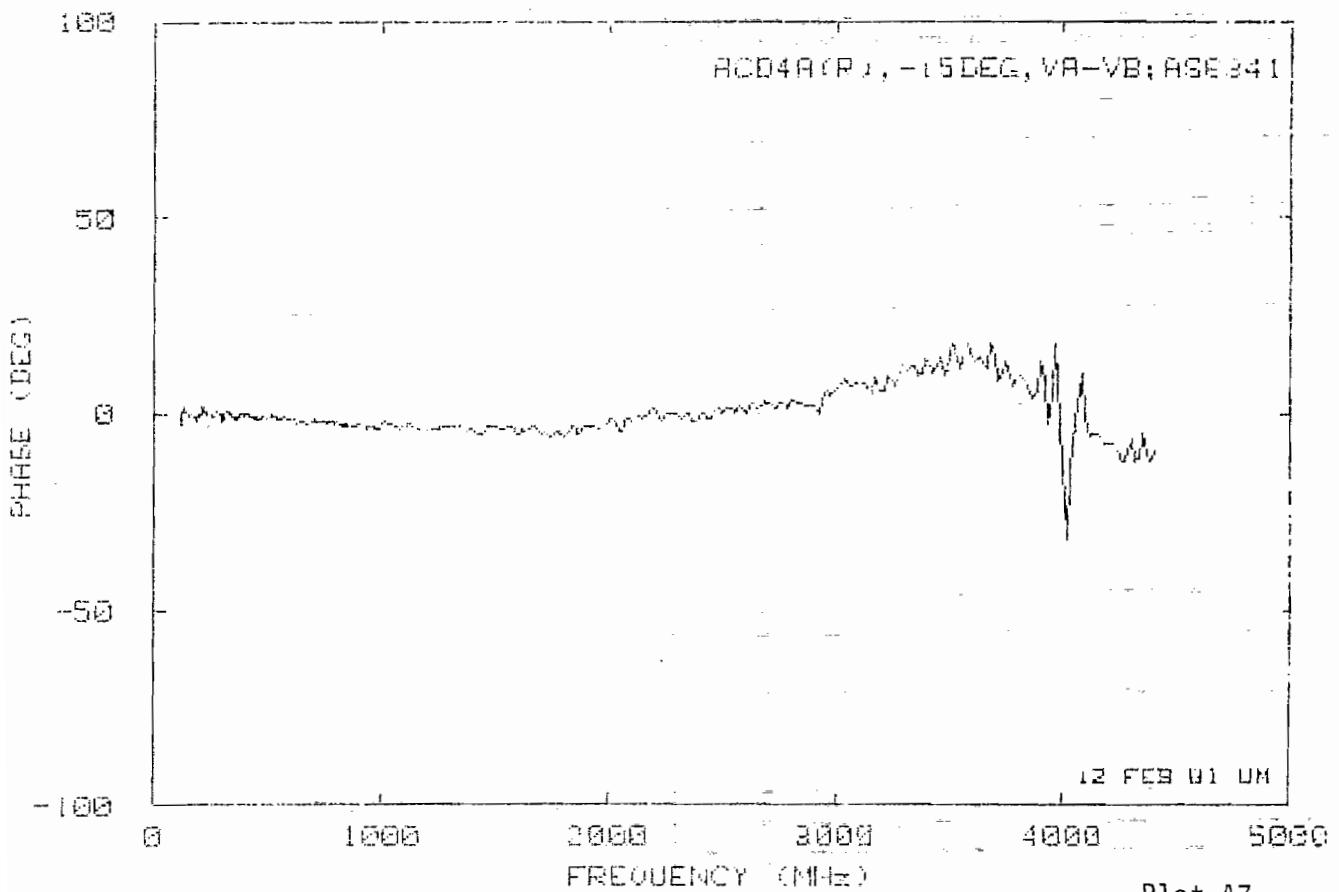
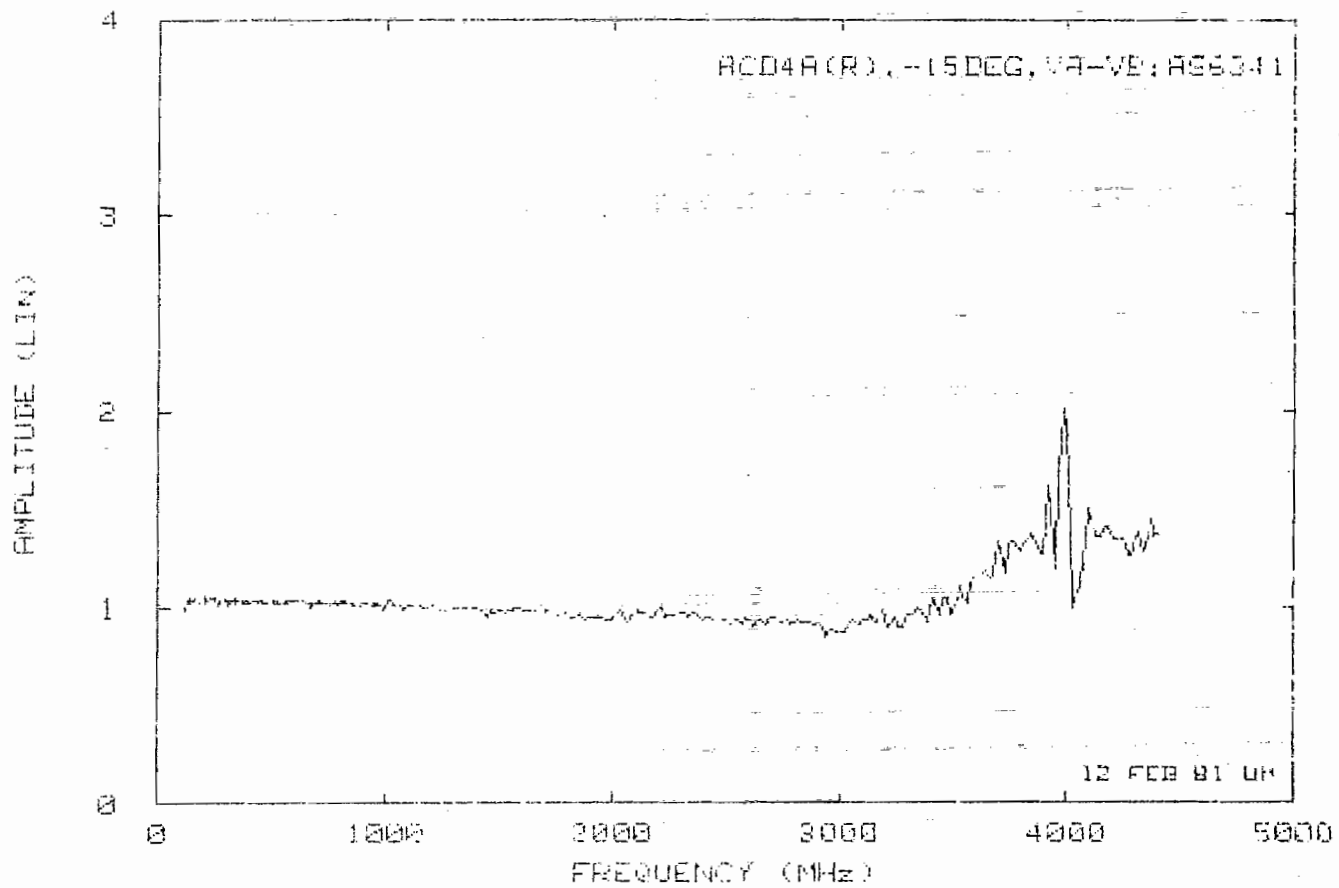
Plot A4



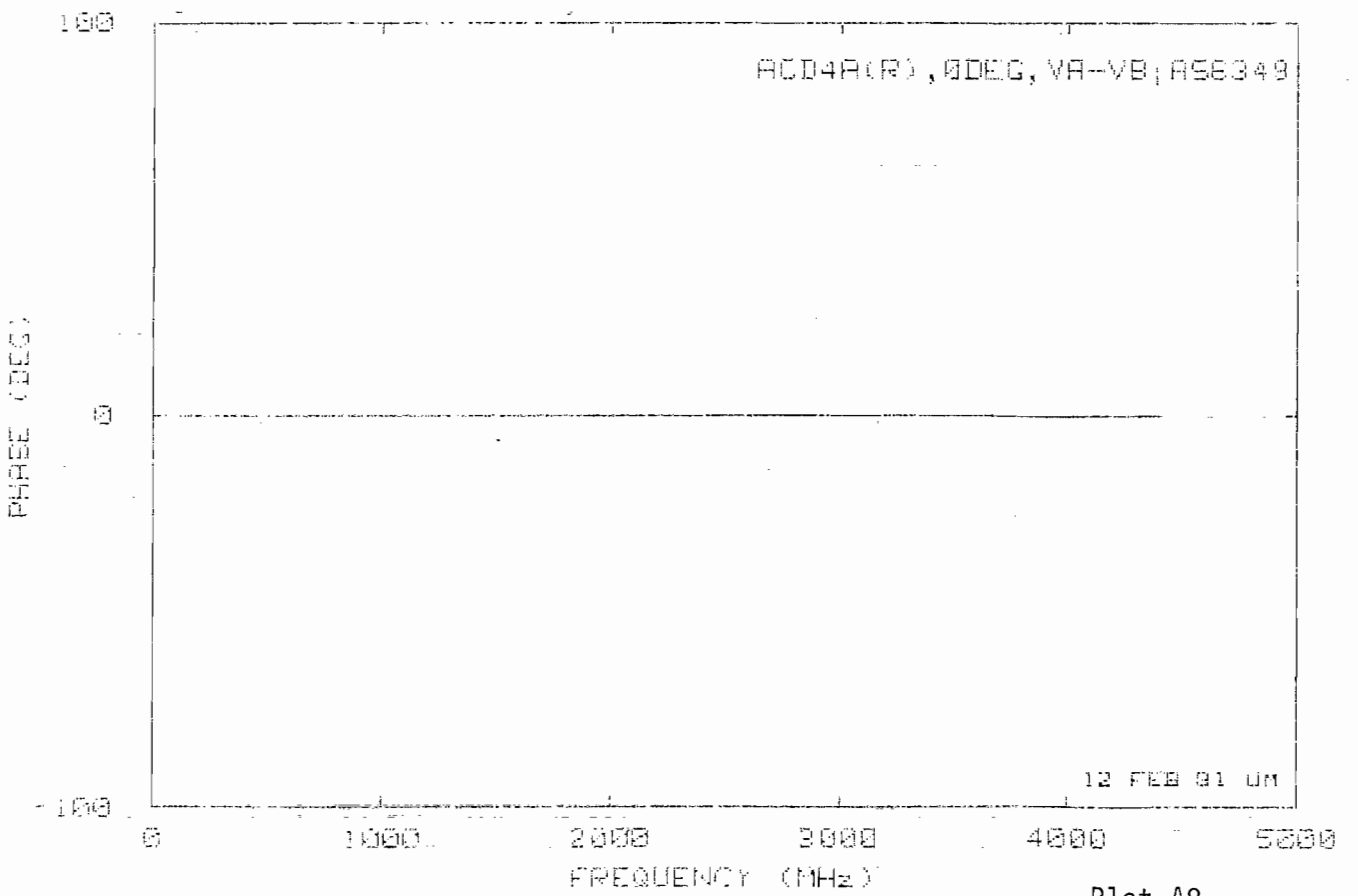
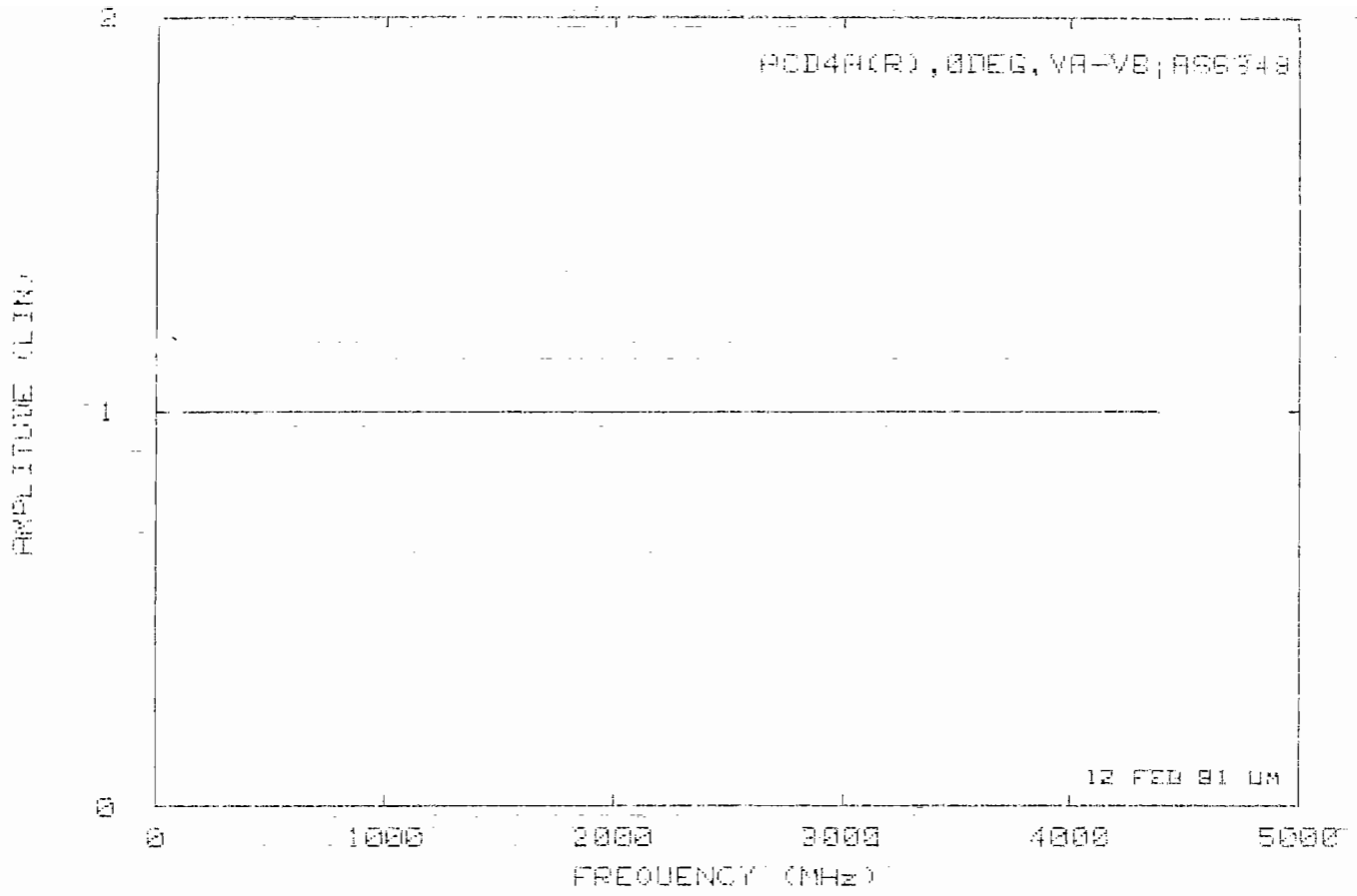
Plot A5



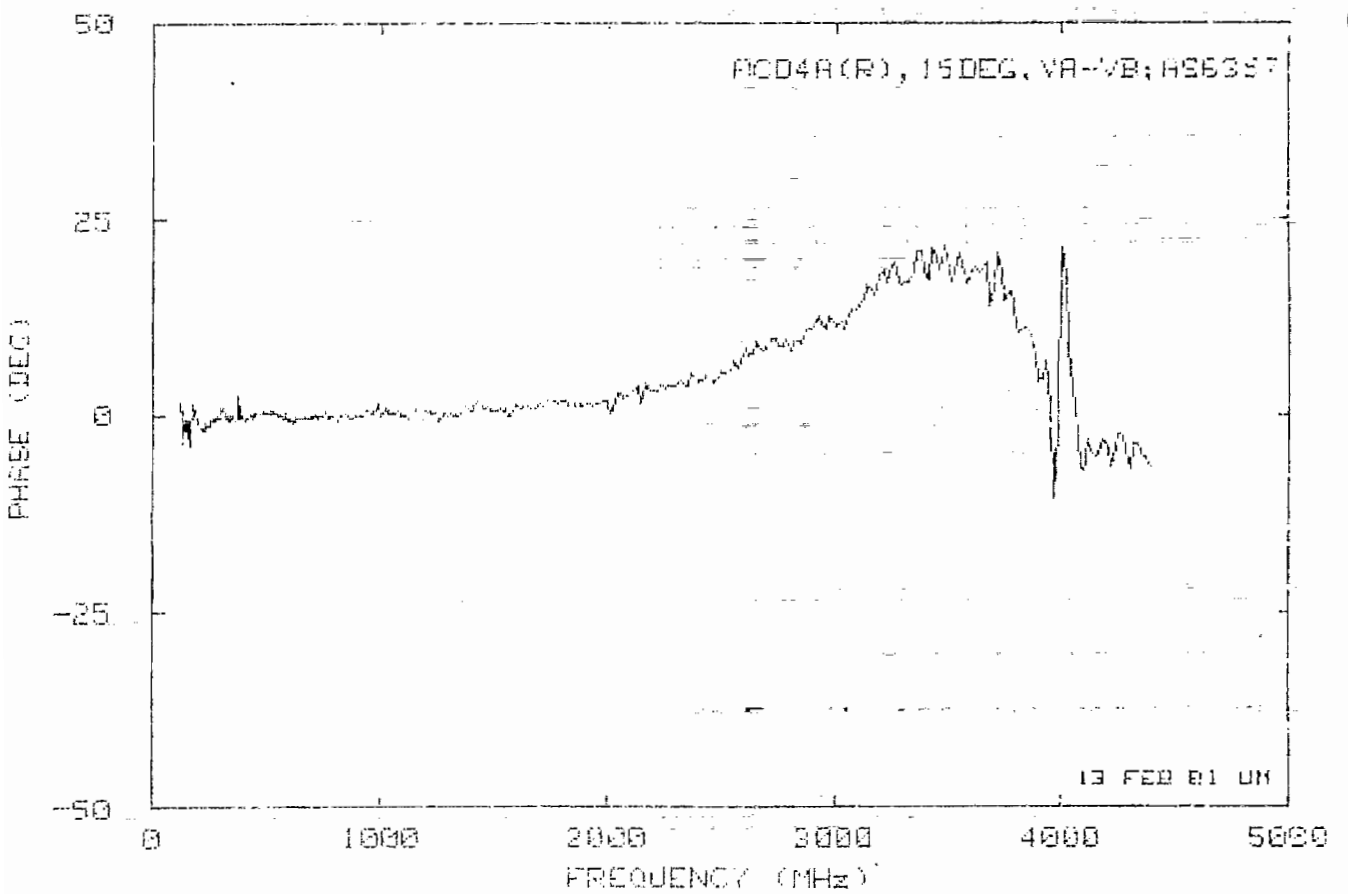
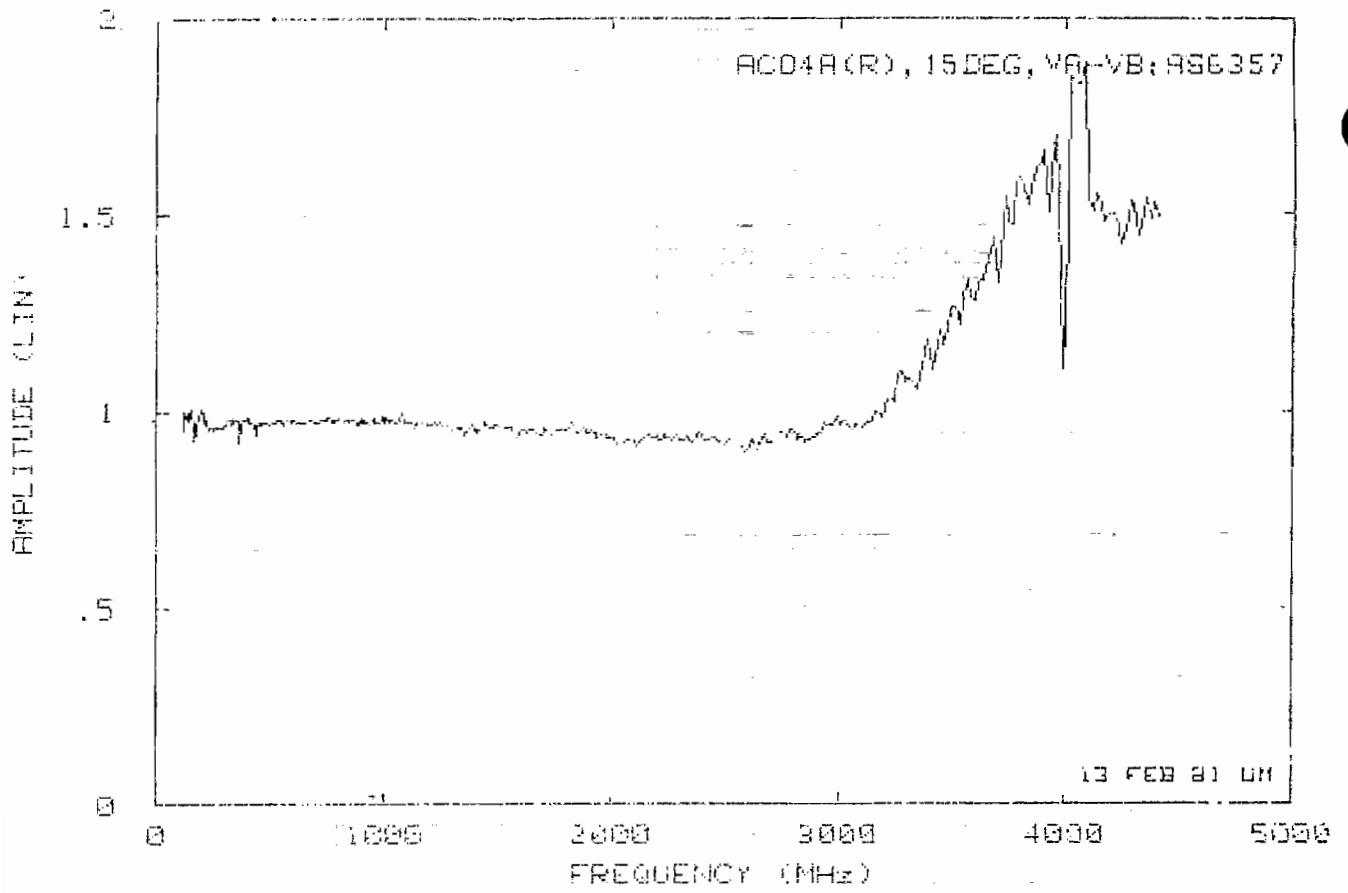
Plot A6



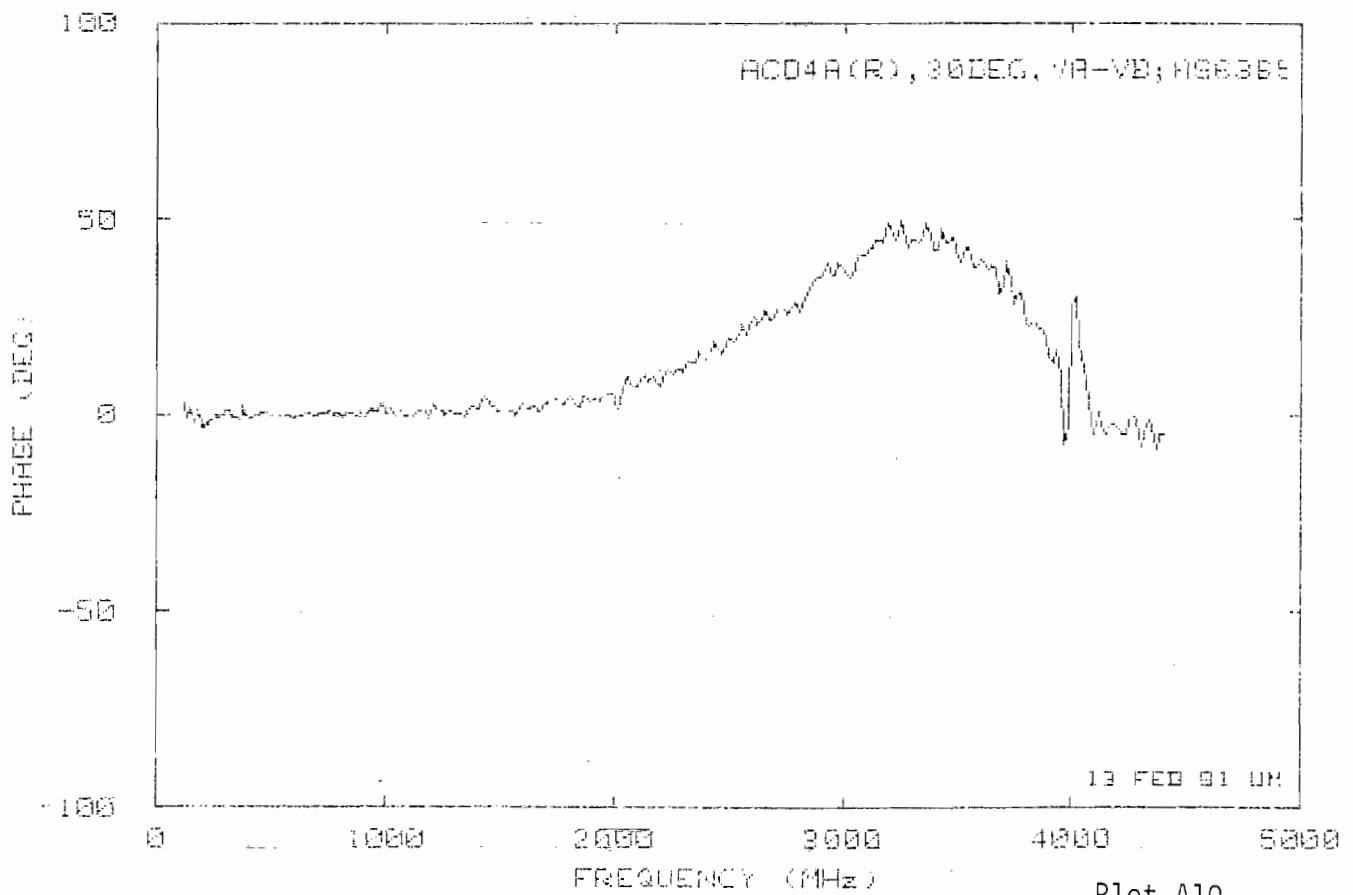
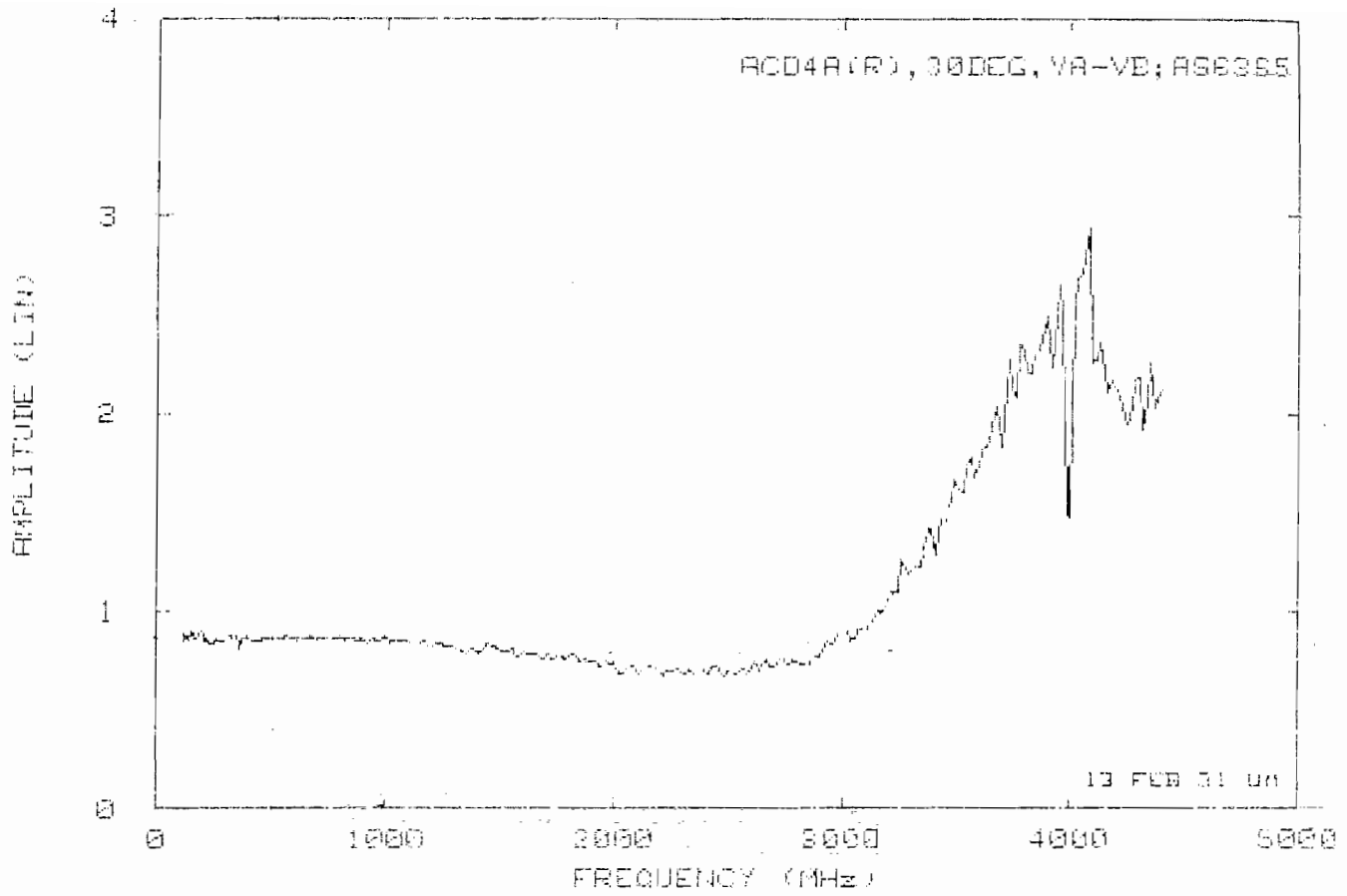
Plot A7

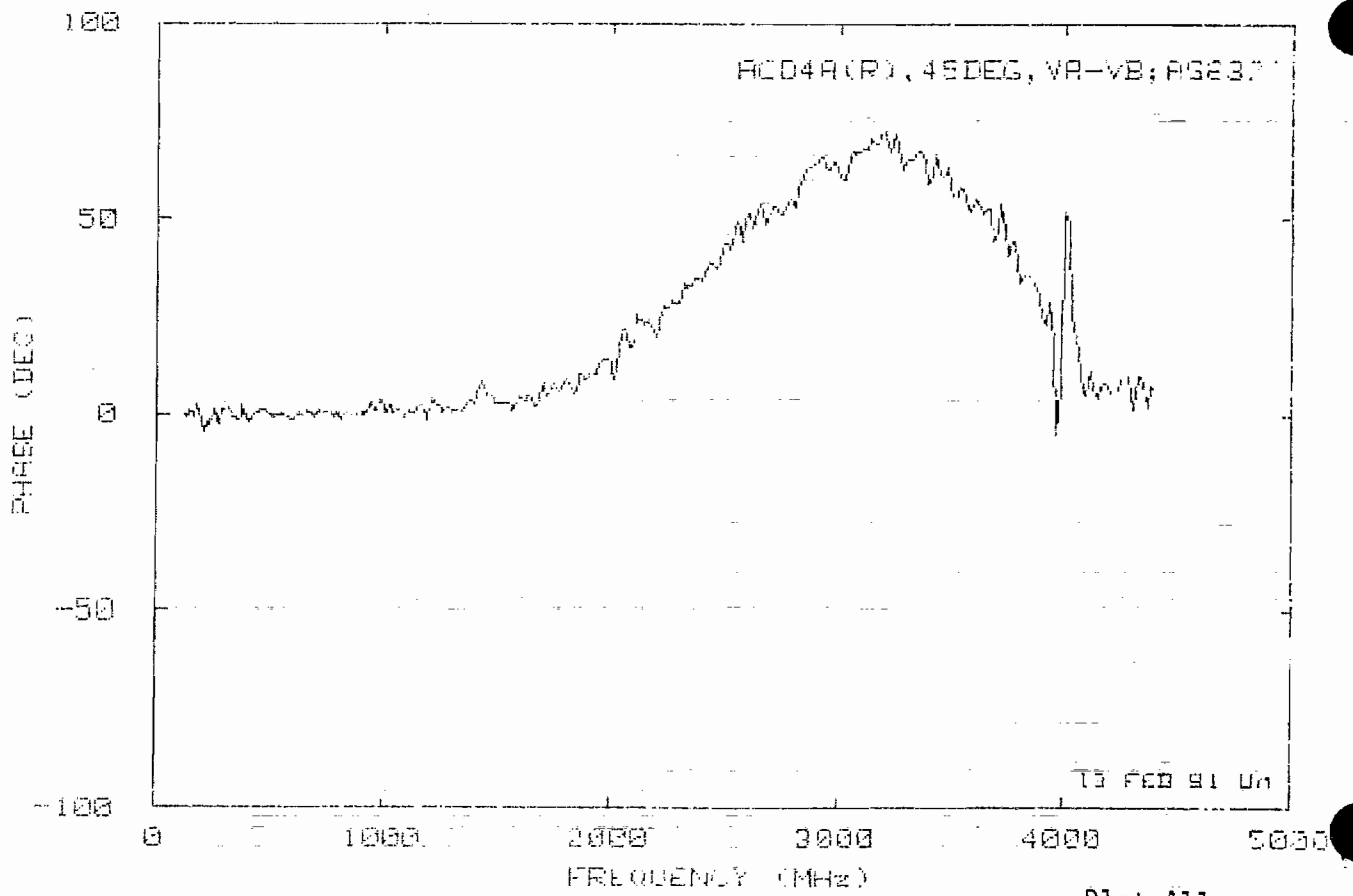
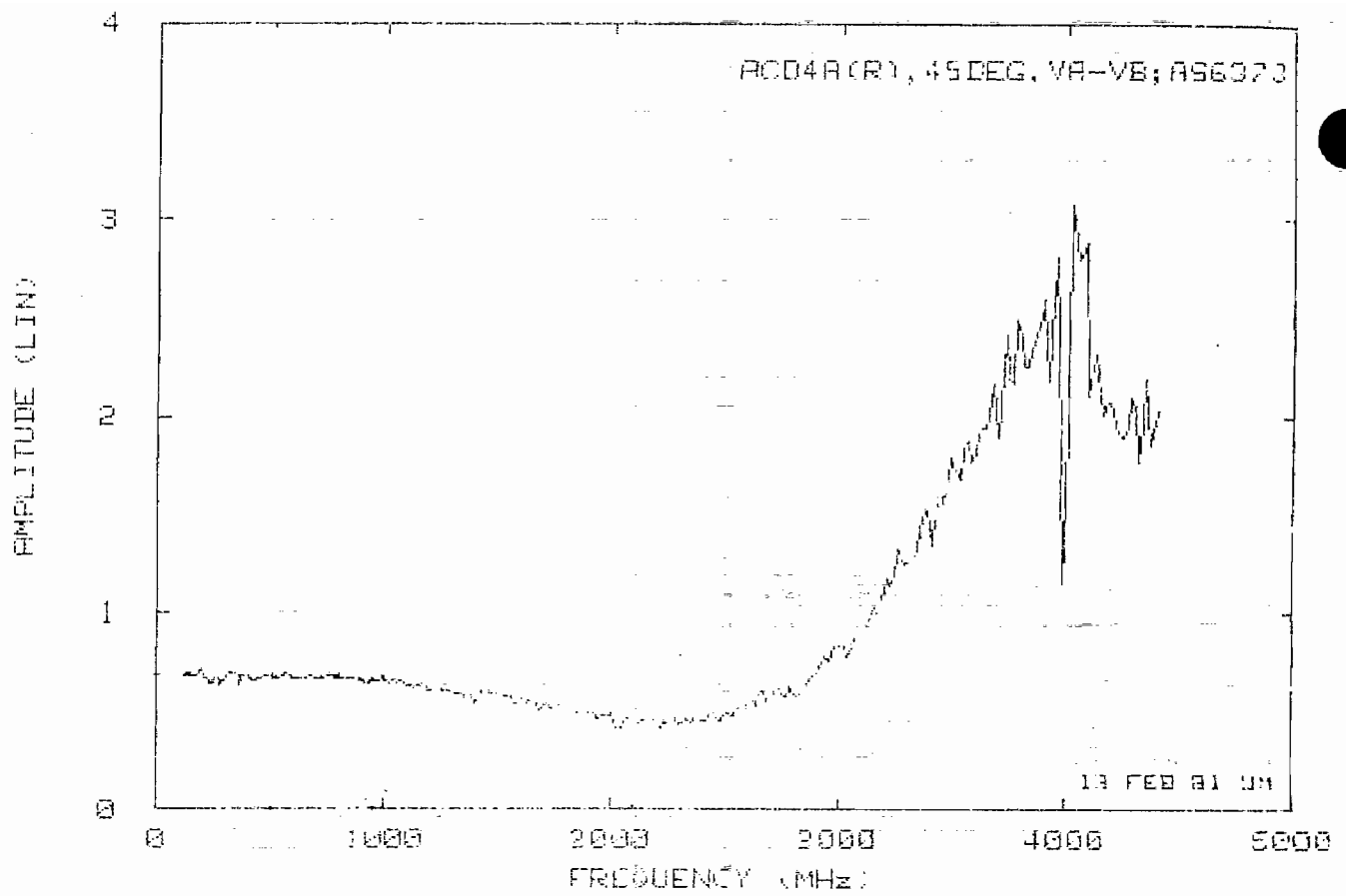


Plot A8

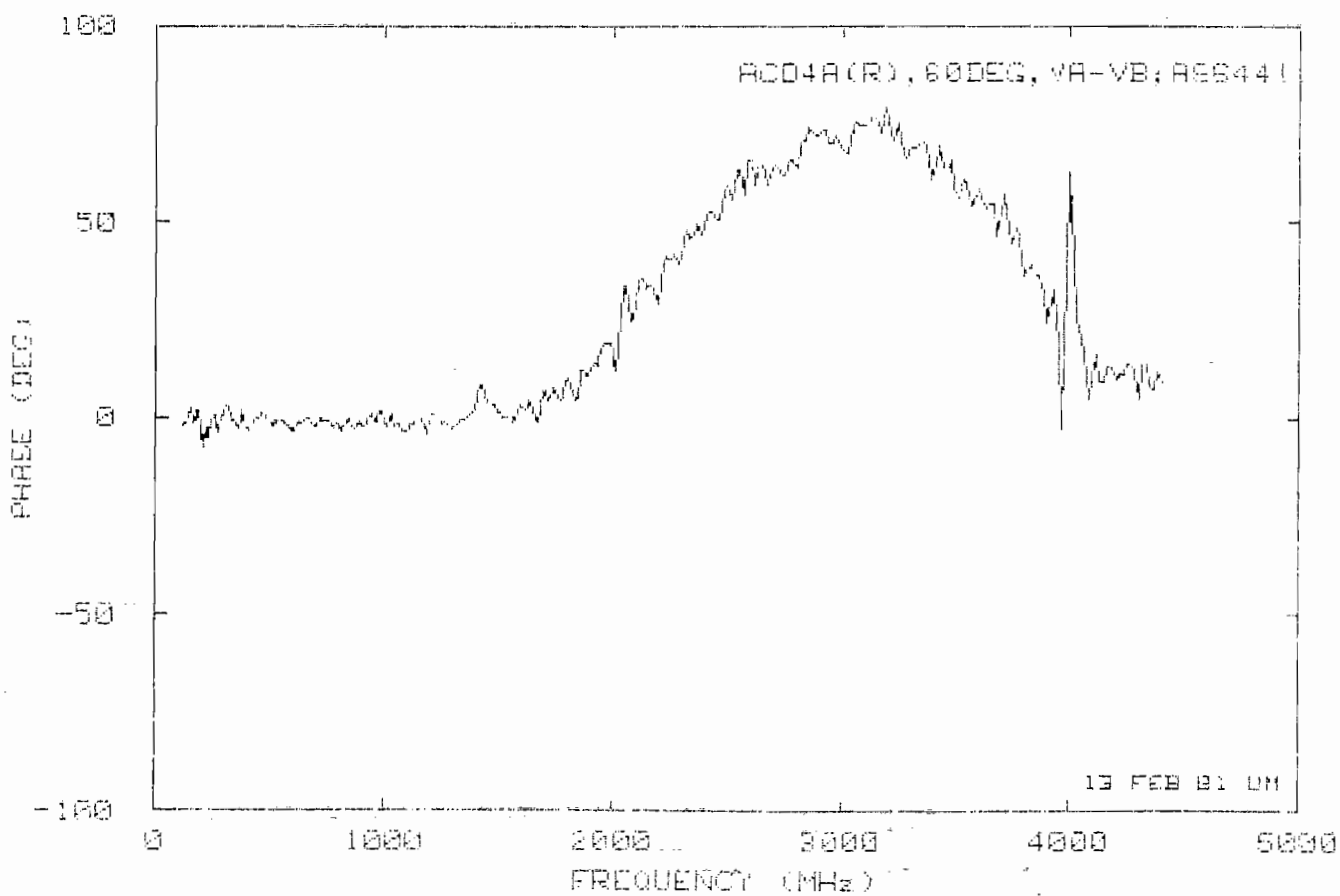
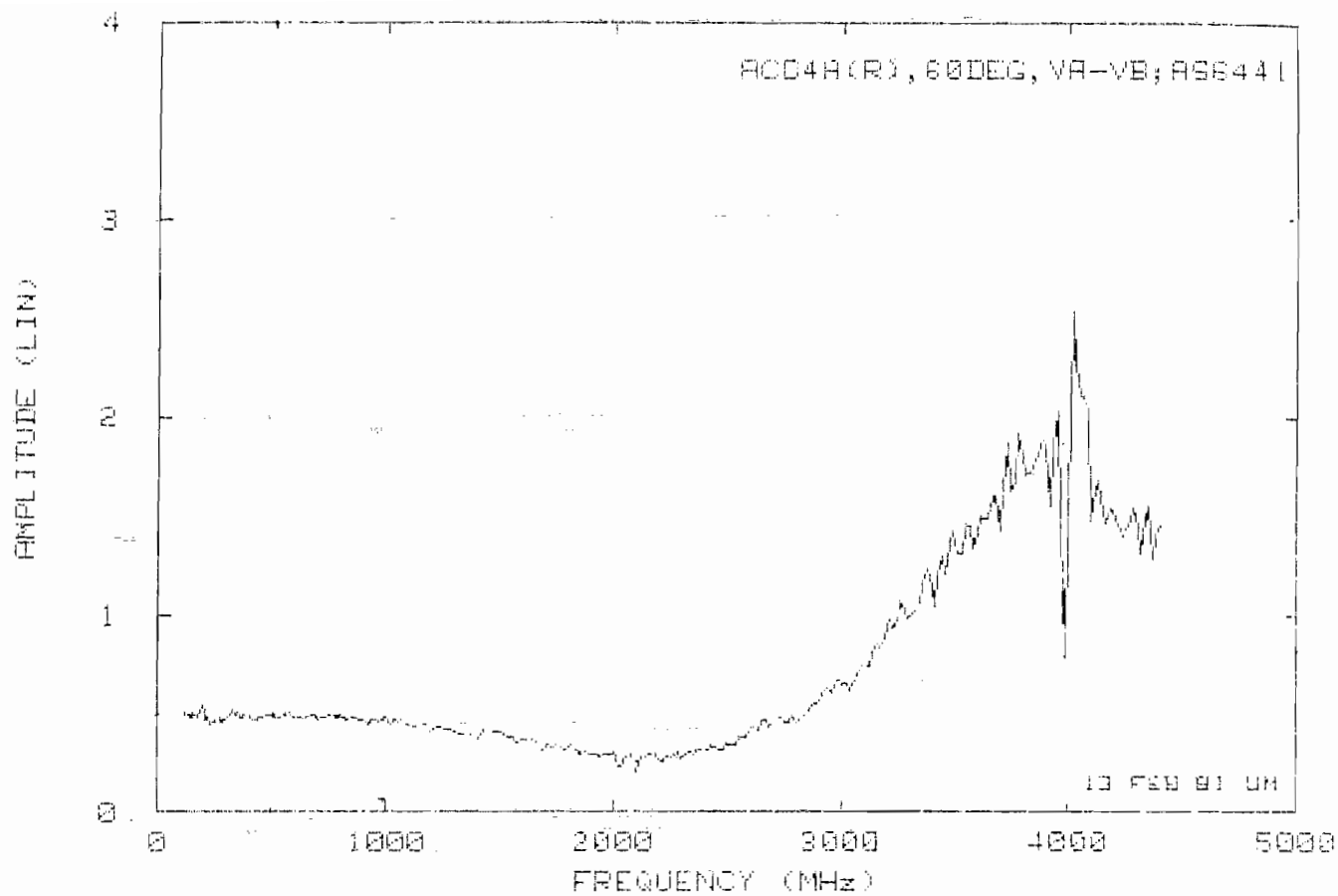


Plot A9

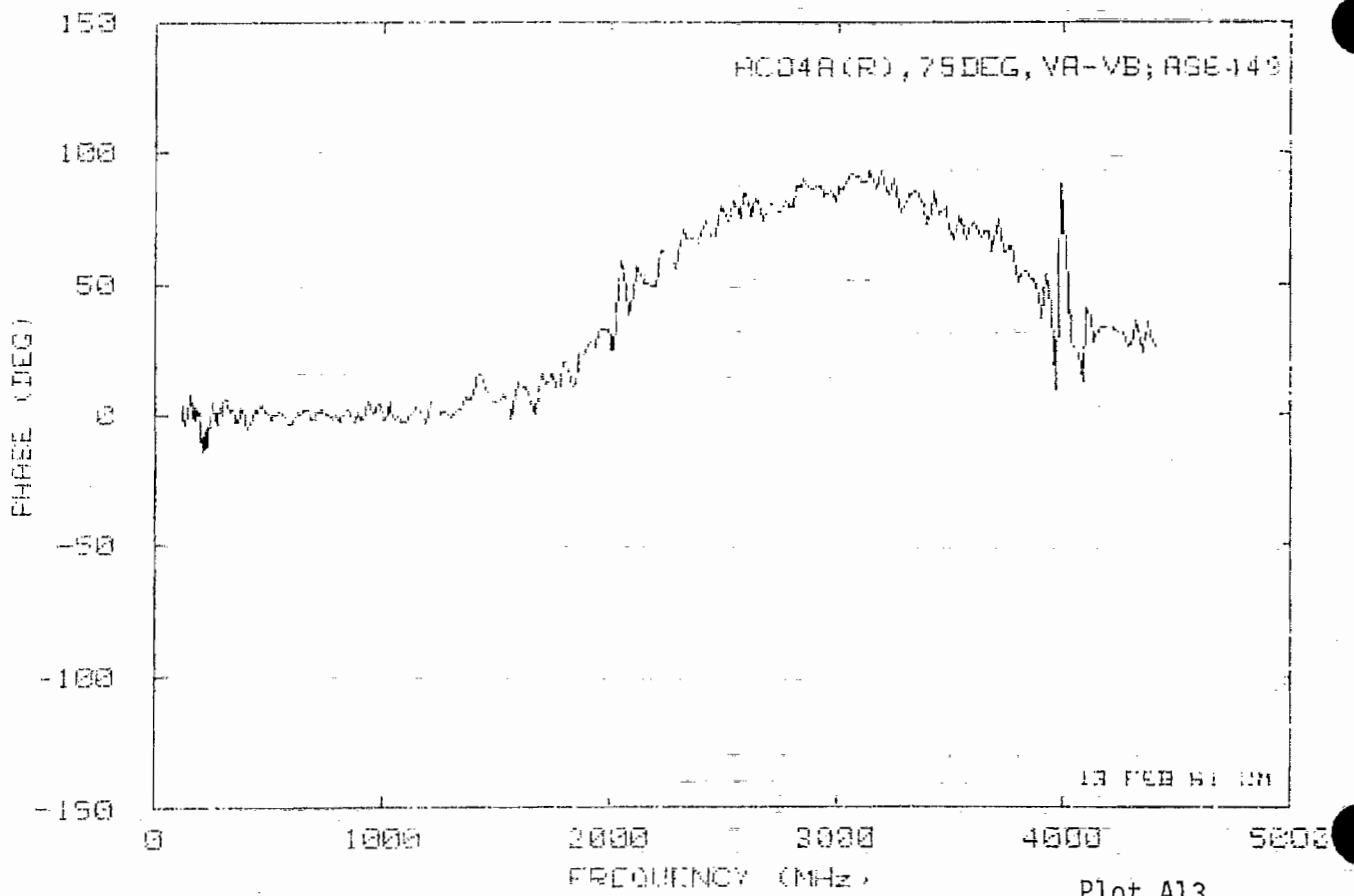
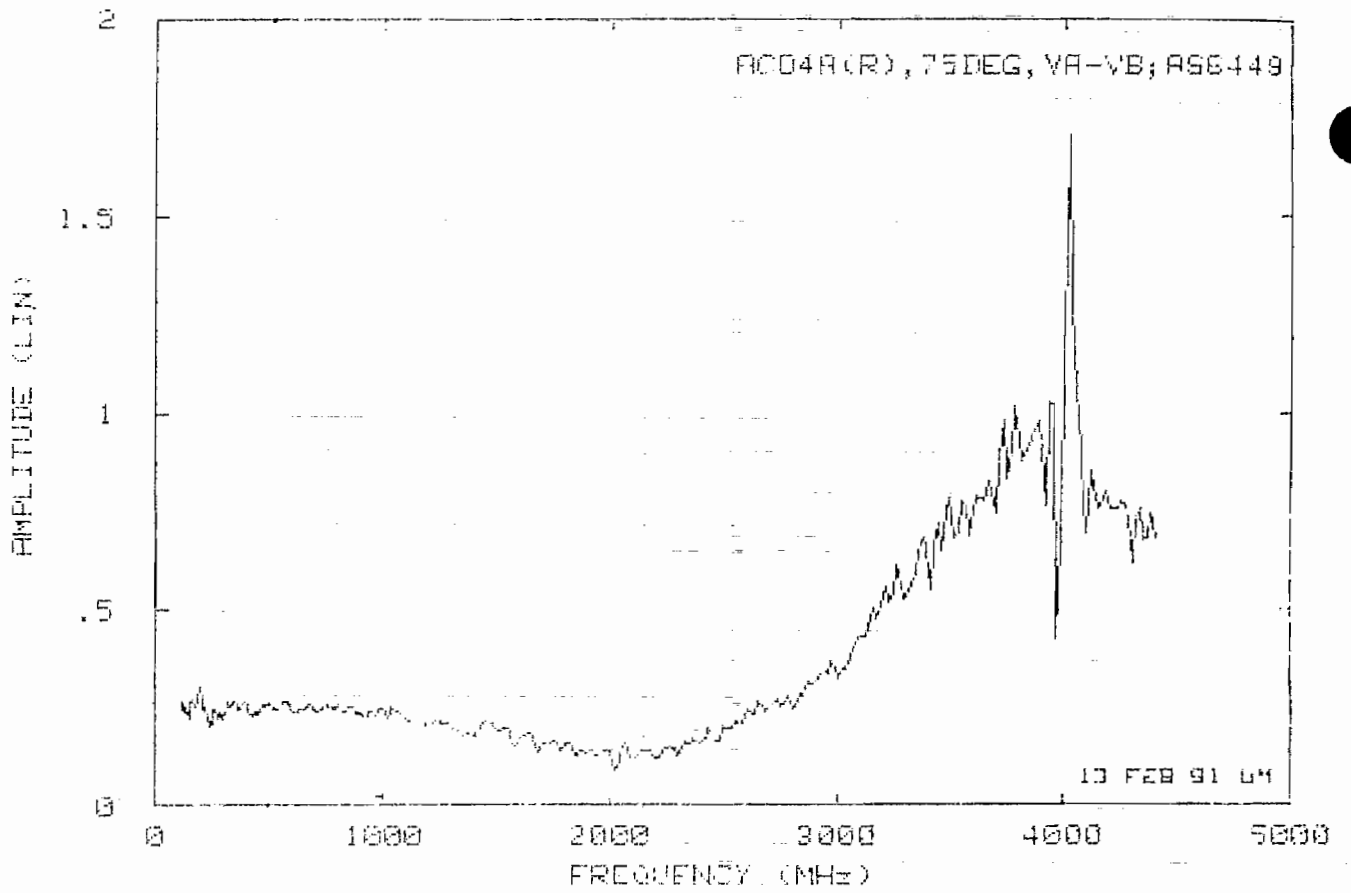


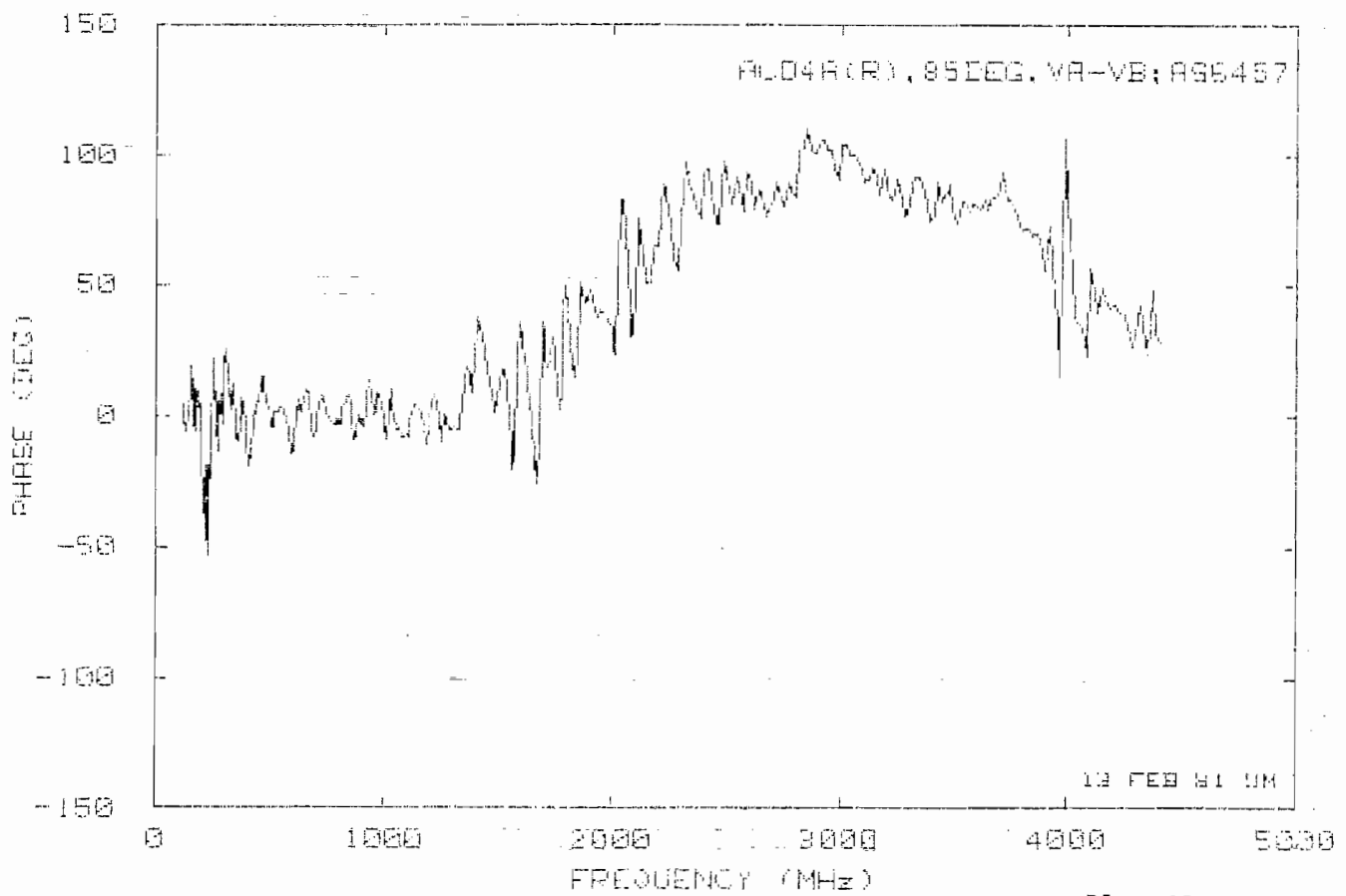
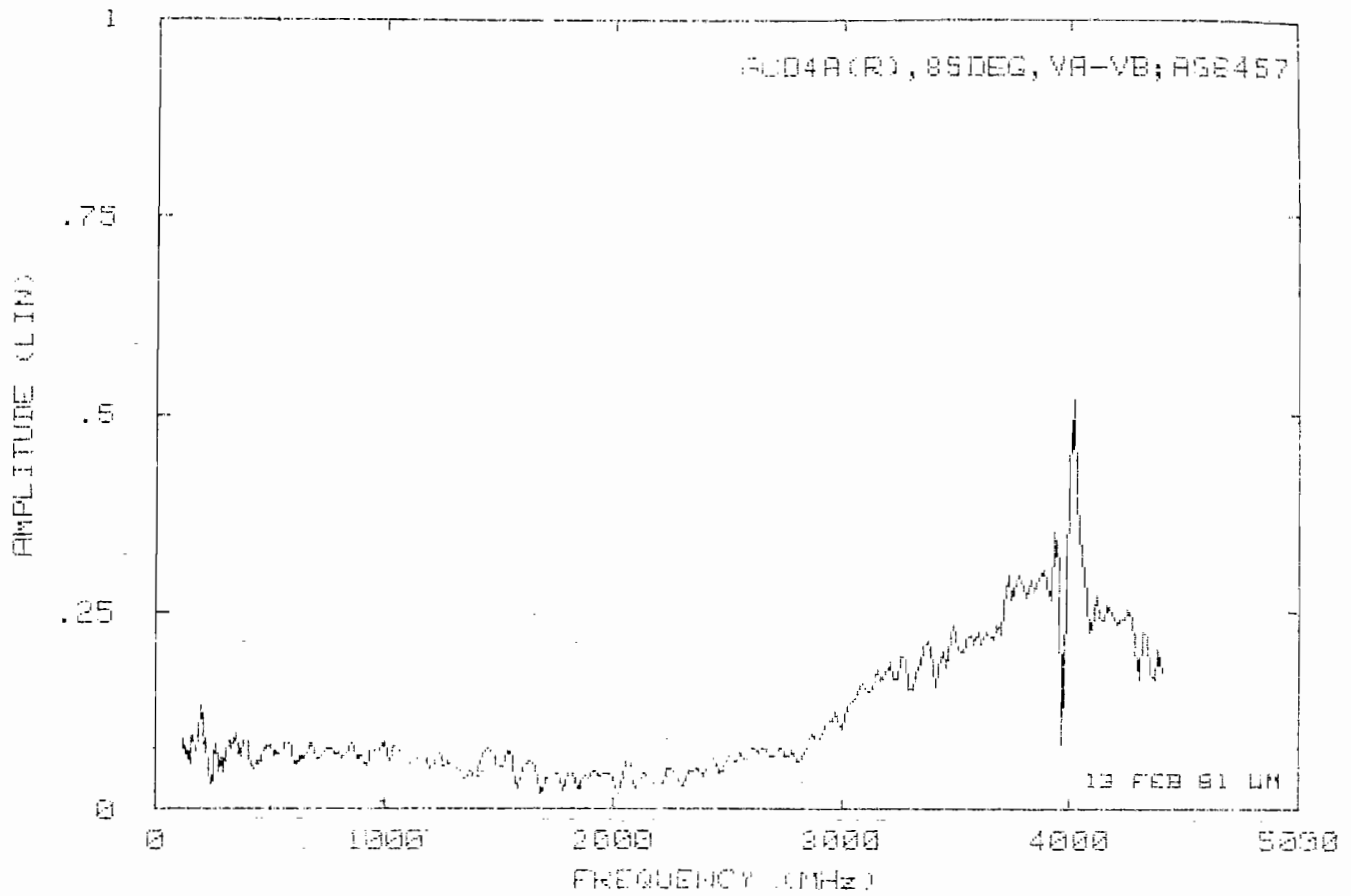


Plot A11

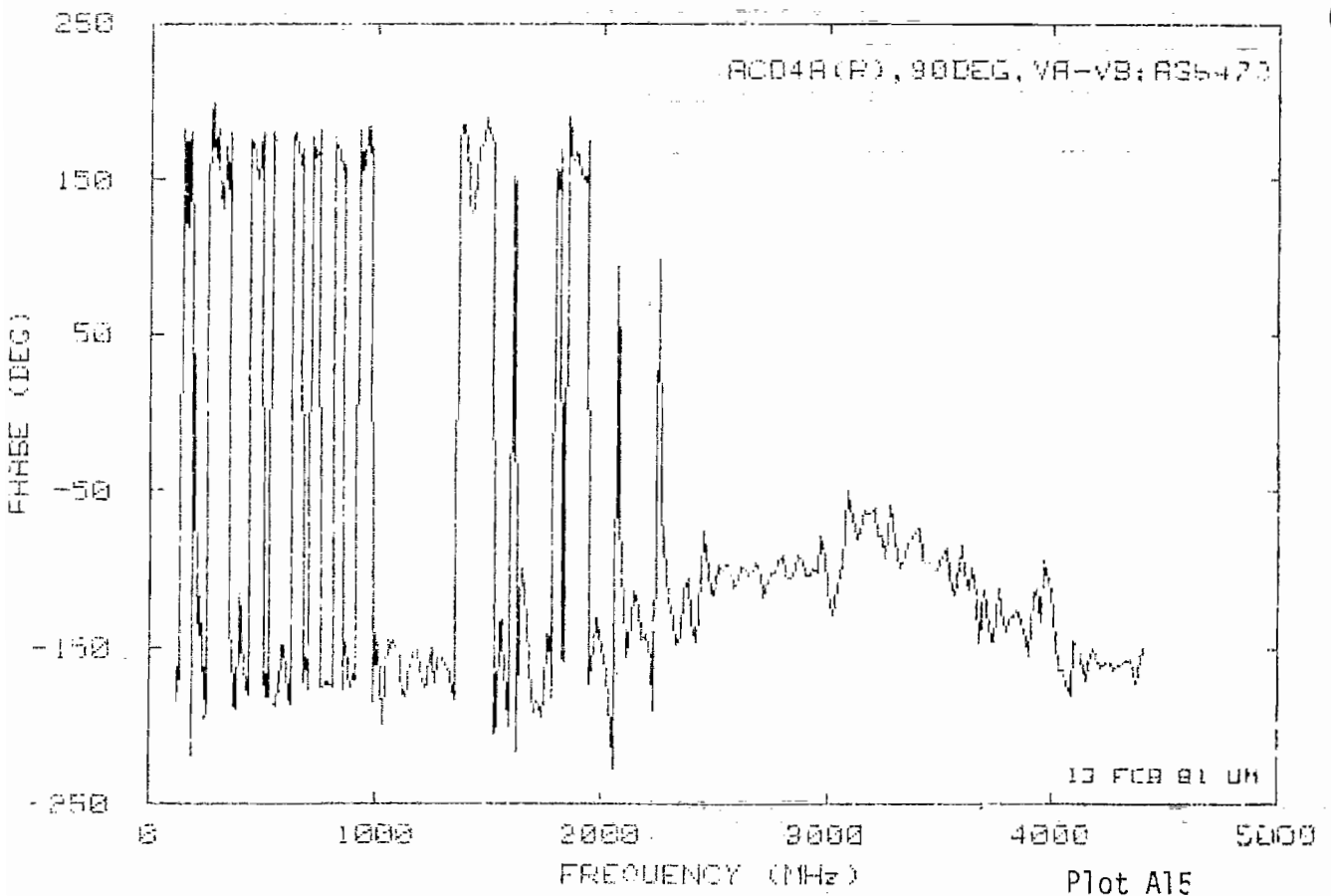
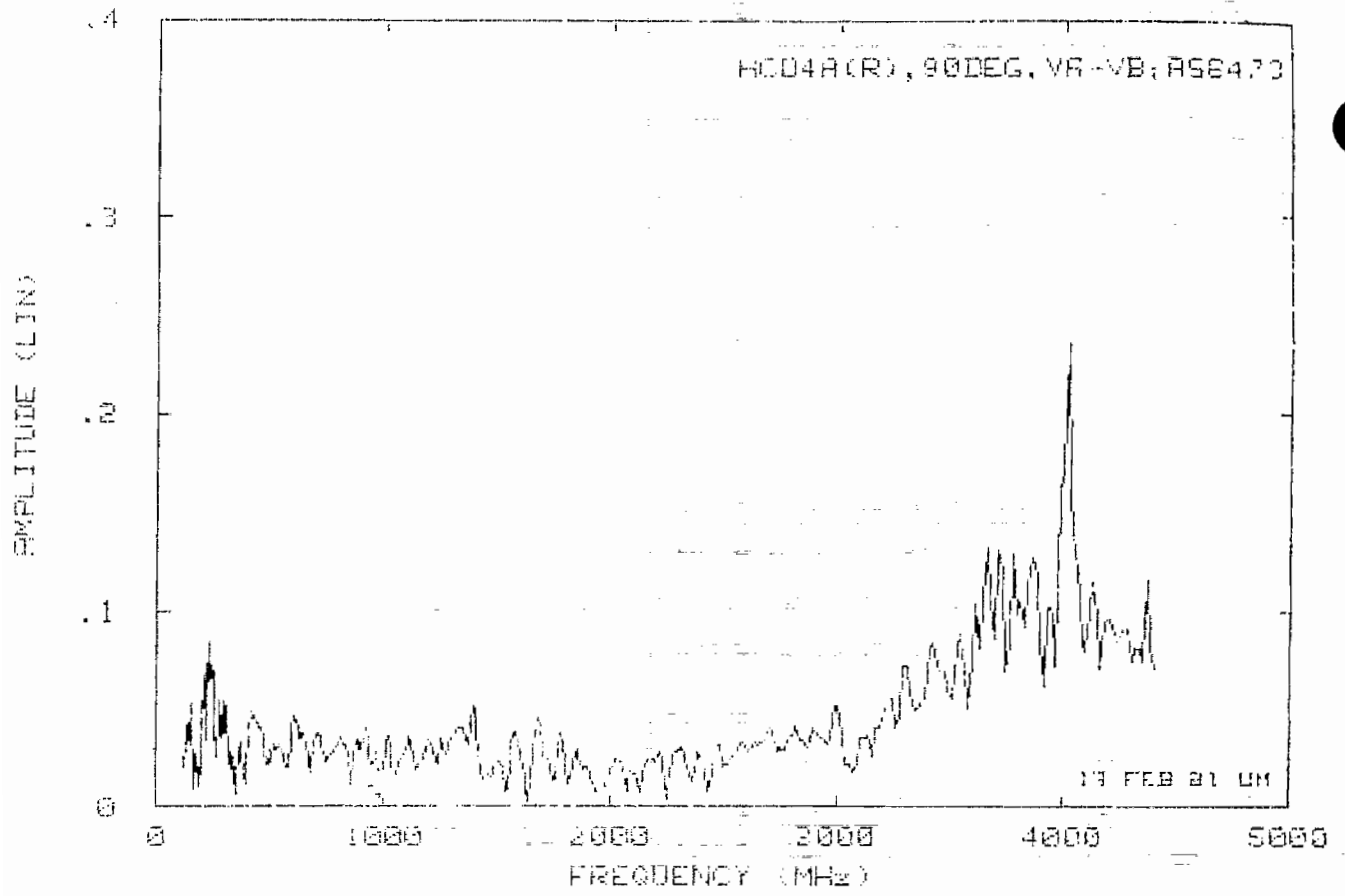


Plot A12





Plot A14



APPENDIX B: MGL-2D(A) AND MGL-6A(A) DIPOLE RESPONSE DATA (RAW)

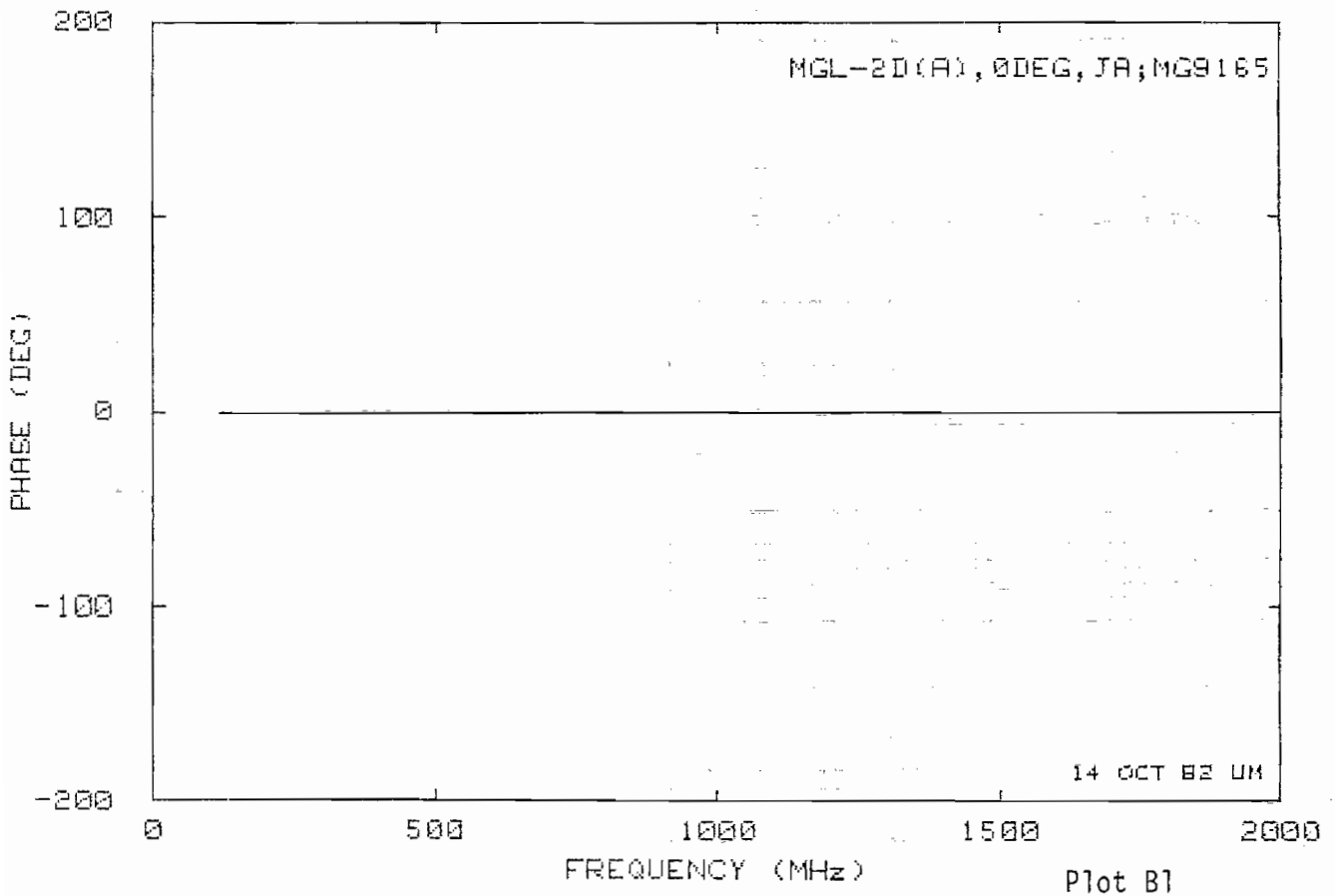
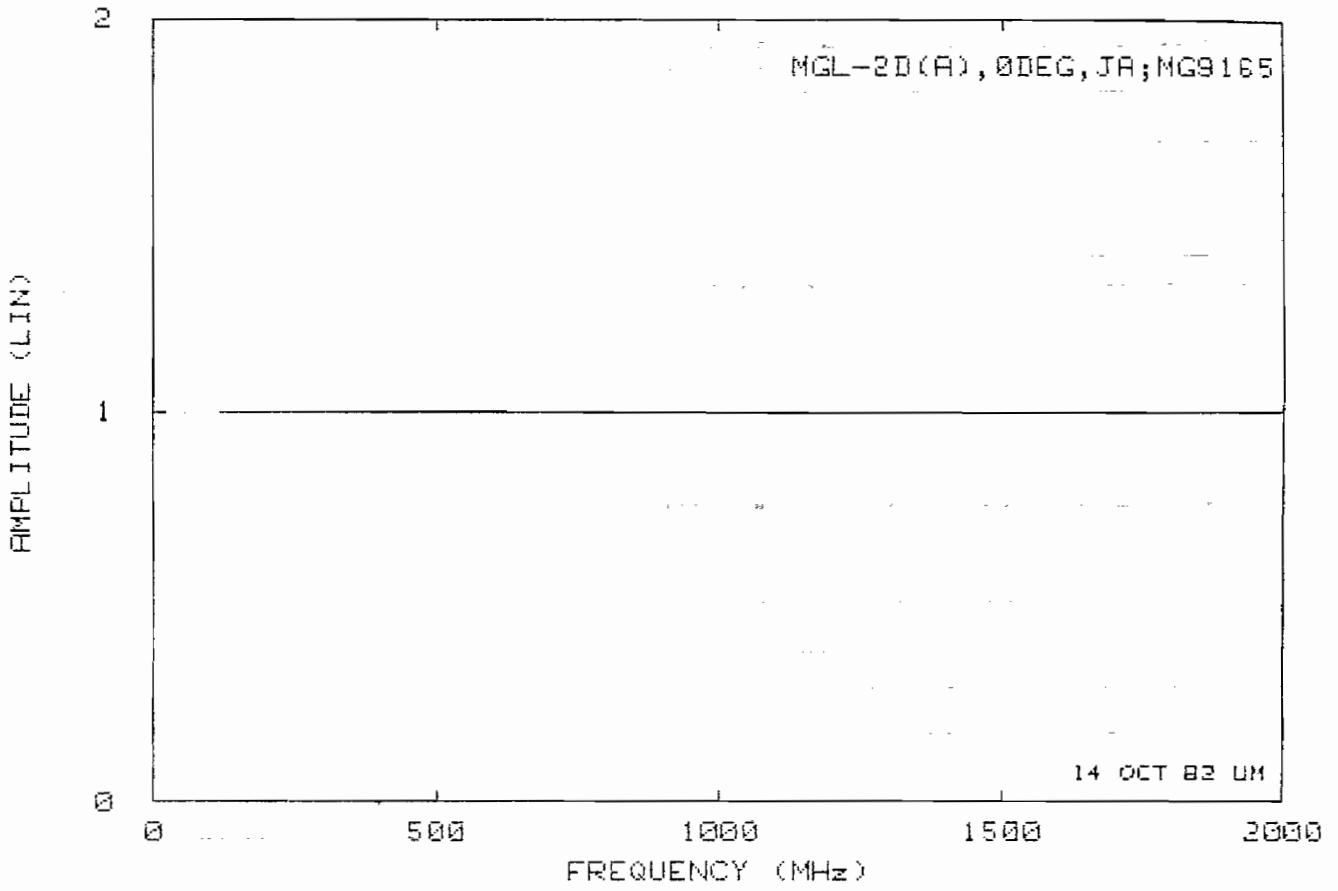
Measured data are presented for the MGL-2 and MGL-6 sensors as functions of frequency for the rotation angles $\theta = 0(15)90$ degrees in the dipole response plane. For each sensor, data are shown for gap No. 1 at $\phi = 45$ and 90 degrees (see Fig. 25), and all data are normalized to the measured values for $\theta = 0$.

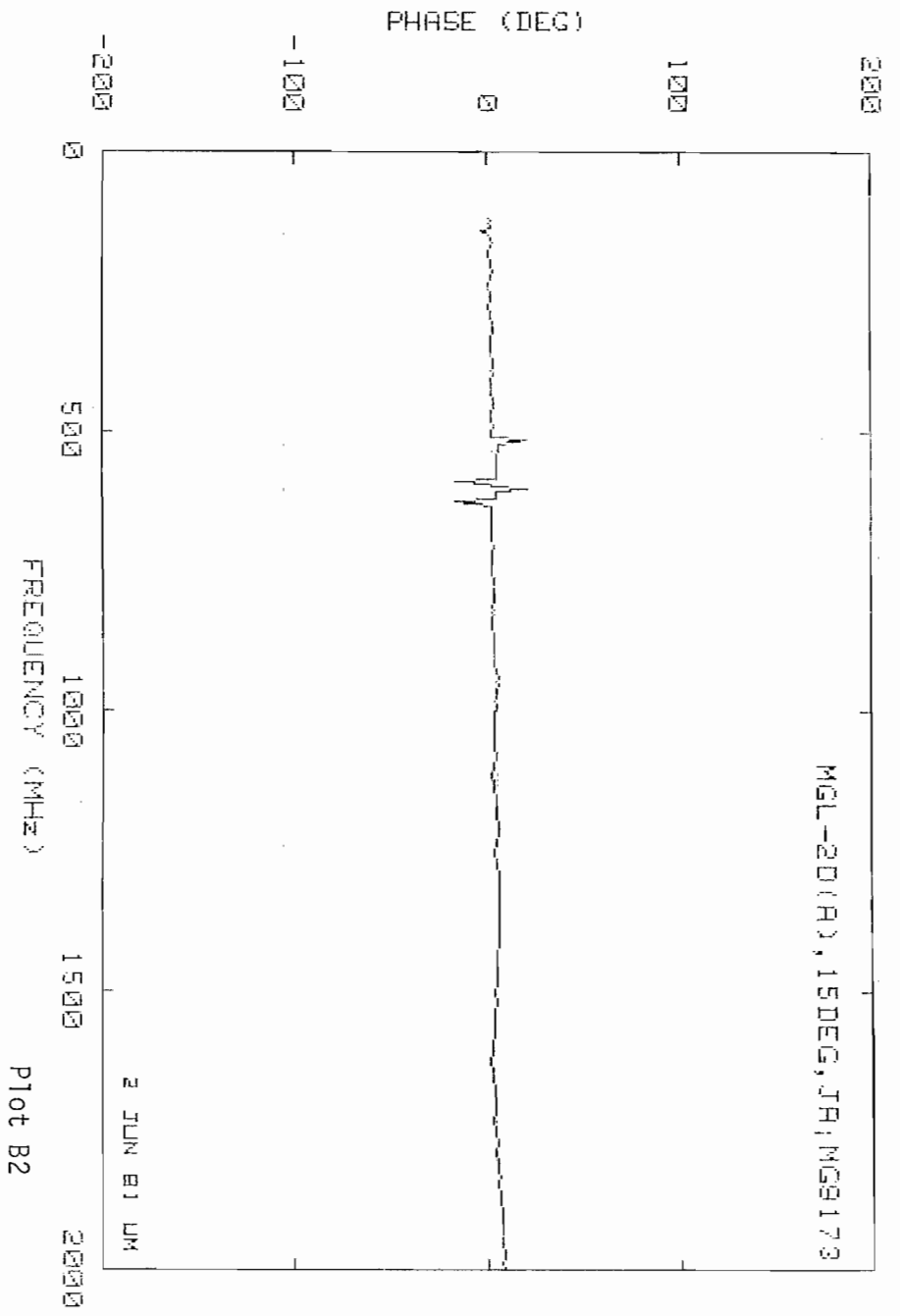
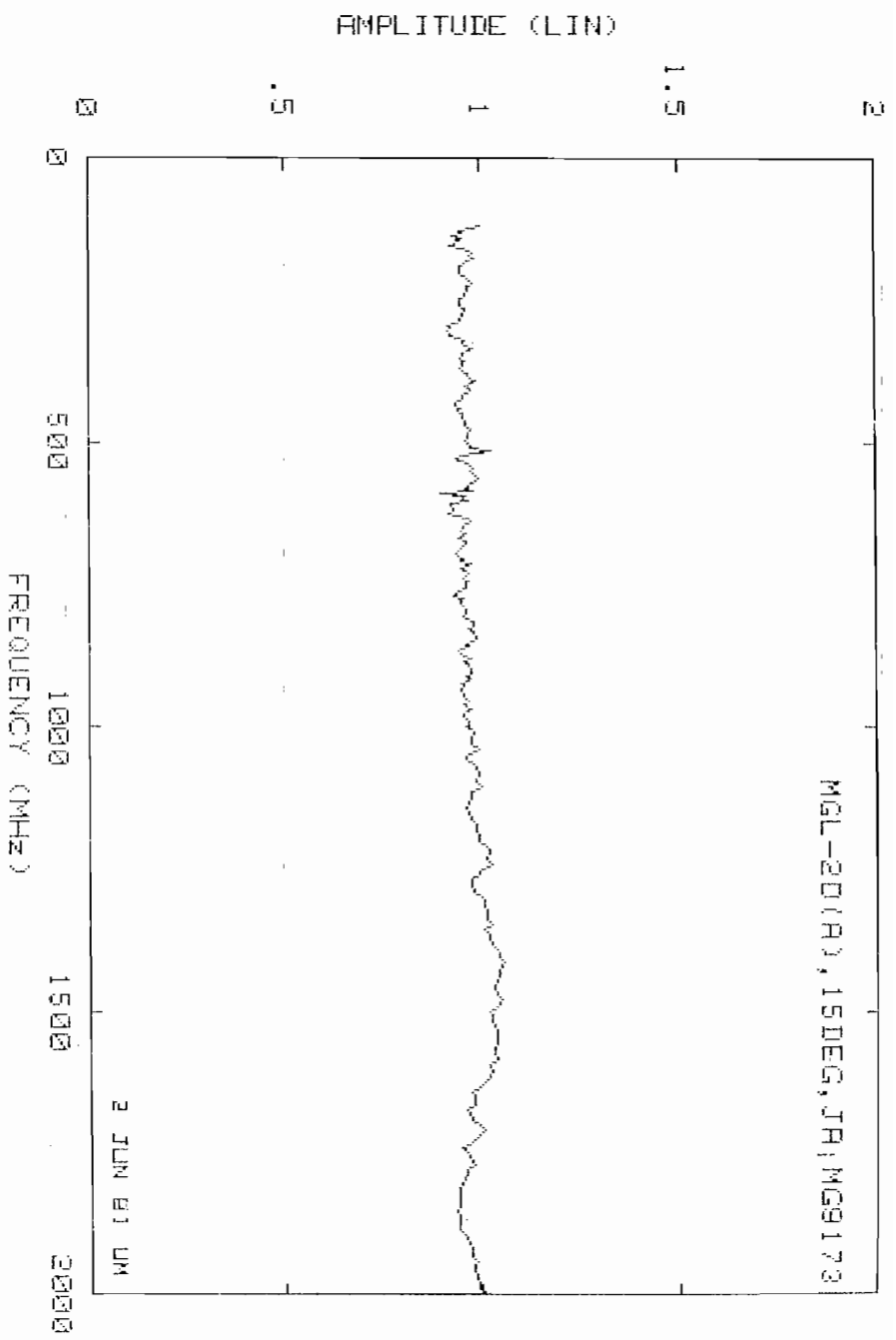
Table B1: List of MGL-2 Dipole Data Plots

θ (degrees)	Gap No. 1 at $\phi = 45^\circ$		Gap No. 1 at $\phi = 90^\circ$	
	Plot No.	File No.	Plot No.	File No.
0	B1	MG 9165	B8	MG 9357
15	B2	MG 9173	B9	MG 9365
30	B3	MG 9201	B10	MG 9373
45	B4	MG 9209	B11	MG 9401
60	B5	MG 9217	B12	MG 9409
75	B6	MG 9225	B13	MG 9417
90	B7	MG 9233	B14	MG 9425

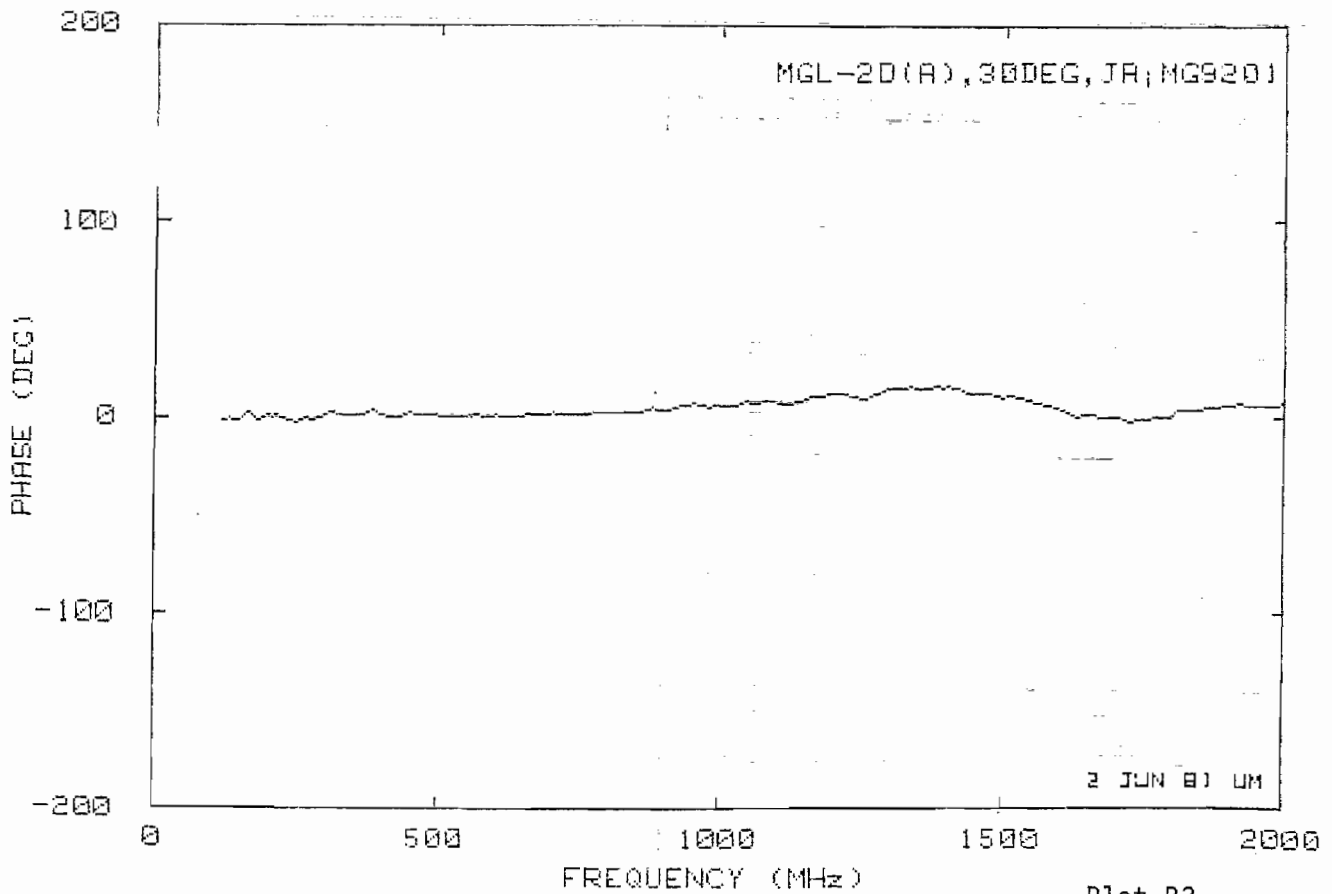
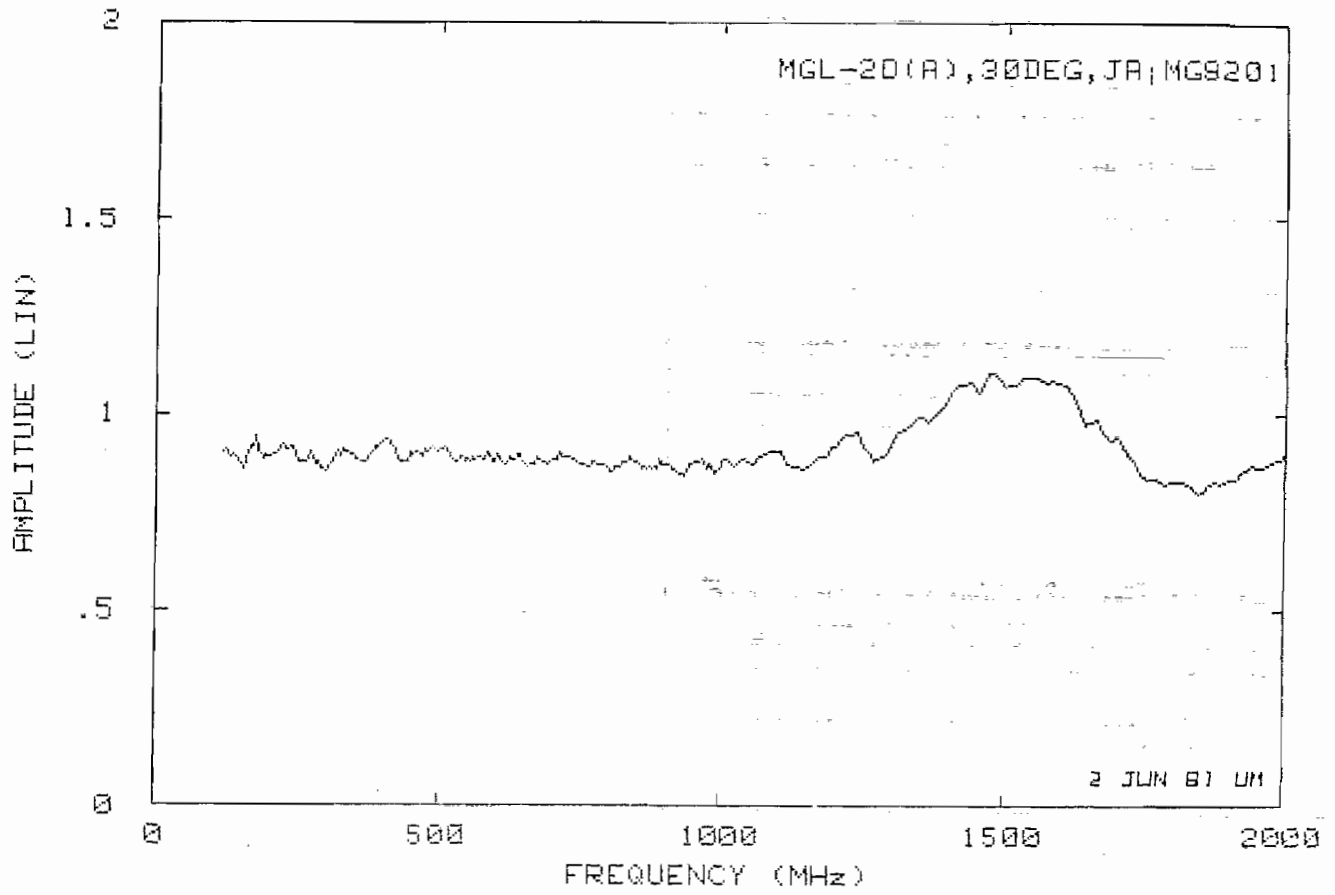
Table B2: List of MGL-6 Dipole Data Plots

θ (degrees)	Gap No. 1 at $\phi = 45^\circ$		Gap No. 1 at $\phi = 90^\circ$	
	Plot No.	File No.	Plot No.	File No.
0	B15	MG 9033	B22	MG 9109
15	B16	MG 9041	B23	MG 9117
30	B17	MG 9049	B24	MG 9125
45	B18	MG 9057	B25	MG 9133
60	B19	MG 9065	B26	MG 9141
75	B20	MG 9073	B27	MG 9149
90	B21	MG 9101	B28	MG 9157

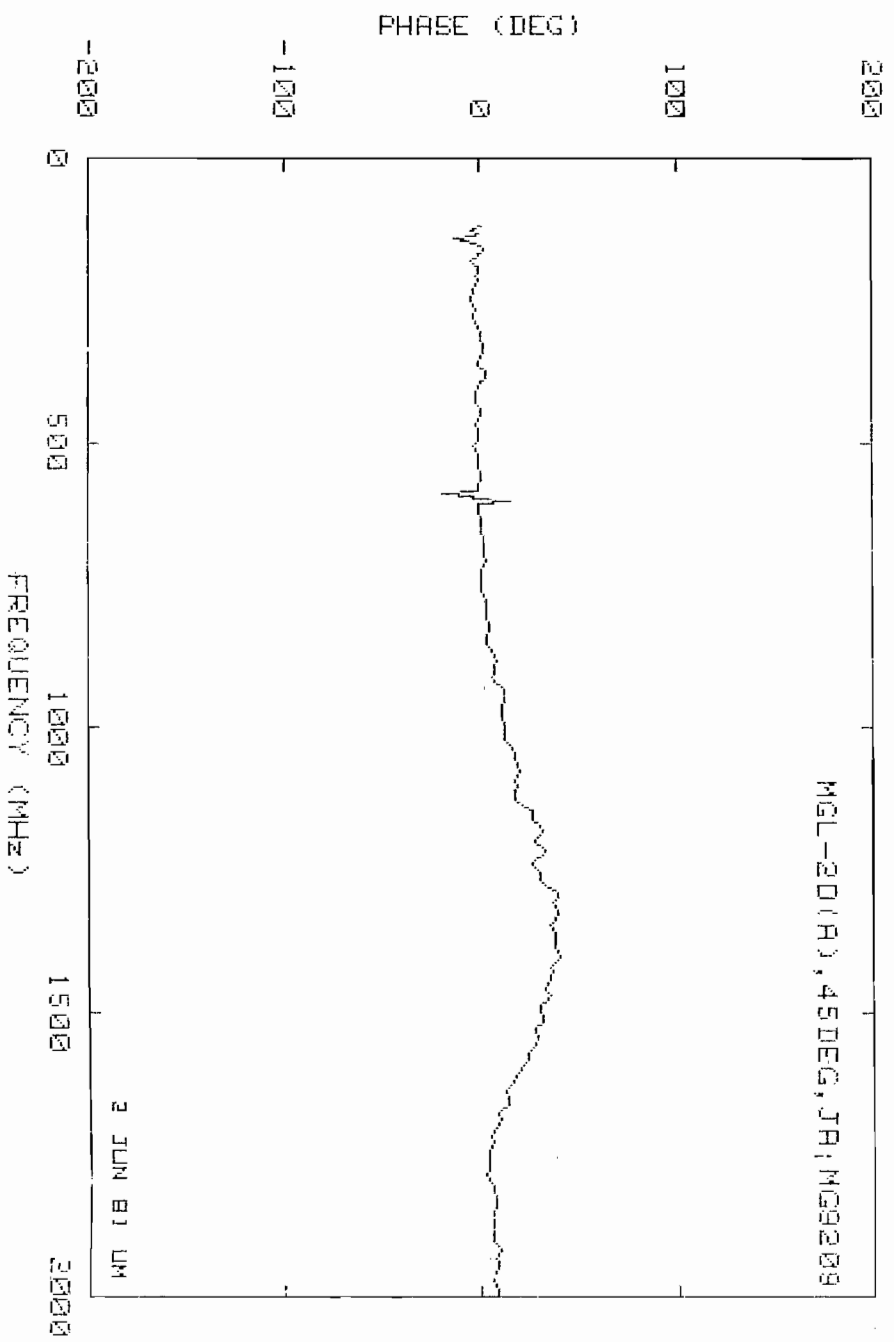
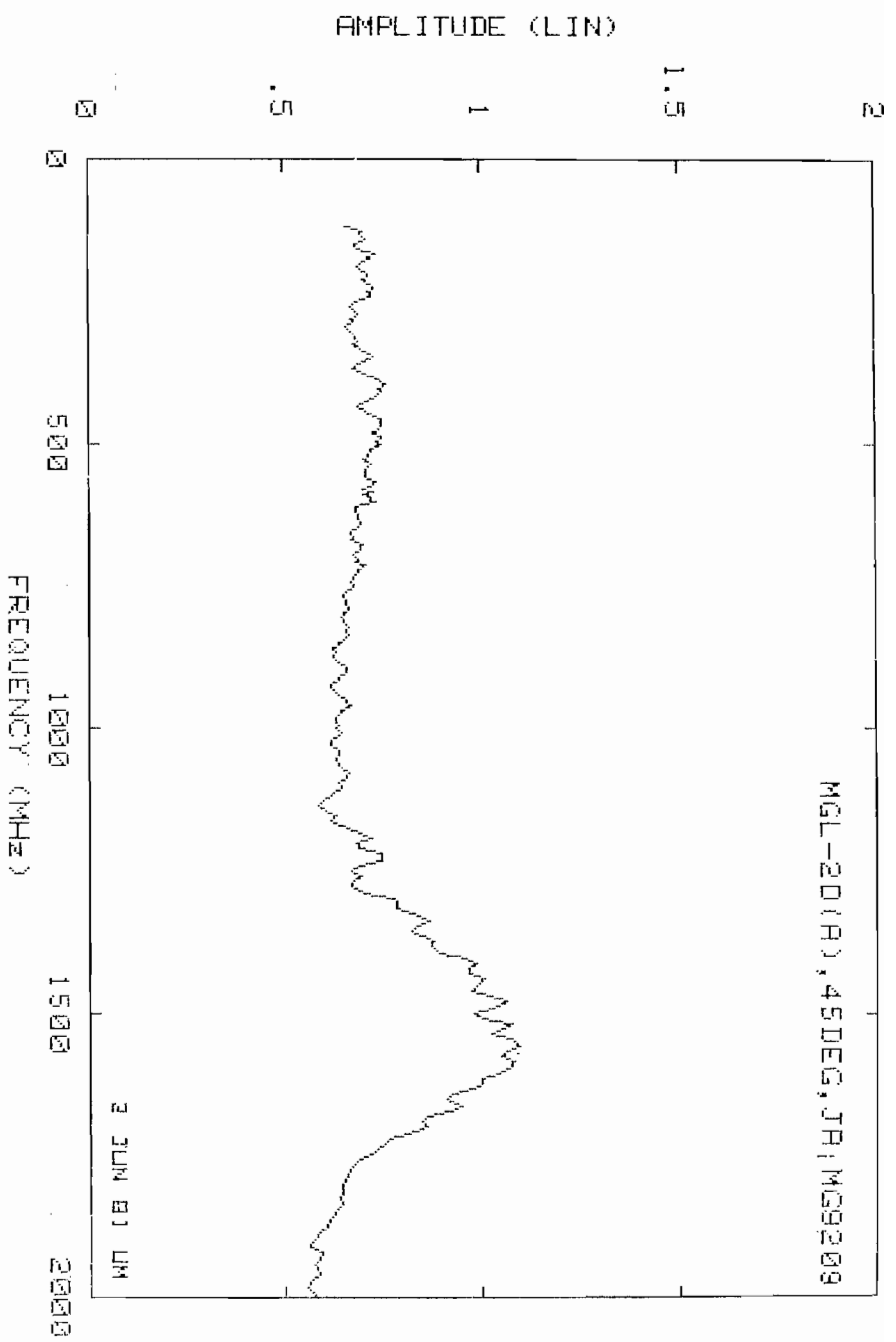


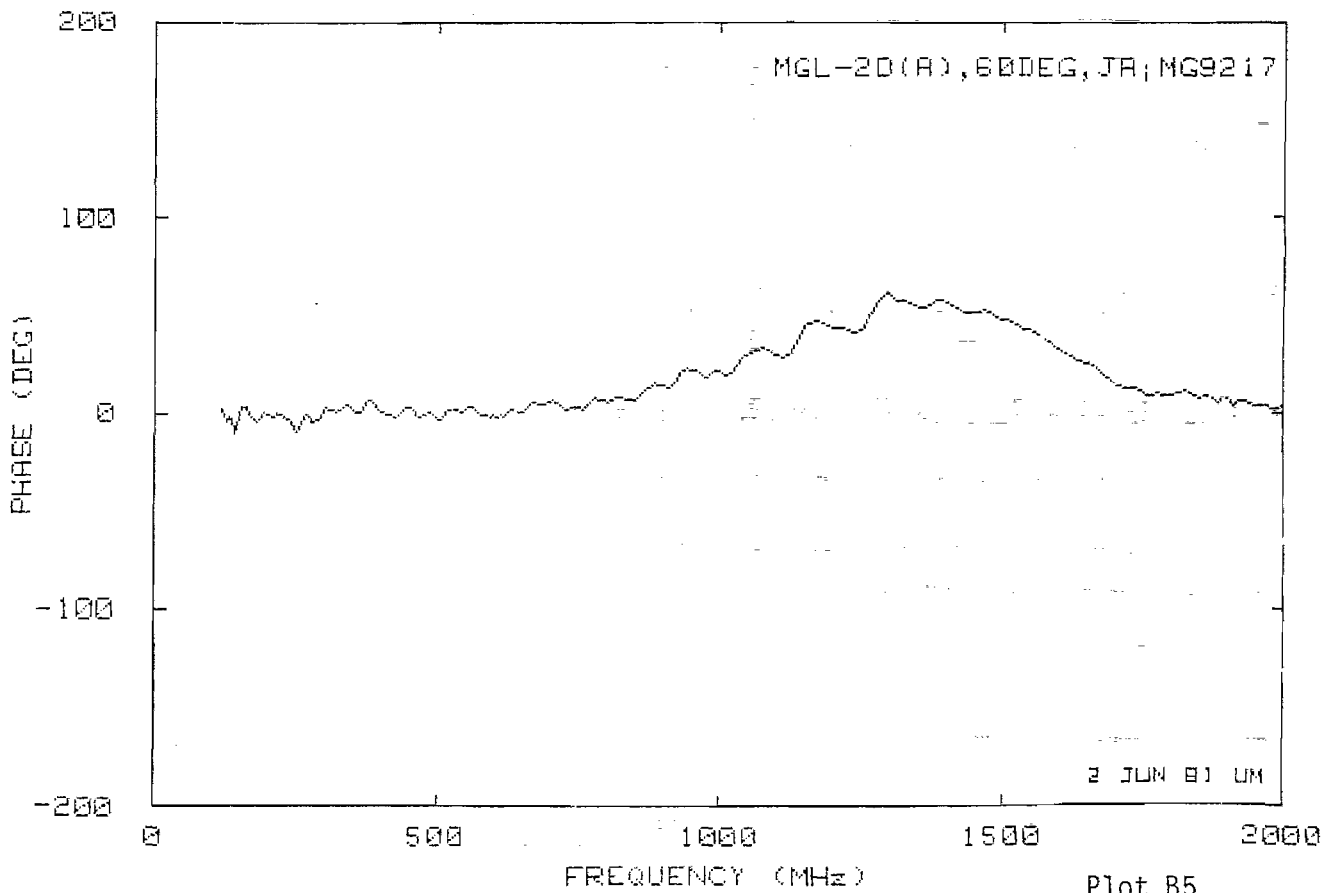
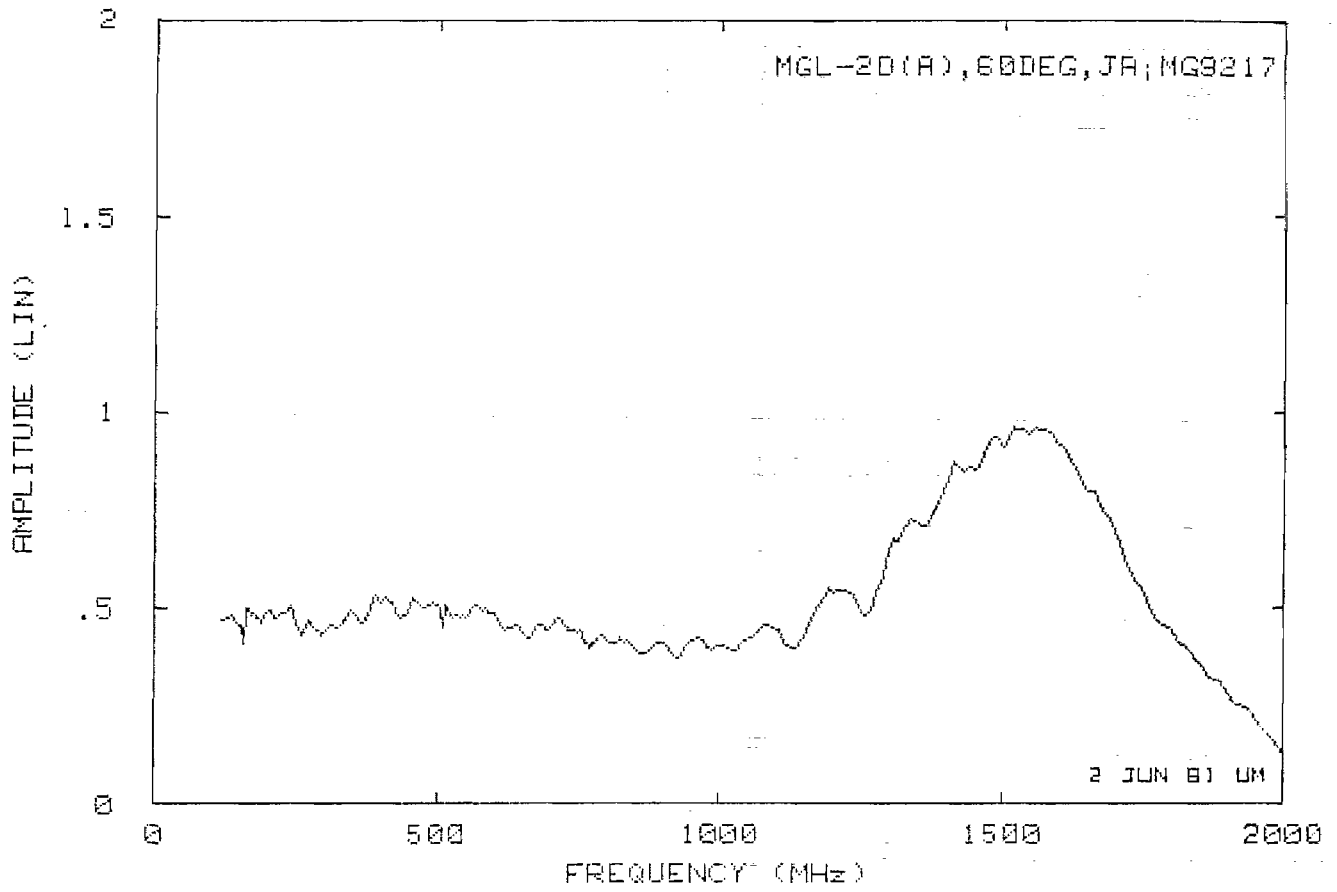


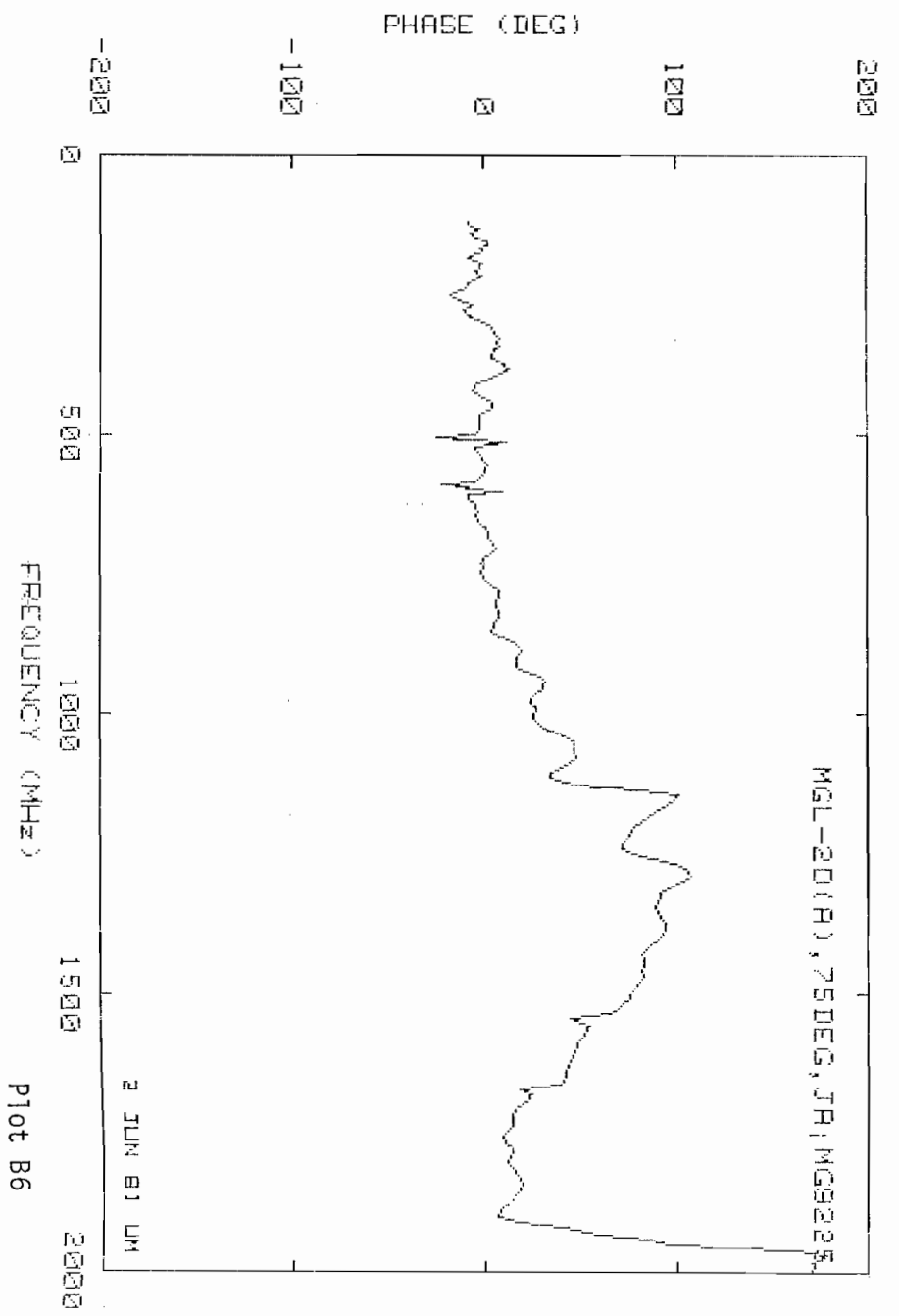
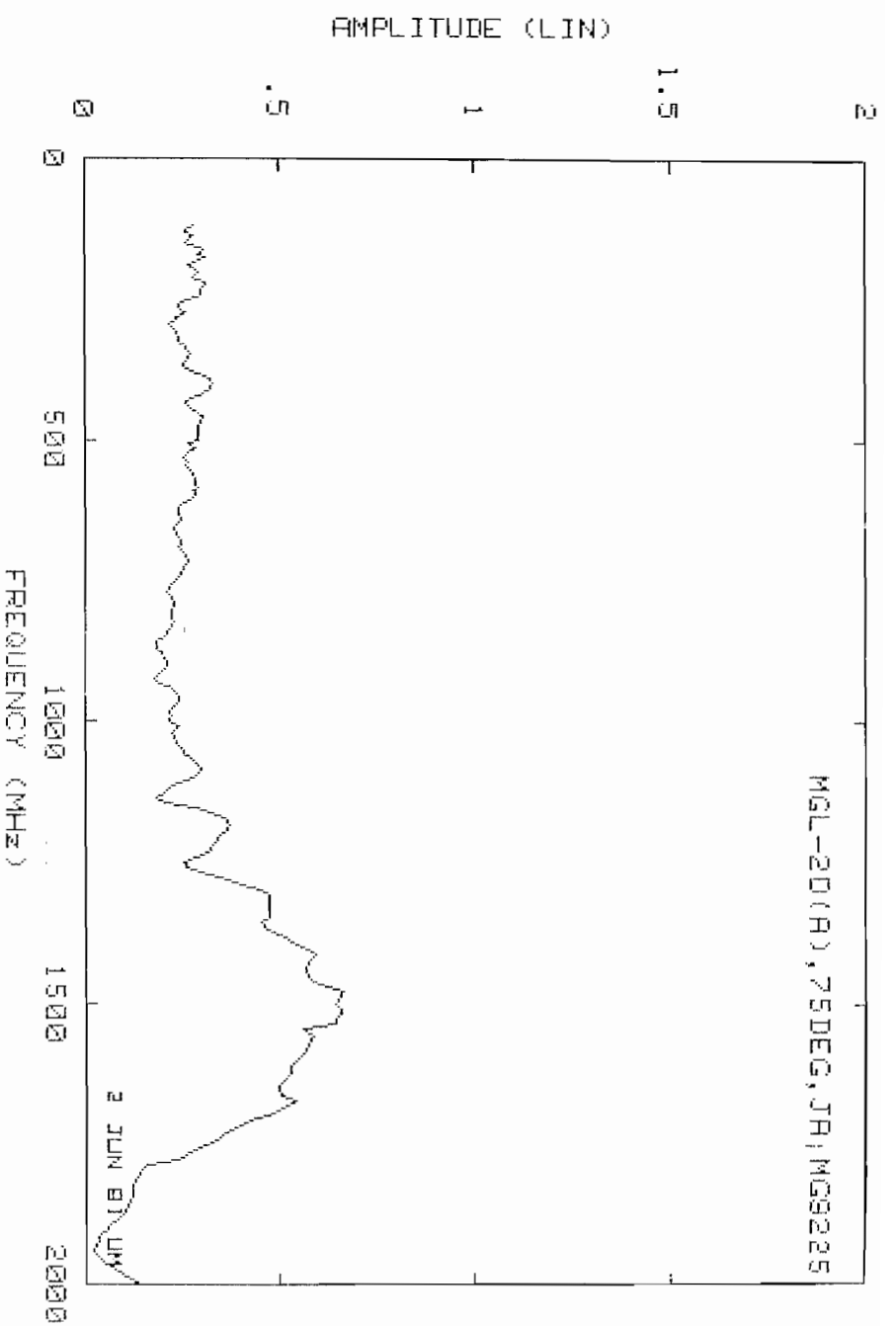
Plot B2

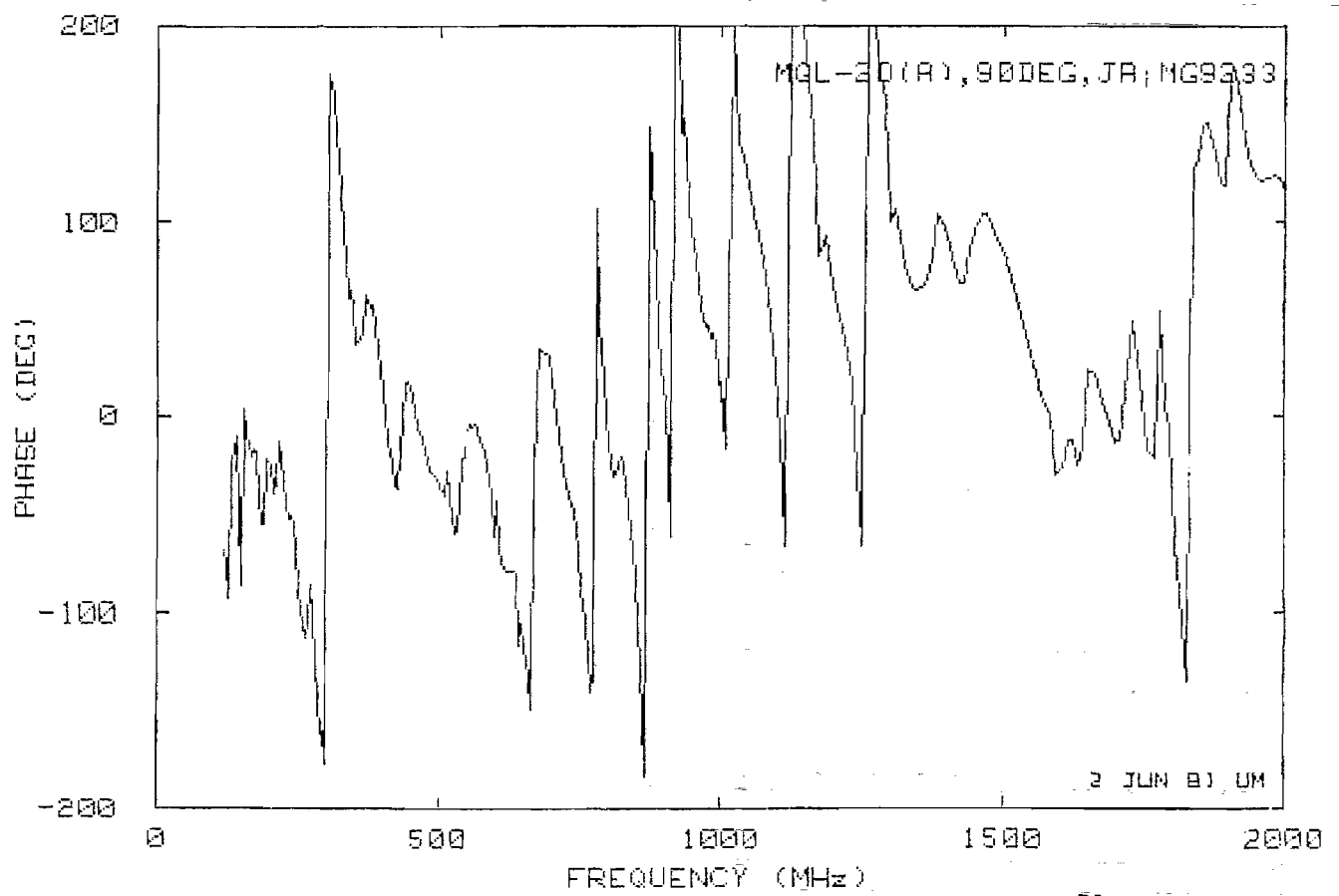
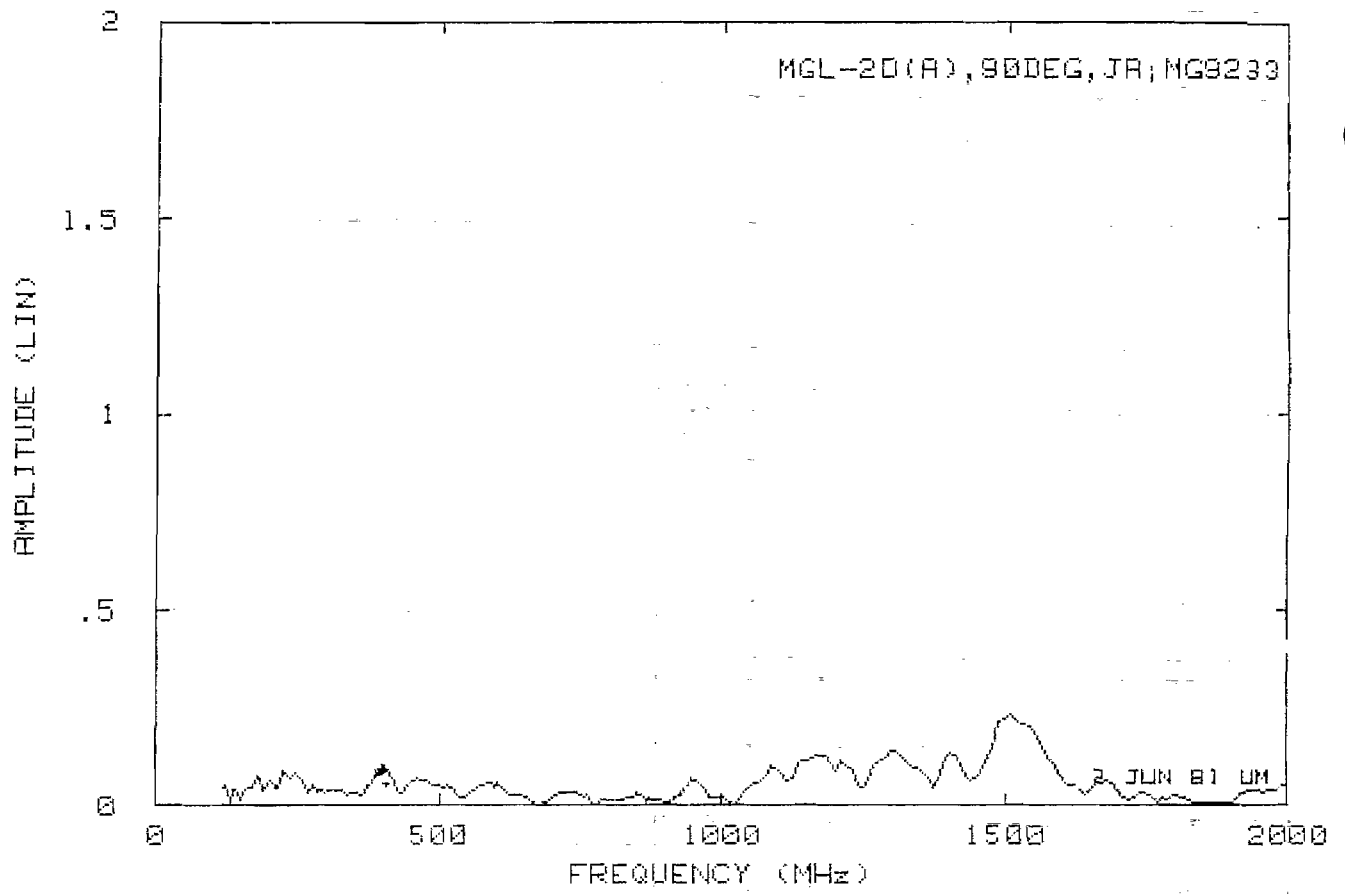


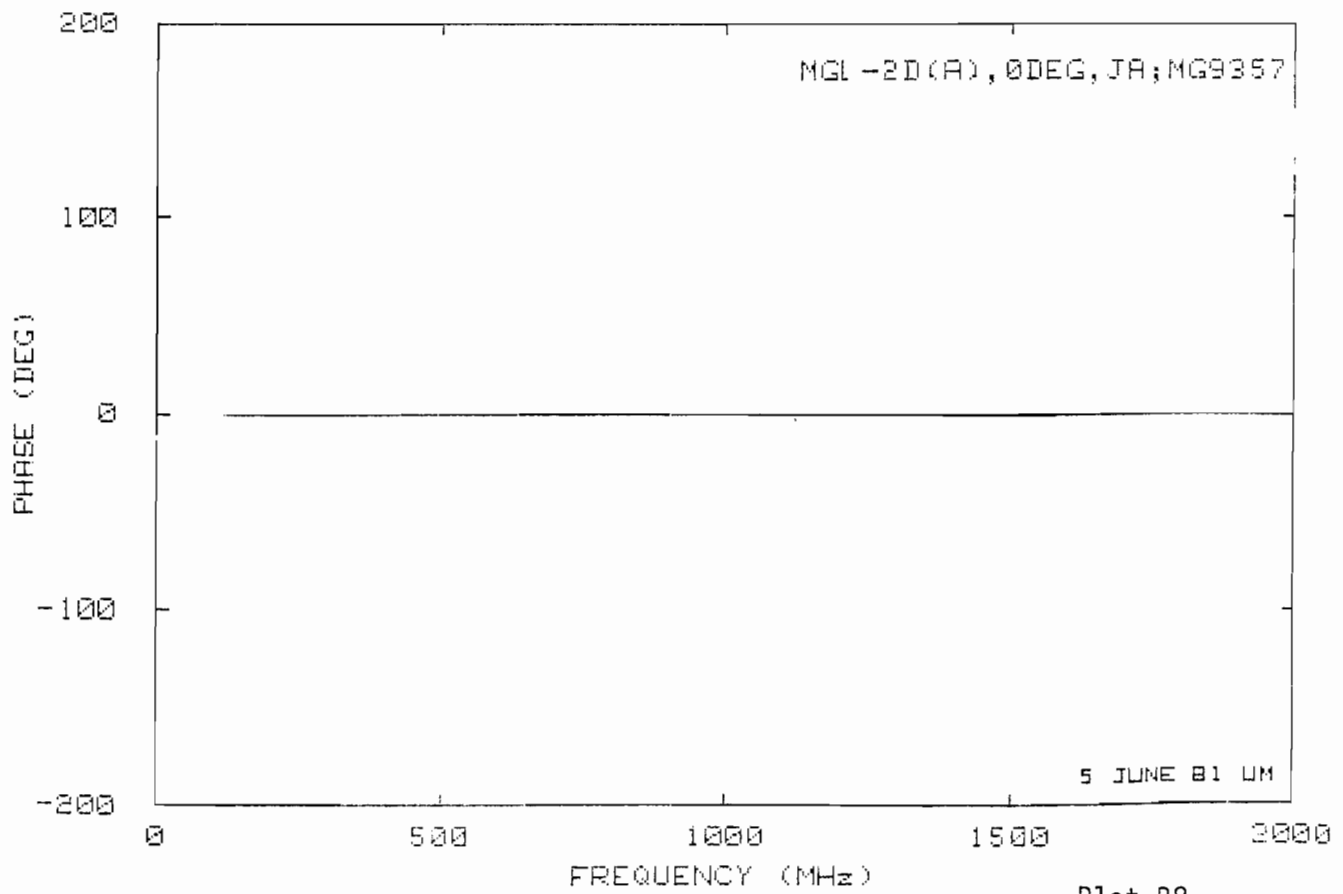
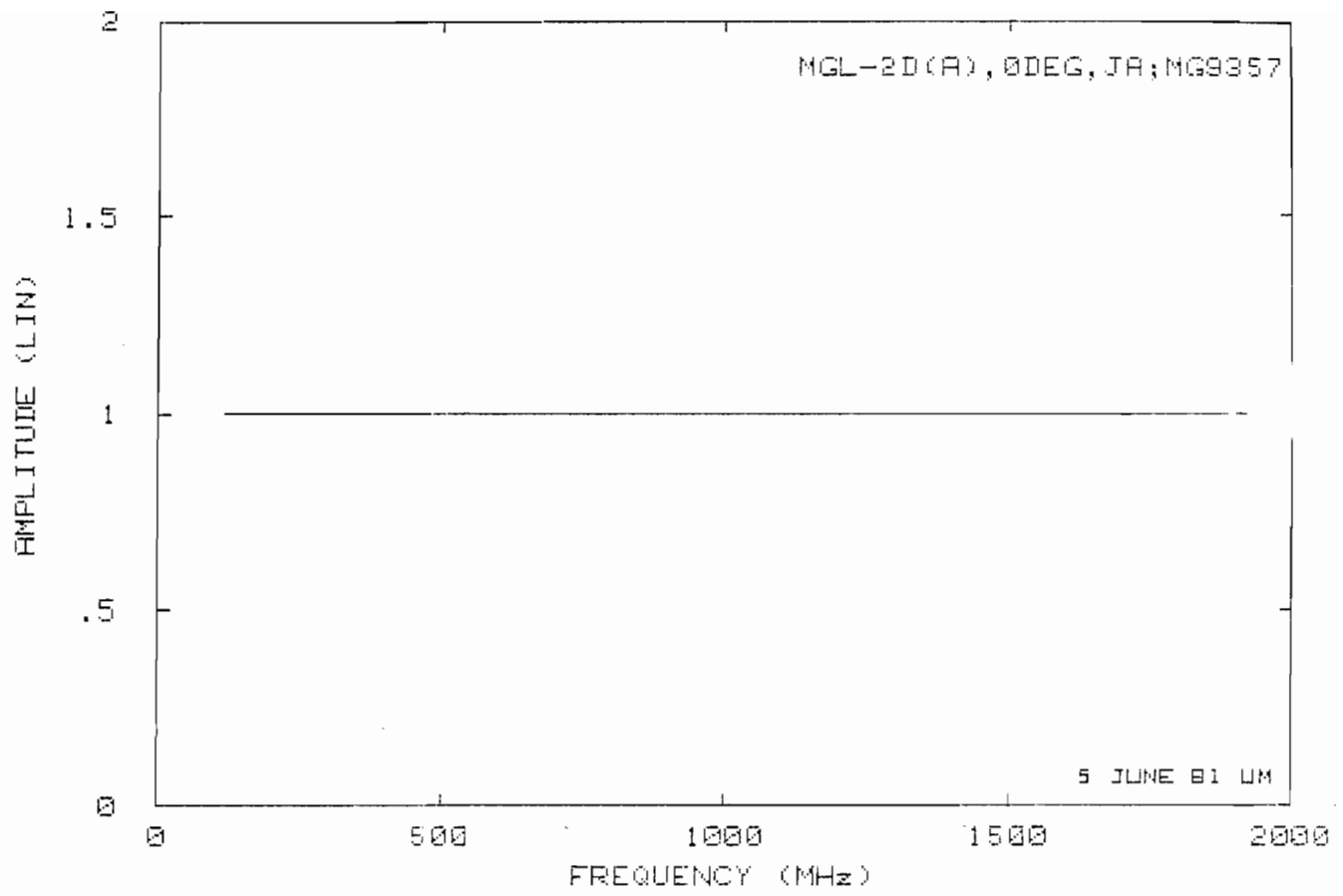
Plot B3



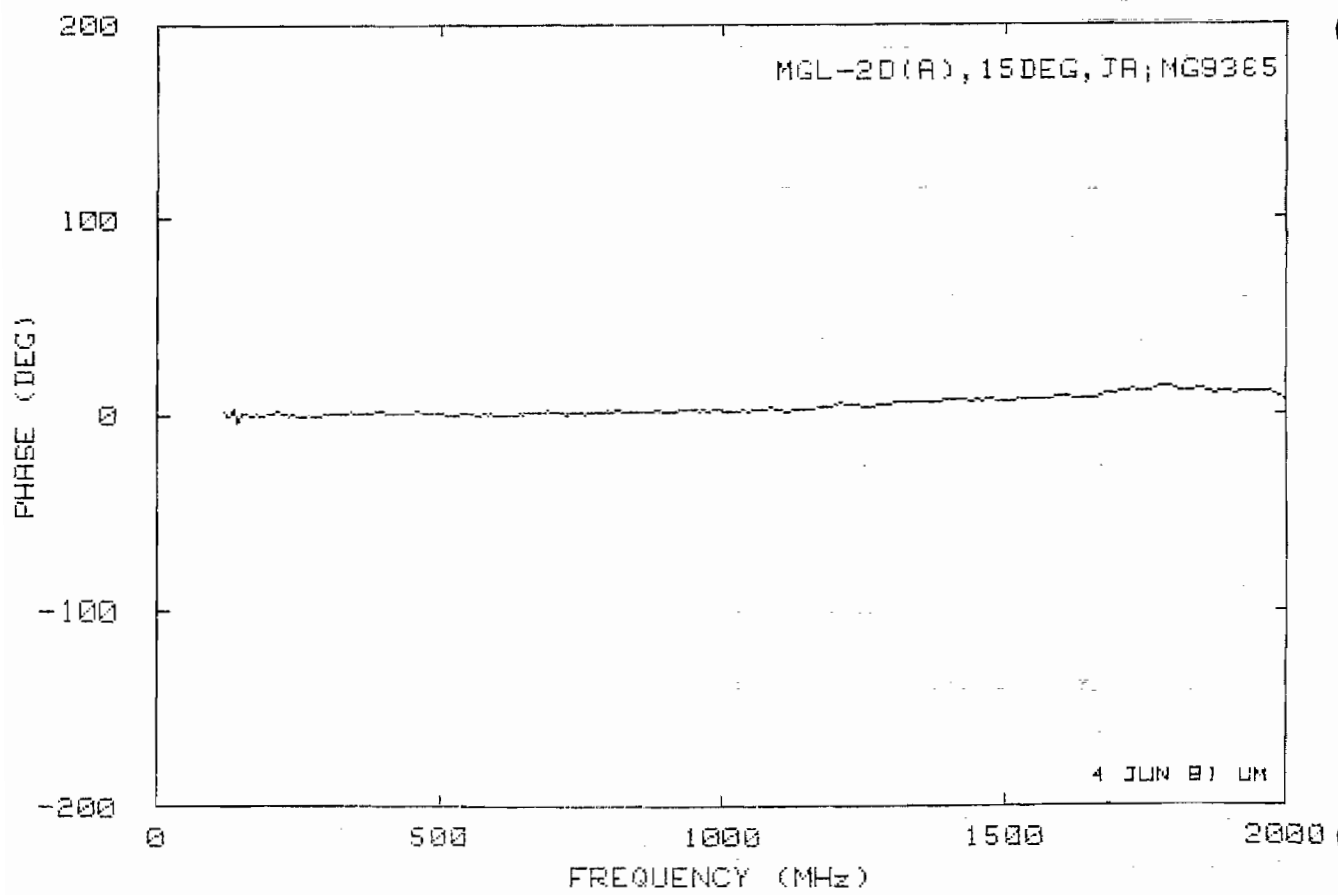
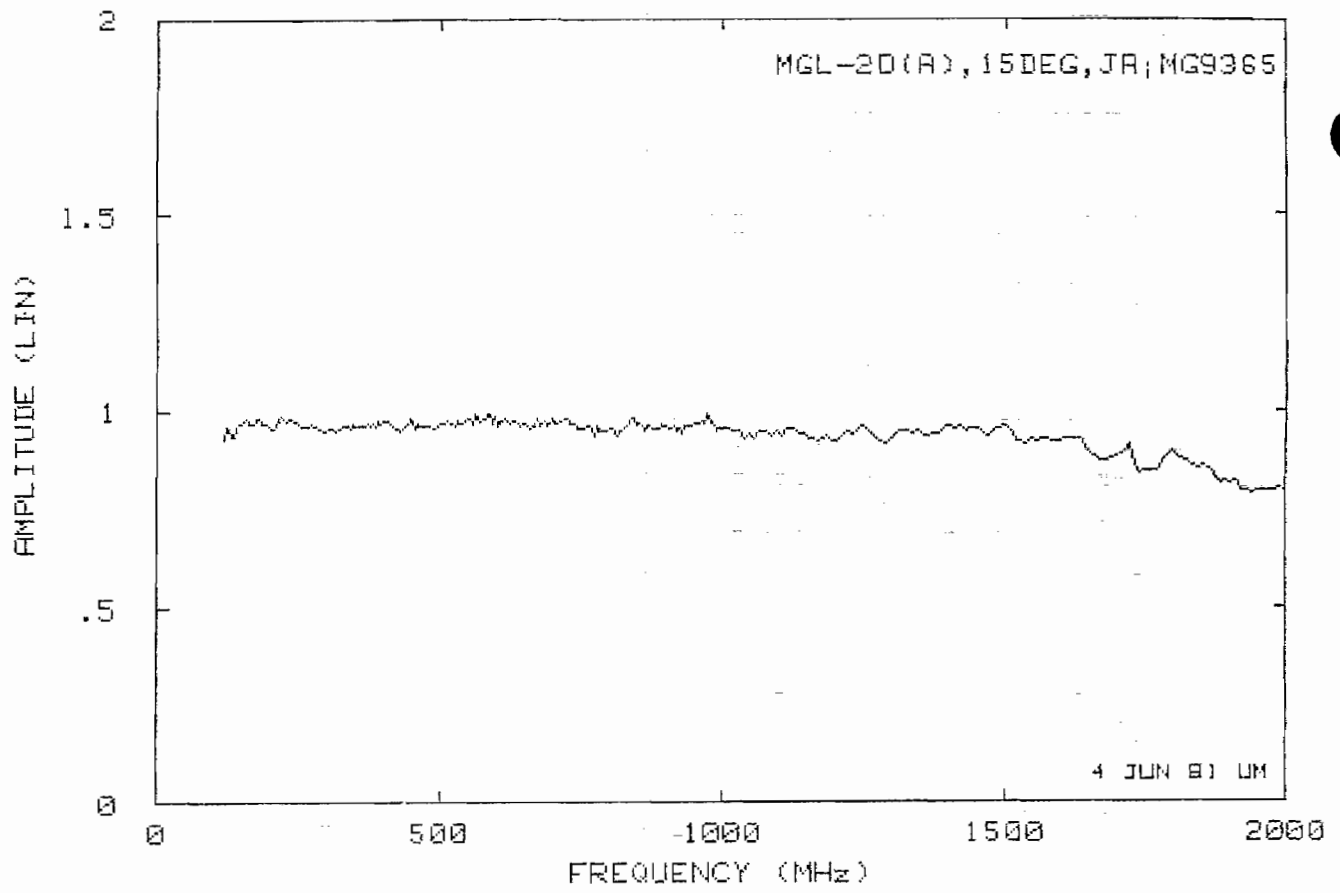




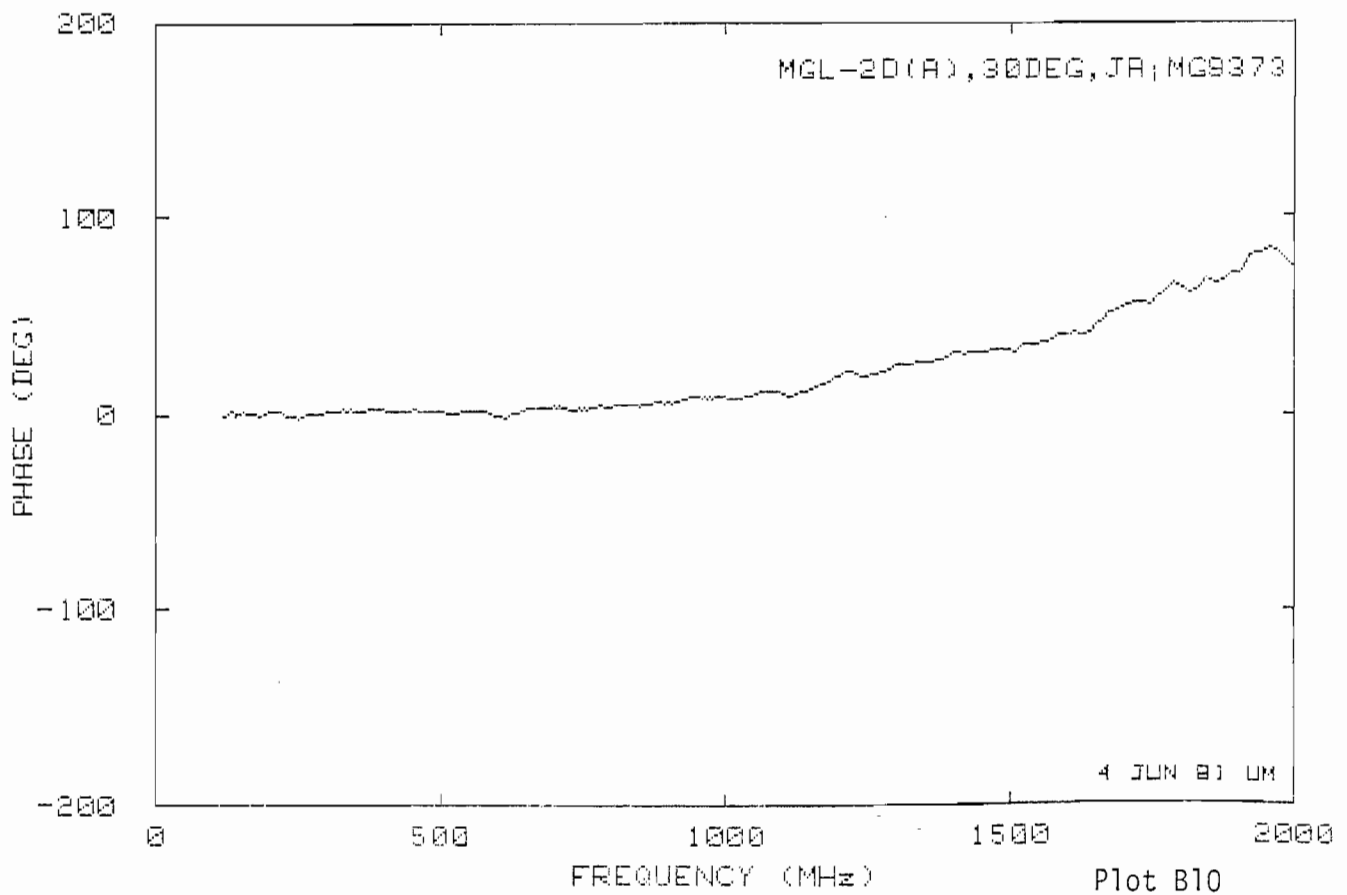
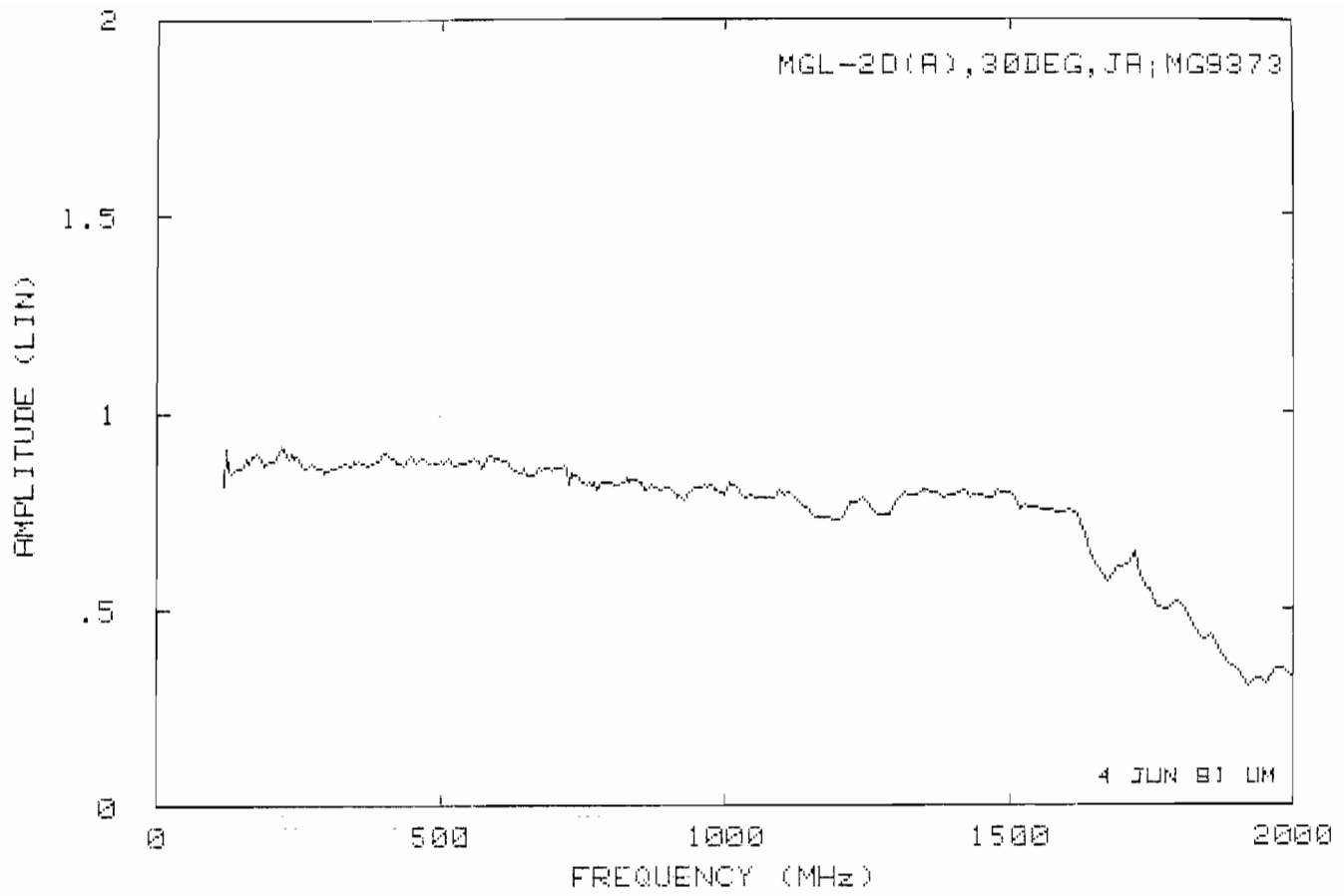


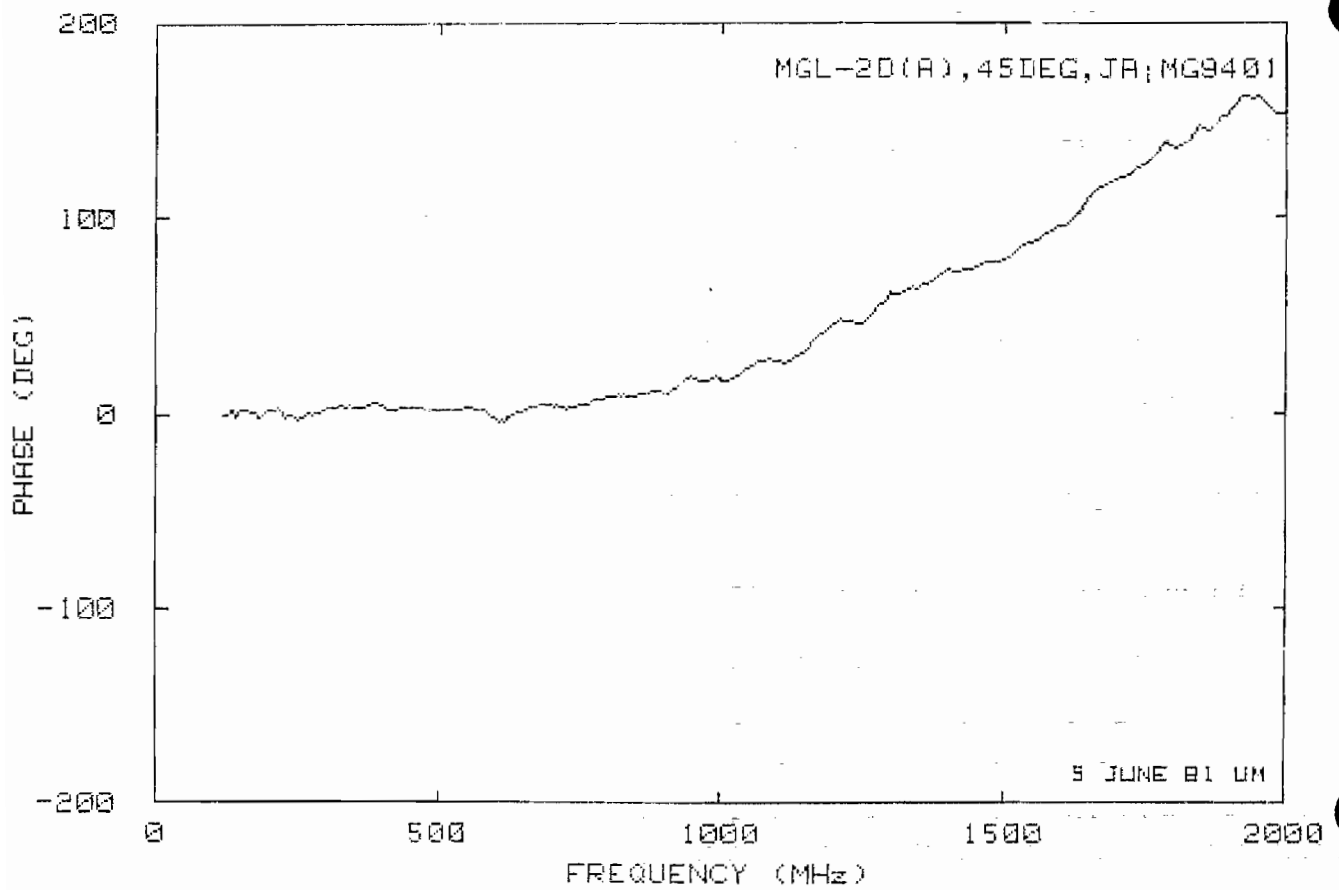
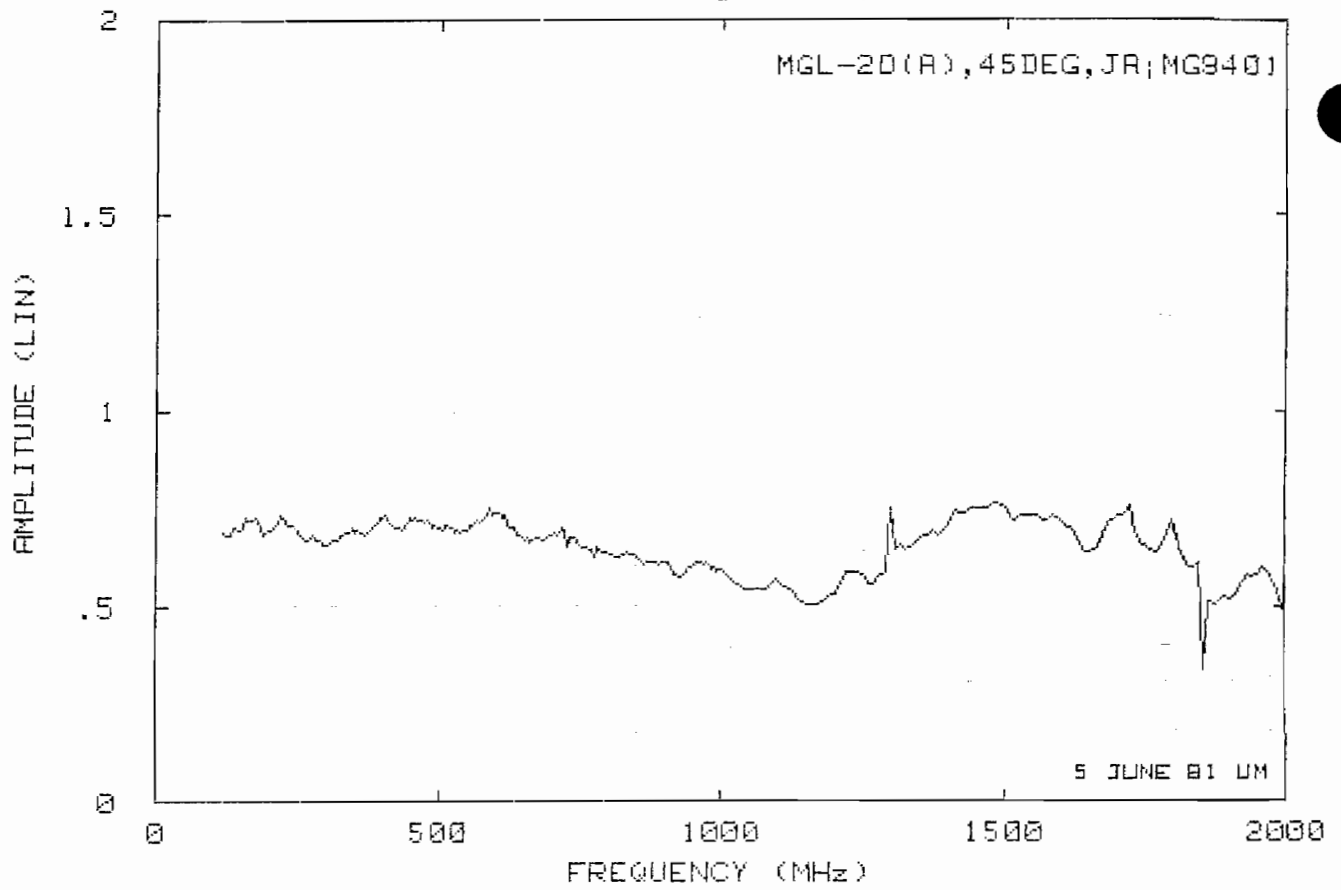


Plot B8

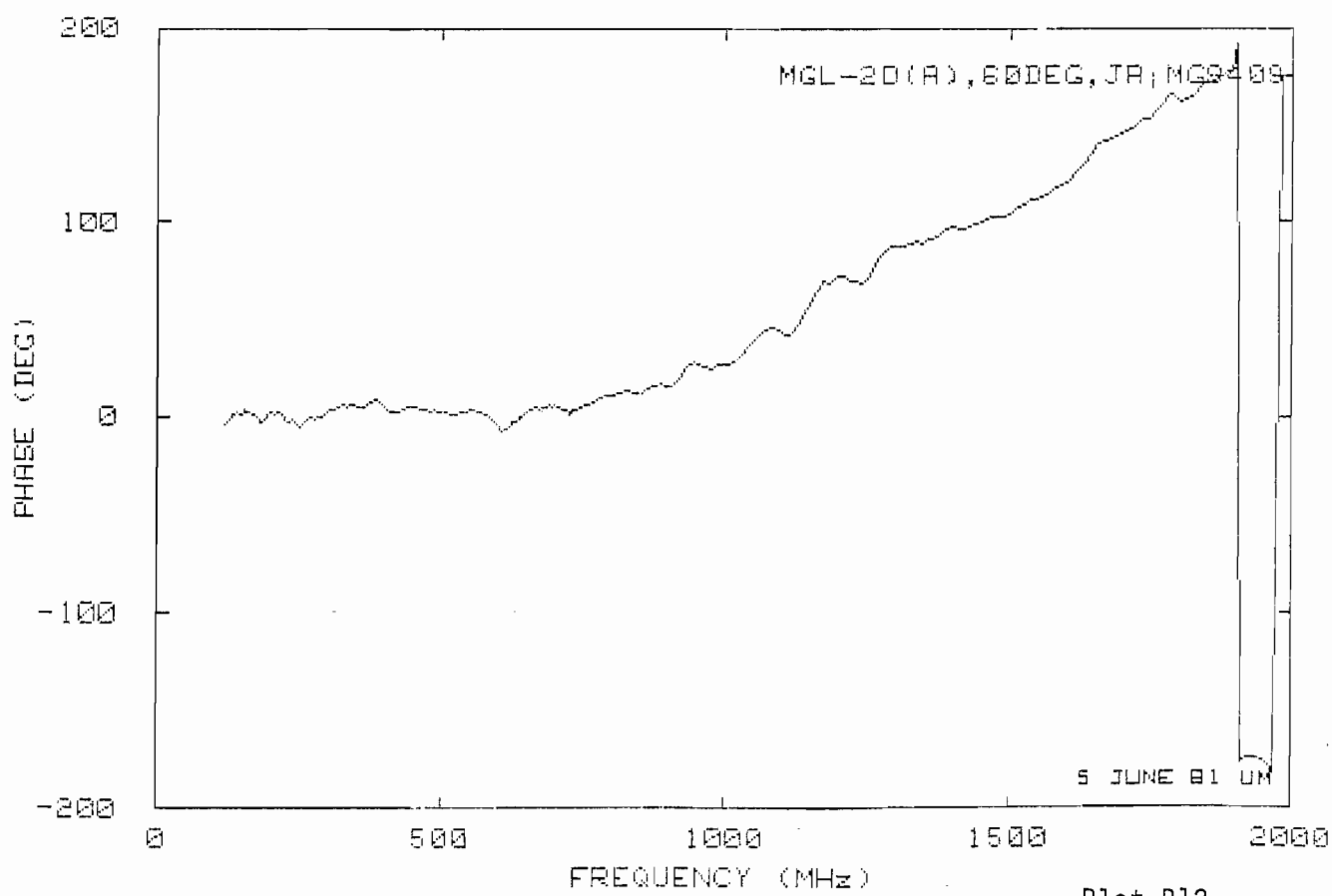
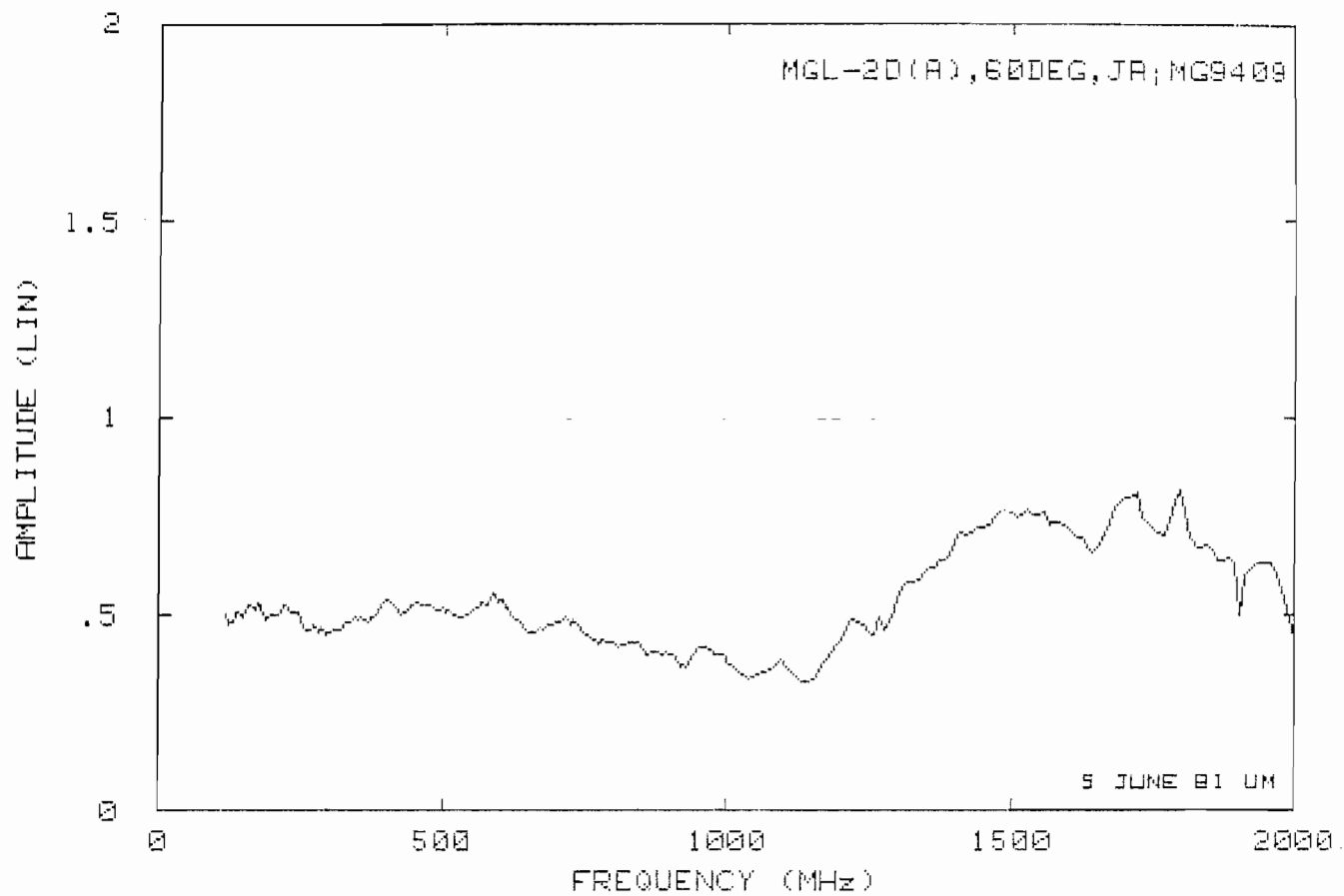


Plot B9

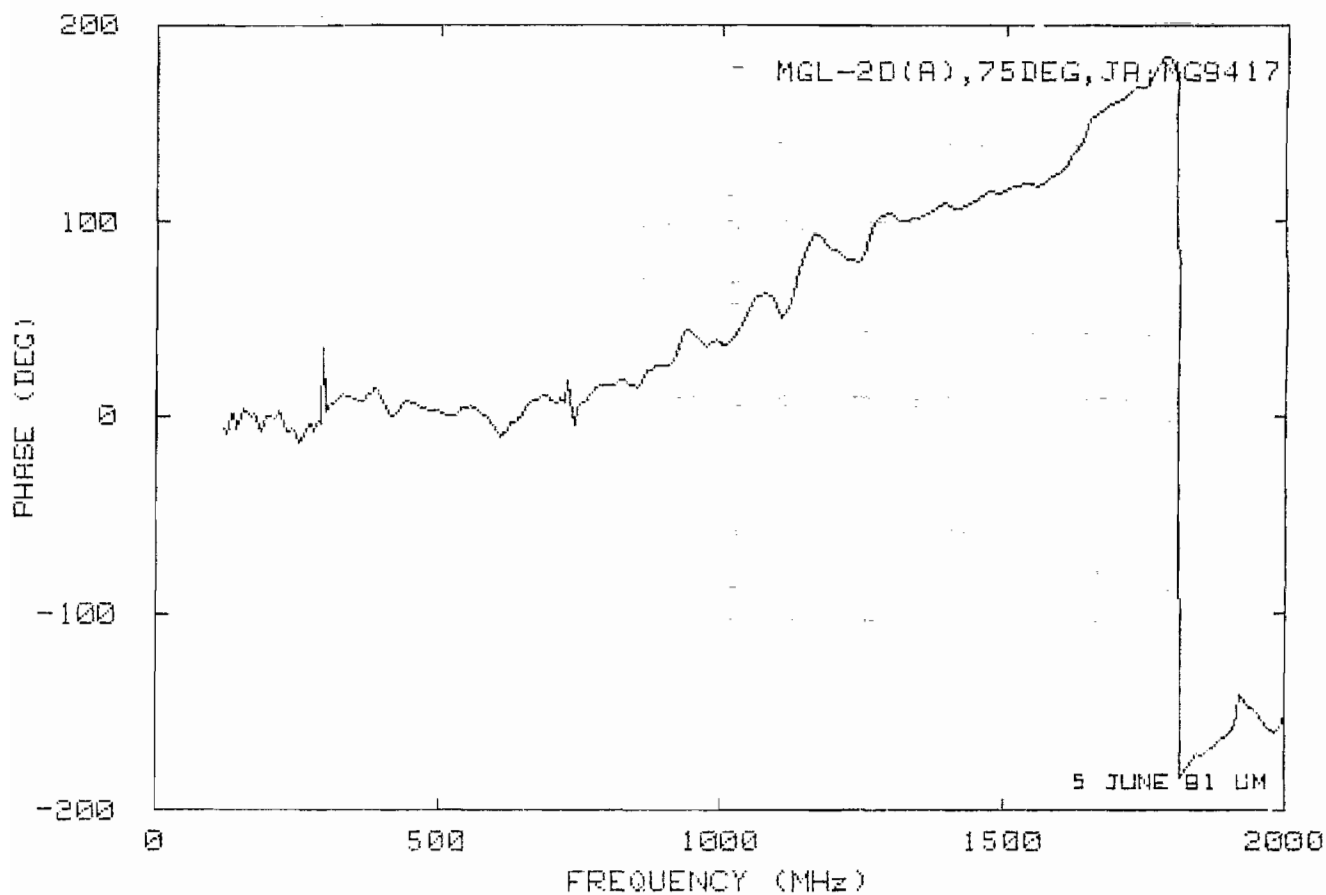
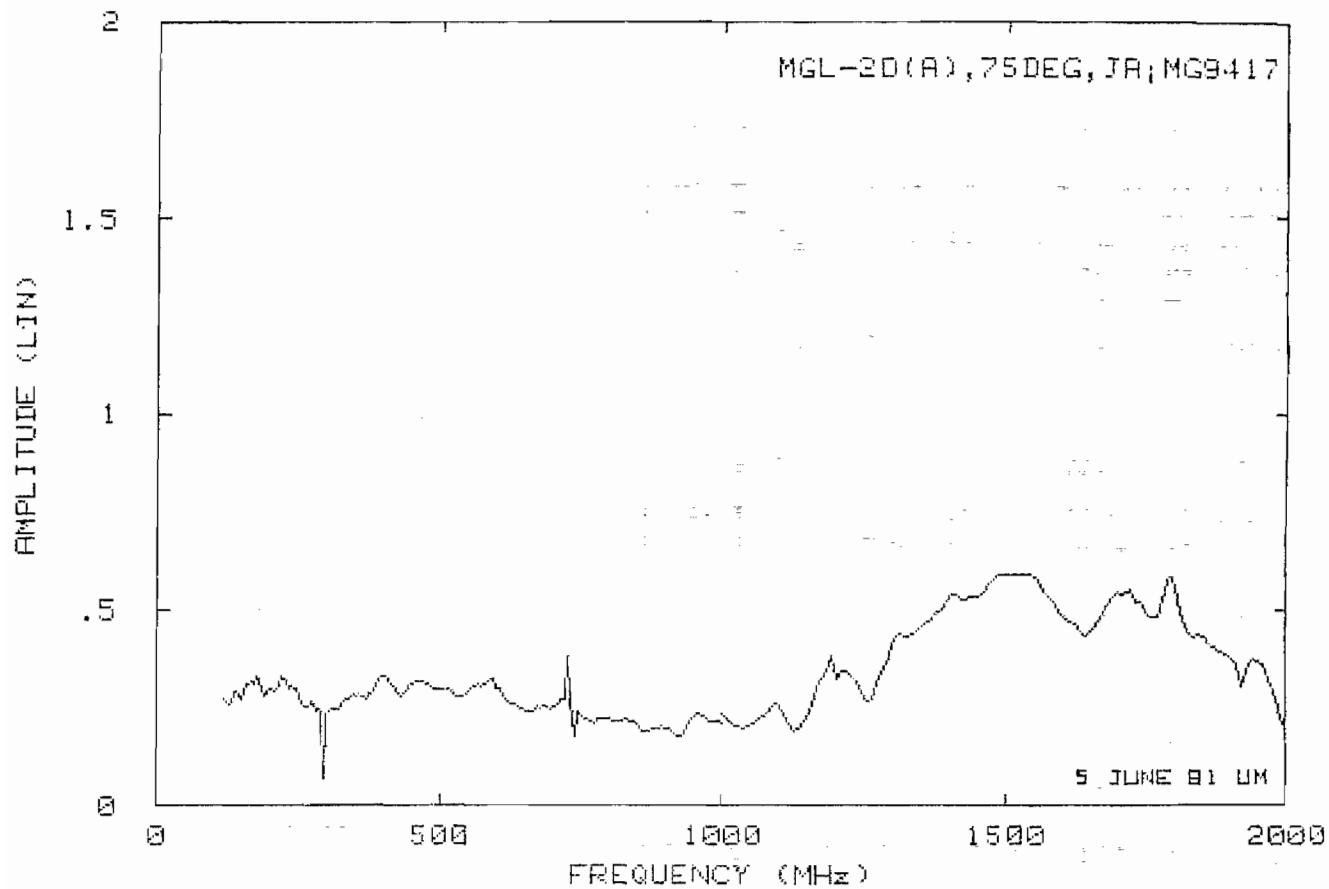




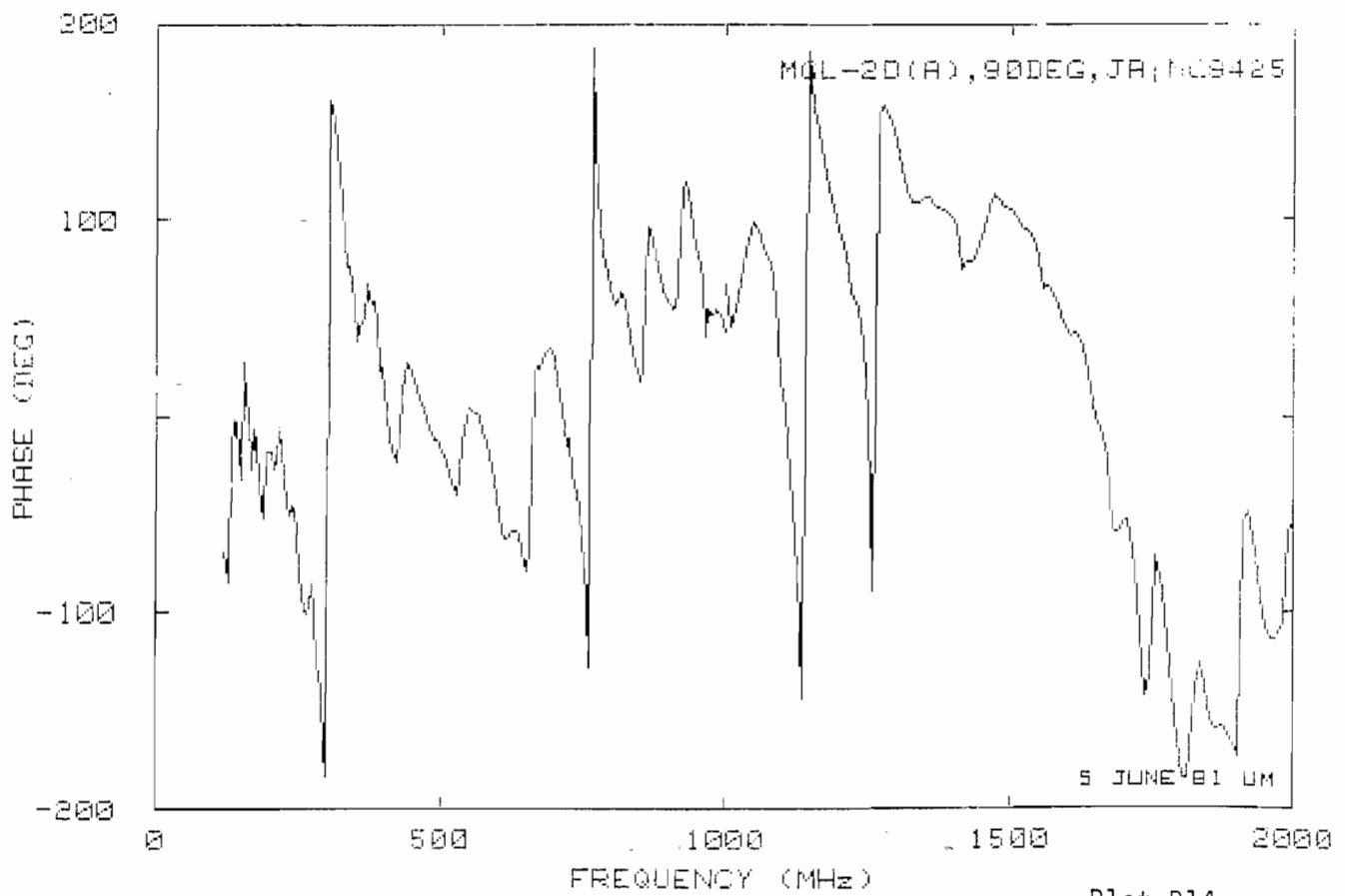
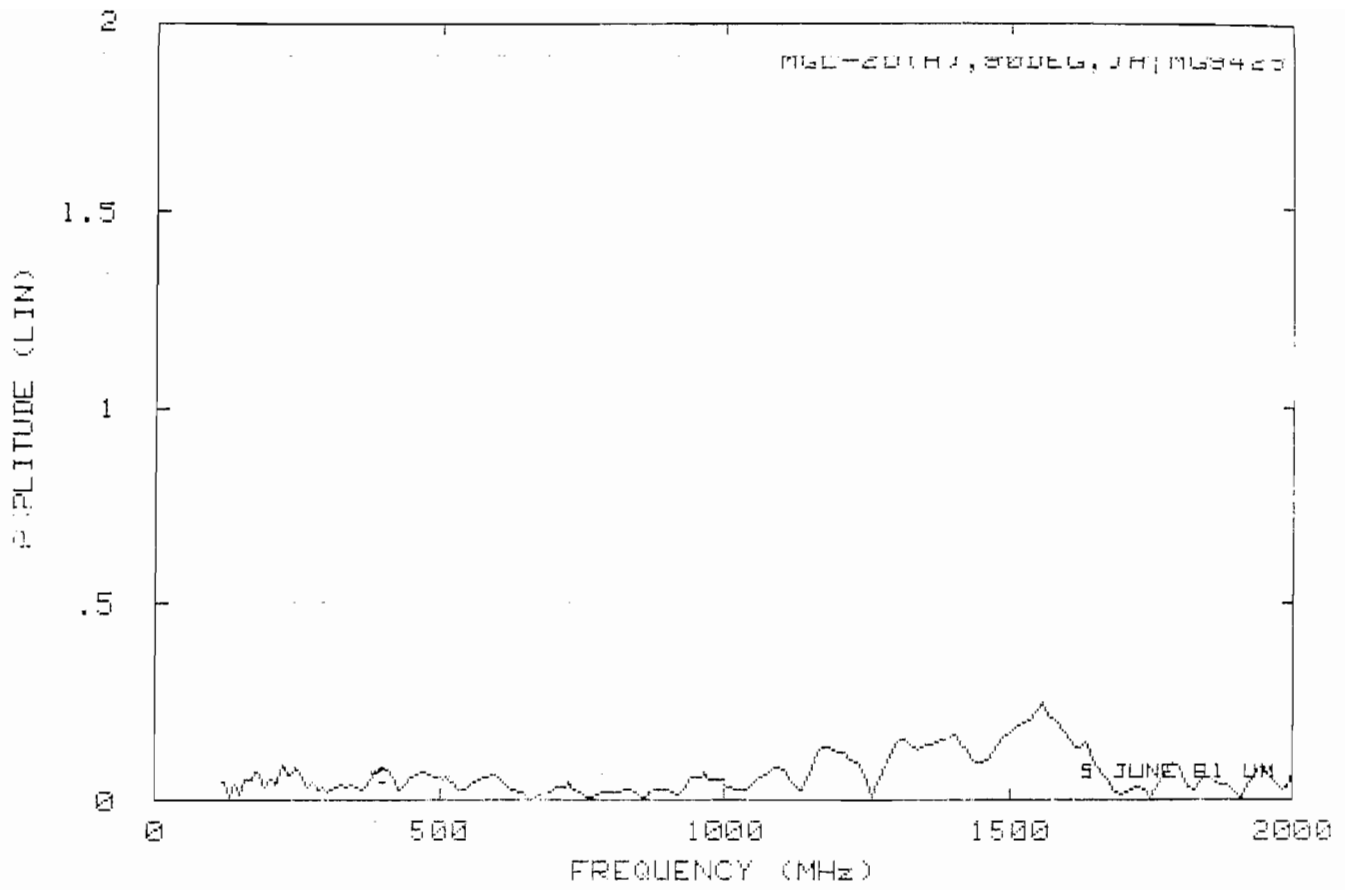
Plot B11



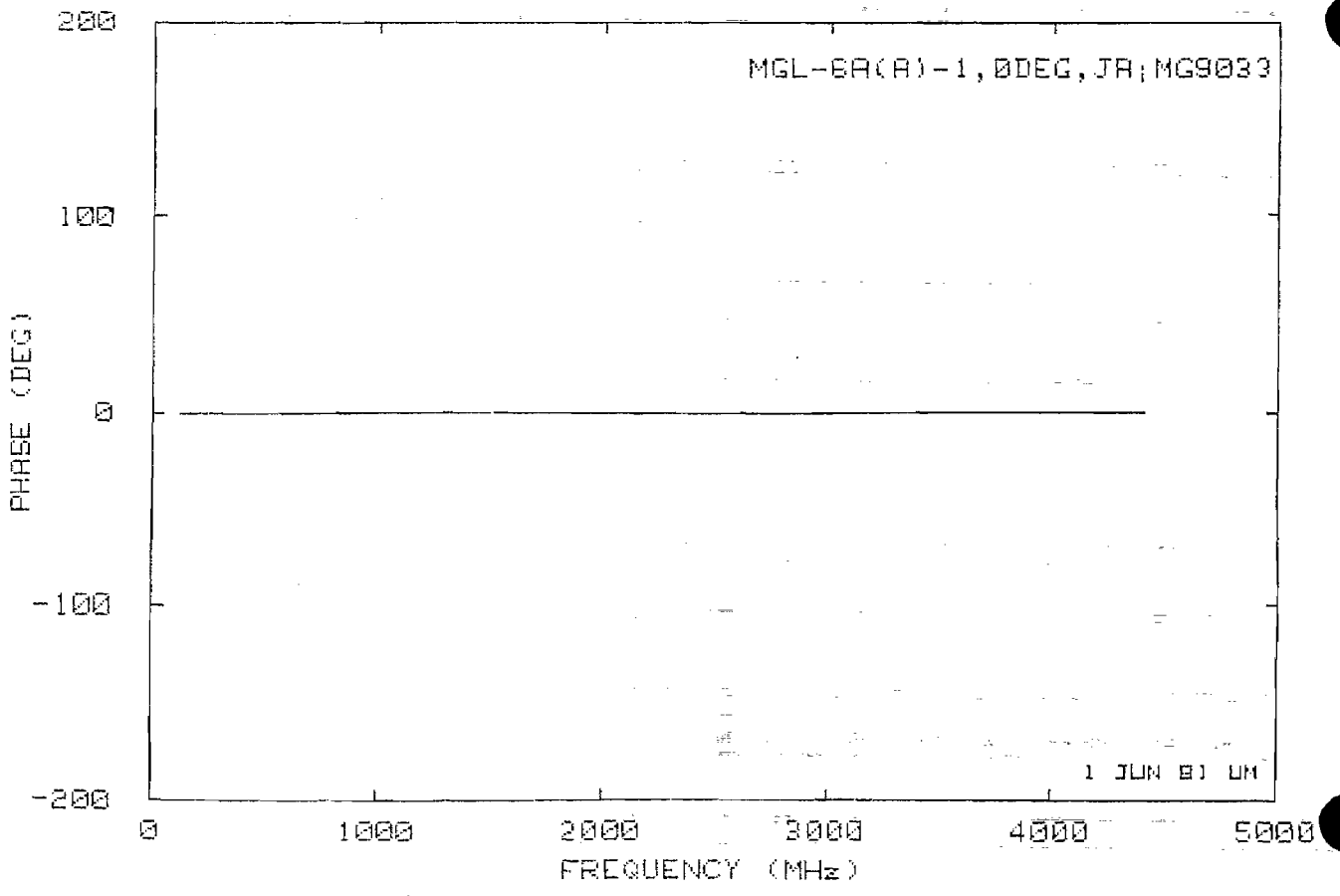
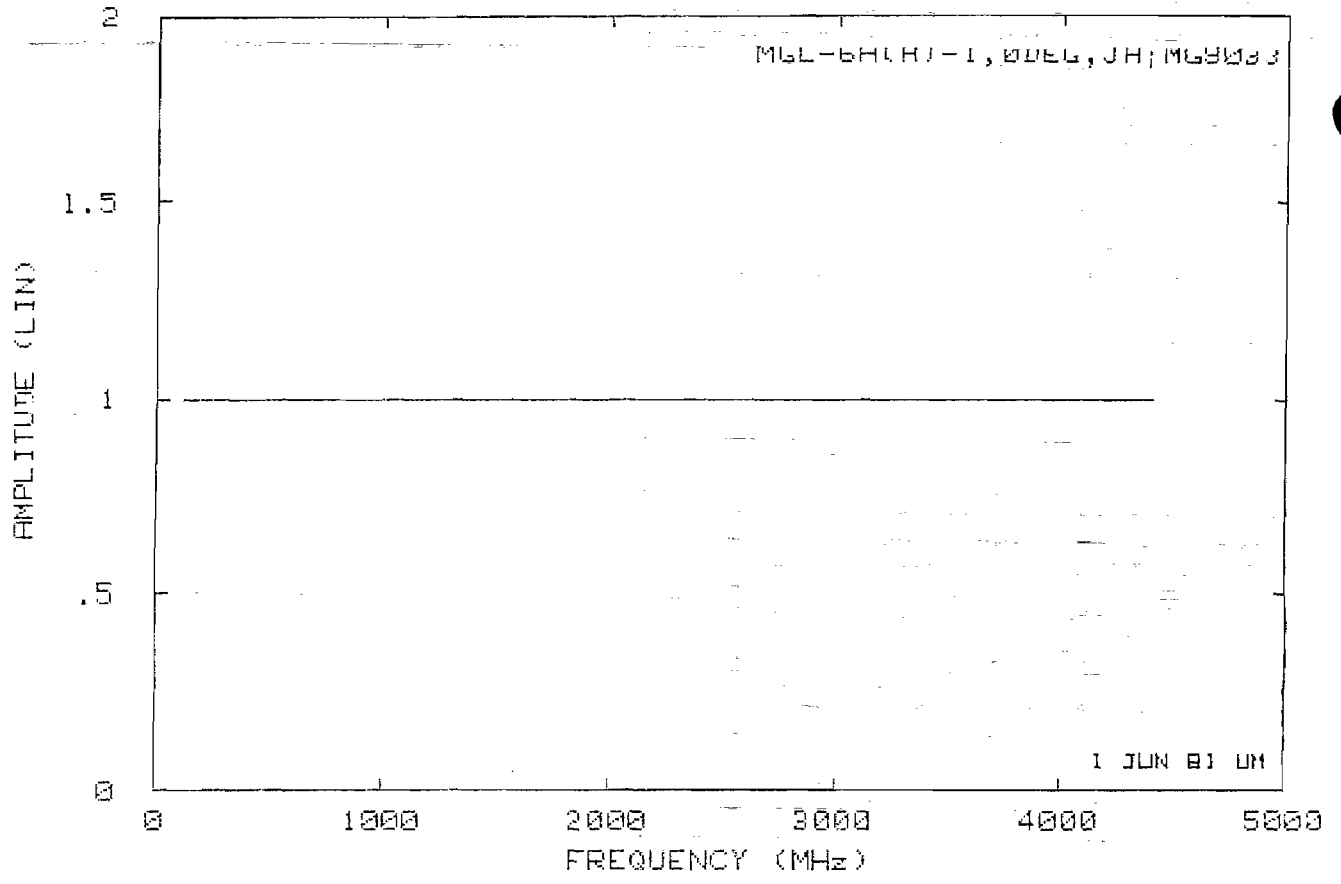
Plot B12

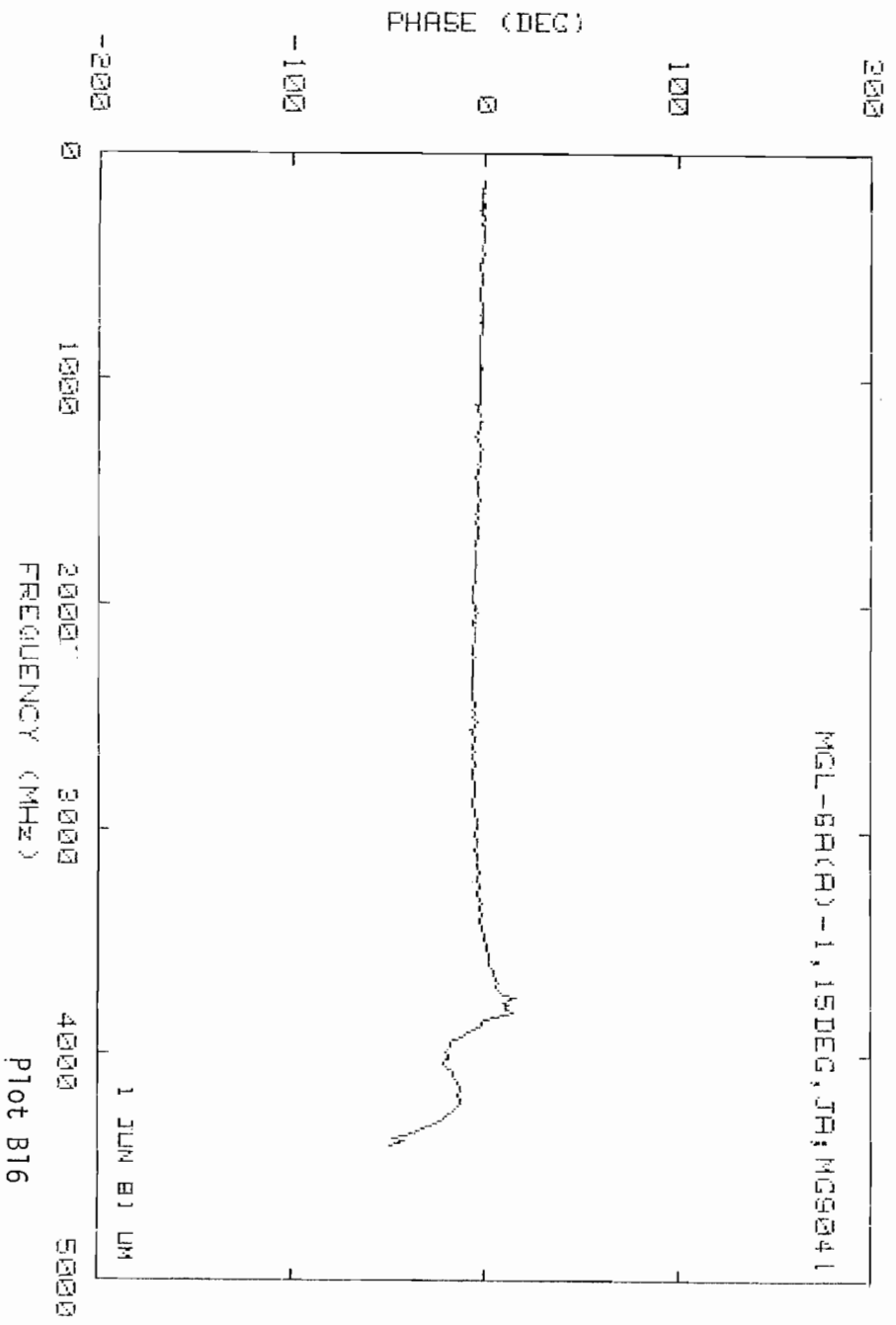
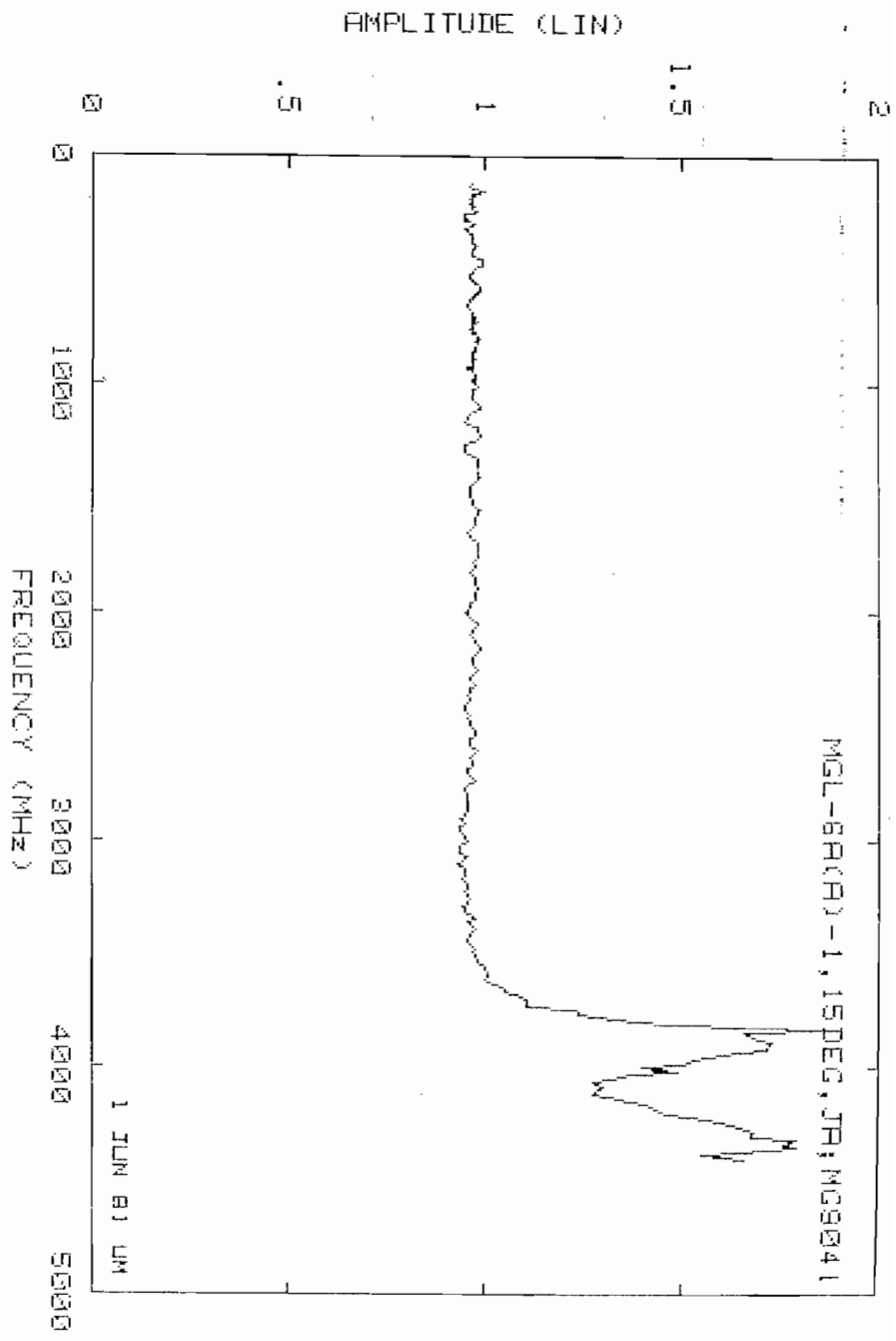


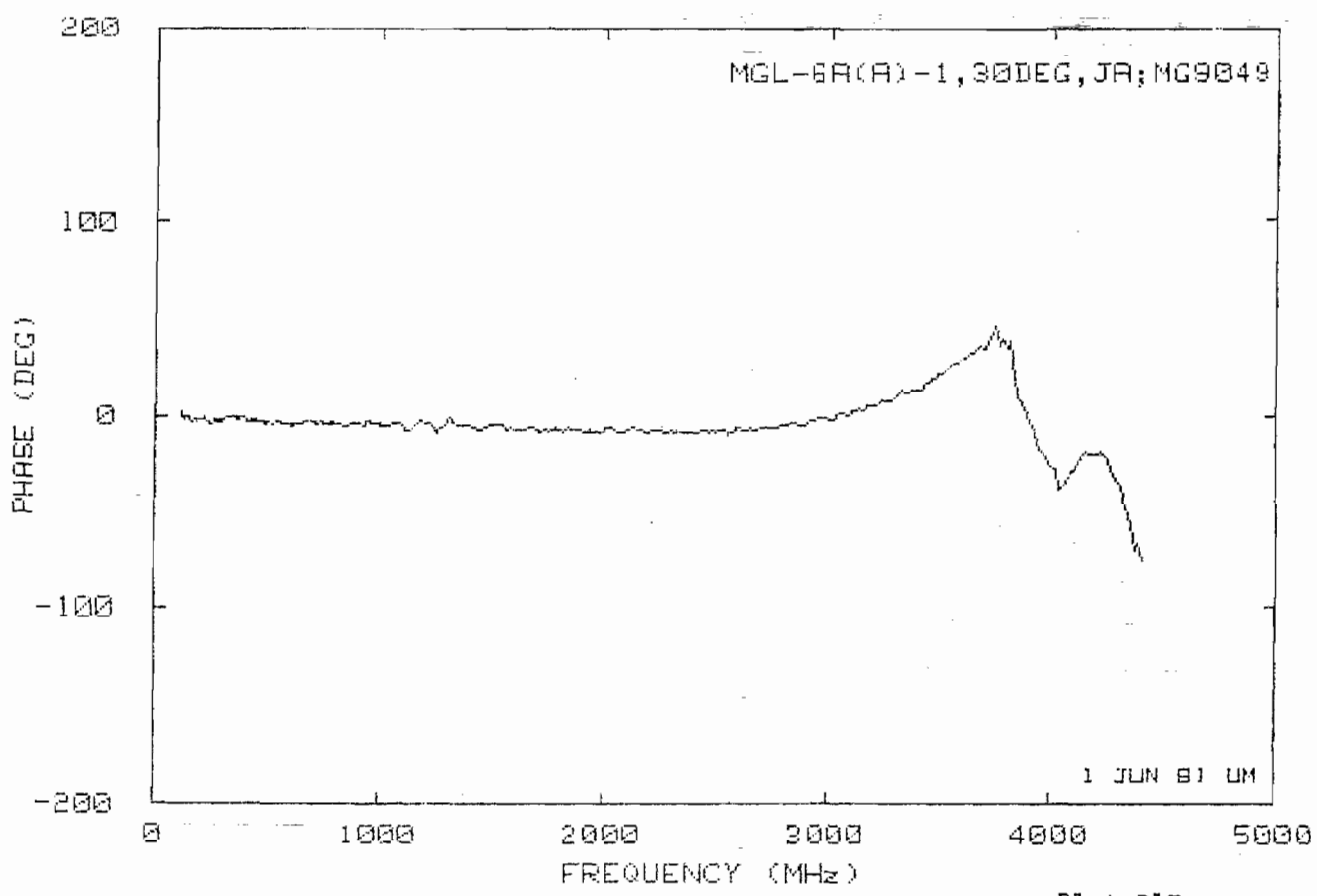
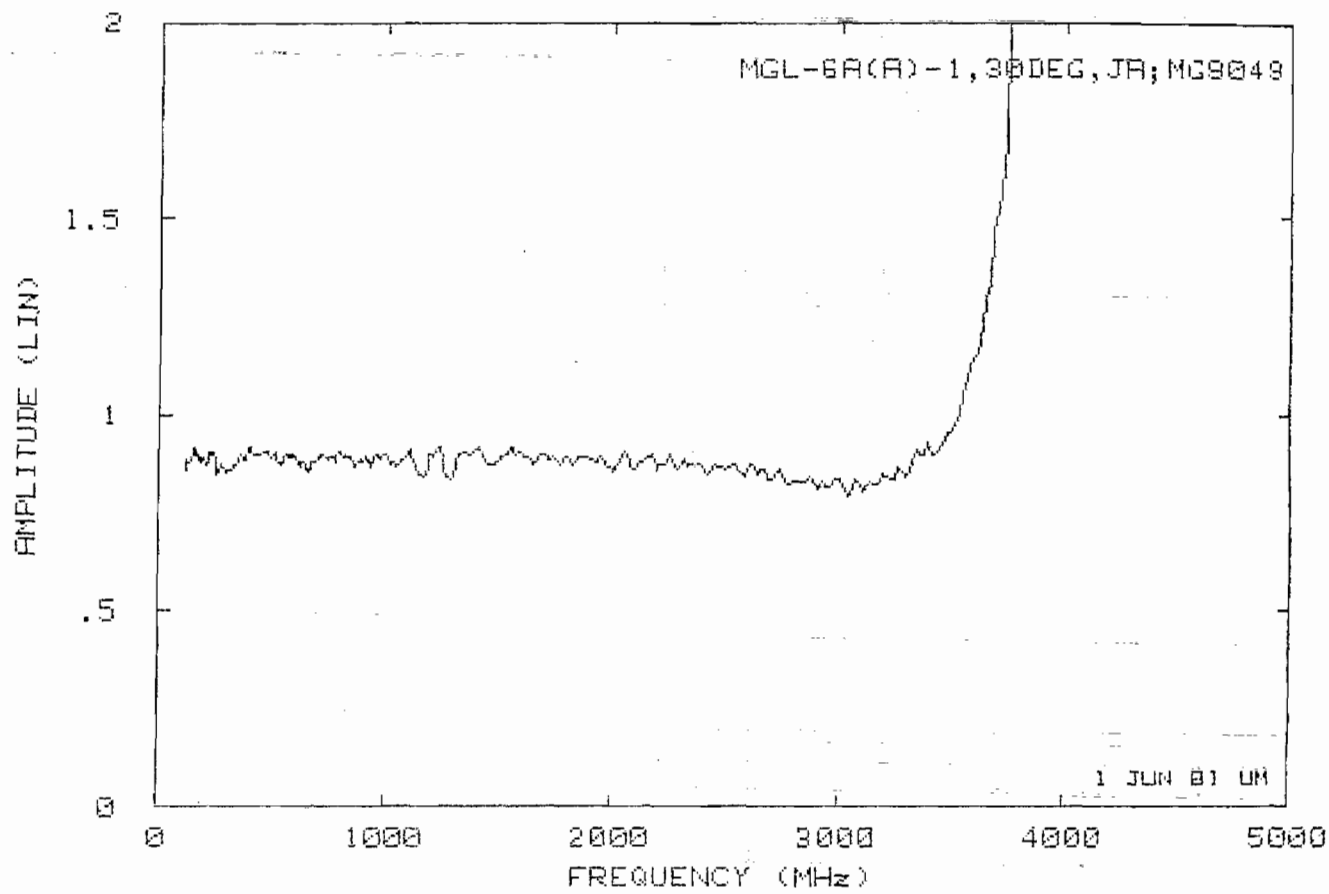
Plot B13



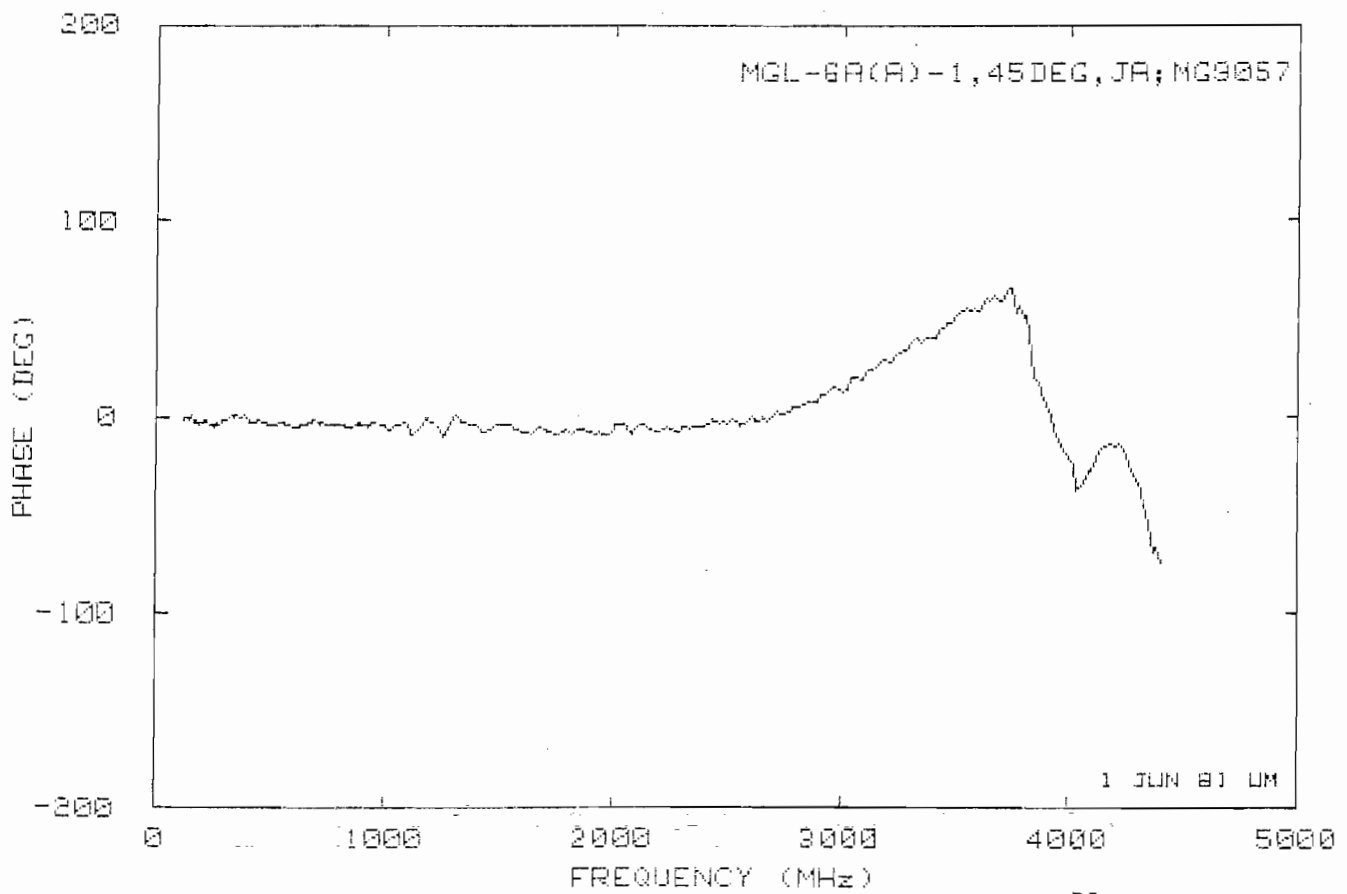
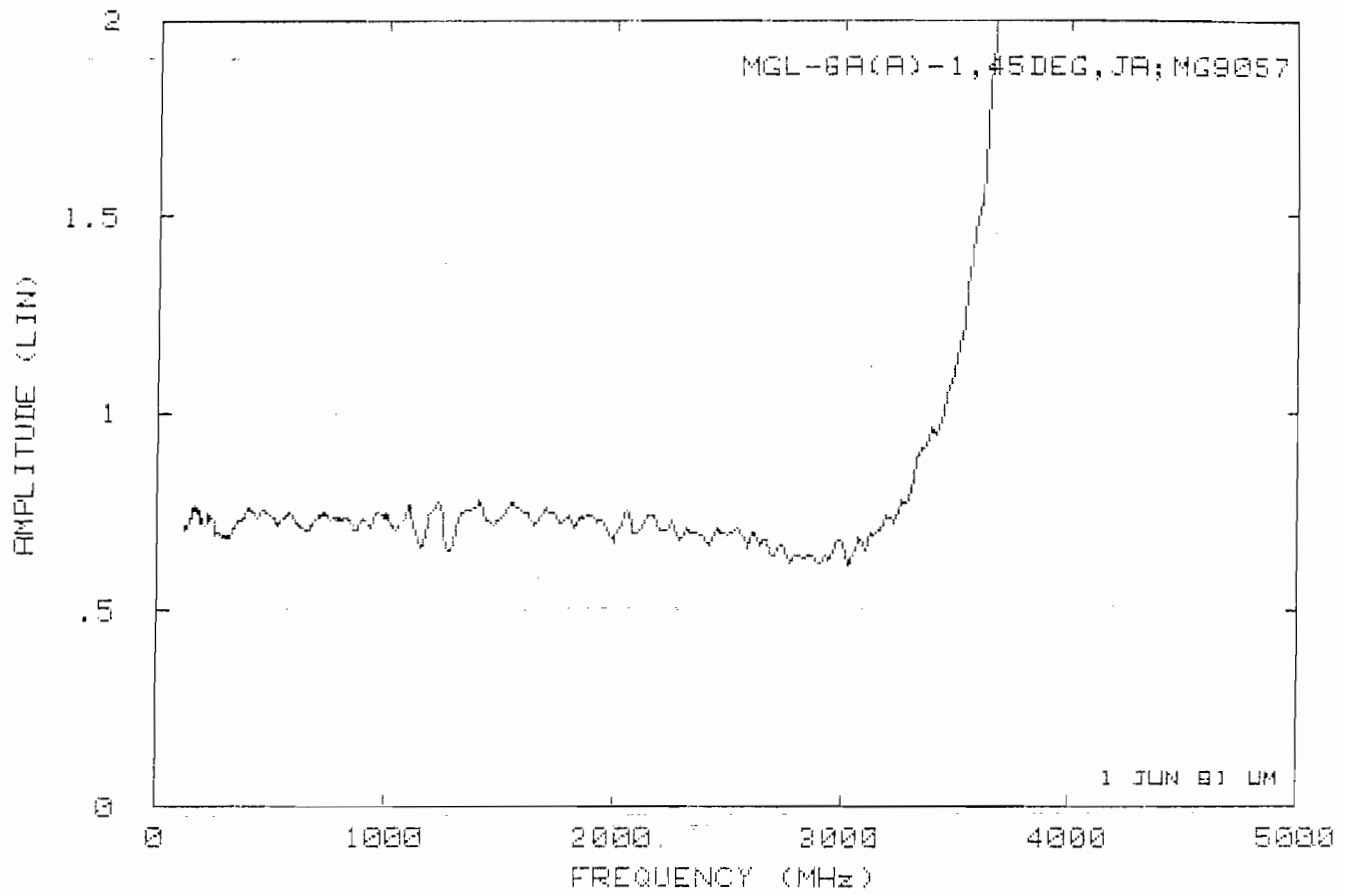
Plot B14



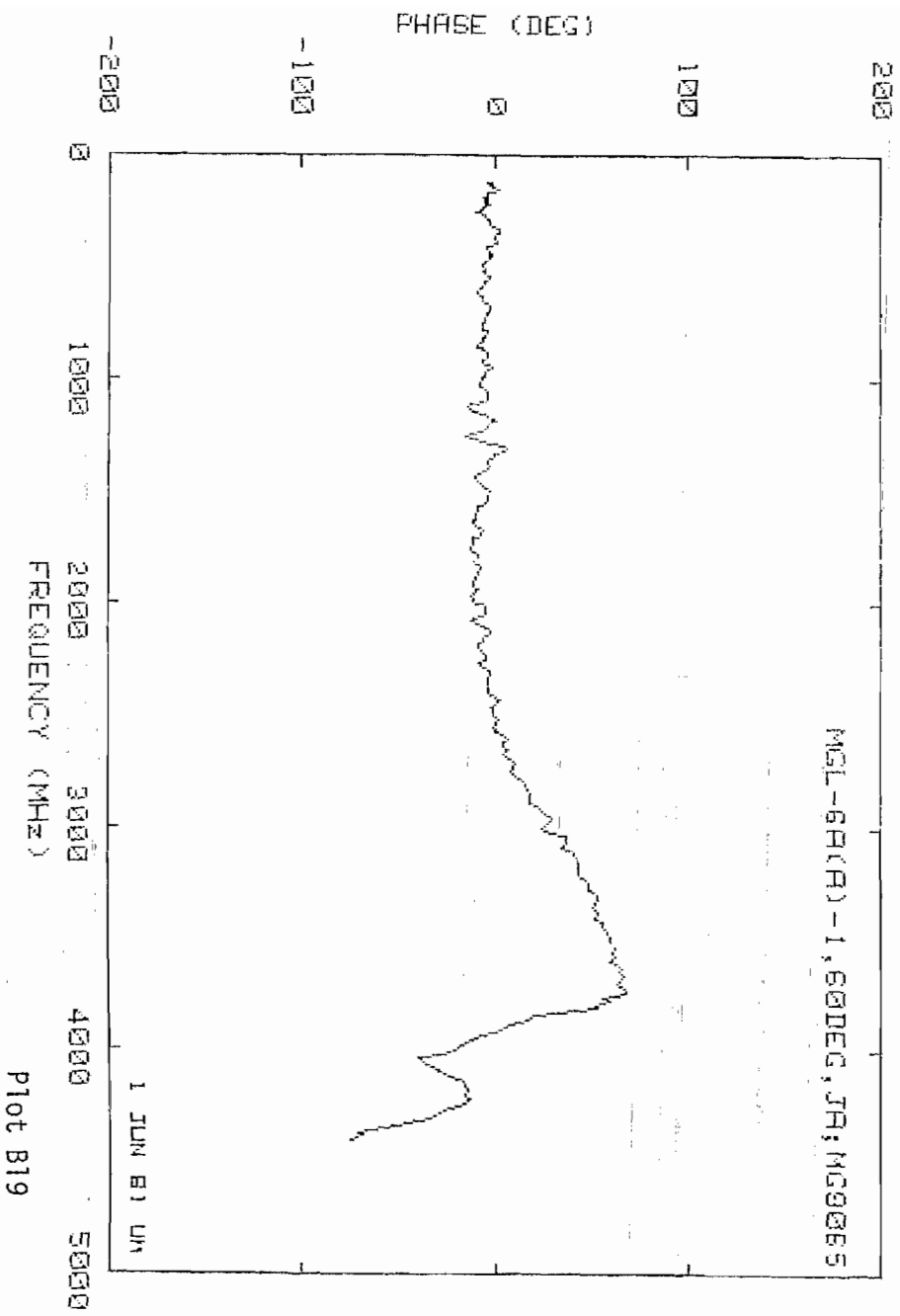
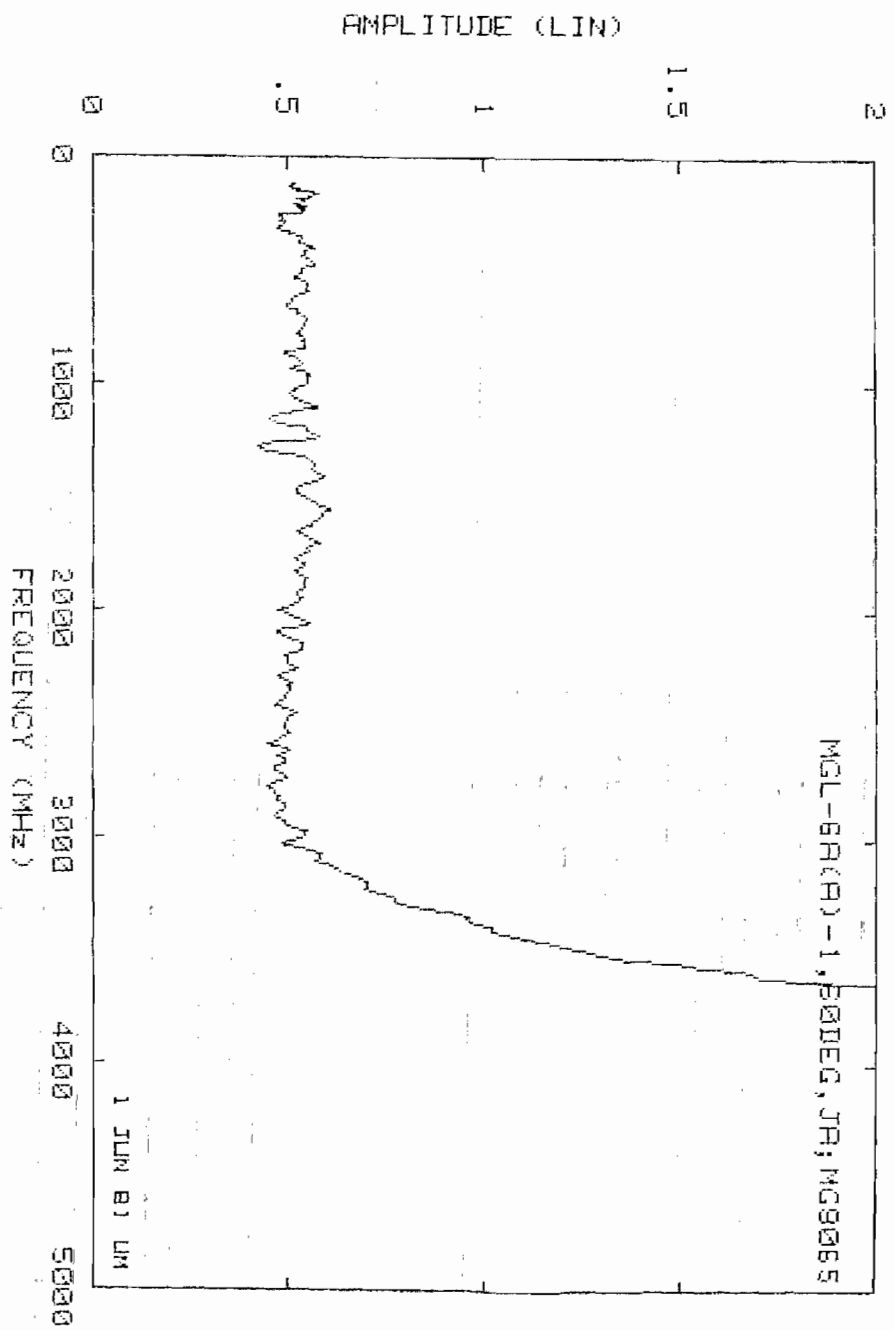


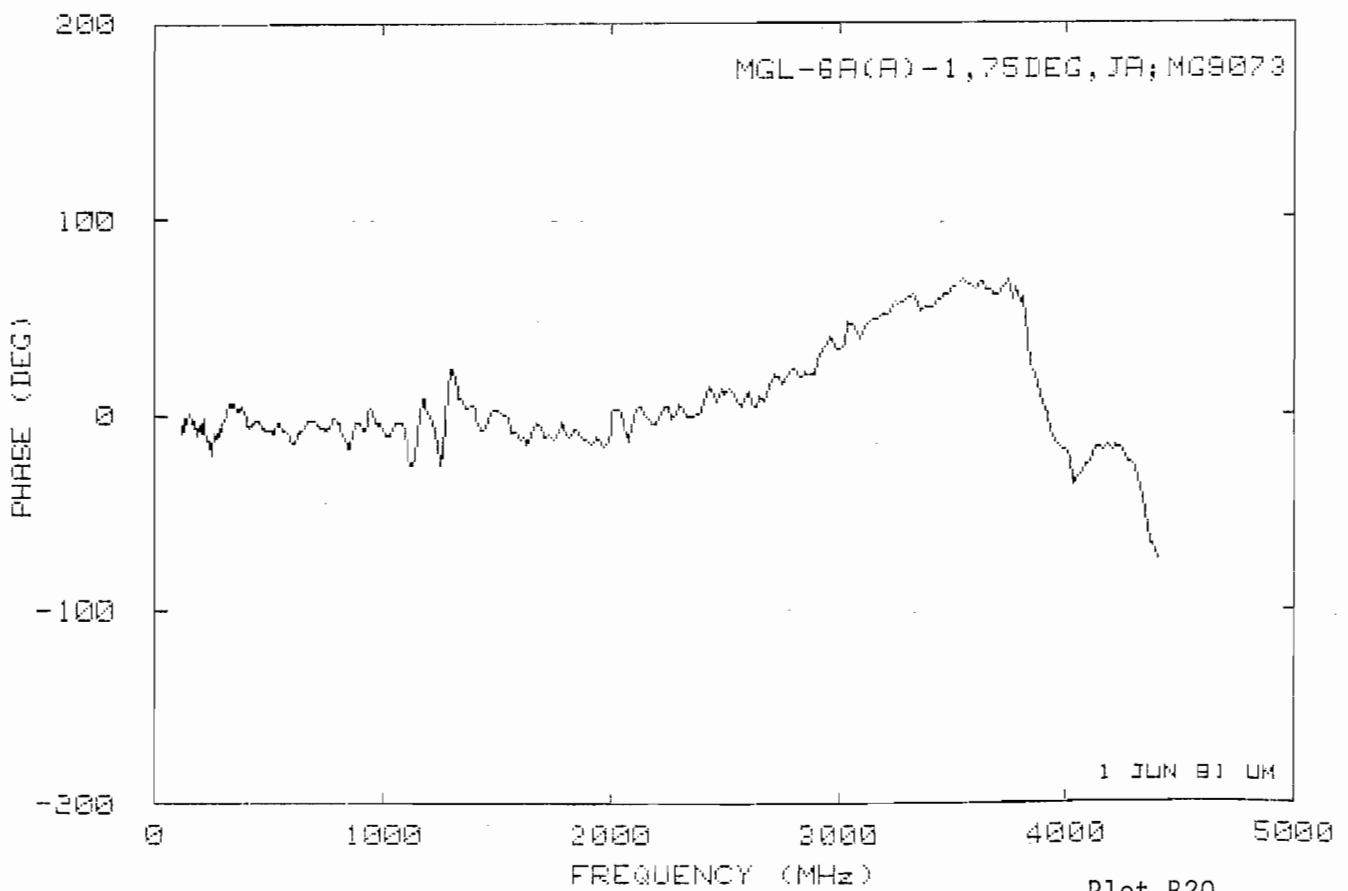
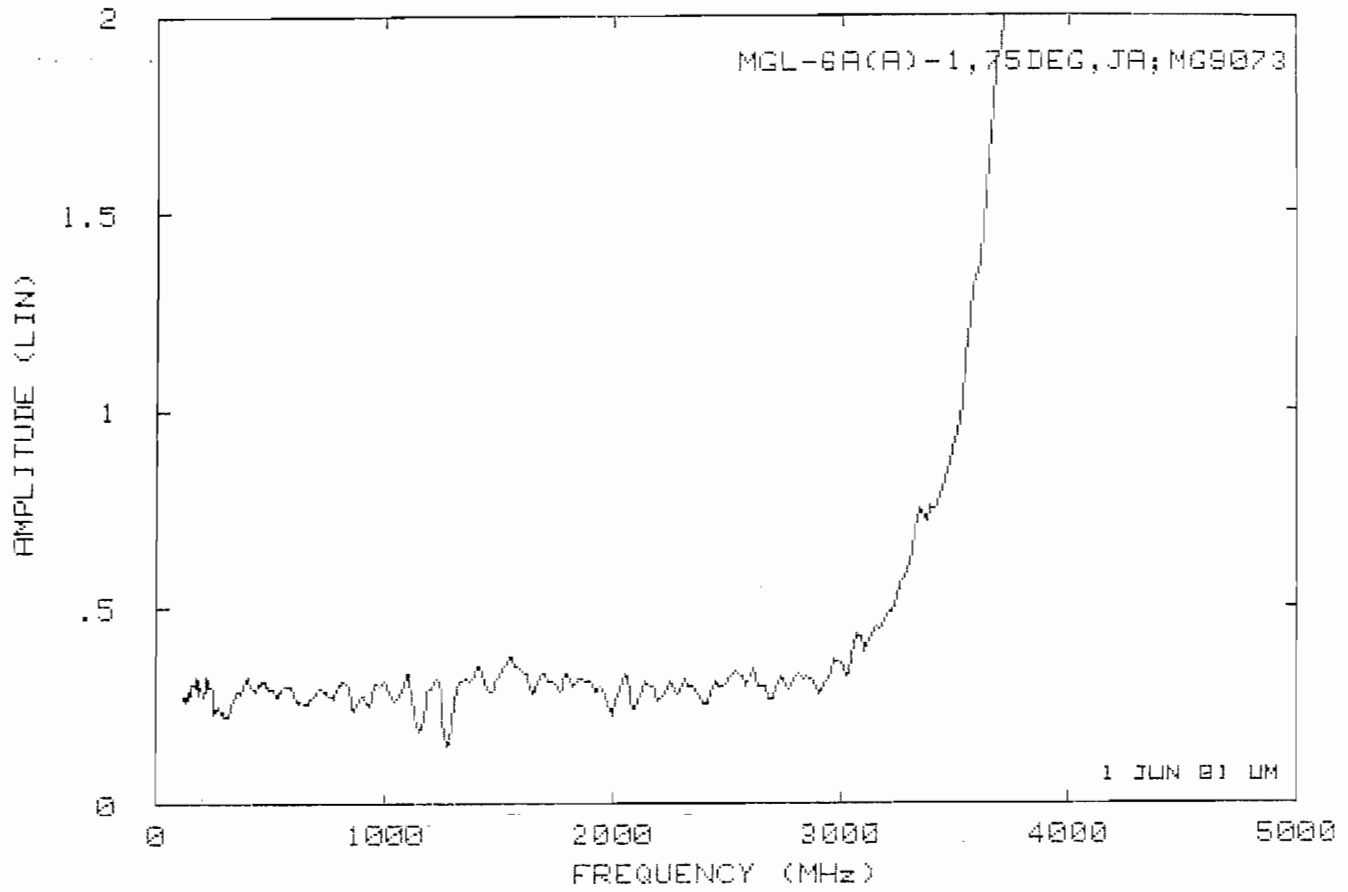


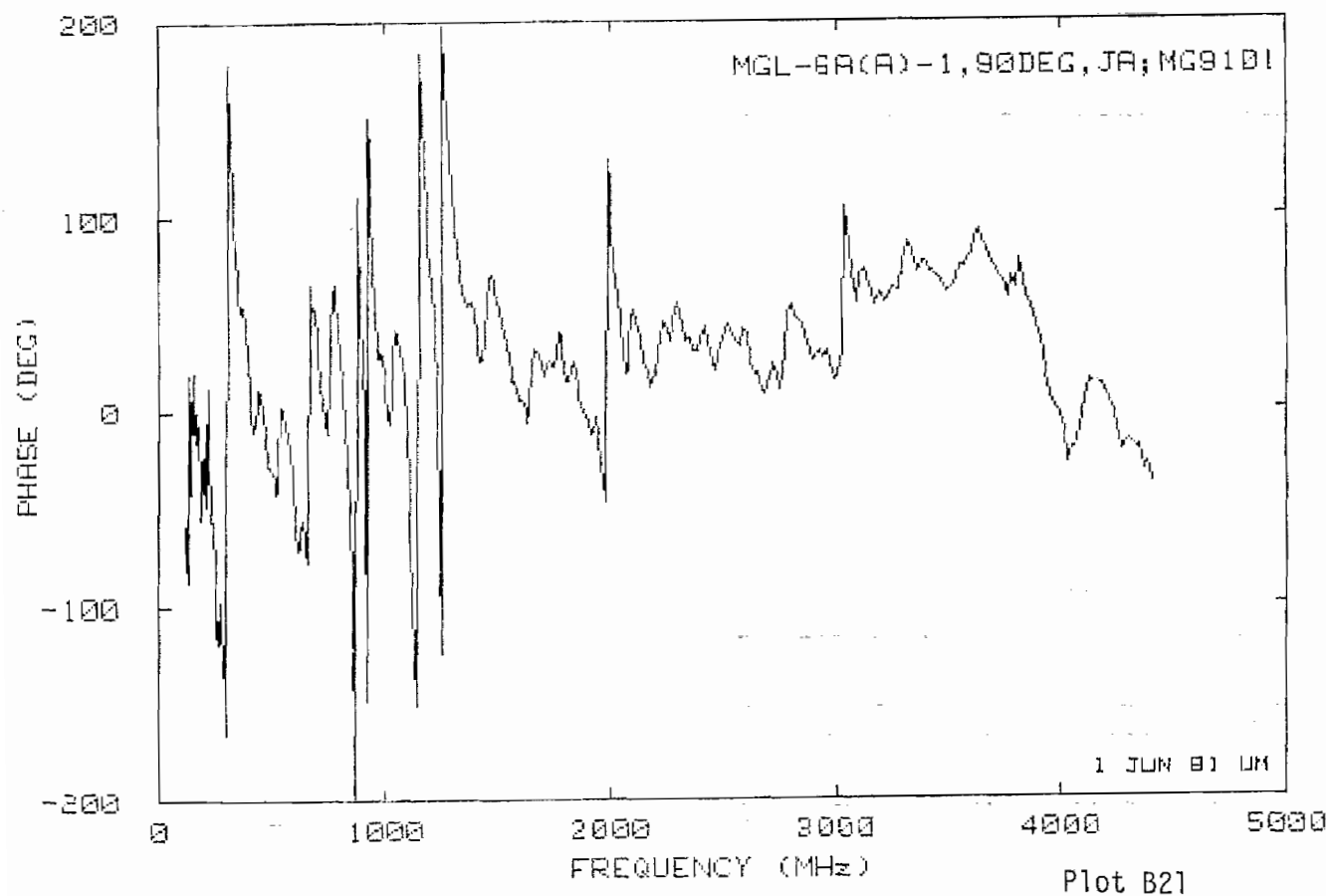
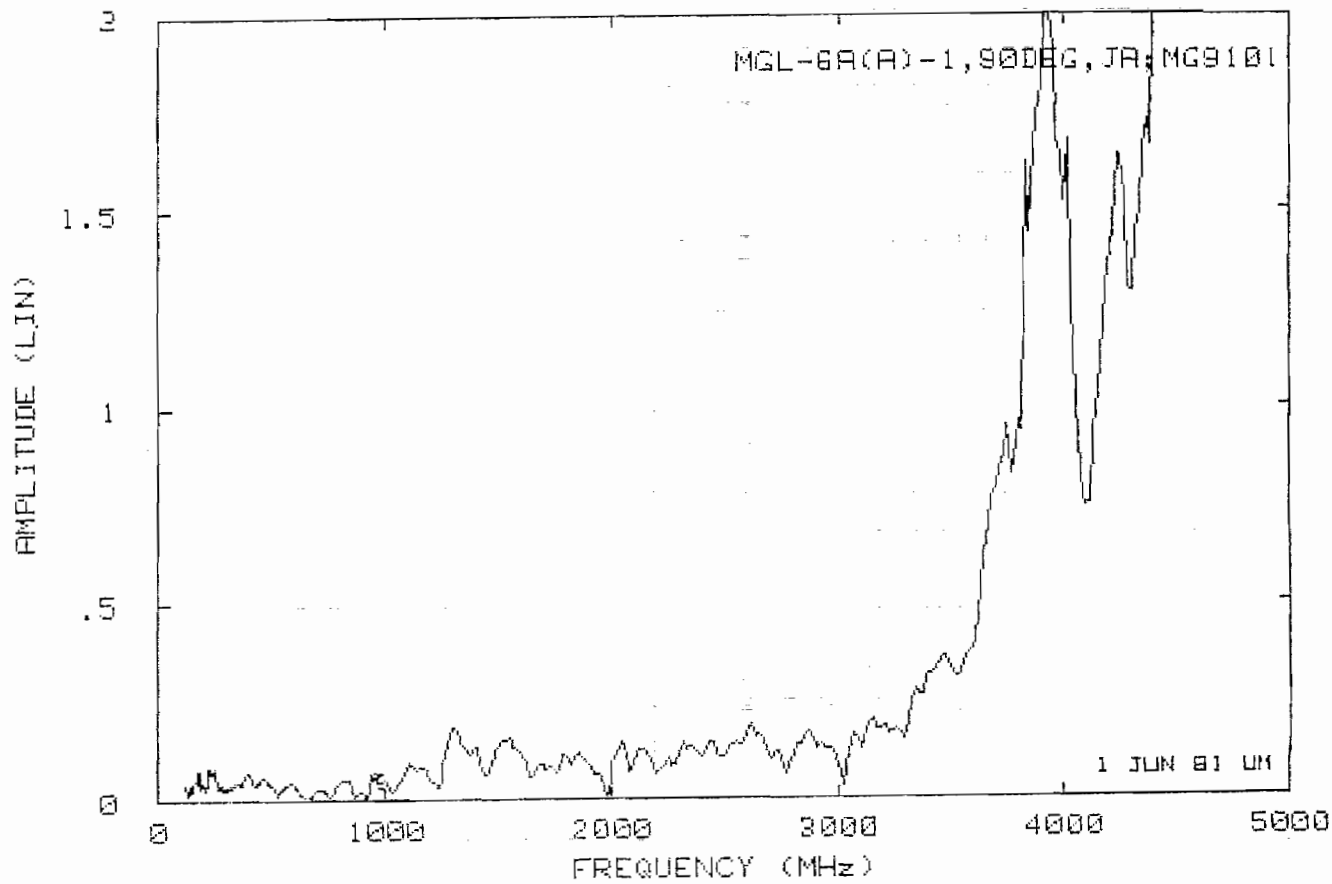
Plot B17

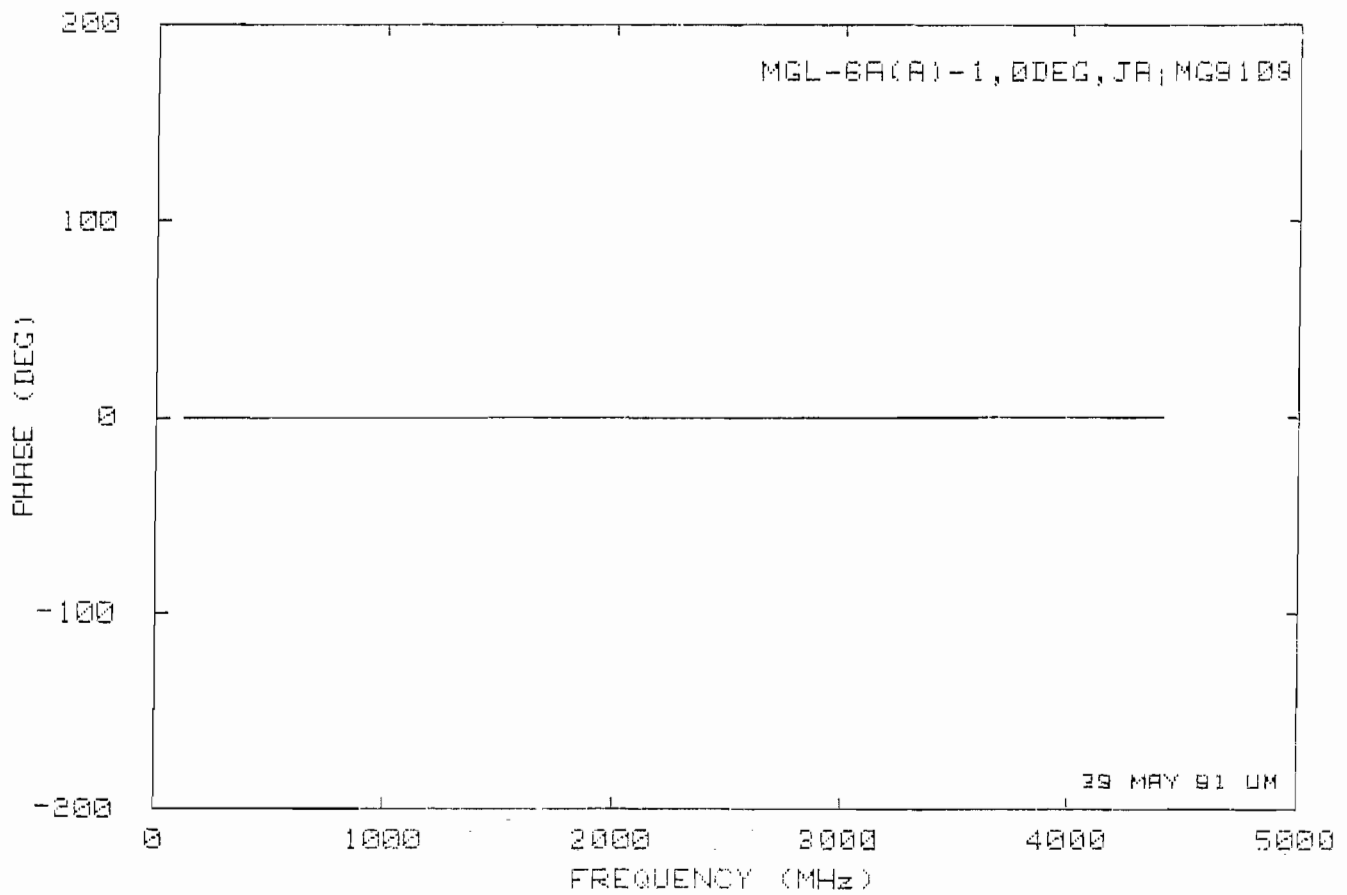
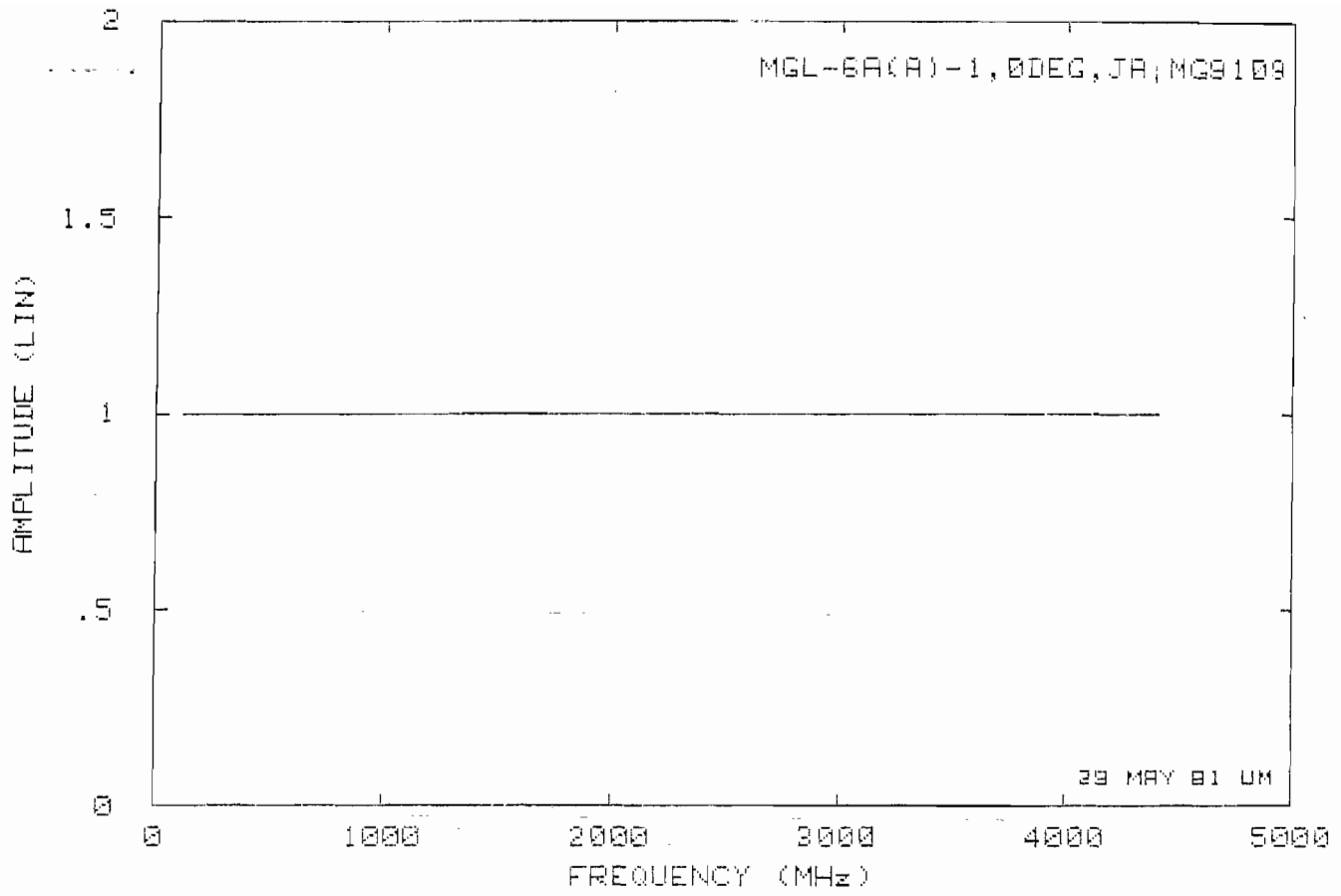


Plot B18

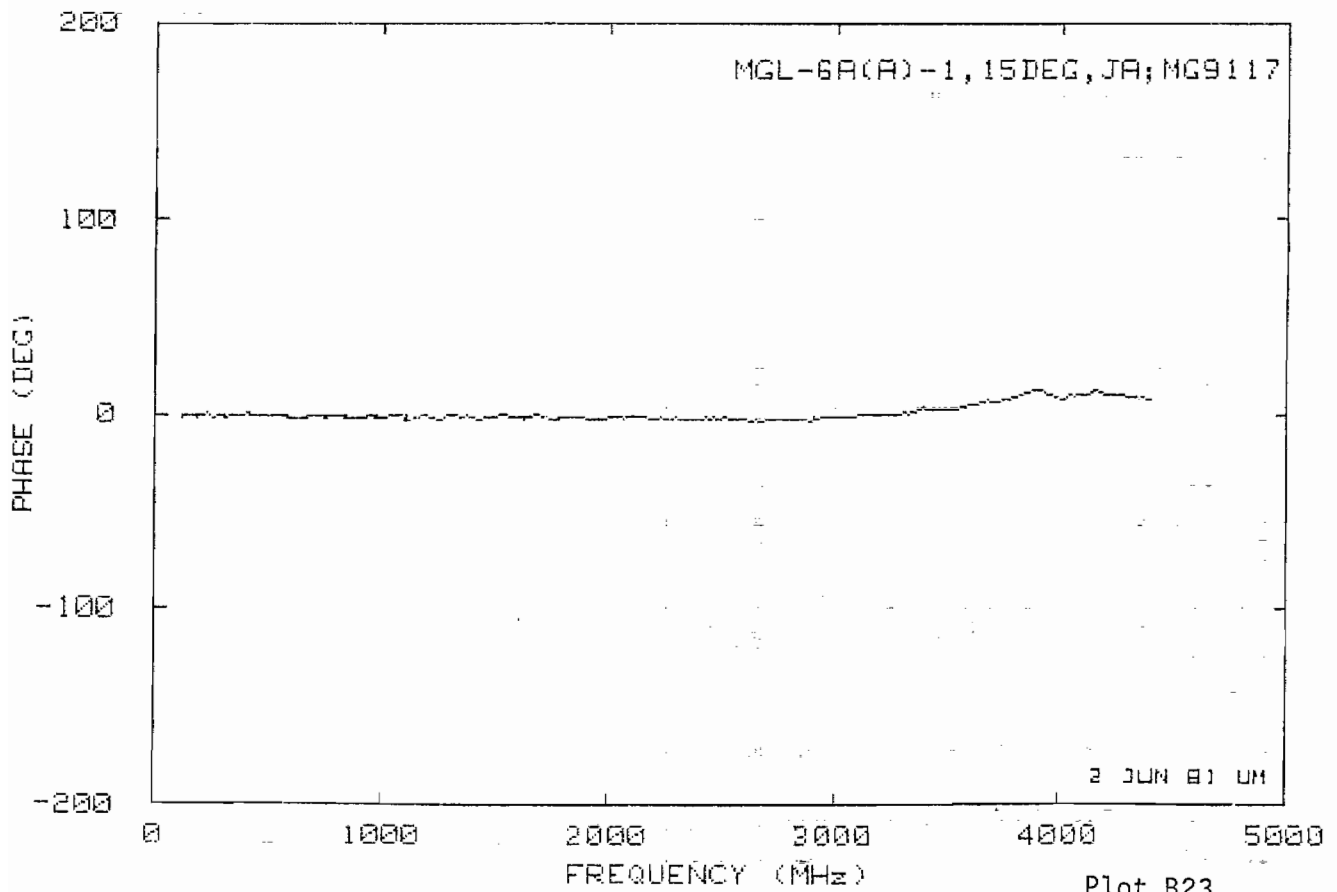
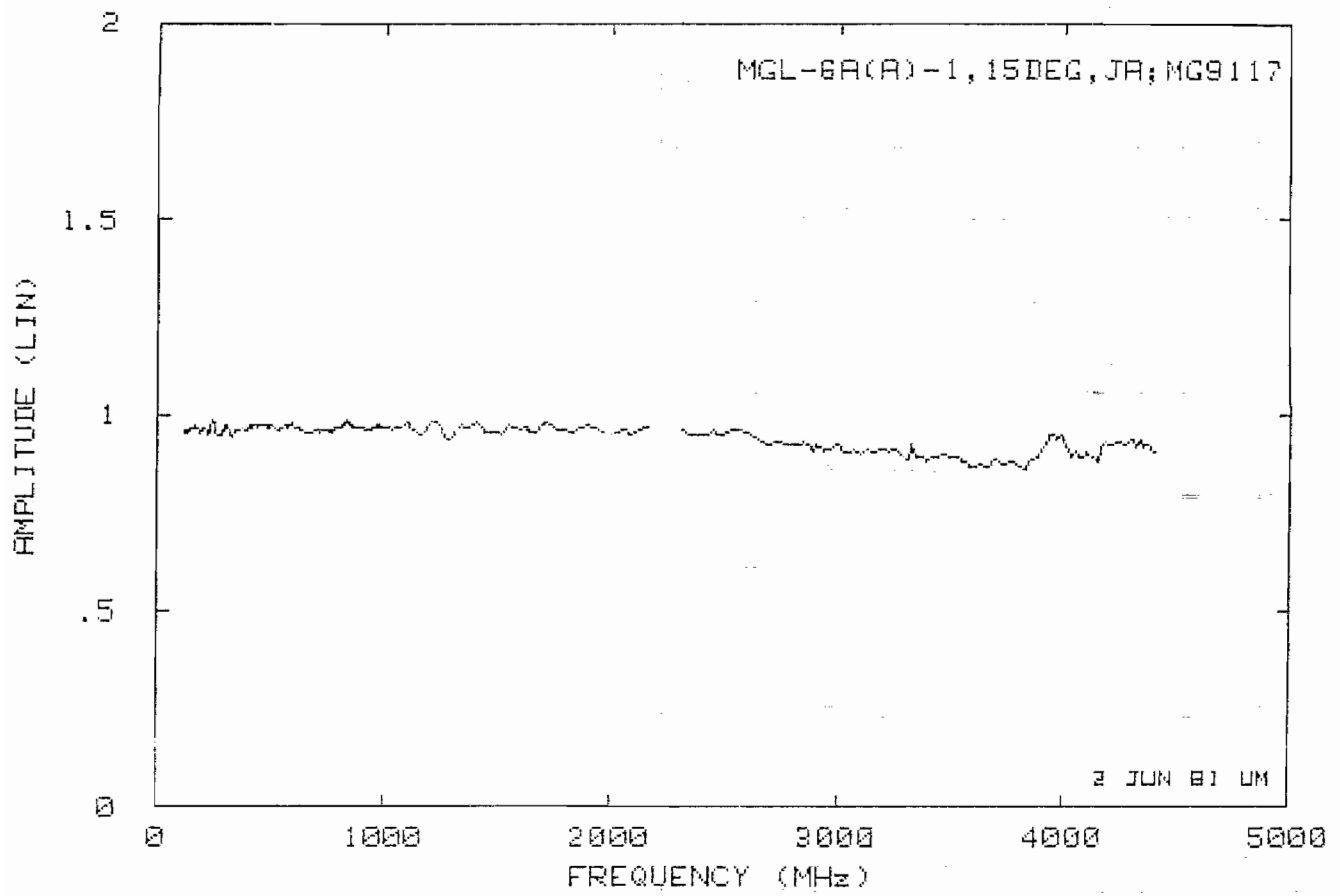


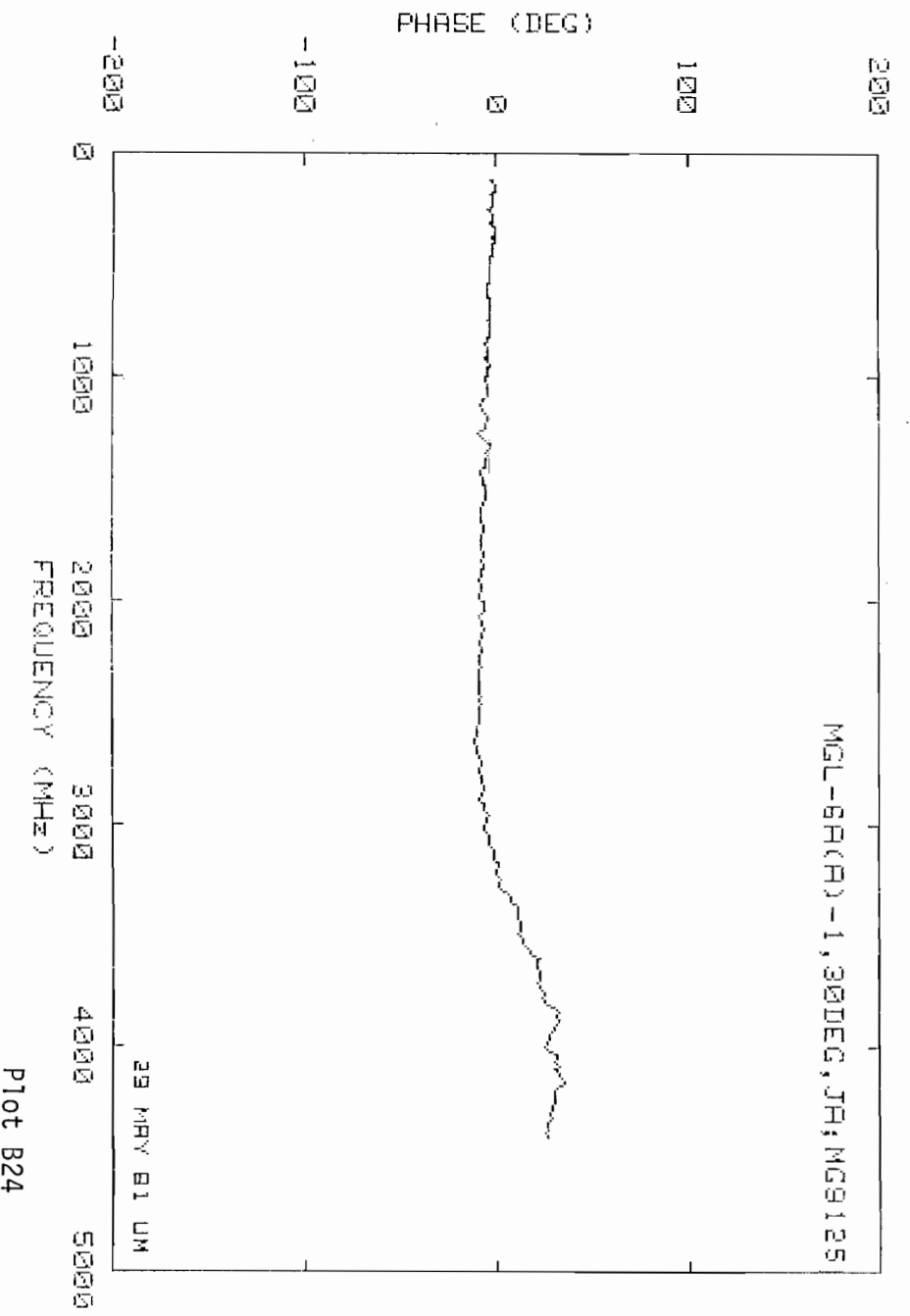
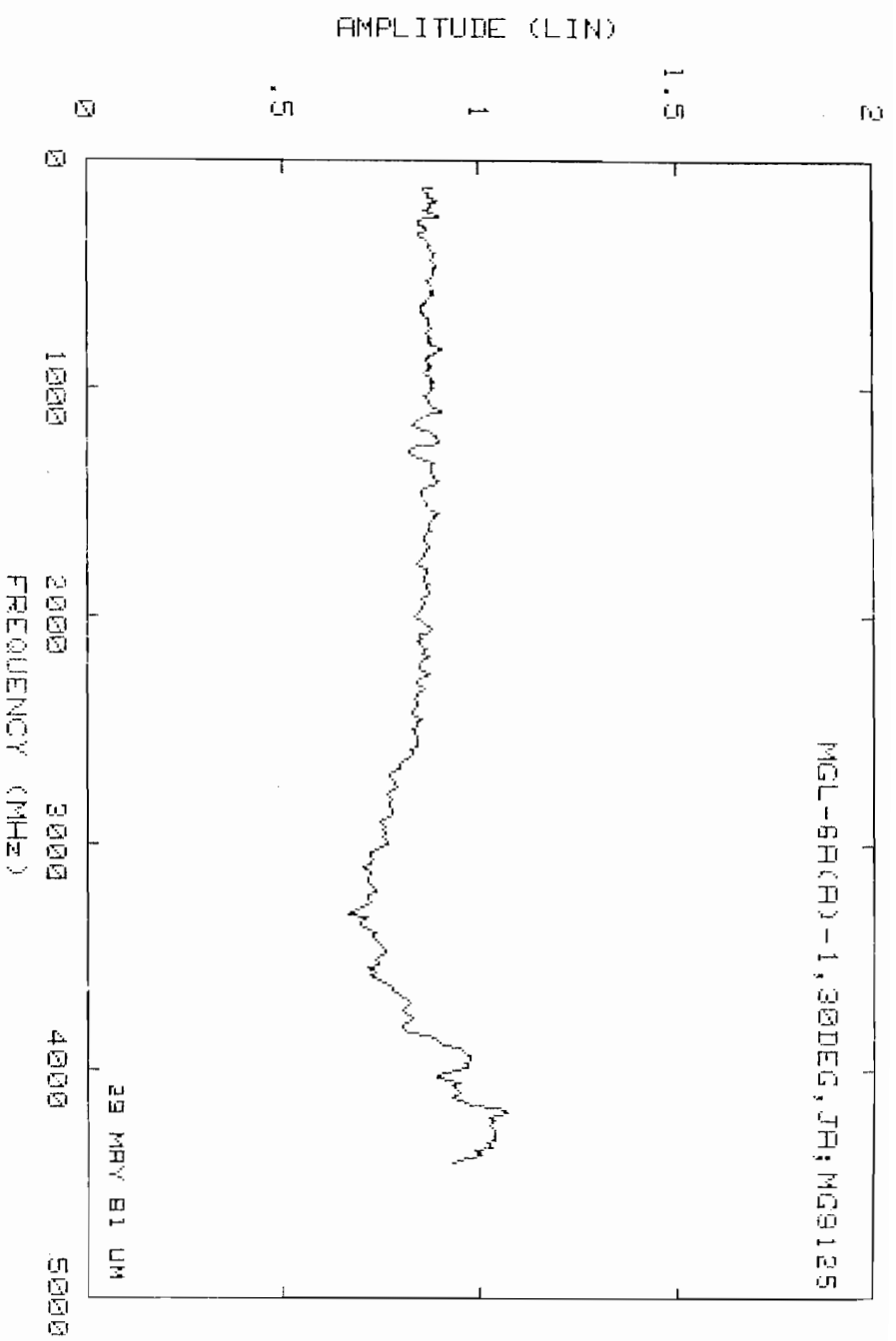


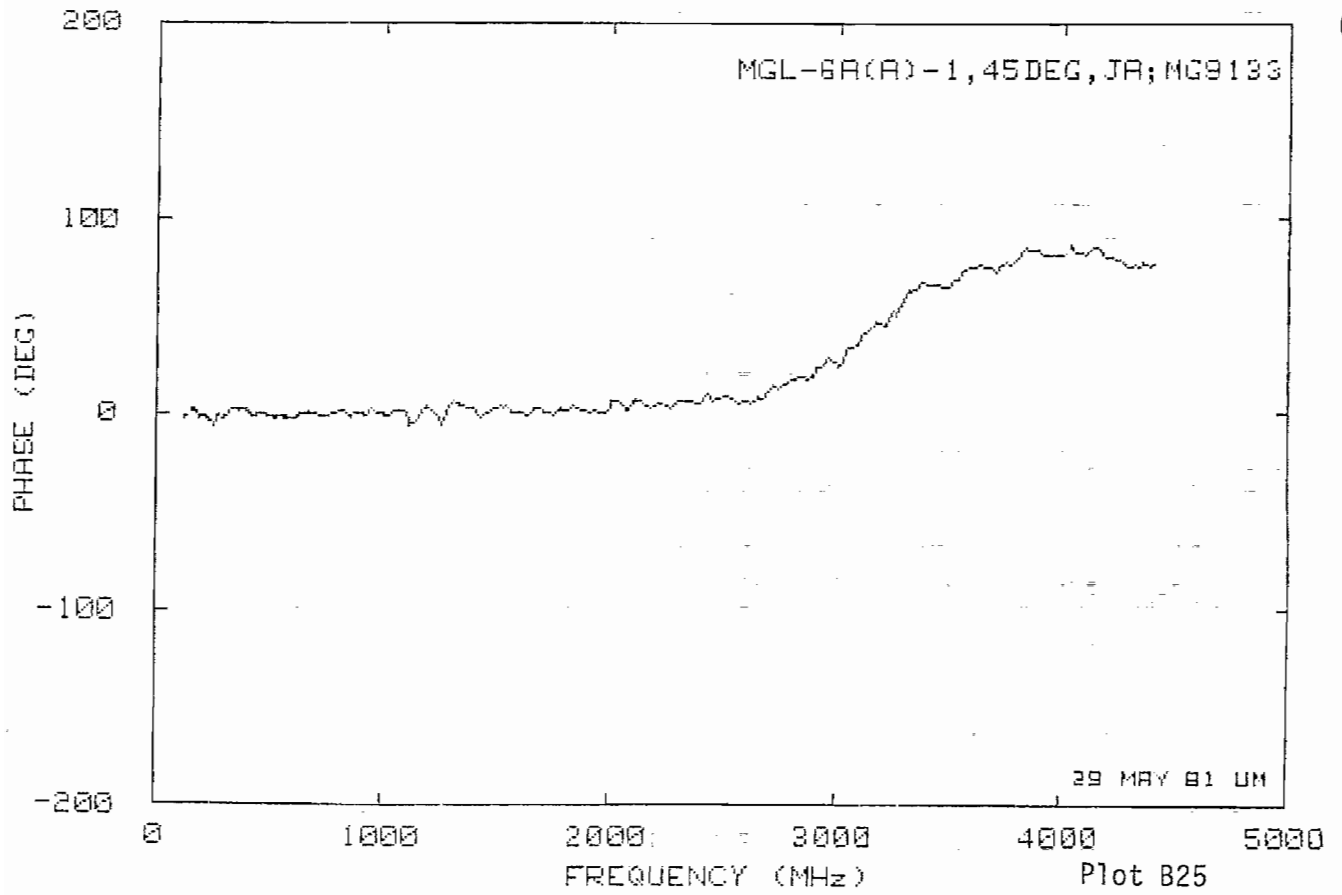
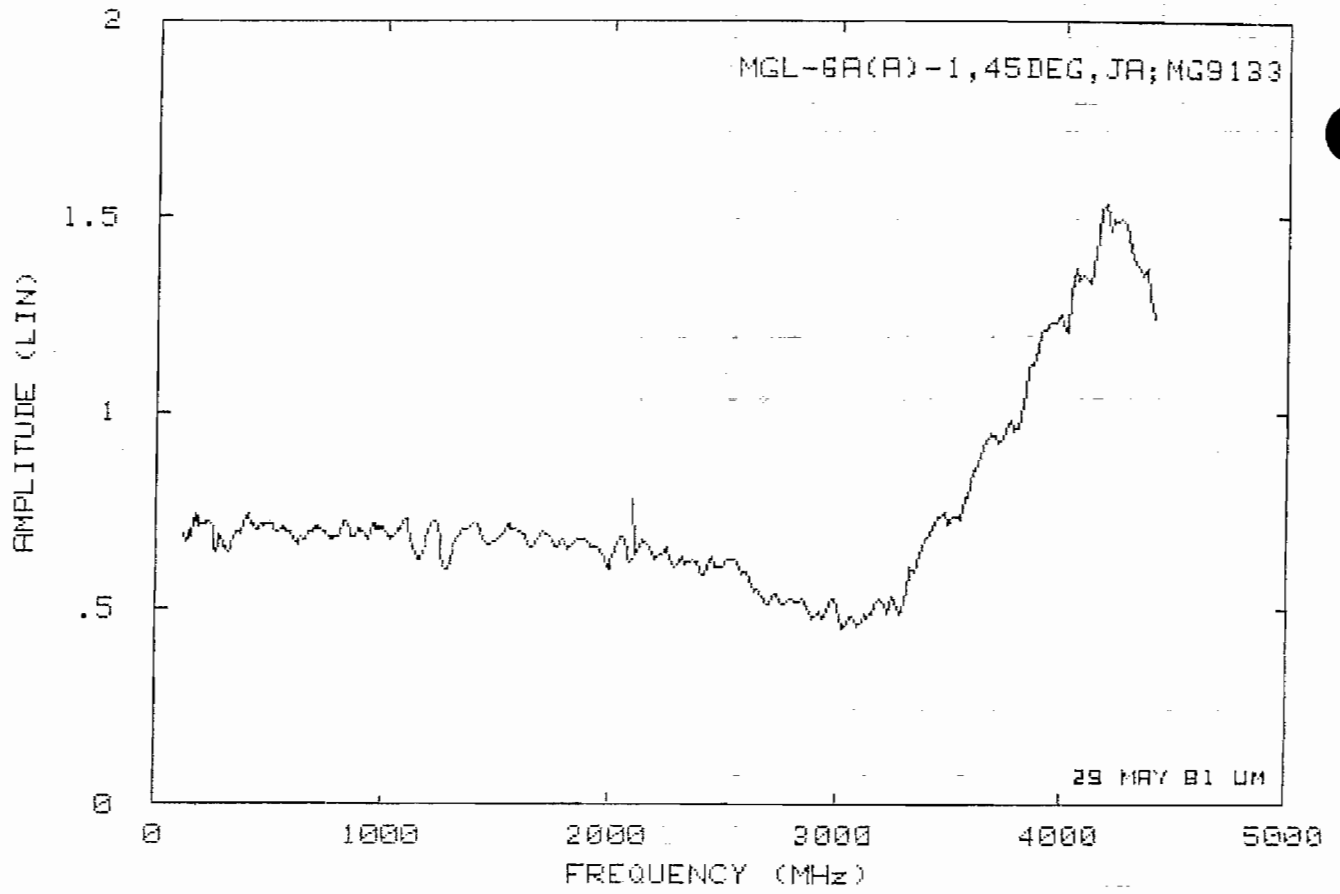


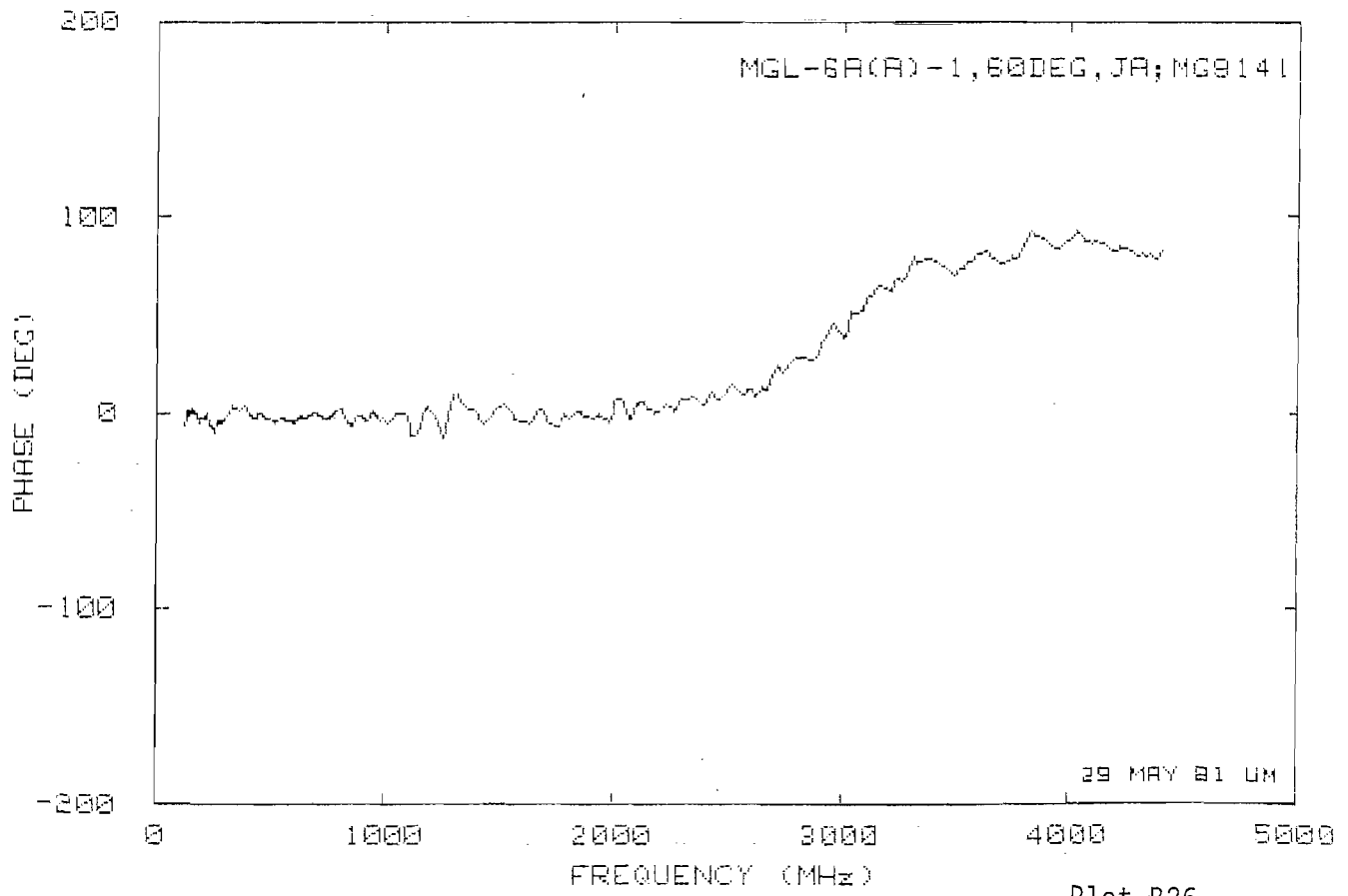
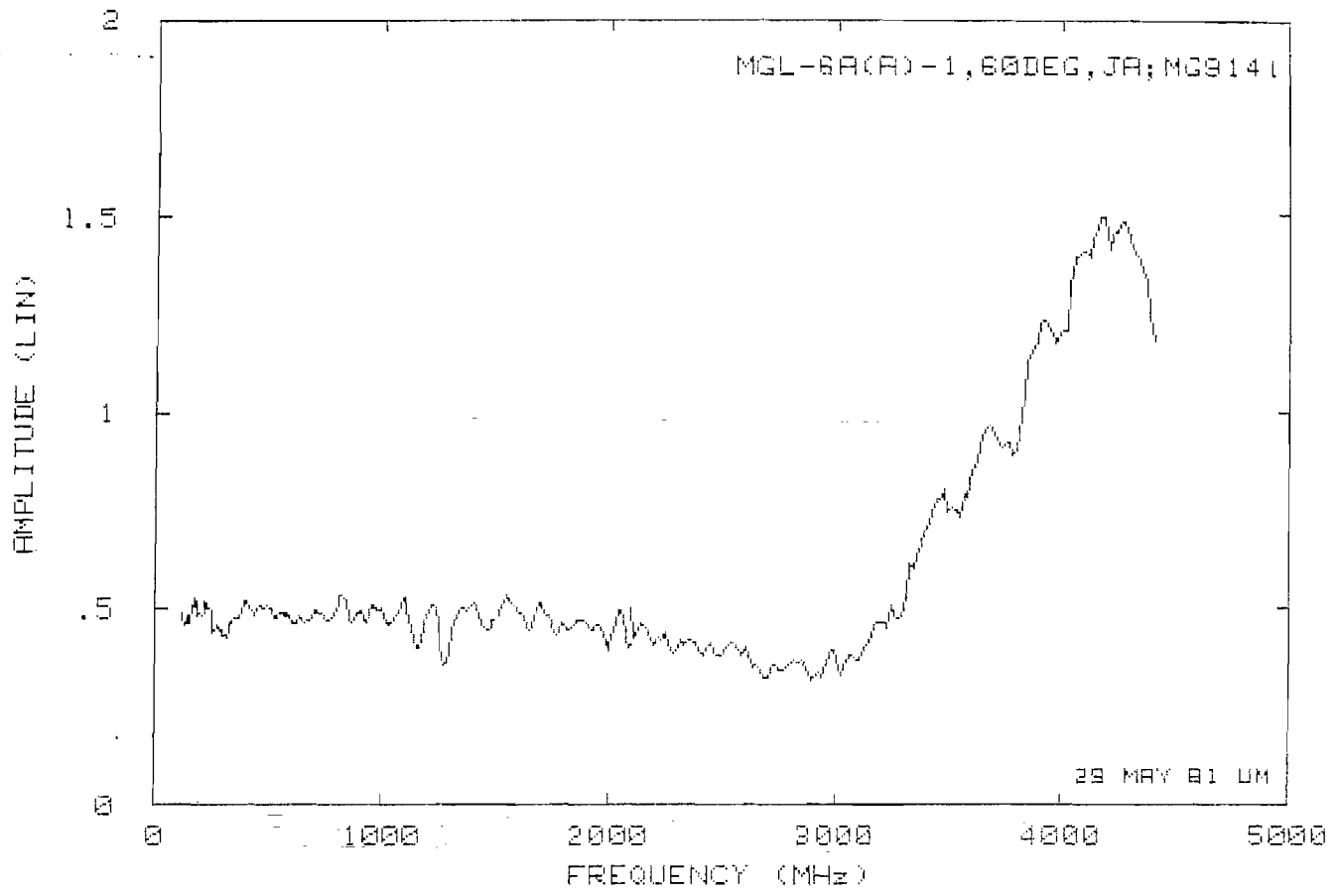


Plot B22

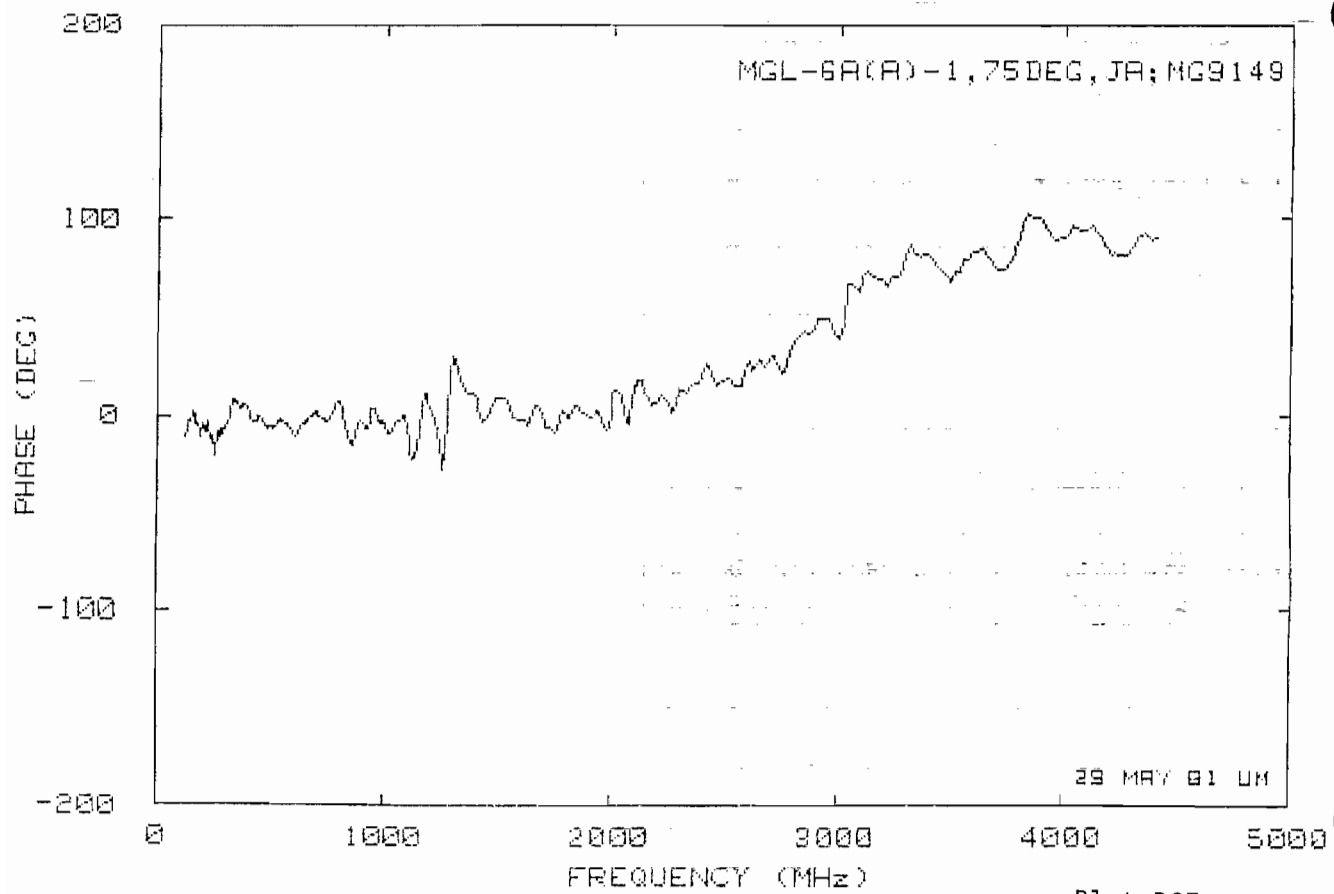
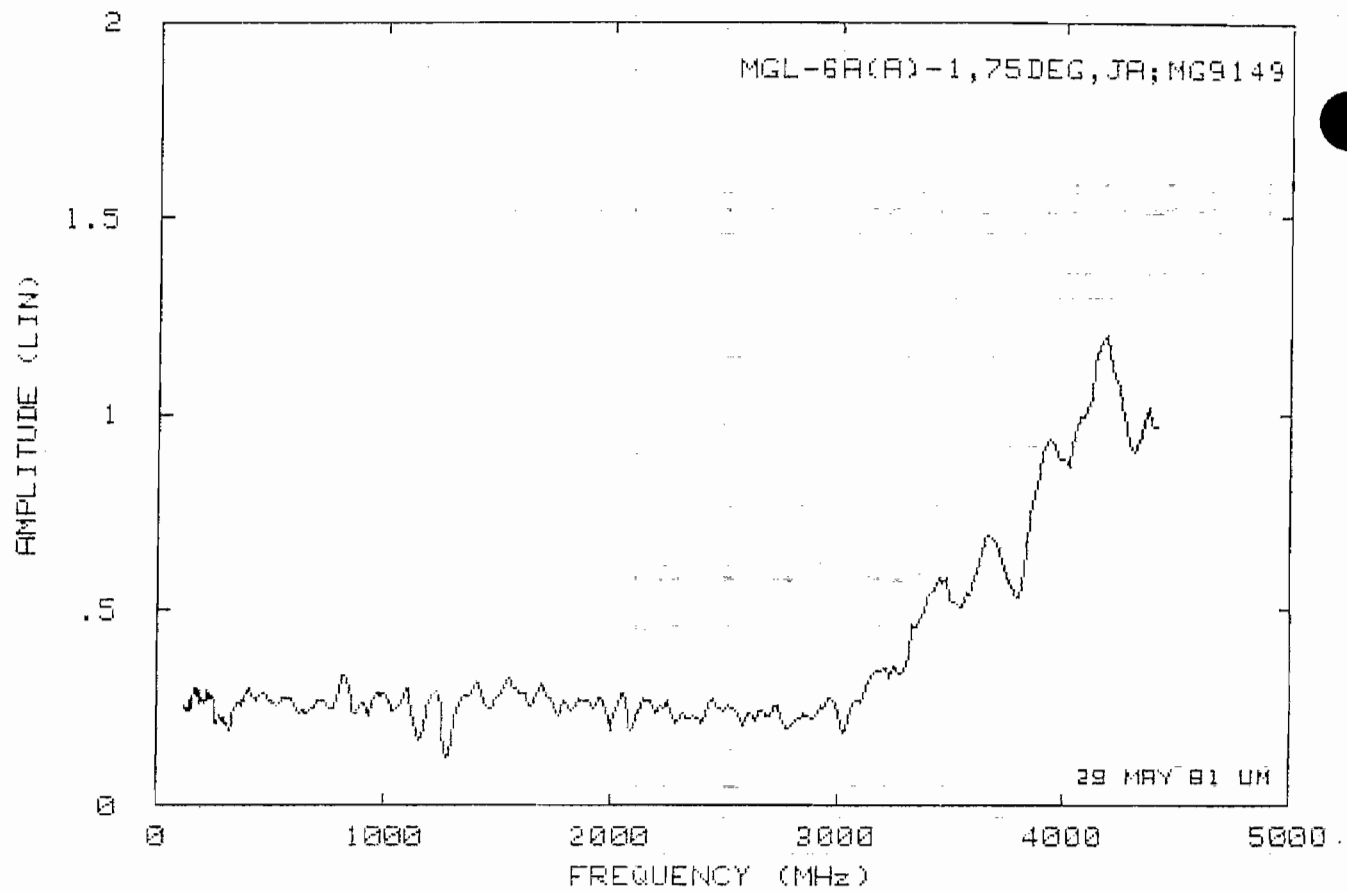




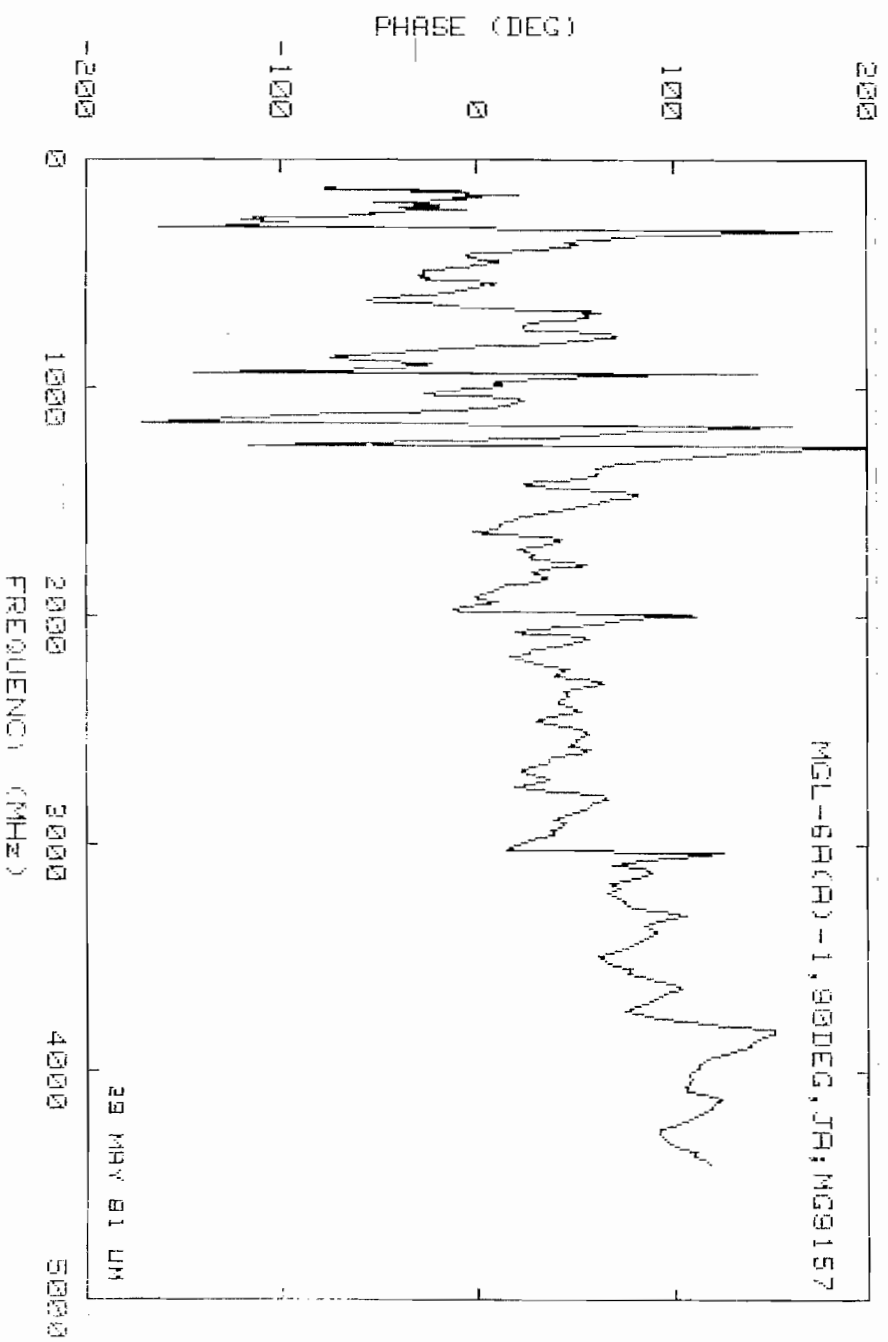
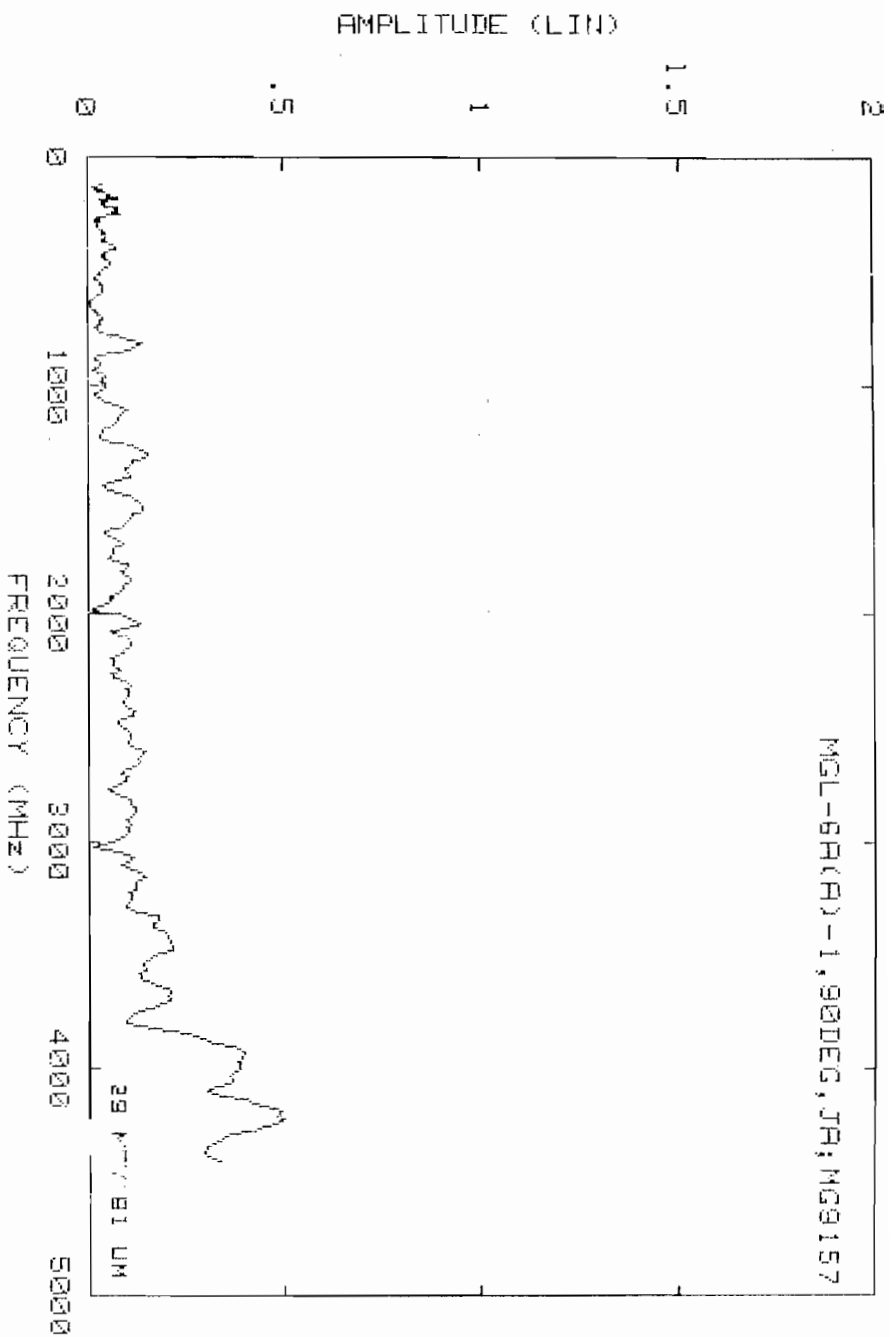




Plot B26



Plot B27

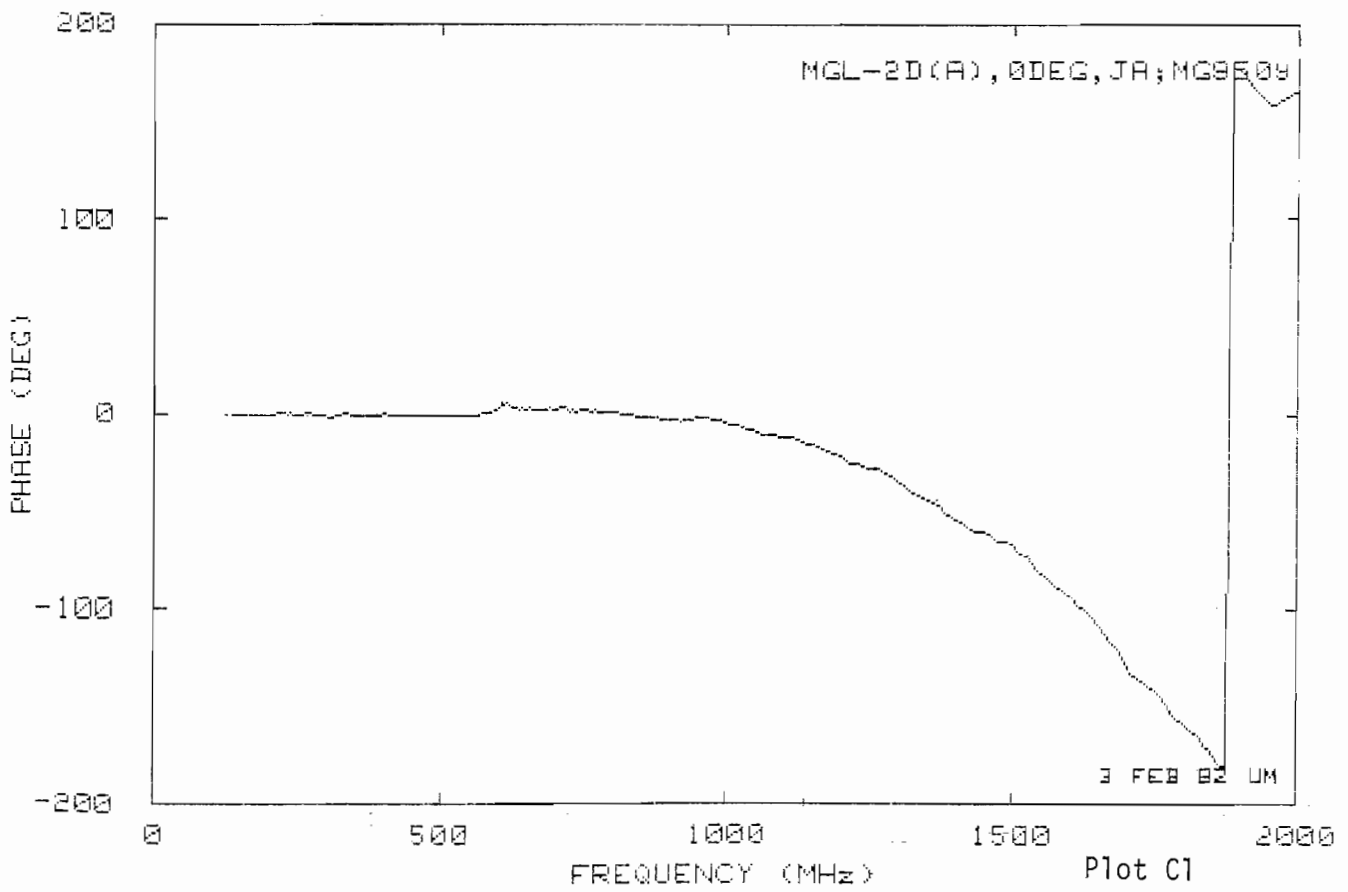
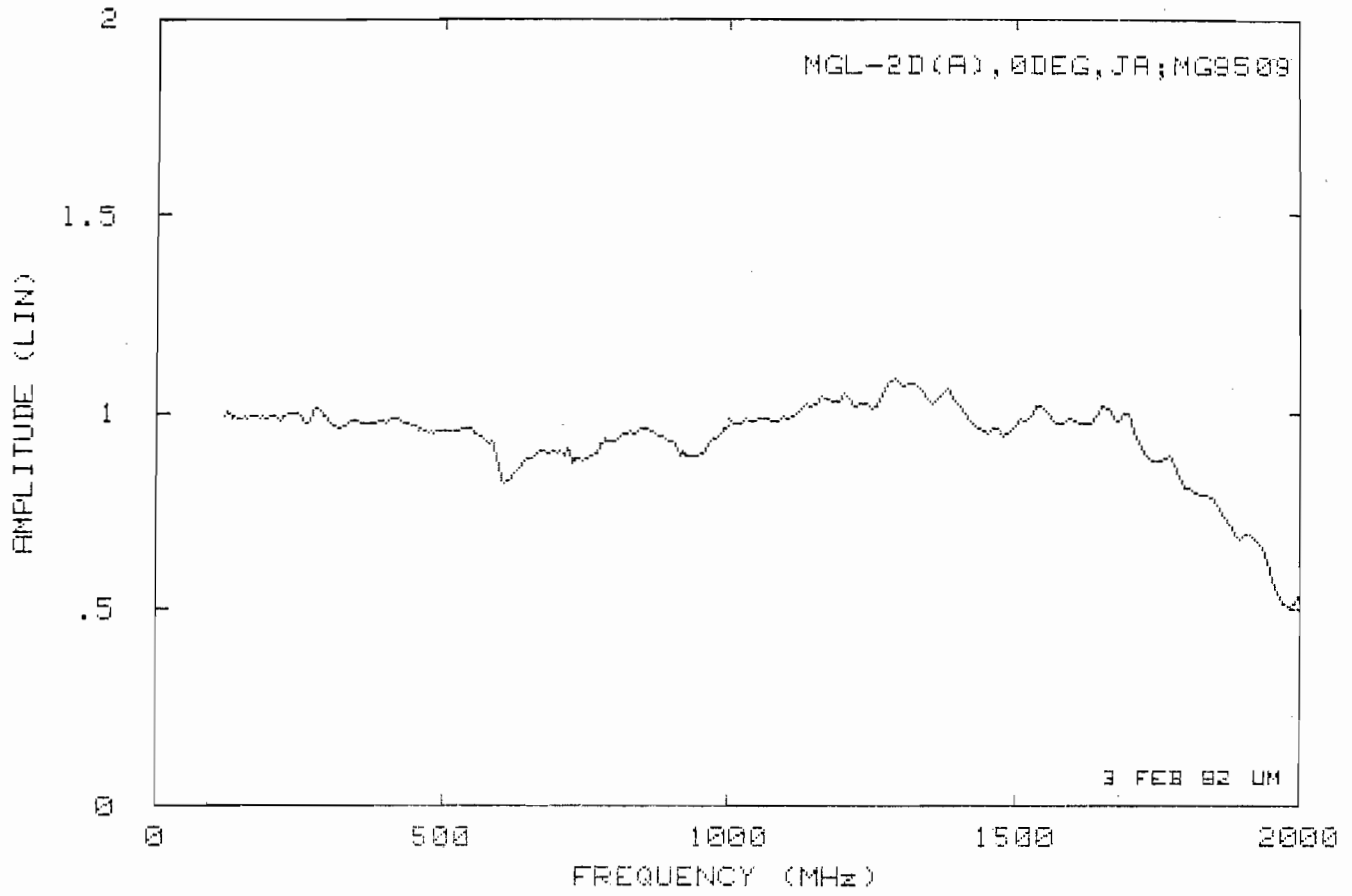


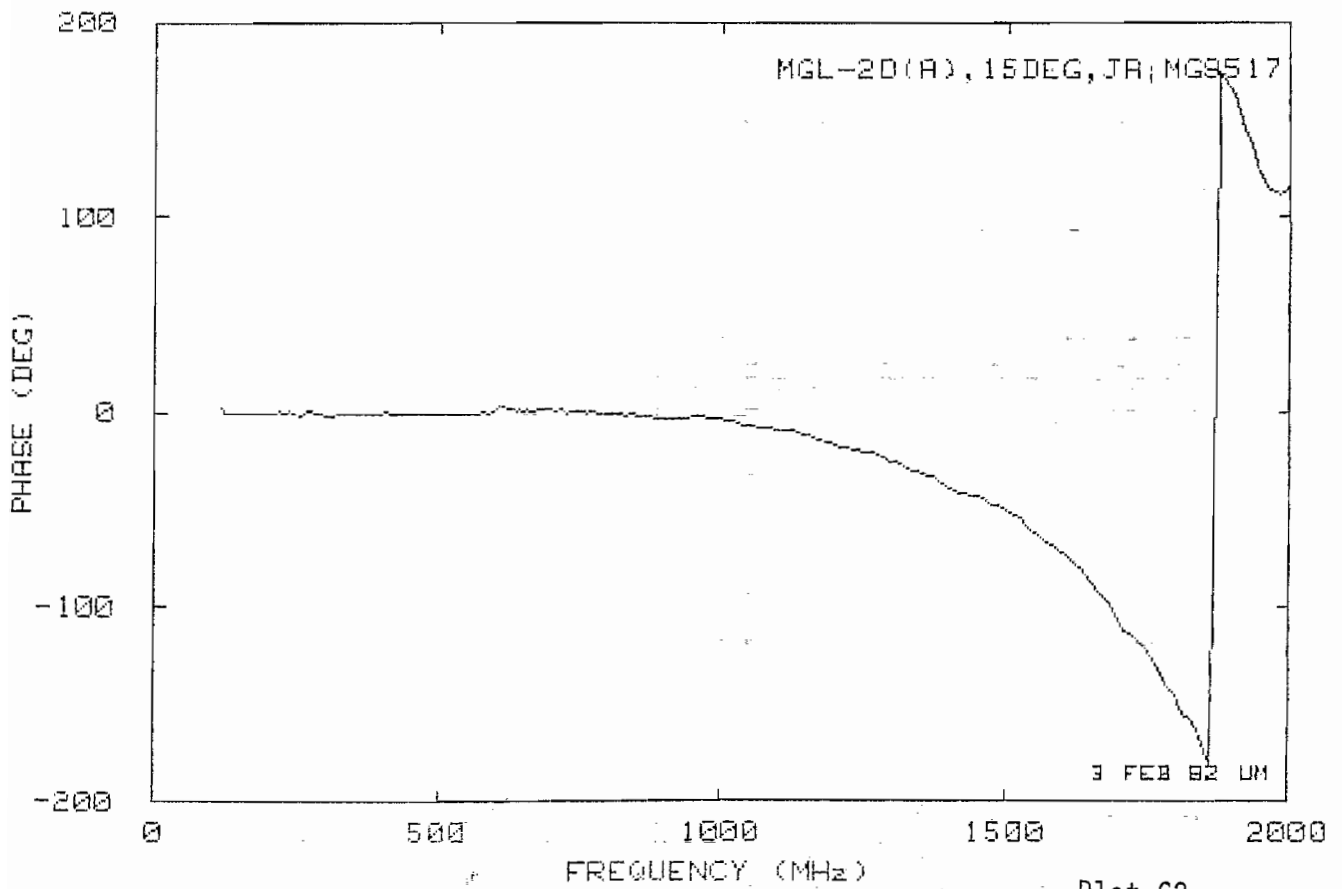
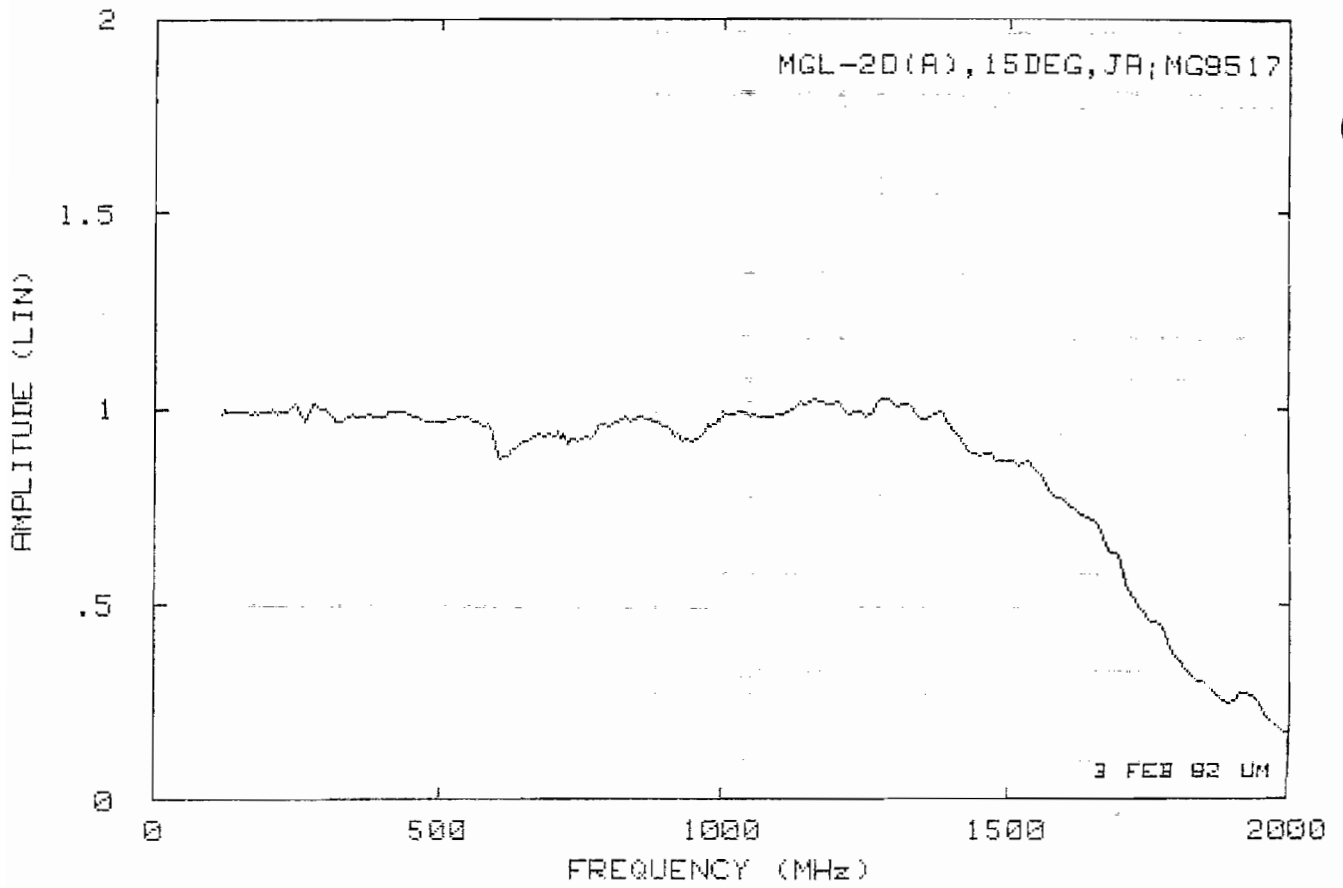
APPENDIX C: MGL-2D(A) AND MGL-6A(A) ROTATIONAL RESPONSE DATA (RAW)

The data presented here were obtained for 7 different angles of rotation of the sensors about their axes, viz $\phi = 0(15)90$ degrees. The angle ϕ is measured from gap No. 2, implying that for $\phi = 0$ the exciting signal is incident on this gap. The data are normalized to the measured values for $\phi = 45$ degrees, corresponding to incidence midway between the two gaps. Because of the symmetry of the sensor designs, data were recorded over a single quadrant only. Ideally, the responses should be independent of ϕ , implying unity plots, but the results show that this is not the case at high frequencies.

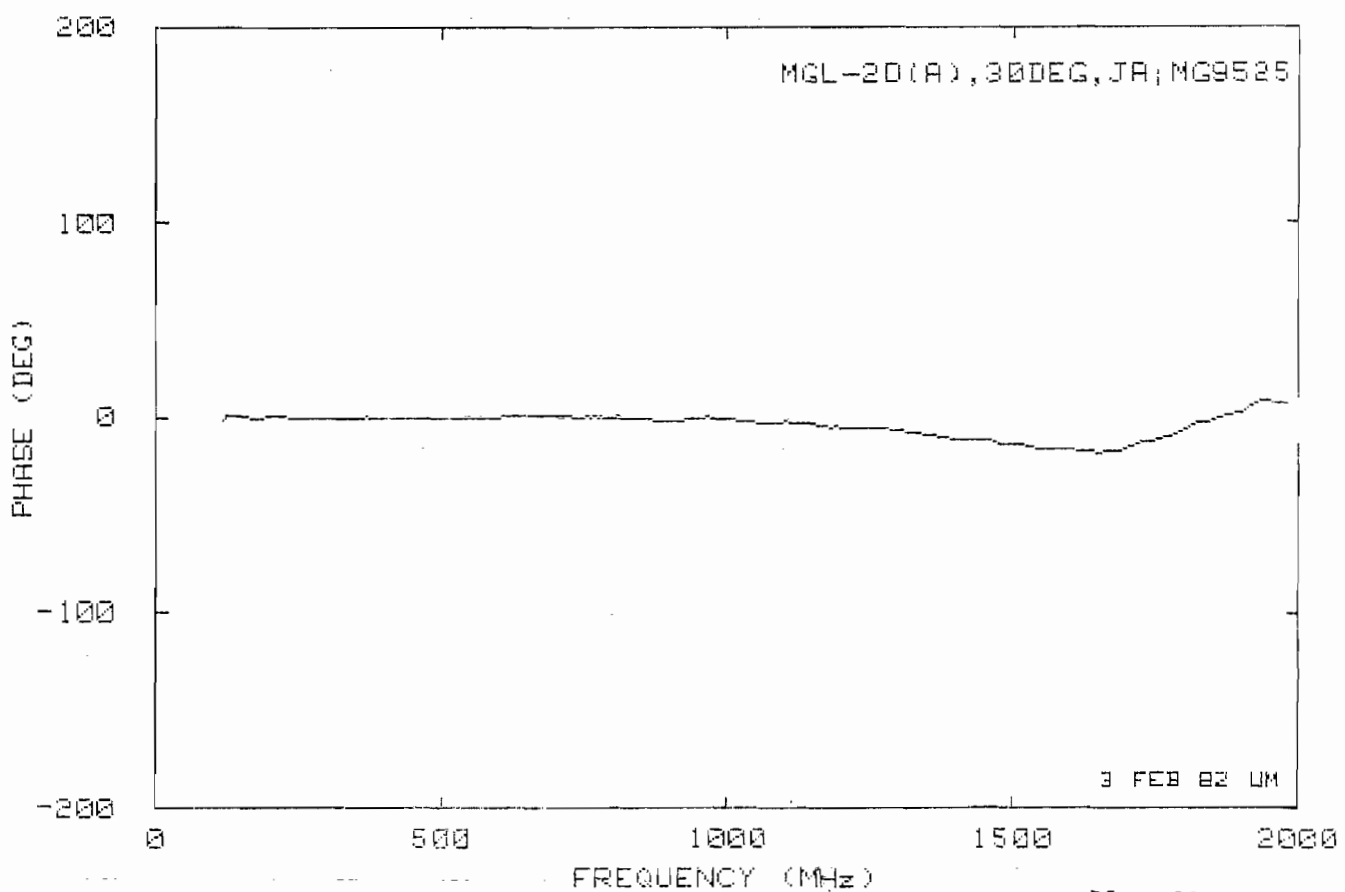
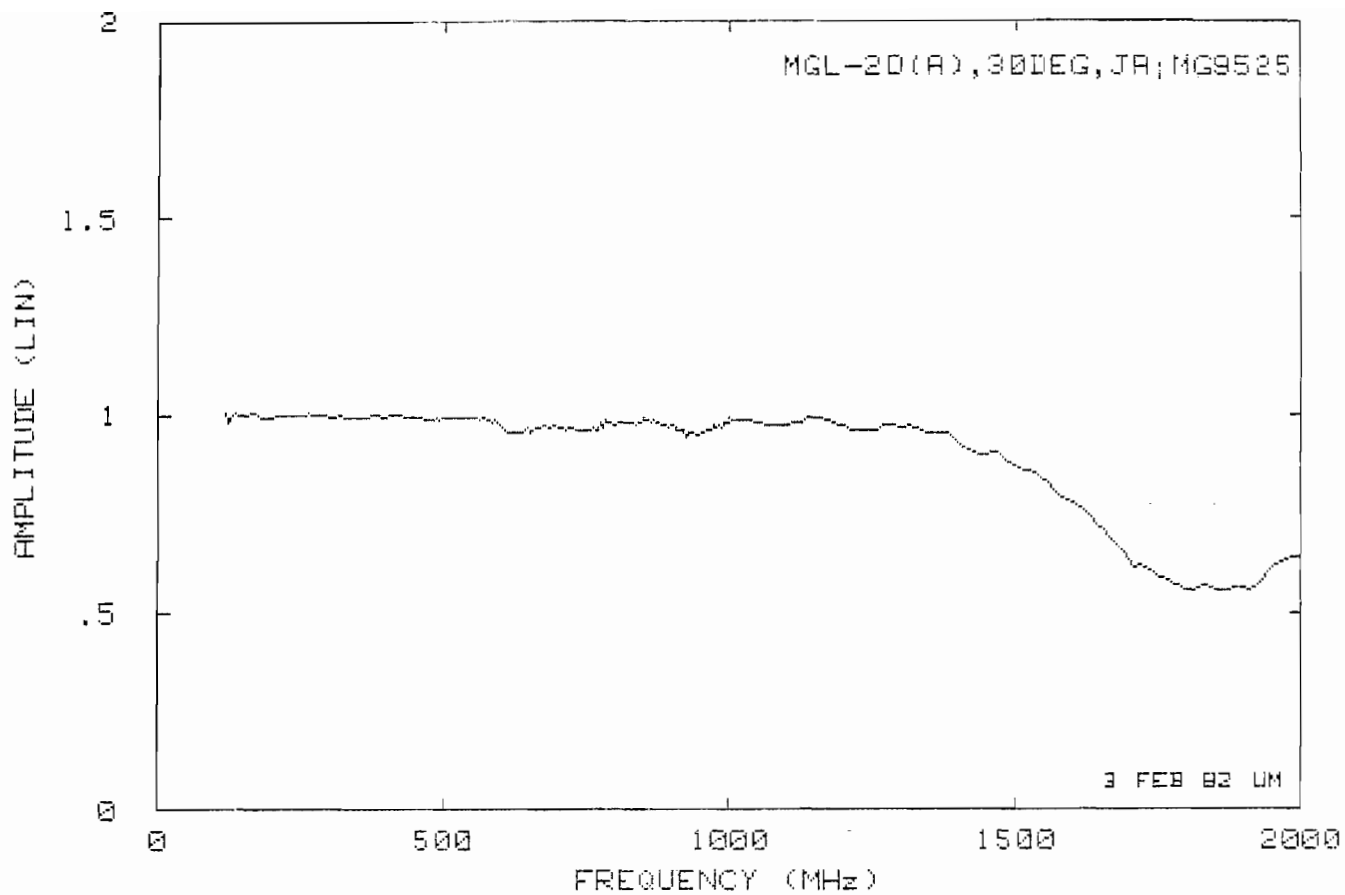
Table C1: List of MGL-2 and MGL-6 Rotational Data Plots

(degrees)	MGL-2		MGL-6	
	Plot No.	File No.	Plot No.	File No.
0	C1	MG 9509	C8	MG 9601
15	C2	MG 9517	C9	MG 9609
30	C3	MG 9525	C10	MG 9617
45	C4	MG 9541	C11	MG 9625
60	C5	MG 9557	C12	MG 9633
75	C6	MG 9565	C13	MG 9641
90	C7	MG 9573	C14	MG 9649

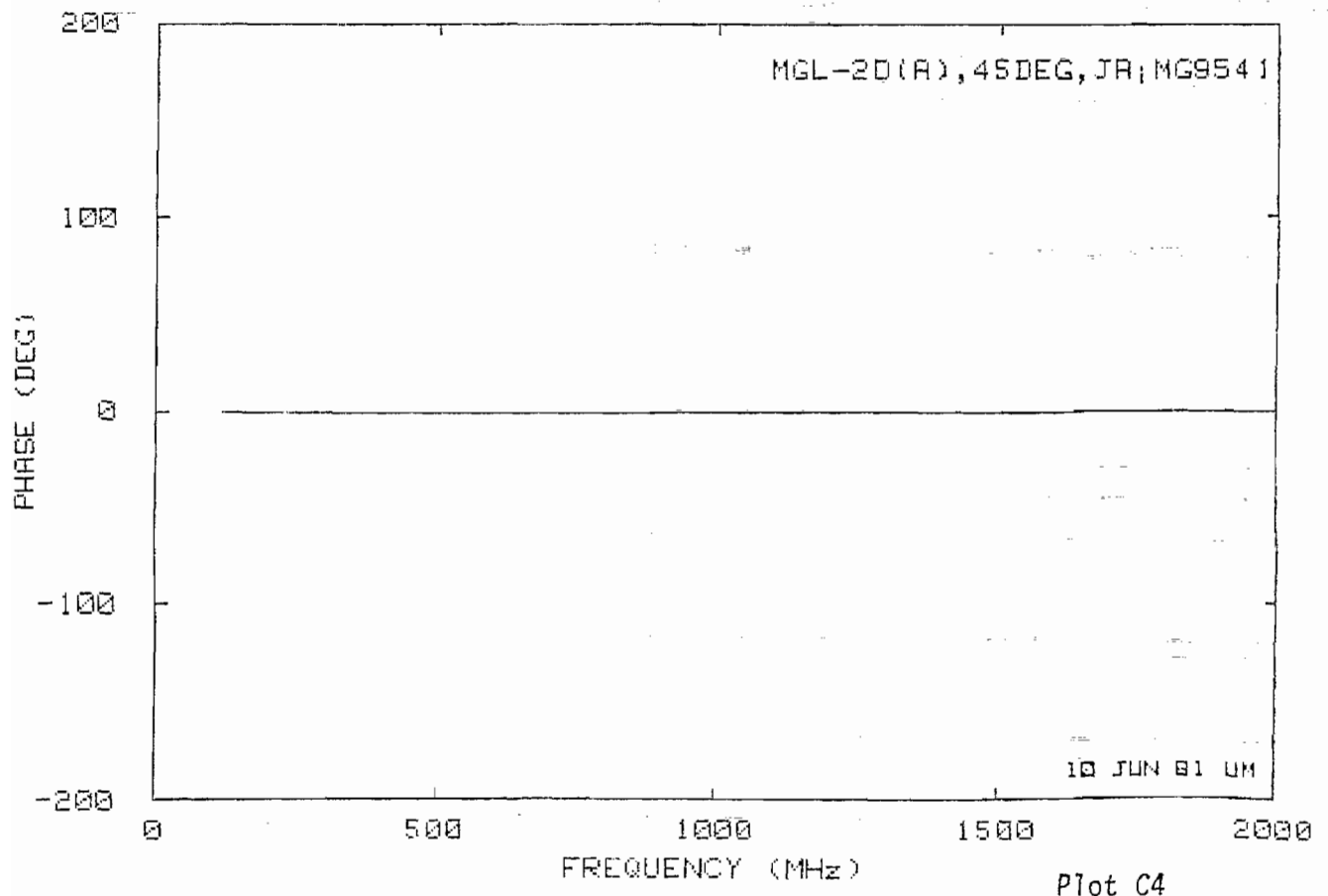
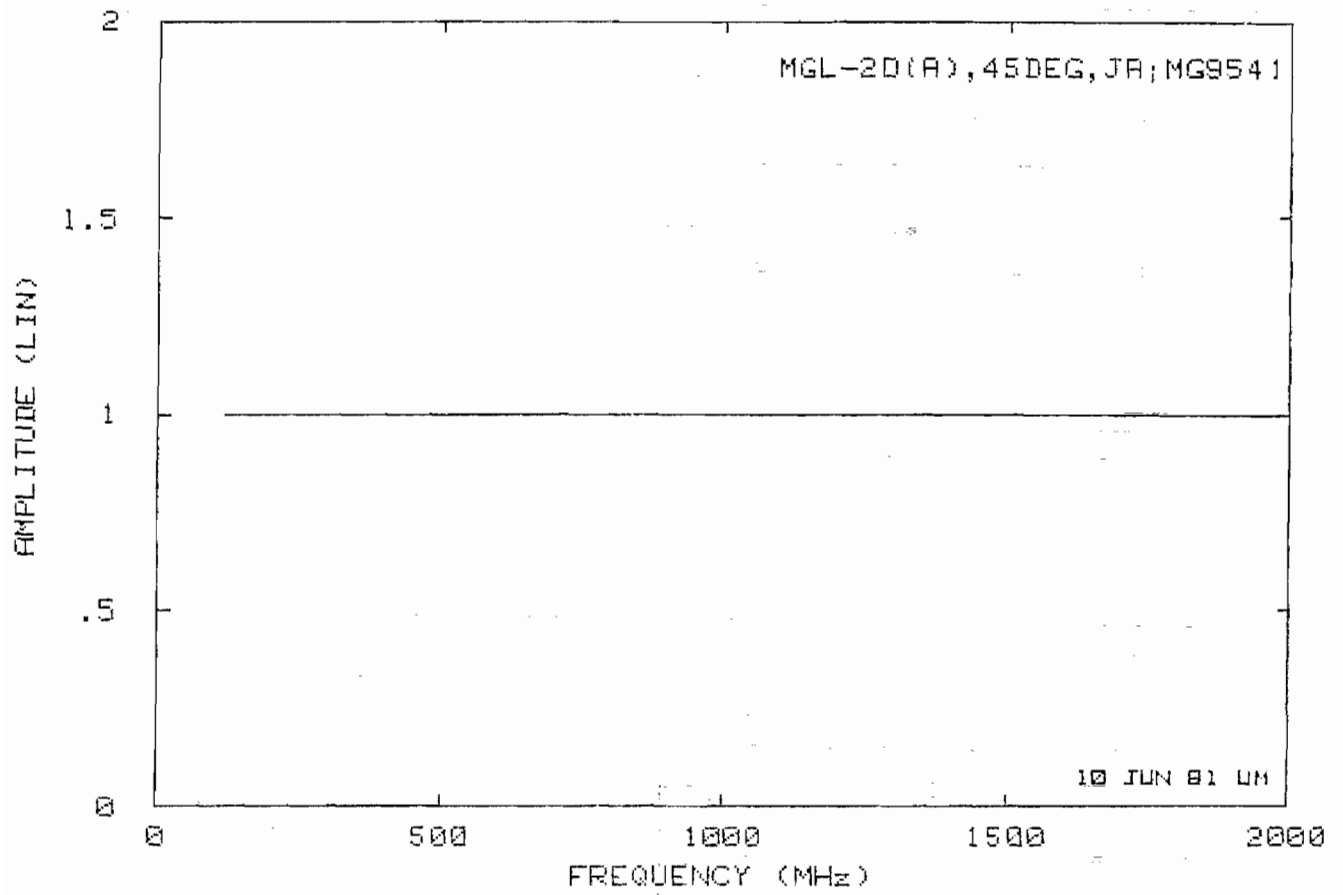


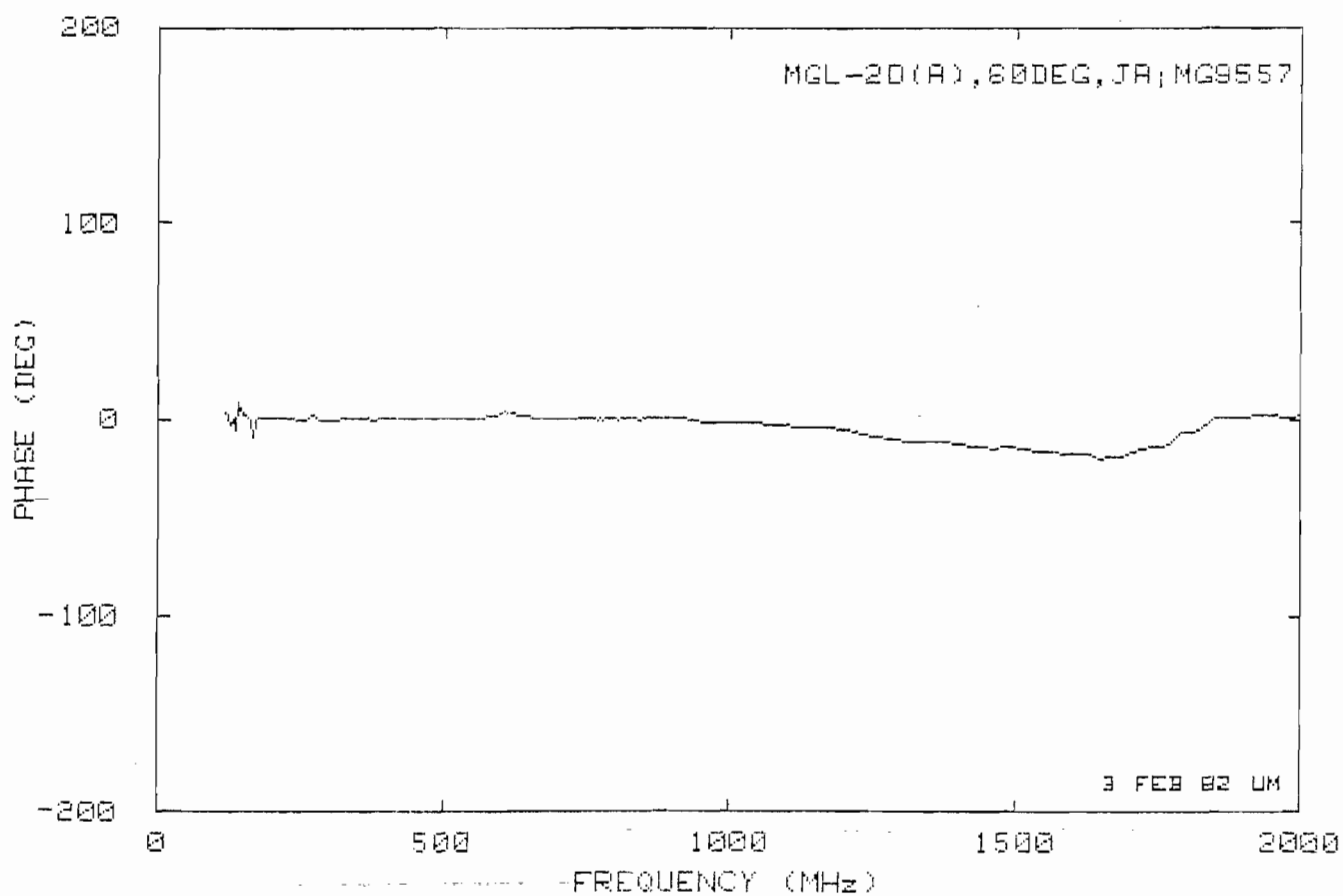
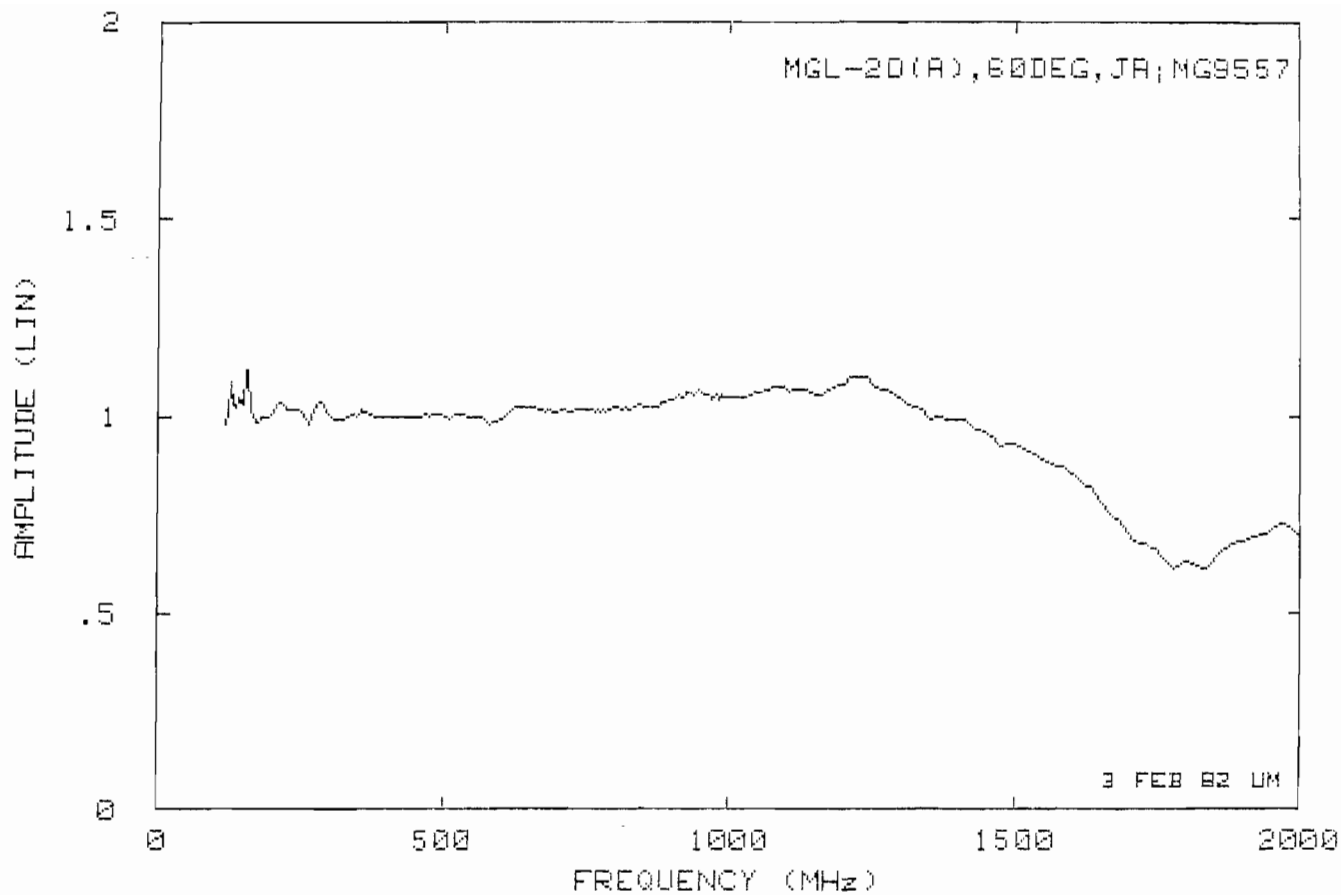


Plot C2

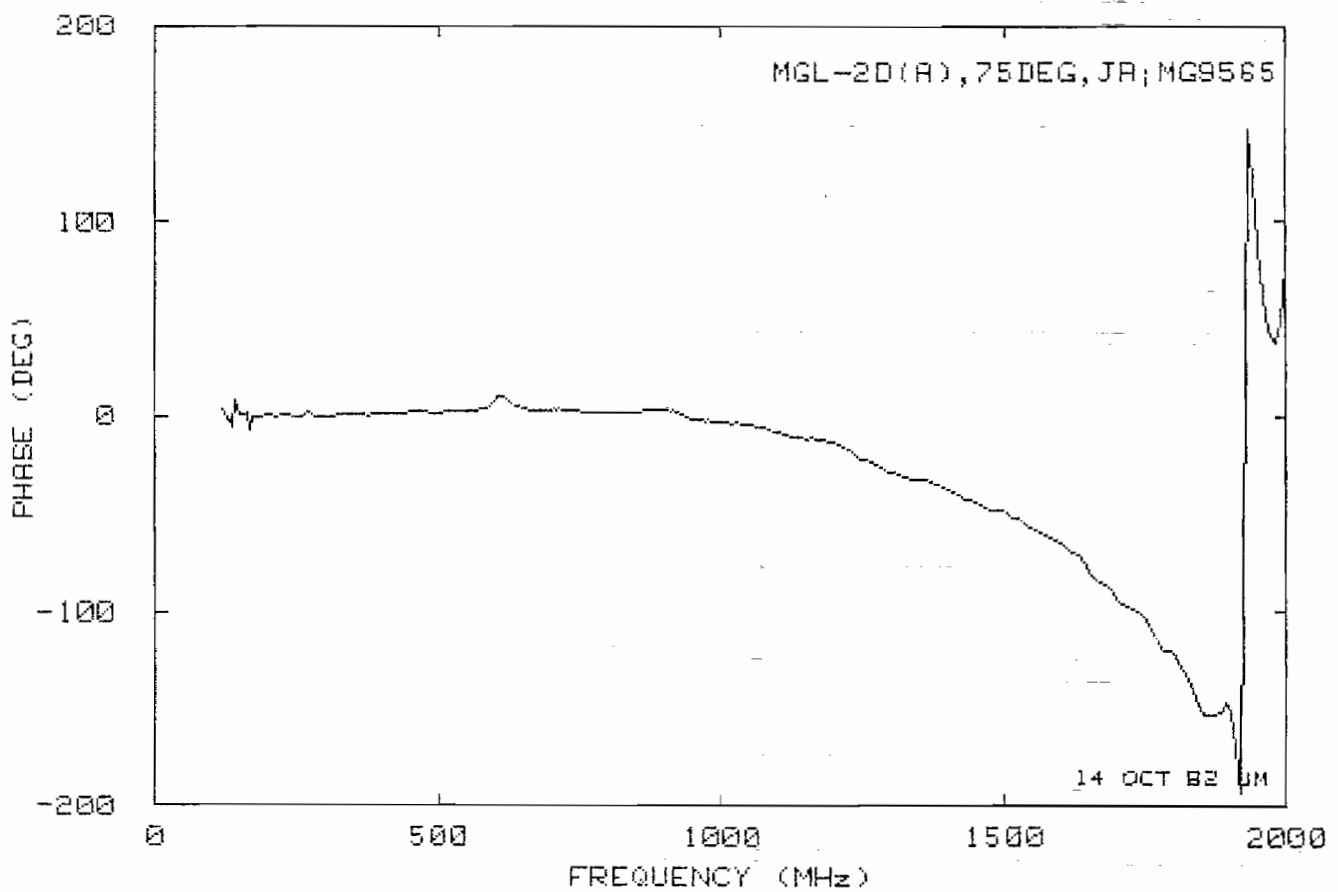
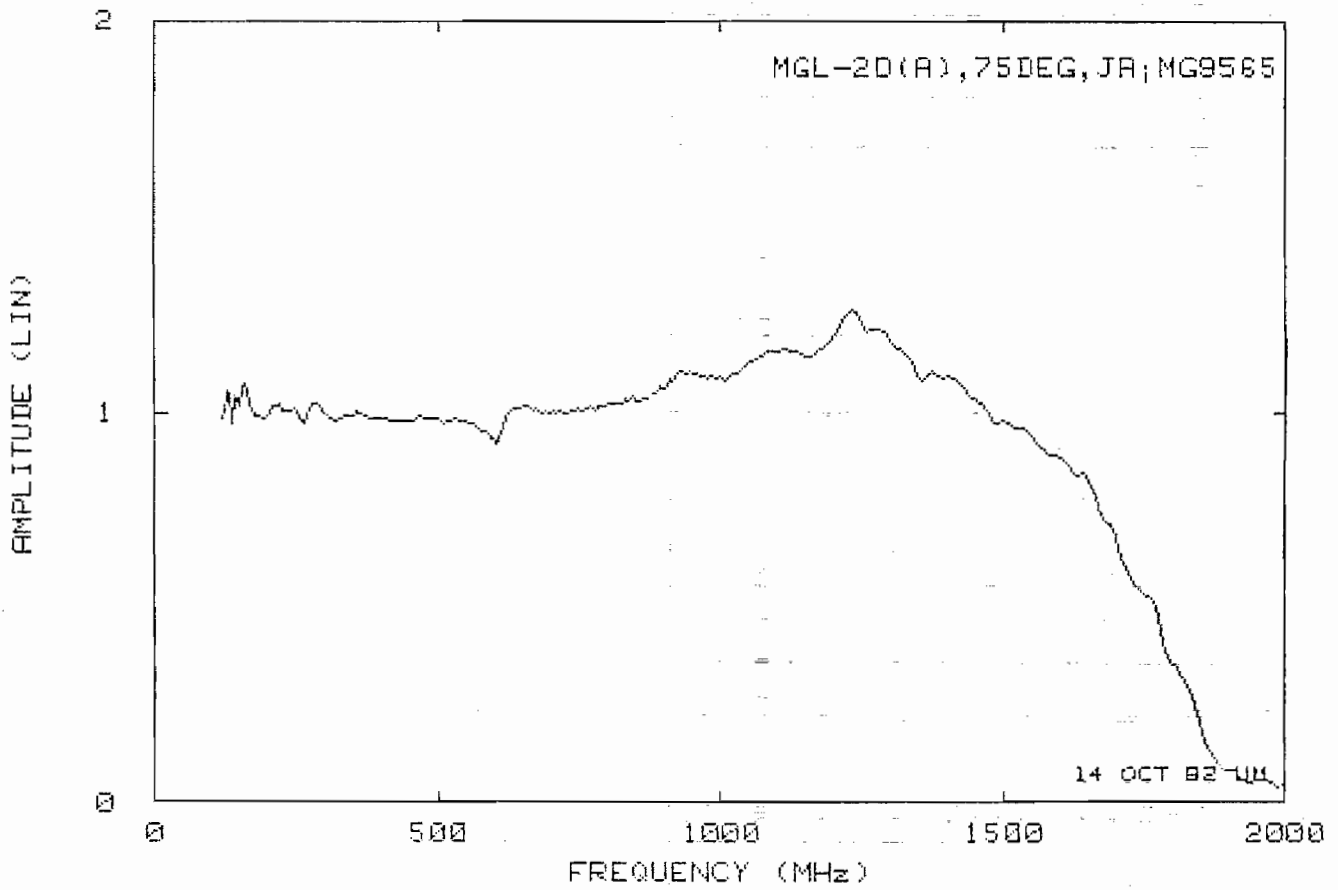


Plot C3

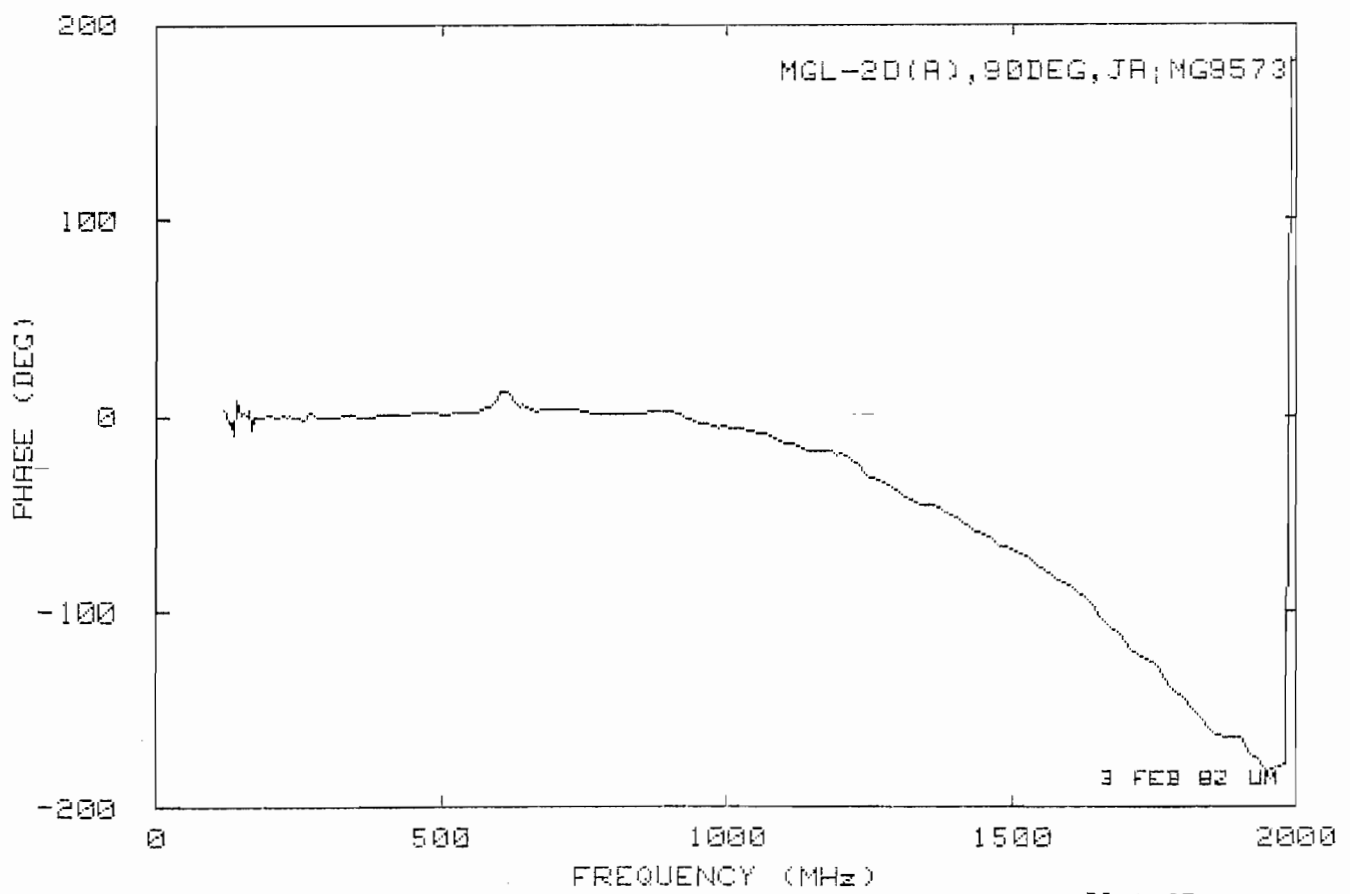
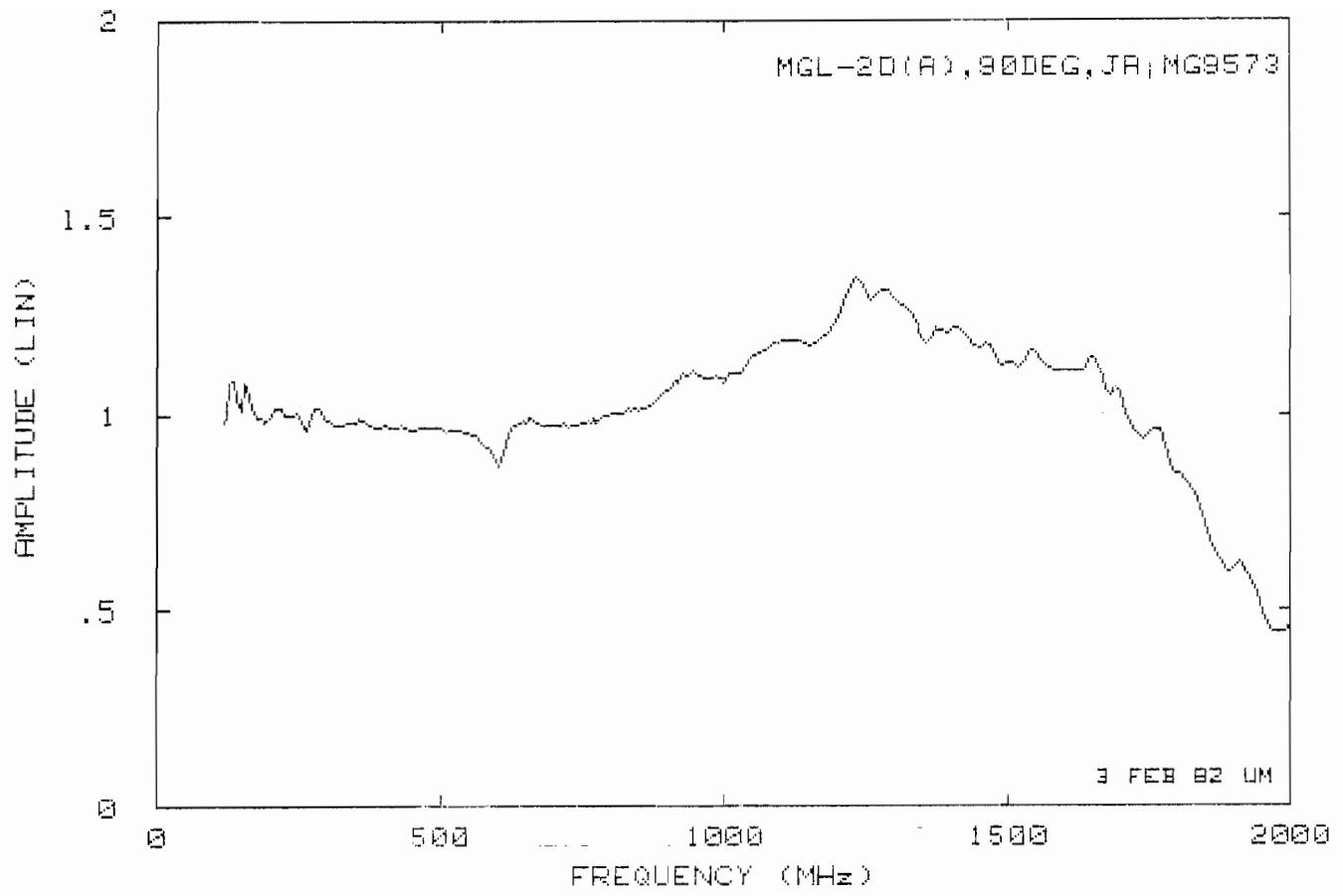




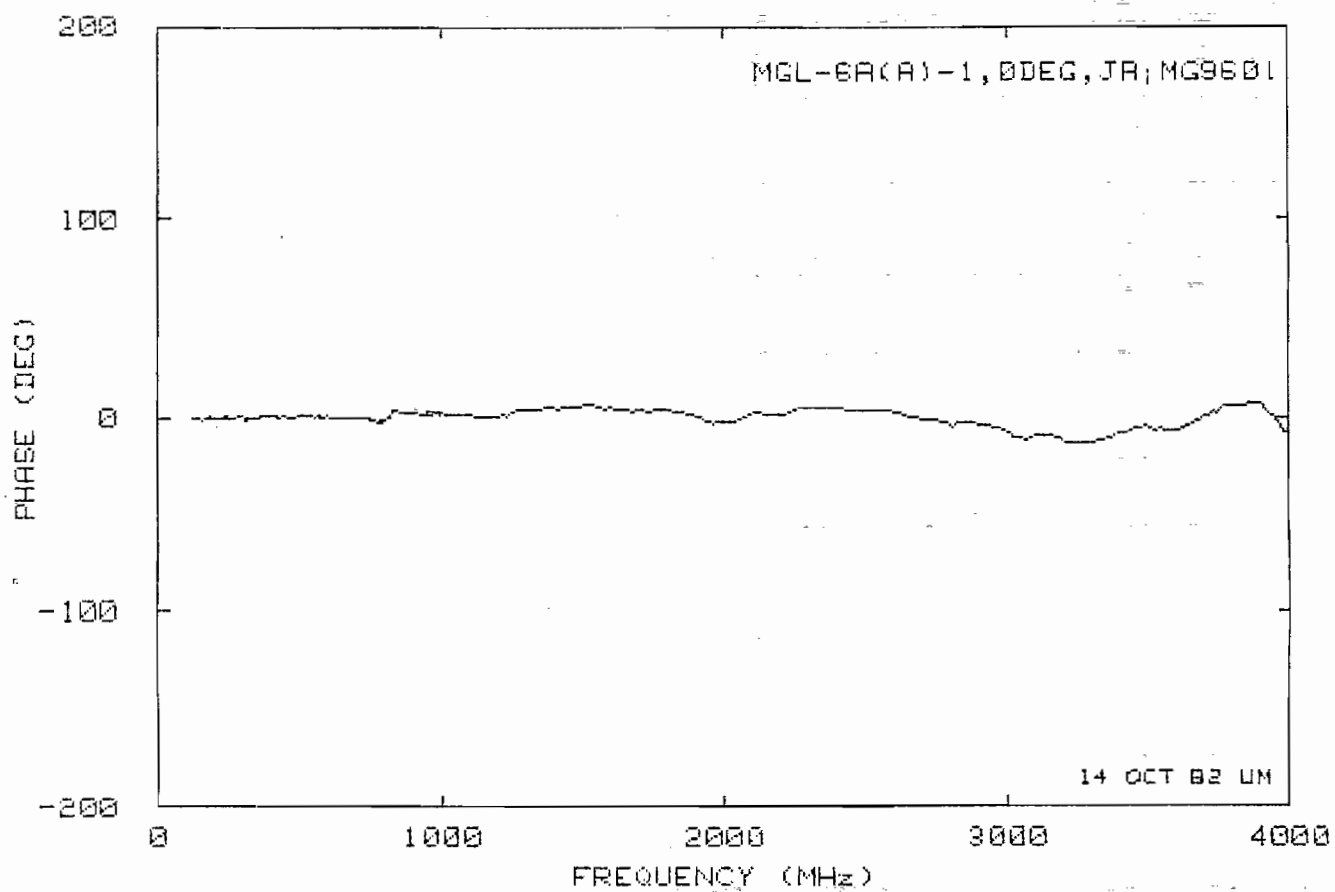
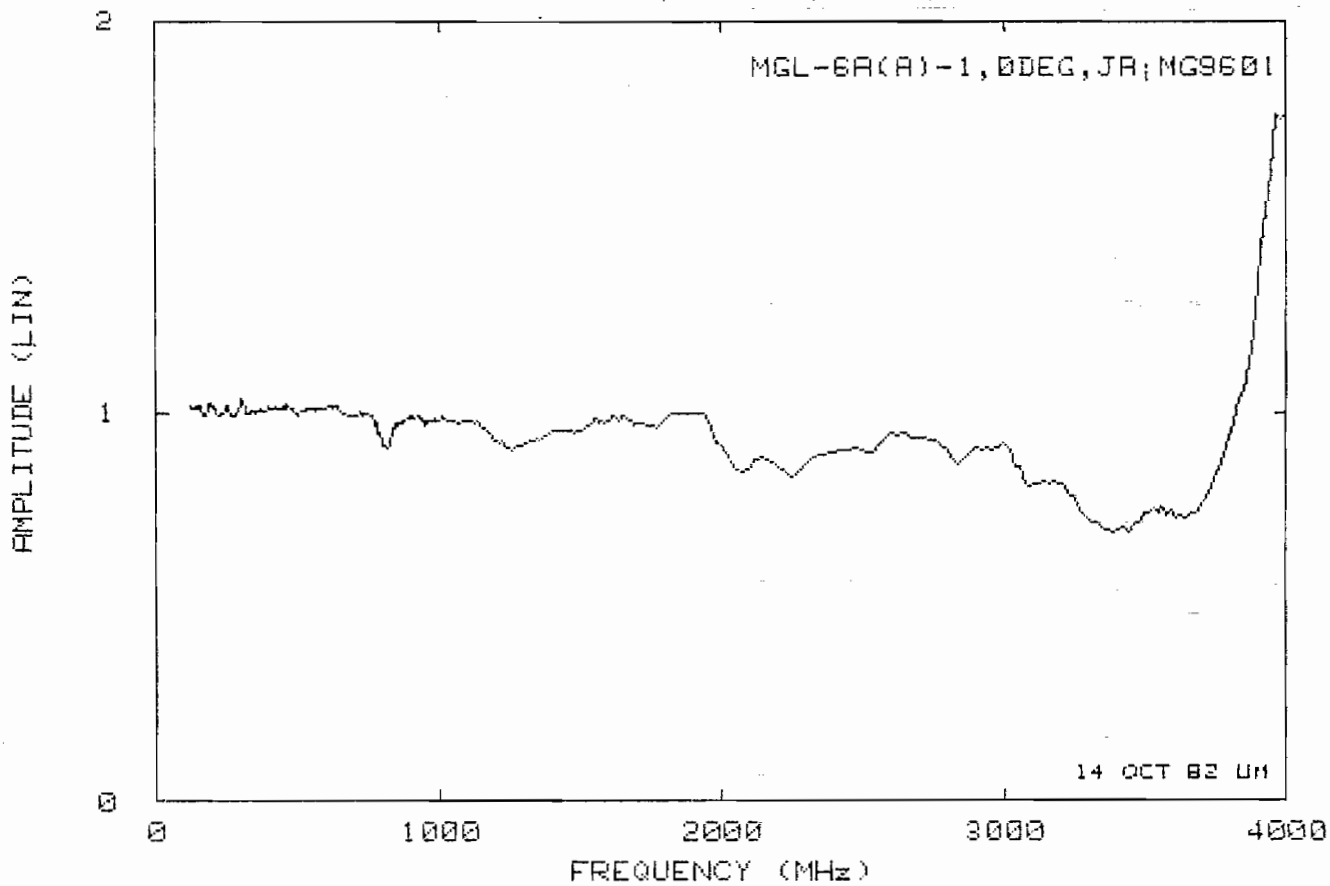
Plot C5



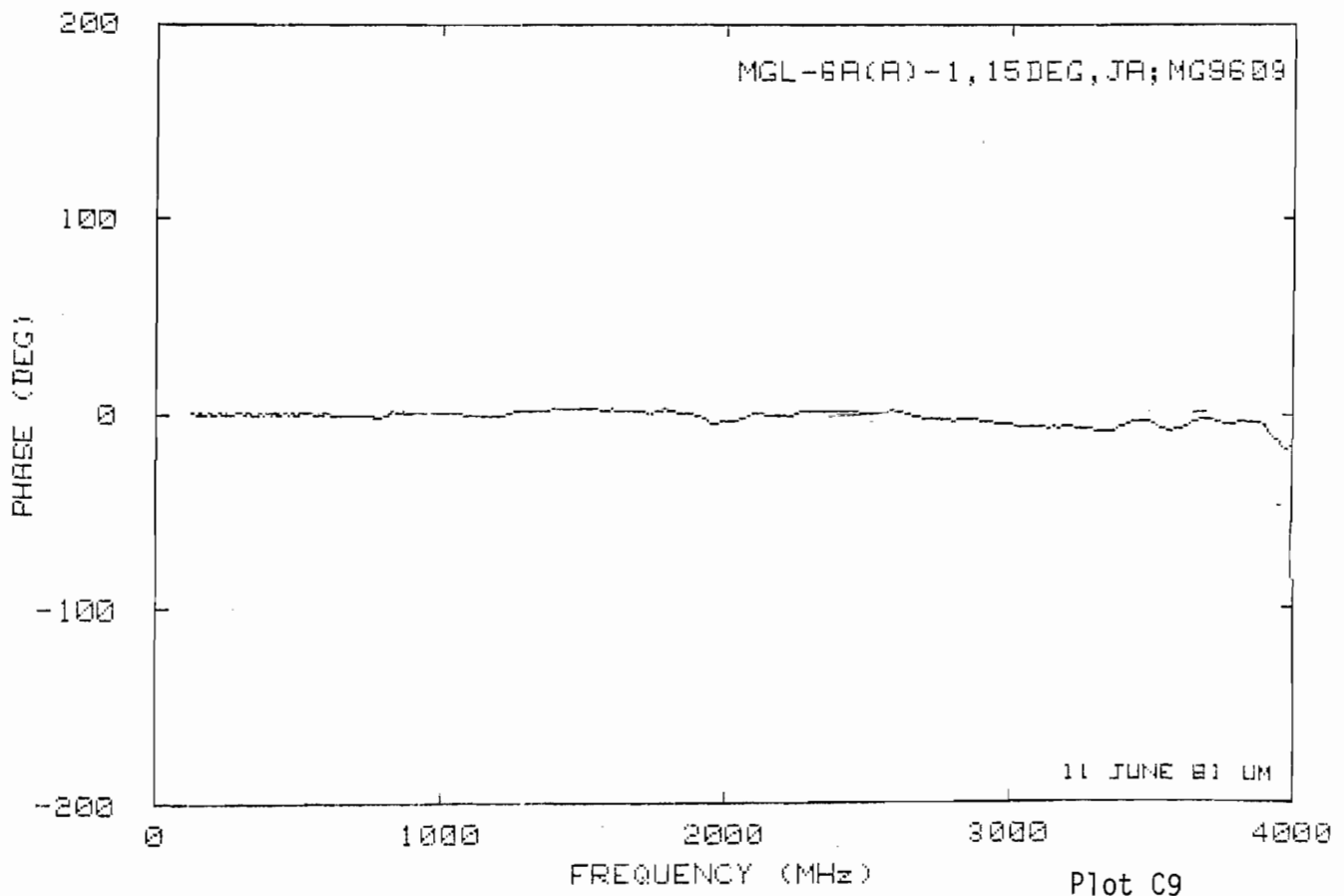
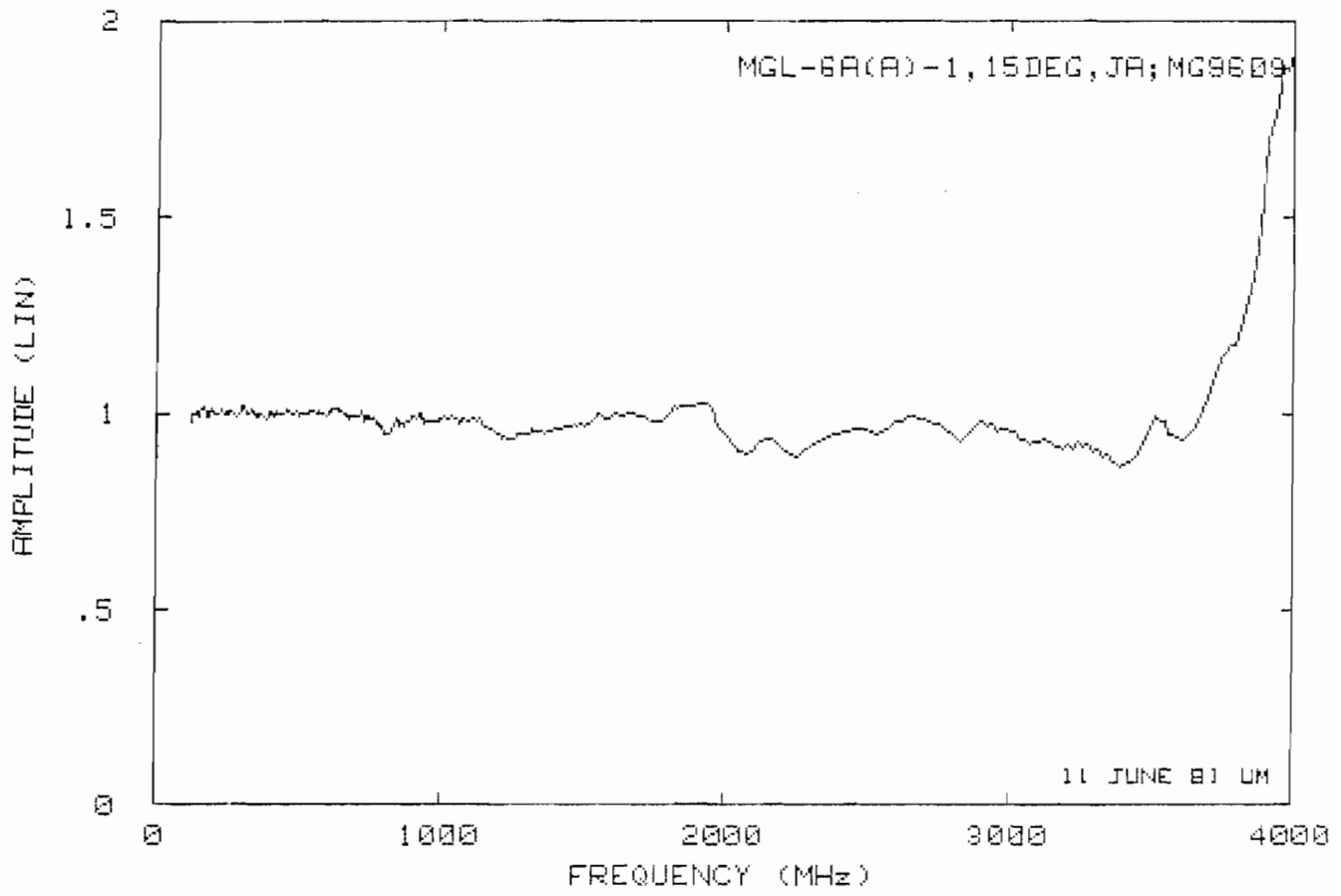
Plot C6

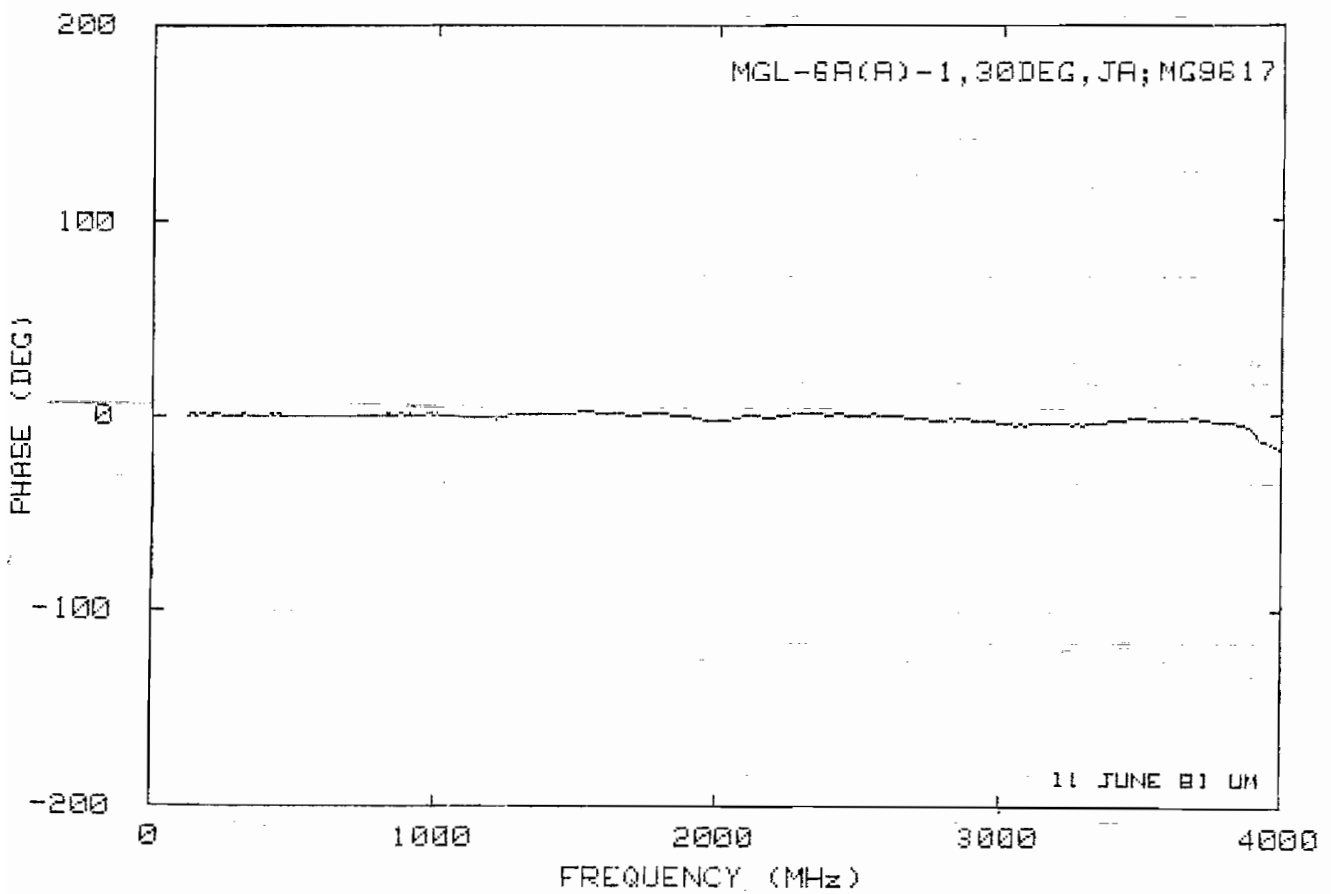
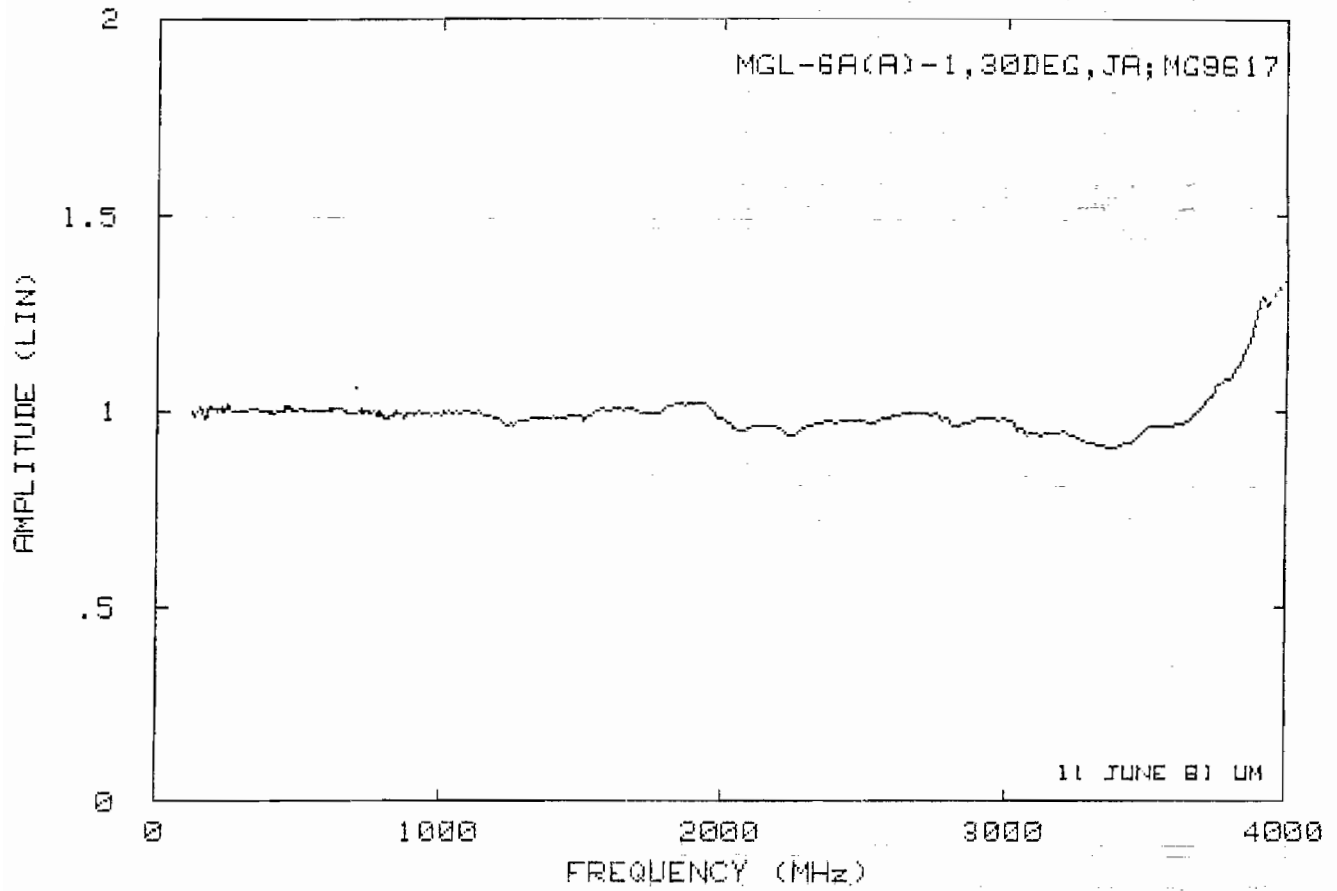


Plot C7

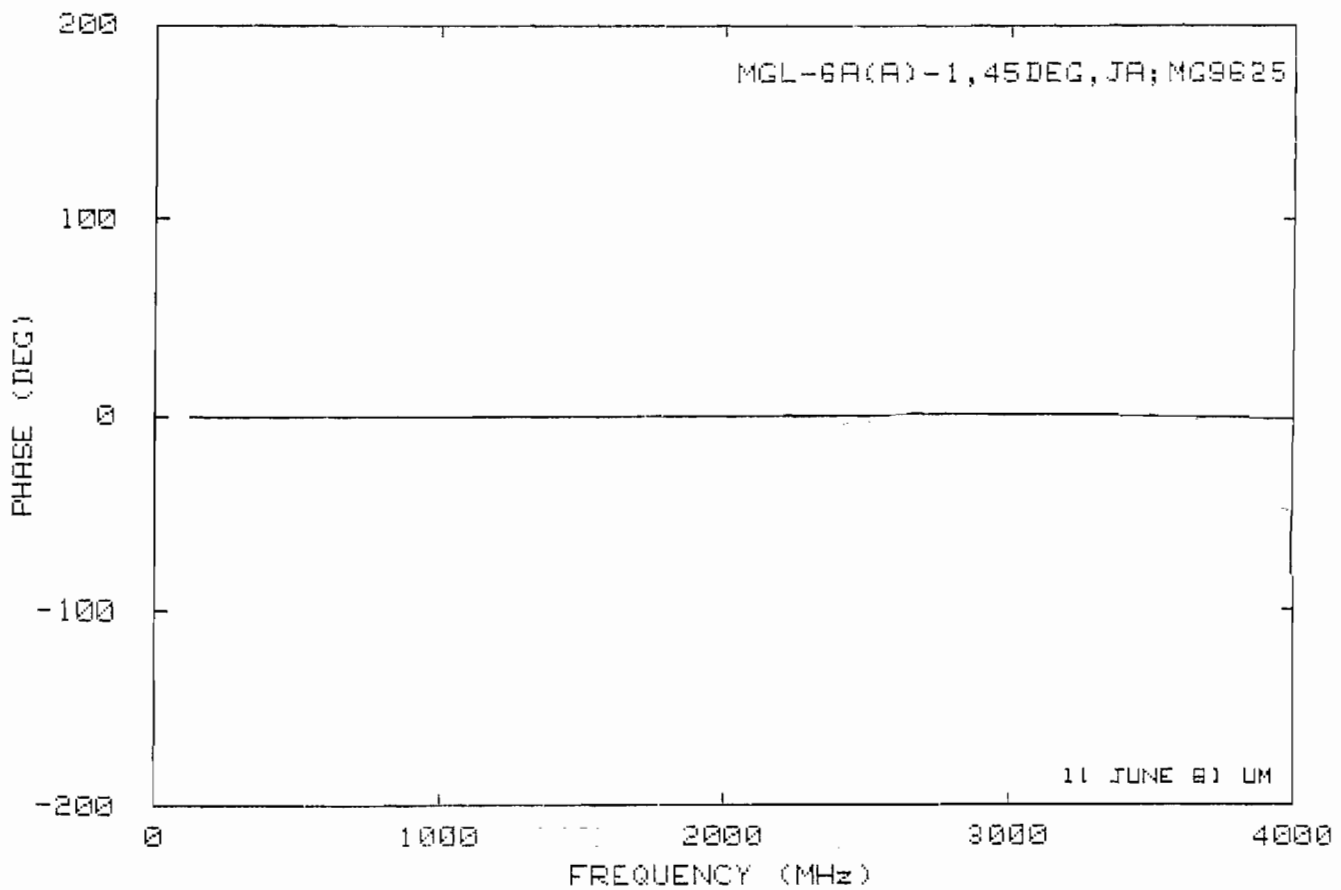
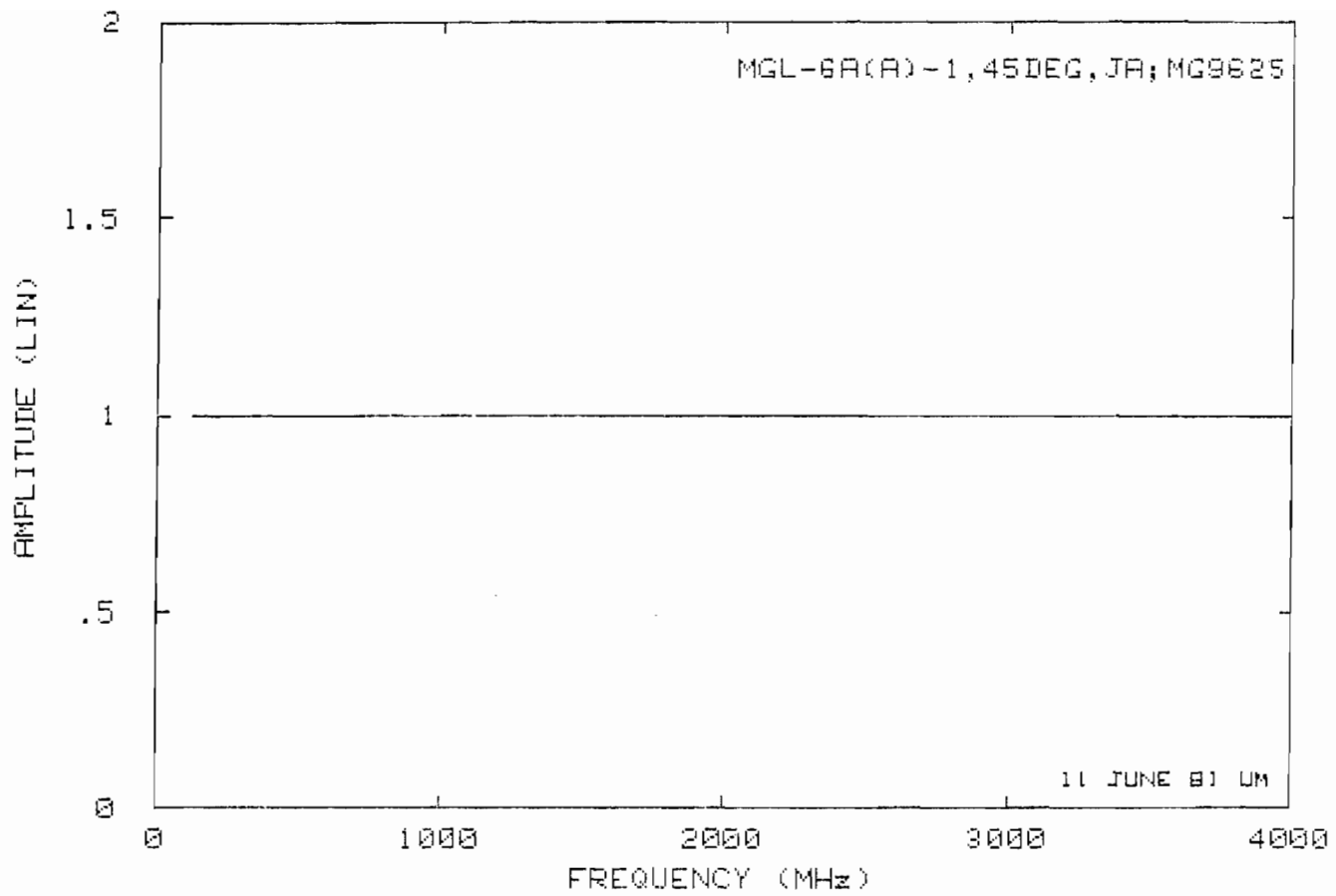


Plot C8

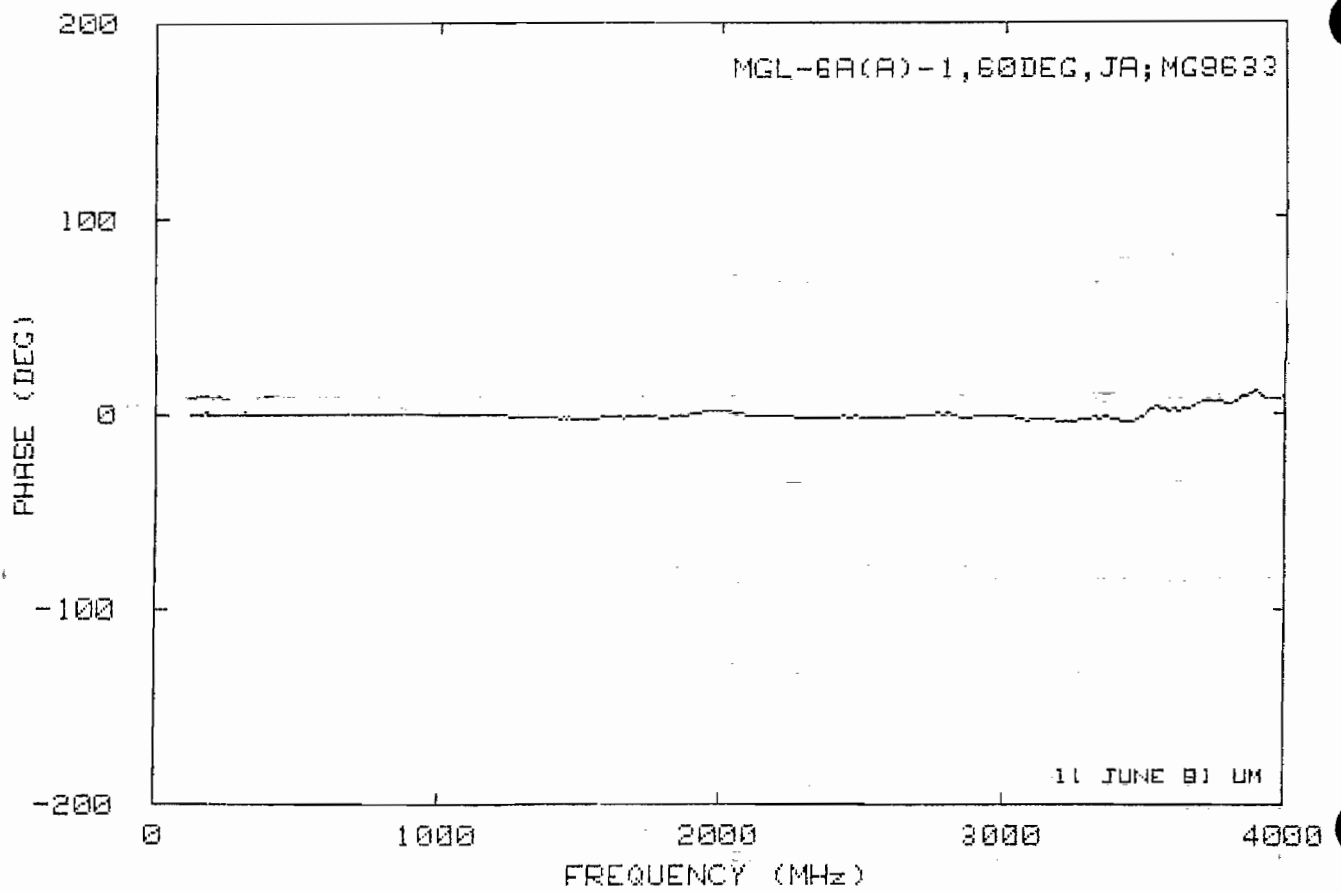
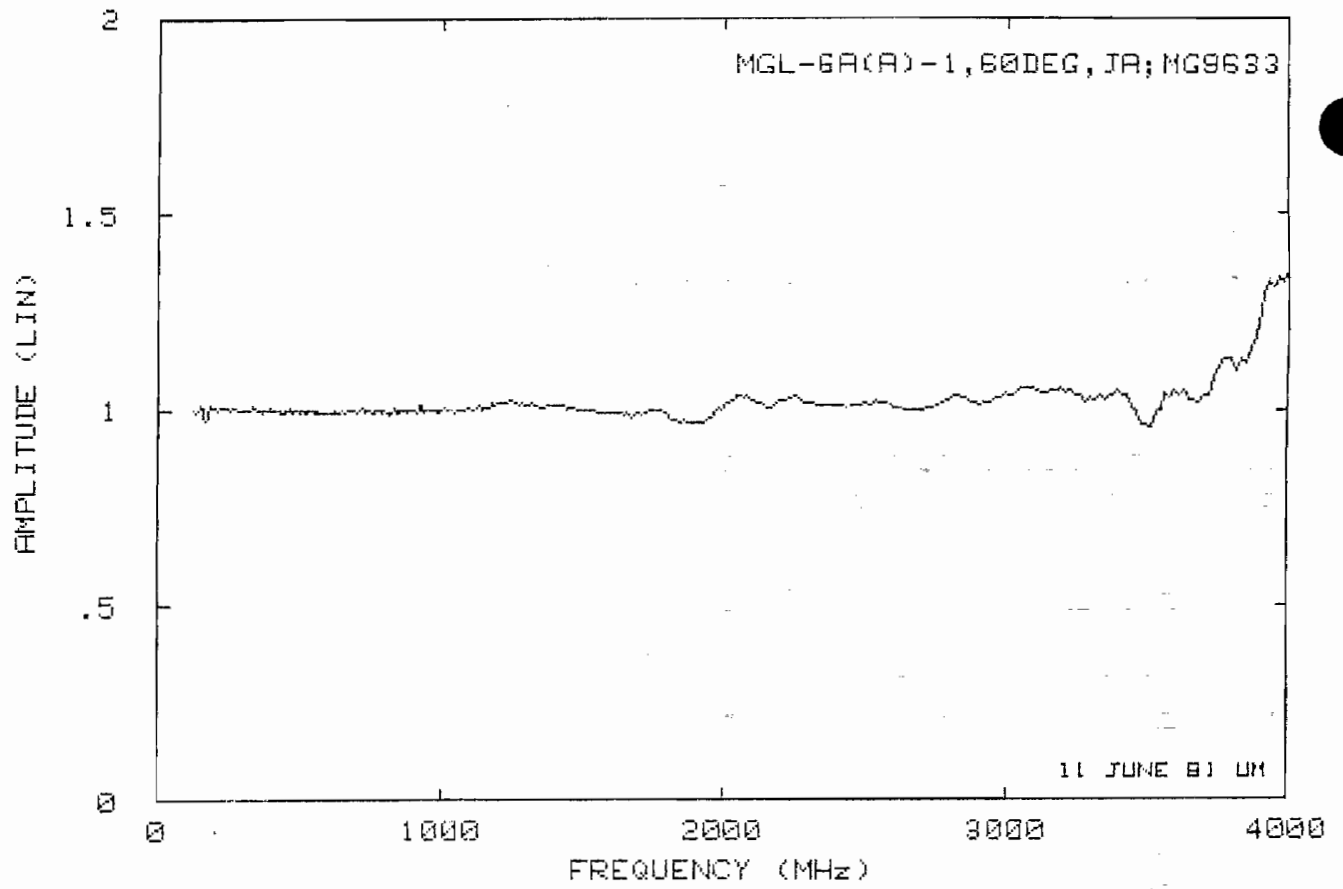




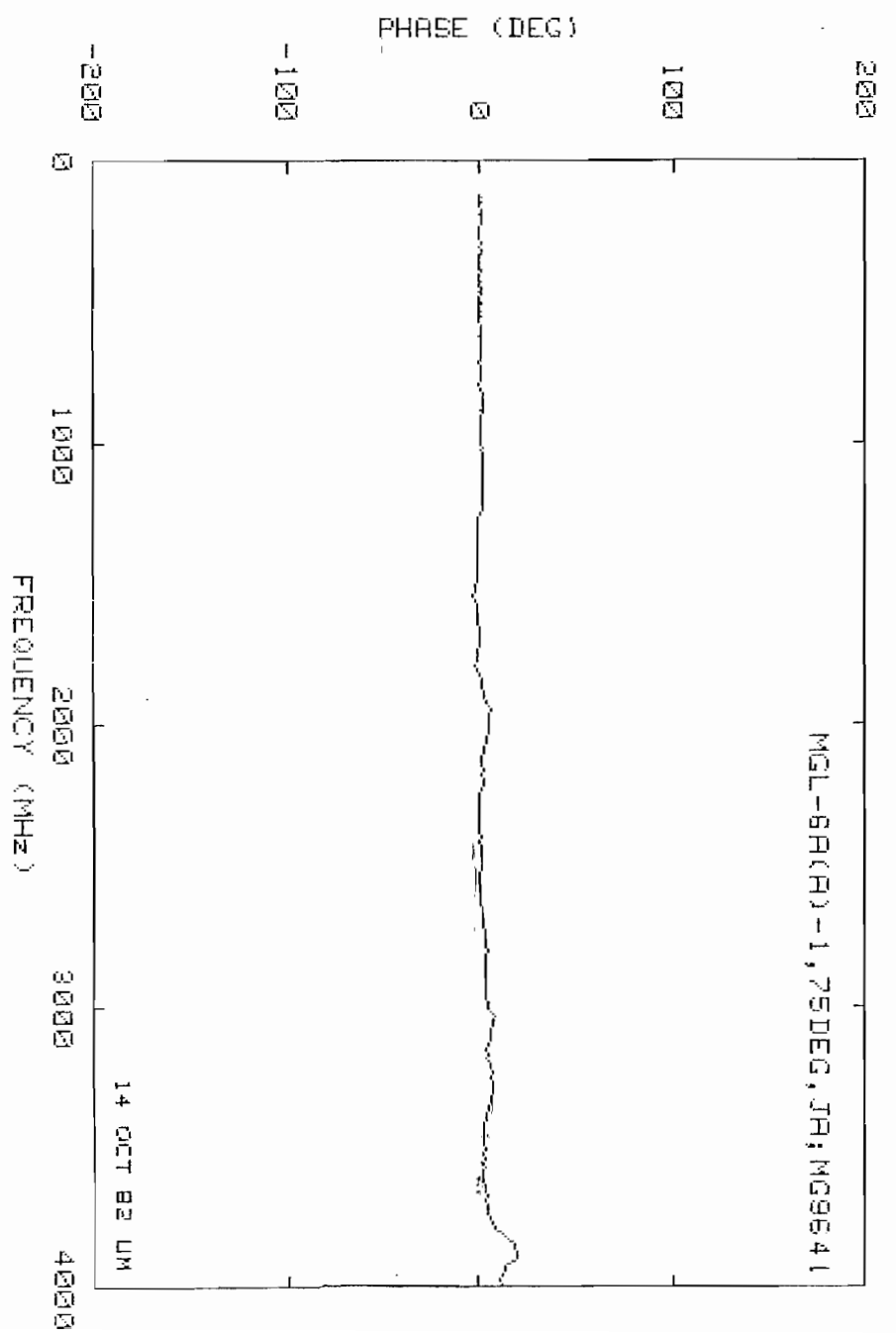
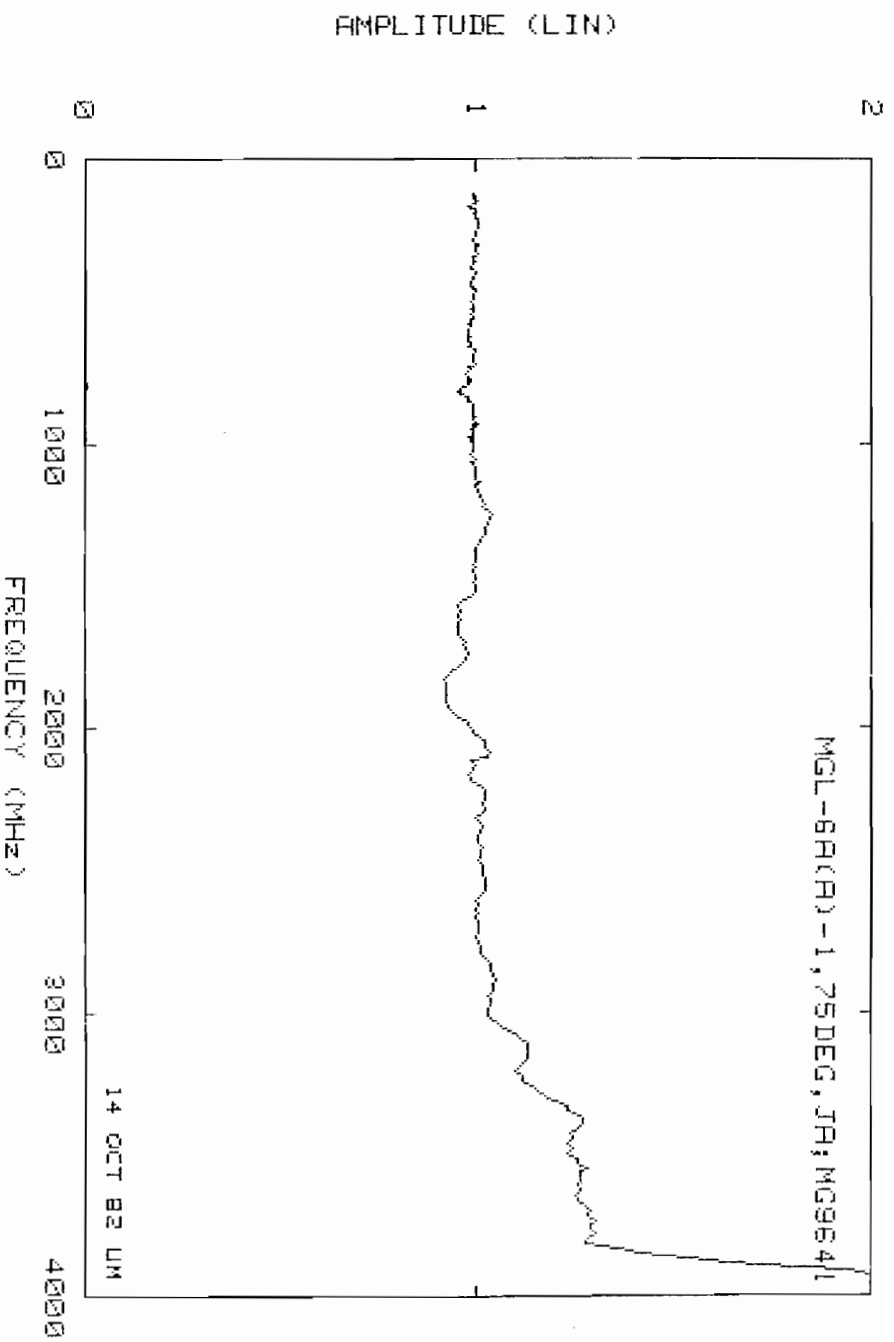
Plot C10

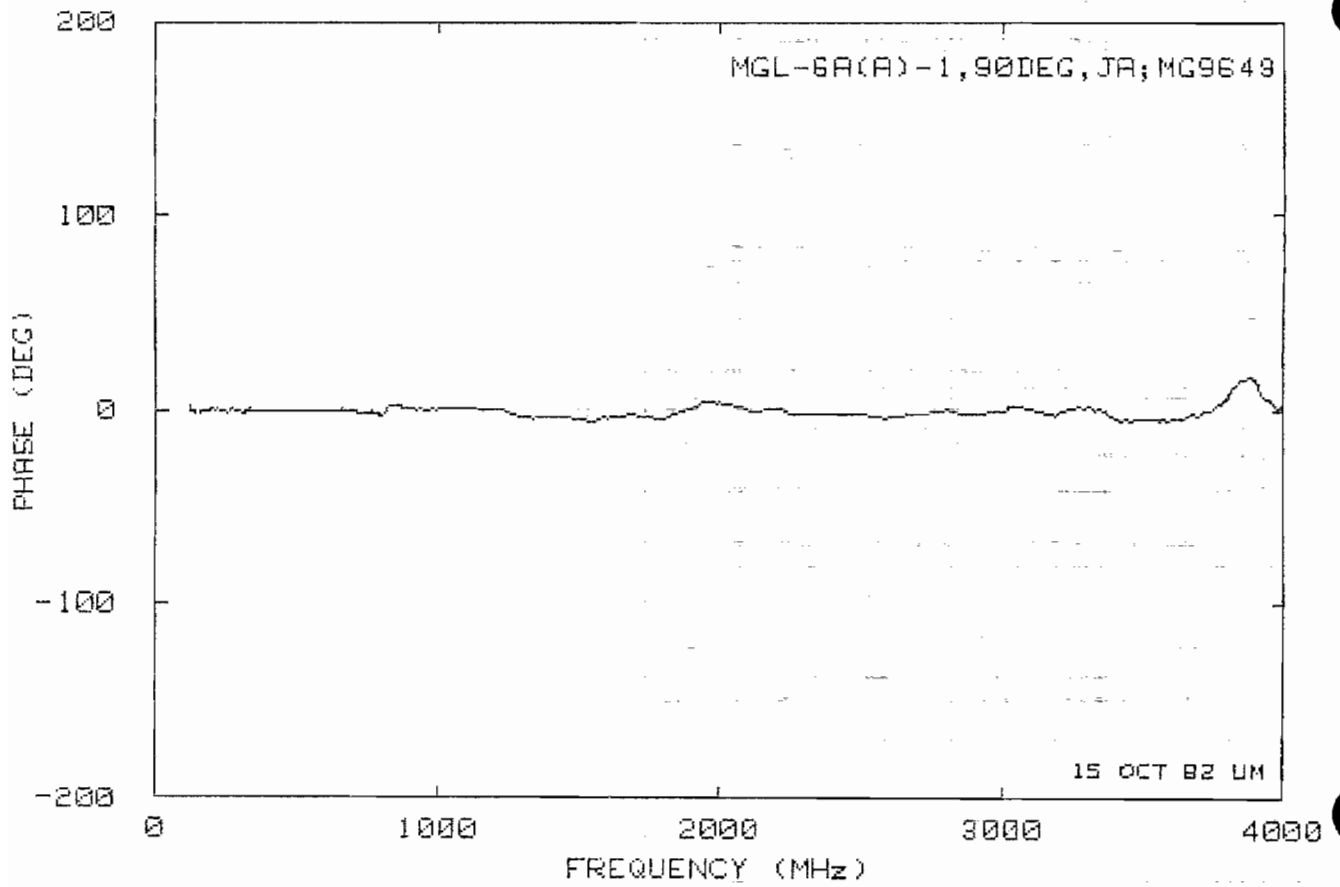
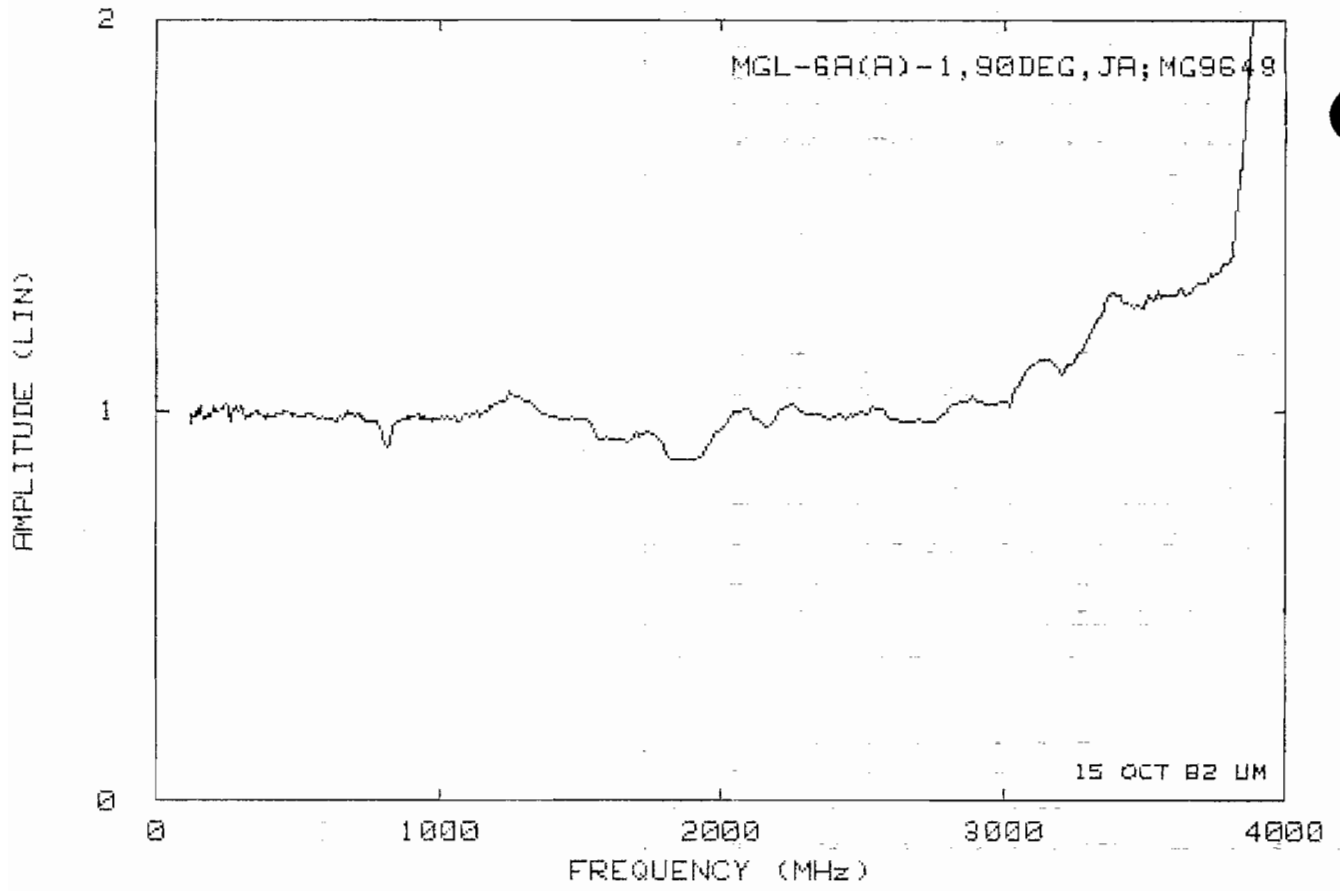


Plot C11



Plot C12





Plot C14